FACULTY
OF MATHEMATICS
AND PHYSICS
Charles University

DOCTORAL THESIS

David Wagenknecht

Theory of spin-dependent transport in magnetic solids

Department of Condensed Matter Physics

Supervisor of the doctoral thesis: doc. RNDr. Ilja Turek, DrSc.
Study programme: Physics
Study branch: 4F3

Prague 2019

I declare that I carried out this doctoral thesis independently, and only with the cited sources, literature and other professional sources.

I understand that my work relates to the rights and obligations under the Act No. 121/2000 Sb., the Copyright Act, as amended, in particular the fact that the Charles University has the right to conclude a license agreement on the use of this work as a school work pursuant to Section 60 subsection 1 of the Copyright Act.

In Prague ..... signature of the author

Dedication

Dedicated to my family, who encouraged me to pursue my dreams and supported me during work on this dissertation thesis.

Acknowledgement

I wish to thank especially to my supervisor Ilja Turek and to my advisor Karel Carva for their precious time, guidance, and patience. I would like to acknowledge collaboration with all coauthors of my publications, especially with Václav Drchal, Josef Kudrnovský, and Libor Šmejkal. I also greatly appreciate discussions with Dominik Legut, Karel Výborý, and Pavel Baláž. For measurement of electrical transport properties of CuMnAs compound, I would like to thank to Klára Uhlířová and Jiří Volný. Last but not least, special thanks go to the Department of Condensed Matter Physics, which is a part of Faculty of Mathematics and Physics of Charles University, and to its members and staff.

Some of the results presented in this thesis were supported by Grant Agency of Charles University under Contract 280815. In part, the work was supported by the Czech Science Foundation under Grants 15-13436S, 14-37427G, 18-07172S, and 17-27790S. Access to computing and storage facilities owned by parties and projects contributing to the National Grid Infrastructure MetaCentrum provided under the programme "Projects of Large Research, Development, and Innovations Infrastructures" (CESNET LM2015042), is greatly appreciated. This work was partly supported by The Ministry of Education, Youth and Sports from the Large Infrastructures for Research, Experimental Development and Innovations project "IT4Innovations National Supercomputing Center – LM2015070".

Title: Theory of spin-dependent transport in magnetic solids

Author: David Wagenknecht

Department: Department of Condensed Matter Physics

Supervisor: doc. RNDr. Ilja Turek, DrSc., Department of Condensed Matter Physics

Abstract: Theoretical and *ab initio* description of realistic material behavior is complicated and combinations of various scattering mechanisms or temperature effects are often neglected, although experimental samples contain impurities and modern electronics work at finite temperatures. In order to remove these knowledge gaps, the alloy analogy model is worked out in this thesis and implemented within the fully relativistic tight-binding linear-muffin-tin orbital method with the coherent potential approximation. This first-principles framework is shown to be robust and computationally efficient and, consequently, employed to investigate bulk solids and their spintronic applications. Unified effect of phonons, magnons, and alloying gives agreement with literature for temperature-dependent electrical transport (longitudinal and anomalous Hall resistivities) and scattering mechanisms are explained from electronic structures. Moreover, novel data help to identify defects in real samples and experimentally hardly accessible quantities are presented, such as spin polarization of electrical current. Calculated results for both zero and finite temperatures are reliable not only for non-magnetic and magnetic transition metals and random binary alloys but also for half-Heusler ferromagnet NiMnSb and antiferromagnetic CuMnAs. Advantages, limitations, and numerical aspects of introduced approaches are discussed with a focus on further usage for even more complex materials and in basic science.

Keywords: ab initio, temperature, electrical transport, magnetism, spintronics

Contents

Introduction

Electrical devices are a part of our everyday life. Computers or gadgets are common and user-friendly; moreover, technology is improved almost every day. Many novel technological approaches are based on discoveries of new physical phenomena, material behavior, or design of complex structures. For example, manipulation of electron spin became in the center of attention of many scientific groups, which led to a new field of physics - spintronics. For these purposes, especially magnetic solids and their transport properties are of a great importance.

Many material properties directly depend on finite temperatures and some of them even dramatically change when temperature is varied, e.g., magnetic properties of solids around their critical temperatures. Experimental examination of all of the material properties and parameters is an almost impossible task; therefore, *ab initio* techniques of modern electron theory of solids are used to design novel materials and related phenomena. Moreover, calculations are the only way to study some of the effects which are not even directly observable in experiments.

More than fifty years after the Hohenberg-Kohn theorems were published, giving rise to nowadays generally used density functional theory, *ab initio* treatment of temperature-induced effects is still a challenging task. On the other hand, finite-temperature phenomena should not be neglected because they may strongly influence, e.g., spintronic devices. Especially electrical transport properties and their correct and efficient first-principles description are essential for the purposes of novel electronics; moreover, their description is needed for complete understanding of basic physical phenomena.

Aims of the thesis Based on the short overview presented above, this thesis is focused especially on:

1. implementation of the alloy analogy model (AAM) for chemical and spin disorder and atomic displacements within the tight-binding linear-muffin-tin orbital (TB-LMTO) method with the coherent potential approximation (CPA),

2. realistic description of finite temperatures, i.e., a combined effect of atomic displacements and fluctuations of magnetic moments on the electronic structure and transport properties, and

3. study of spintronic materials influenced by various types of disorder (impurities, phonons, and magnons).

In details, the AAM deals with atomic displacements (shifts of nuclei from equilibrium positions, phonons) and magnetic disorder (fluctuations of magnetic moments, magnons) similarly to a description of multicomponent alloys. Presented methods are based on the AAM implemented within the CPA. This thesis presents theoretical investigation of spin-dependent transport in magnetic solids, numerical treatment of materials or phenomena relevant for spintronics (such as spin-disorder resistivity and structural and magnetic anisotropy), and implementation of the AAM in the existing TB-LMTO *ab initio* numerical codes.

Especially electrical transport properties are studied in this thesis for temperatures T both $T = 0$ and $T > 0$. Finite-temperature phenomena (phonons and magnons) are employed as a scattering mechanism, which gives finite electrical conductivities even for systems without chemical impurities. A combined effect of different disorders is also studied both in the scalar-relativistic and in the full Dirac approaches and calculated results agree to great extent with literature. The AAM is also used by other authors but nearly no applications of this model to electrical transport properties in complex systems (Heusler alloys, antiferromagnets, etc.) have been published; see Sec. 2.1 for an overview of approaches.

Structure of the thesis To investigate accurateness and robustness of presented methods, the treatment of finite temperatures was firstly tested on simple systems (transition metals, binary alloys). Afterwards, the combination of phonons, magnons, and impurities for complex systems (especially NiMnSb and CuMnAs) were studied. The thesis is structured in the following way: (i) Current knowledge and existing *ab initio* methods are introduced in Chapter 1, whereas later parts of the thesis show novel approaches and results. (ii) Our techniques developed or modified in order to deal with finite temperatures are presented in Chapter 2. (iii) The Chapter 3 is focused on numerical details of our methods and implementation of AAM. (iv) Calculated electrical resistivity and conductivity are discussed in Chapter 4 and the agreement with experimental or other theoretical data is shown for transition metals and random alloys. Moreover, it also shows investigation of spin-resolved conductivities and spin polarization of electrical current, which are of extreme importance for spintronics. (v) Last but not least, Chapter 5 is devoted to comprehensive studies of half-Heusler NiMnSb and antiferromagnetic CuMnAs.

Overview of publications Results presented in this thesis may be mostly found in following publications that were published (P) or submitted (S); two manuscripts are in preparation (IP) and close to a submission:

- Ref. [1] (P): An implementation of the AAM within the scalar-relativistic formalism is tested on the electrical resistivity of transition metals; finite temperature is described only by atomic displacements.

- Ref. [2] (P): Ni and Cu-Ni alloys are studied by the fully-relativistic approach; the electrical resistivity and anomalous Hall conductivity with atomic displacements are demonstrated together with the high-temperature state (disordered local moments with high magnitudes of displacements).

- Ref. [3] (P): A necessity to include spin fluctuations (stabilized by magnetic entropy) for a study of Fe and Fe-Si random alloy at the conditions of the Earth's is presented together with a discussion of atomic displacements at high temperatures.

- Ref. [4] (P): Longitudinal conductivity, the anomalous Hall effect, and spin-resolved electrical transport are investigated in Pd and Cu-Ni alloys to show an importance of the fully-relativistic transport calculations with atomic displacements.

- Ref. [5] (P): Disordered Ni-Fe alloy is described with atomic displacements and with an extension of the disordered local moment with fixed spins for two magnetic species.

- Ref. [6] (P): A pilot study of half-Heusler alloy NiMnSb with both phonons and magnons which shows half-metal's electrical transport properties including the spin-polarization of the electrical current up to the Curie temperature.

- Ref. [7] (P): The spin-disorder resistivity obtained within the scalar-relativistic formalism agree with experimental data for a wide range of magnetic materials.

- Ref. [8] (P): Different scattering mechanisms (chemical disorder, phonons, magnetic fluctuations, and electron-electron correlations) are investigated for iron-based alloys at the Earth's core conditions to investigate a validity of the Matthiessen's rule.

- Ref. [9] (S): Detailed investigation of NiMnSb presenting satisfactory agreement of the AAM with experimental data; both the temperature-induced disorder and chemical impurities are included for a treatment of electrical resistivity, the anomalous Hall effect, and the spin-polarization of the electrical current.

- Ref. [10] (IP): Anisotropy of resistivity induced by the hexagonal structure of Co, Ru, Os, and Co-based alloys is studied with finite temperatures being used as one of the scattering mechanisms.

- Ref. [11] (IP): Comprehensive study of electrical transport properties of bulk tetragonal CuMnAs comparing experimental and calculated data, including finite-temperature resistivities and anisotropic magnetoresistence for various chemical impurities.

A complete list of publications including full names of the articles and authors is at the end of this thesis.

1. Electronic origins of materials behavior

1.1 Material properties

Crystalline solids, which are in the center of attention of this thesis, exhibit various properties. With an increasing performance of computers, not only experimental techniques are used to characterize materials but also the *ab initio* methods are employed. They are based on diverse theoretical and experimental approaches and they may describe a wide range of material behavior [12, 13].

We focus on bulk magnetic materials that are relevant for spintronic applications. Among all possible properties, the most important for this thesis is the electrical transport of materials influenced by disorder, especially by chemical impurities and finite temperatures (phonons and magnons). This Chapter presents material properties that are studied on specific systems in the later parts of the thesis.

1.1.1 Magnetism

Magnetism is, in general, caused by electrical current, i.e. moving electrons, or magnetic moments of particles. This thesis is focused on transition-metal based magnetic materials. Their magnetism mostly arises from uncompensated spin magnetic moments of electrons. We note that nuclei may be also a source of magnetism, but it is negligible with respect to the magnetization caused by electrons [14]. The orbital magnetic moment of the electrons in solids is usually a few percents of their total moment (sum of spin and orbital moments).

Based on behavior in an external magnetic field, materials may be divided into several groups: diamagnets, paramagnets (PM), ferromagnets (FM), antiferromagnets (AFM), and ferrimagnets [14–16]. Moreover, other kinds of magnetism exist, e.g., superparamagnetism or spin glasses, but they are beyond the scope of this thesis.

All materials tend to oppose their orbital magnetic moments to an external magnetic field, this property is called diamagnetism. The diamagnetism is usually overwhelmed by another kind of magnetic response and the pure diamagnetic response is observed only in materials having no unpaired electrons.

The PM materials have unpaired electrons and an applied magnetic field aligns the electrons' spins to be parallel to the field. It produces net attraction of the material to the field. In the first approximation, the magnetization $\mathbf{M}$ of the PM materials is proportional to the magnetic field $\mathbf{H}$. The Curie's law then states [15]

$$\mathbf{M} = \chi \mathbf{H} = \frac{C}{T}\mathbf{H} \,, \tag{1.1}$$

where χ is a material-specific susceptibility. The second part of the Eq. 1.1, where C is the Curie constant, describes a decrease of the magnetization for nonzero temperature T.

The magnetic moments of the FM materials are aligned by the external field similarly to the PM systems; moreover, the moments have a tendency to be parallel to each other. They are aligned in this way bellow the Curie temperature T_C and for $T > T_C$ the temperature-induced fluctuations of the magnetic moments overwhelms the decrease of energy caused by the FM order. For the susceptibility

above T_C, the following holds (the Curie–Weiss law, [15])

$$\chi = \frac{C}{T - T_C} \ . \tag{1.2}$$

The AFM materials have zero net magnetization, which is caused by compensation of the magnetic moments on different sublattices. The compensation may be based on strictly opposite magnetic moments (on two sublattices) or on more directions of the moments canceling out each other (noncollinear AFM). Various directions of the moments also lead to geometric frustration observed for some of the AFM, i.e., a possibility of different ground states [17]. The AFM behavior is observed bellow the Néel temperature T_N.

The ferrimagnets have also antiparallel alignment of the magnetic moments, but the magnitudes on the different sublattices are not identical, which results in nonzero net magnetization.

1.1.2 Chemical disorder

Real crystalline materials, which can be found in nature, are almost never perfectly pure and ideal because they are influenced by both chemical impurities and geometrical defects. Similarly, it is difficult to prepare ideal samples, even by state-of-art experimental methods. For example, in Sec. 5.1 we study half-Heusler NiMnSb and we note that defects are discussed intensively in literature even for thin layers created by state-of-art molecular beam epitaxy [18]. The situation is even more complicated in more complex materials such as antiferromagnetic CuMnAs, see Sec. 5.2 or Ref. [19]. Because of that, combined experimental and theoretical effort for identification of defects in real samples is of extreme importance. Material behavior influenced by chemical disorder has been a point of interest of many studies and substitutional disorder (in random alloys on a non-random lattices) is usually treated by the CPA (Sec. 1.2.5 or Ref. [12]) or supercell techniques. For purposes of this thesis, we consider chemical disorder to be well described by uncorrelated impurities on different atomic sublattices that are analytically averaged by the CPA. The *ab initio* approaches are usually based on an assumption that impurities causing a microscopic fluctuations in chemical composition do not influence original symmetry of a perfect crystal on a macroscopic scale.

Specific selections of chemical disorder extremely depend on studied systems and relevant experimental data. Criteria for examination of impurities are usually based on their formation energies and agreement of the residual resistivity (later ρ_0 in Fig. 1.1) with experiments. However, the impurities may influence not only ρ_0 but also slopes of resistivities as functions of temperature, see later Sec. 5.1.

1.1.3 Finite-temperature phenomena

Electrical transport at finite temperatures Zero-temperature electrical transport properties are influenced mainly by chemical disorder or by electron scattering related to noncollinear magnetic moments, e.g., in AFM materials. Although many *ab initio* studies describe systems without temperature-induced disorder, real-life material behavior may vary dramatically with changing temperature. For electrical transport properties, the most important temperature

dependent scattering mechanisms are phonons (displacements of nuclei from their equilibrium positions) and magnon (fluctuations of magnetic moments).

An illustration of different scattering mechanisms influencing transport properties is shown in Fig. 1.1. (The illustration is only schematic; e.g., depending on the contributions of magnetic disorder, the shown extrapolation may be quadratic instead of linear.) Validity of the Matthiessen's rule is assumed in this Figure, i.e., the total resistivity is given by the sum of different contributions (inverse values of scattering times coming from the different mechanisms add up).

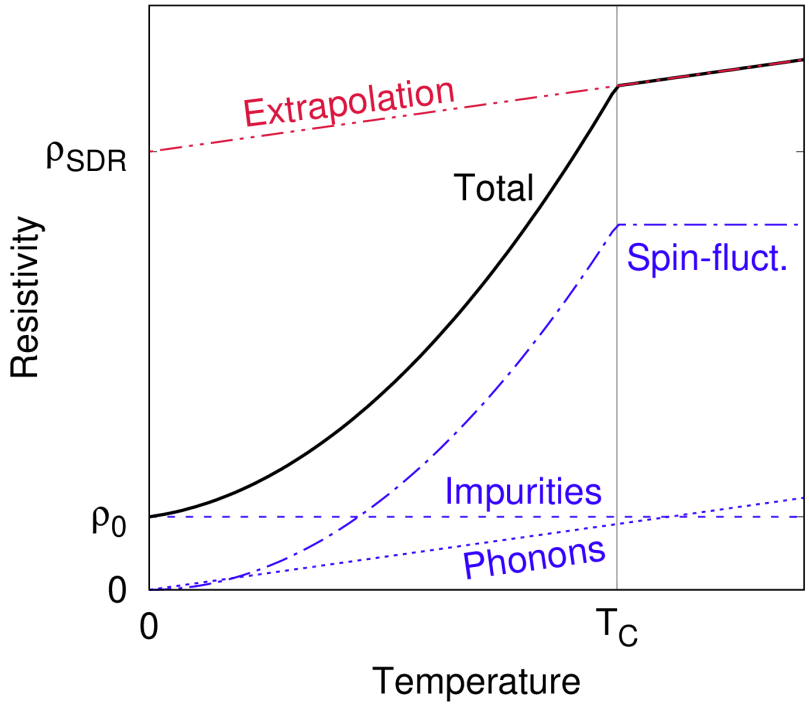

Figure 1.1: If we assume validity of the Matthiessen's rule, different scattering mechanisms linearly contribute to the total resistivity. In this schematic dependence of resistivity in a magnetic material $\rho_{\text{imp.}} = \text{const.}$, $\rho_{\text{phon.}} \sim T$, $\rho_{\text{sf}} \sim T^2$ (bellow T_C), and the total resistivity is the sum of them. Extrapolation from the temperatures above T_C to $T = 0$ gives the spin-disordered resistivity ρ_{SDR}.

The total longitudinal resistivity ρ then has an approximate form [20]

$$\rho(T) \sim \rho_{\text{imp.}} + AT + BT^2 \tag{1.3}$$

which was originally obtained for Heusler alloys [21] and where A and B are material specific parameters. Number of chemical impurities does not change with temperature; therefore, the resistivity caused by them $\rho_{\text{imp.}}$ is assumed to be constant and equal to the residual resistivity at zero temperature. The linear dependence on temperature comes from phonons ($\rho_{\text{phon.}}$) and it is valid for temperatures above the Curie temperature, i.e., for $T \gg T_C$ [20, 22]. This dependence comes from the number of phonons that contribute to the scattering. For temperatures much lower than the Debye temperature Θ_D, the behavior of the resistivity is more complicated and one can expect the dominant contribution of the Bloch T^5 law giving [22, 23]

$$\rho \sim T^5 \quad \text{for} \quad T \ll \Theta_D\,. \tag{1.4}$$

This thesis deals with the most basic scattering effect in crystalline solids, i.e., displacements of nuclei from their equilibrium positions. For this purpose, we omit more advanced phenomena that may affect the temperature-dependent electrical transport. We also omit phenomena related to complex behavior of the electronic structure such as the Kondo effect [15] or the decrease of resistivity with increased temperature in metallic systems [24] that are not directly included in the linear response theory.

Spin fluctuations (resistivity ρ_{sf}) play important role at high temperatures (with respect to the T_C) in materials with nonzero magnetic moments, see later Fe or Ni in Sec. 4.2. The contribution of magnons is approximately quadratic on temperature; therefore, the low-temperature behavior is usually given by impurities and phonons. Disorder caused by fluctuating magnetic moments reaches the maximum at T_C and above it a ferromagnetic material behaves like a paramagnetic one. Spin-disordered resistivity ρ_{SDR} may be obtained from both experimental and theoretical data by extrapolating a high-temperature resistivity from the region with constant ρ_{sf}, i.e., $T > T_C$, to the zero temperature and as such it describes the effect of magnetic disorder alone.

We would like to emphasize that Eq. (1.3) is only approximate and many experimental studies interpolate measured data in order to obtain more precise dependence for investigated materials [25]. For examples, semi-Heusler compound NiMnSb (T_C = 730 K) has $\rho \sim T^{1.35}$ for T below the room temperature and $\rho \sim T^2$ for less than 50 K [26].

Deviation from Matthiessen's rule, i.e., the resistivity is not given by a mere addition of independent contributions originating from individual effects, was observed for BCC iron at ambient [27].

Phonons Phonons, i.e., collective movement of atoms in studied (elastic) bulk solids, are usually treated as quantized vibrations of interacting particles. They are characterized by modes of vibrations having energies and, consequently, by phonon spectra specific for each material. Phonons may be described by both classical and quantum models, as well as by *ab initio* approaches, and they are closely related to a wide range of phenomena such as heat capacity or magnetostriction [13, 15, 23]. Here we present only the most important characteristics of atomic vibrations relevant for our purposes.

The Debye and Einstein models describe phonon spectra by normal-mode dispersion relations of simple structures [23]. The first one approximates all branches of the spectrum by the same linear dispersions and, moreover, integration over the Brillouin zone is replaced by an integral over a sphere (maximal phonon frequency ω_D). It is also convenient to introduce the Debye temperature Θ_D (the temperature above which all modes begin to be exited) by the relation

$$\Theta_D = \frac{\hbar v}{k_B}\left(\frac{6\pi^2 N}{V}\right)^{1/3}, \tag{1.5}$$

where $\hbar$ is the reduced Planck constant, k_B is the Boltzmann constant, v is the constant velocity of sound, and N is the number of atoms in the volume V [15]. The Debye temperature typically ranges from 100 K to 600 K for transition metals, it may be used as a single empirical parameter in a relation for the specific heat, and (in the harmonic approximation) it also connects the specific

heat to phonon spectra [23]. In the Debye model, also the optical branches of the phonon spectrum are approximated by a linear relation; it may be improved by the Einstein model which describes the optical branches by constant frequency.

Limitations of both models can be shown in terms of the phonon density of states. For the Debye approach, it is parabolic below ω_D and zero for frequencies $\omega > \omega_D$ [23]; however, this is not always true for real phonon density of states. Figure 1.2 shows measured data for iron at several pressures [28] and the densities may be even more complicated for more complex systems. Despite that, the mean-squared displacement of atoms (a deviation of particles due to temperature-induced excitation) derived from the Debye model is often used and it gives satisfying results for many materials [29–32], see later Sec. 2.3.1. We note that even *ab initio* treatment of phonons often neglects their mutual relations with magnons or other effects and advanced methods such as atomistic spin dynamics simulations [33] are needed for more proper description.

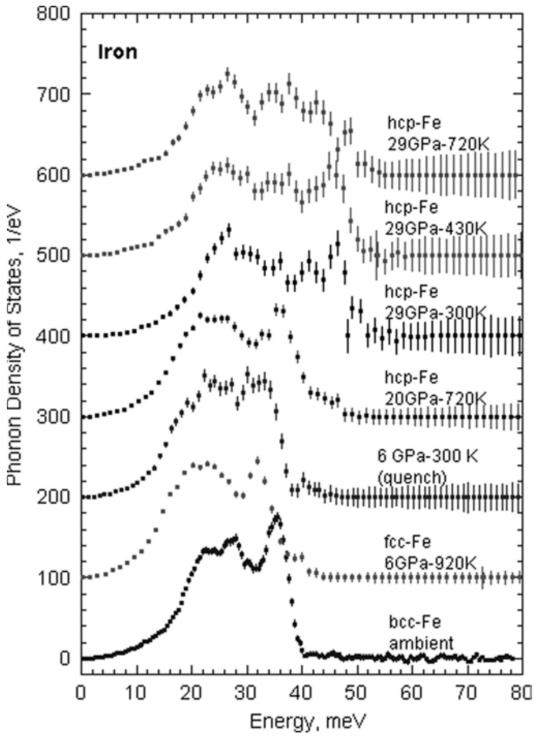

Figure 1.2: Phonon density of states of iron is parabolic-like only for small energies. Obtained from Ref. [28], vertical offset used for different measurements.

Magnetic disorder caused by finite temperatures Magnetic materials consist of atoms that have their magnetic moments mutually aligned. The main contribution to atomic magnetic moments comes from the spin of their unpaired valence electrons and the minor one is caused by their orbital angular momenta. Materials with positive interatomic exchange interactions in the Heisenberg Hamiltonian favor spontaneous order with parallel magnetic moments – ferromagnets; compared to that, negative results in antiferromagnetic ordering [15].

For nonzero temperature, the exchange interaction competes with thermal fluctuations of local moments. If temperature is higher than a critical point,

temperature-induced fluctuations are stronger than the magnetic interaction. Consequently, it leads to paramagnetic behavior of previously ordered materials. This is an effect of the second-order phase transition and the critical point is called the Curie (T_C for FM) or Néel (T_N for AFM) temperature. Typical Curie temperature is several hundred kelvins ($T_C^{\mathrm{Fe}} \approx 1043$ K, $T_C^{\mathrm{Co}} \approx 1400$ K, $T_C^{\mathrm{Ni}} \approx 627$ K) and magnetization of FM, which is largest at zero temperature, vanishes at this point.

In the first order approximation for low temperature T, the dependence of spontaneous magnetization for systems with negligible magnetic anisotropy is described by the Bloch's law [23]

$$m(T) = 1 - \left(\frac{T}{T_C}\right)^{3/2} \tag{1.6}$$

with $m(T) = M(T)/M(T=0)$ being reduced spontaneous magnetization. For example, $M(T=0) = 2.23\mu_B$ for Fe and $M(T=0) = 0.69\mu_B$ for Ni. A better description is obtained by fitting experimentally observed magnetization to a function [34]

$$m(T) = \left[1 - s\left(\frac{T}{T_C}\right)^{3/2} - (1-s)\left(\frac{T}{T_C}\right)^{p}\right]^{1/3} \tag{1.7}$$

with empirical parameters p and s (Fe: $p = 4$, $s = 0.35$; Ni: $p = 5/2$, $s = 0.15$). This dependence is shown in Fig. 1.3 for Fe and Ni. We note that for $T = T_C^{\mathrm{Ni}}$, where the magnetization of Ni vanishes, the magnetization of iron is still above 90 % of its maximal value.

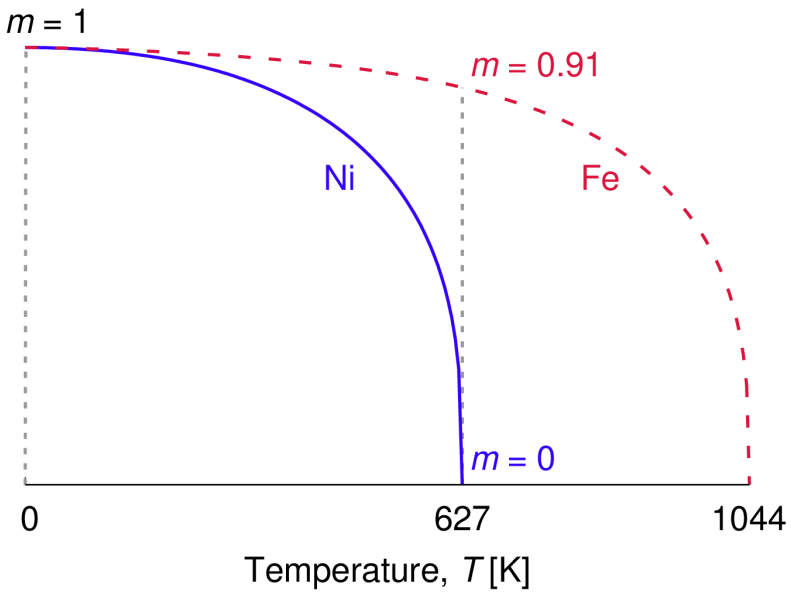

Figure 1.3: Reduced spontaneous magnetization decreases slowly from temperatures higher than approximately half of the Curie temperature; above this value the decrease is much more significant. It is illustrated on comparison of Ni and Fe having $T_C^{\mathrm{Ni}} \approx 0.6 T_C^{\mathrm{Fe}}$.

Better and more precise dependence of magnetization on temperature is obtained by *ab inito* simulations [29, 32, 33, 35], but expression (1.7) is accurate enough to, e.g., obtain temperature dependence of resistivity, see later Sec. 4.2.

1.1.4 Electrical transport

A detailed description of electrical transport properties and their evaluation within the TB-LMTO method with the CPA is described later in Sec. 1.3 and 2.4. Here we present a short summary of the electrical transport from the point of view of material behavior. For details, see, e.g., [15].

A basic division of materials based on their electrical transport properties leads to three groups: conductors, semiconductors, and insulators. Insulators contain no free charge carriers; therefore, they do not conduct electric current. The presence of no free charge carriers is related to their large energy-gap (large energy difference between the valence and conduction band) and no electron states at the Fermi level. Semiconductors have the energy gap of a few eV, e.g., from almost zero to approx. 2 eV (2.3 eV for GaP, 2.5 eV for CdS) [15]. However, there are also the wide-bandgap semiconductors having the gap even about 4 eV and sometimes also diamonds (with impurities) are considered to be semiconductors with the gap about 5.4 eV [15]. The large gap is suitable, e.g., for optics or radars. We note that the division is not given strictly and the possibility of nonzero electrical conductivity depends on many external phenomena such as temperature or applied voltage, which may excite charge carriers.

For the purposes of this thesis, the conductors are the most important. We focus on metals having free electrons because of their metallic bonding and we only note that also other mechanisms of electrical conduction exist, such as solved ions in melting or dissolving salts. From the point of view of the electronic structure, metals have nonzero density of states (DOS) at the Fermi level, i.e., no energy gap. Because of that, the carriers may move from the valence to conduction band when only a small voltage is applied. Although most of the metals have carriers on the Fermi level because of a crossing of energy bands, semimetals have the lowest part of the conduction band in a different part of momentum space than the top of the valence band. Therefore, there is no crossing of the bands and semimetals can be formally described as semiconductors with the negative band gap. For example, alkaline earth metals are the most famous semimetals, but we do not investigate semimetals in this thesis. Half-metals are metals which conduct electric current only for one spin channel, the second is insulating [36]. It is caused by the nonzero total DOS for one spin orientation but zero for the opposite one. Half-metals have many potential applications in spintronics, one of the most famous half-metallic compounds is a class of Heusler alloys; Sec. 5.1 of this thesis is focused on half-Heusler NiMnSb, including a discussion of its half-metallic character.

The temperature-dependent resistivity behaves differently for the above mentioned groups of materials. In a typical metallic systems influenced by phonons and magnons, the electrical resistivity increases with temperature (see Fig. 1.1). On the other hand, insulators do not conduct electric current at any temperature; therefore, the conductivity is always zero. Semiconductors have zero conductivity without temperature-induced disorder; however, increasing temperature may excite carriers to the conduction band and the electrical conductivity then becomes nonzero. Therefore, in contrast to metals, electrical resistivity of semiconductors decreases with temperature.

The electrical properties of monocrystals are usualy described by a tensor of electrical conductivity $\boldsymbol{\sigma}$ with components $\sigma_{\mu\nu}$, where $\mu, \nu \in \{x, y, z\}$. It

characterizes a response (in terms of the current density $\mathbf{j}$) of a material when the electric field (with intensity $\mathbf{E}$) is applied. The Ohm's law then states

$$\mathbf{j} = \boldsymbol{\sigma}\mathbf{E} \ . \tag{1.8}$$

The often used resistivity tensor $\boldsymbol{\rho}$ is given as the inverse value of the conductivity, i.e., $\boldsymbol{\rho} = \boldsymbol{\sigma}^{-1}$. The antisymmetric part of the conductivity tensor describes the anomalous Hall conductivity (AHC).

Both the electrical resistivity and the electrical conductivity are intrinsic properties, i.e., they do not depend on geometrical characteristics of samples. Therefore, they are used in this thesis focused on *ab initio* calculation of material properties. The most simple connection to real measurements can be done for an ideal wire with the length l and the cross-sectional area A. It has resistivity ρ_{xx} if the measured electrical resistance R_{xx} along the $x-$direction is

$$R_{xx} = \frac{l}{A}\rho_{xx} \ . \tag{1.9}$$

To eliminate an influence of the shape, more advanced multiple-probes techniques such as the van der Pauw method are often used for measurements.

1.1.5 Galvanomagnetic phenomena

Knowledge of the electrical conductivity tensor opens a possibility to study also the anomalous Hall effect. If the magnetization in a system points to the $z-$axis, we have for the AHC

$$\mathrm{AHC} = \sigma_{xy} \ , \tag{1.10}$$

which is a nondiagonal element of the conductivity.

The AHC is often divided into intrinsic and extrinsic contributions. The first one depends only on the electronic structure of a material, whereas the second one is explained by the side jump and skew scattering mechanisms [37]. The intrinsic AHC, independent on the longitudinal σ_{xx}, can be obtained in terms of geometric Berry-phase curvatures and, therefore, it is a property of a perfect crystal [37]. Later, see discussion of AHC and its contributions in NiMnSb in Sec. 5.1.

The anisotropic magnetoresistance (AMR) is defined by [38, 39]

$$\mathrm{AMR} = \frac{\rho_{\parallel} - \rho_{\perp}}{\rho_{\mathrm{avg.}}} \ , \tag{1.11}$$

where $\rho_{\parallel}$ and $\rho_{\perp}$ are the longitudinal resistivities for currents parallel and perpendicular, respectively, to the magnetization and $\rho_{\mathrm{avg.}}$ is an average resistivity. Assuming cubic symmetry (the magnetization in the $z-$direction, $\sigma_{xx} = \sigma_{yy} \neq \sigma_{zz}$), one can immediately obtain

$$\mathrm{AMR} = \frac{\rho_{zz} - \rho_{xx}}{\rho_{\mathrm{avg.}}} \ . \tag{1.12}$$

We note that the definition of the AMR may slightly differ according to different authors [38–41]: The average resistivity may be $\left(\rho_{\parallel} + 2\rho_{\perp}\right)/3$ or $\left(\rho_{\parallel} + \rho_{\perp}\right)/2$, but since $\rho_{\parallel}$ and $\rho_{\perp}$ are usually close to each other, the difference is typically

negligible. Moreover, the sign of the AMR depends on the definition, i.e., the order of terms in the numerator of Eq. (1.11) or (1.12). The standard definition of the AMR (1.11) can be extended and its origin explored in terms of noncrystalline and crystalline components, see Ref. [42] for cubic systems.

1.1.6 Spintronics and related materials behavior

Spintronics is a field of physics focused on manipulation with spins of electrons. There is no exact year when the spintronics was founded; however the spin-resolved conductivity became more important after it had been described by the two-current model [43, 44]. In recent years, it resulted in many novel employed techniques, discovered phenomena, and designed devices. For detailed review of spintronics, we refer to [45] and for summary of spintronic materials to [46]. Moreover, the AFM spintronics became popular, see Ref. [47, 48]. Although a complete overview of current spintronic topics is beyond the scope of this Section, we comment about some of them.

Longitudinal electrical transport and the spin polarization The longitudinal electrical transport had been studied even many years before the spin degree of freedom and related properties of electrons were discovered. On the other hand, when the majority-spin and minority-spin channels of the electrical current can be distinguished, it is convenient to define the spin polarization, see later Eq. (2.51). (The notation of the carriers majority and minority spin is usually used in FM materials [45].) The polarization is closely connected to the spin injection of the polarized electrons and especially half-metallic materials are studied because of their ideal polarization being almost unity. Theories and experiments related to the spin injection are summarized in Ref. [45]. We note that not only electrical injection but also optical methods may be used to generate the spin-polarized currents [45].

Hall effects The family of the Hall effects contains phenomena related to transverse electrical transport influenced by a magnetic field or local magnetic moments. The external field is necessary for the (original) ordinary Hall effect and the quantum Hall effect; the field of local moments is sufficient for an observation of the anomalous Hall effect. The spin Hall effect describes an electric current causing a spin current. It is caused by both the intrinsic (asymmetries in the material lead to disordered trajectories of carriers due to spin–orbit interaction) and extrinsic (spin-dependent Mott scattering) mechanisms [49]. In two-dimensional semiconductors with strong spin-orbit coupling, such as in HgTe, the quantum spin Hall effect may be observed [50]. It results in edge channel transport of current in absence of external magnetic field. Moreover, also fractional Hall effects exist, but they are above scope of this thesis.

The interaction between the charge carriers and the moments is related to the relativistic phenomena (spin-orbit coupling); therefore, they are closely connected to the spintronic field of interest. For specific applications, there are many possible usages of the Hall effects. For example, the anomalous Hall effect [37] in antiferromagnets was proposed to be used for switching and memory devices [51] and it was recently turned on and off by the strain in Mn_3Pt [52]. Similarly, the

spin Hall effect [53] was predicted to be able to induce measurable spin polarization [54]. We note that some of the Hall effects may be undiscovered; see, e.g., the recently described crystal Hall effect [55].

Real spintronic devices Much effort has been devoted to research and design of novel electrical devices based on spintronic principles. If not only the presence of electrons but also their spins can be manipulated, it could lead to much better efficiency of the devices or even to a construction of completely new components for the present electronics. For a review of spintronic-based random access memories, see [56]. To name some of the novel devices or possible applications of spintronics, the electric currents were proposed to be used for an ultrafast spin-axis reorientation in AFM in 2014 [57]. It was used only two years later to manipulate the magnetic moments in AFM CuMnAs [58], and in 2018 the spin-orbit torques were used to achieve a large change of resistivities in AFM Mn_2Au [59].

1.2 Density functional theory

In this section, we introduce the density functional theory (DFT) and methods of *ab initio* calculations. Especially those used in the rest of this thesis are described in more details and with the focus on electrical transport properties. The starting point is to find a solution of the Schrödinger or Dirac equations for a many-body system. Exchange-correlation potentials are then discussed and the fully-relativistic DFT is described. Last but not least, the tight-binding (TB) linear-muffin-tin orbital (LMTO) method and the coherent potential approximation (CPA) are introduced.

1.2.1 Short overview of DFT approaches

Calculations from the first principles, or *ab initio* calculations, represent a generic name for a large area of computational methods that focus on obtaining results, usually material properties, "from the very beginning". It means that no assumptions or models should be taken into account except of basic physical laws and values of physical constants. In the condensed matter physics, quantum mechanics is considered to be the set of these established laws of nature and the "beginning" is usually based on solving the Schrödinger or Dirac equation. Solutions are often obtained within the Born-Oppenheimer approximation that assumes fixed positions of nuclei. This approximation is usually sufficiently accurate for crystalline solids studied in this thesis.

The DFT treats all ground-state properties of many-electron systems as functionals of electron density. Although it may be considered as a rough approximation, it provides an exact theoretical framework and it gives reasonable results, it may be modified for a wide range of purposes, and it makes numerically expensive tasks solvable. For example, iron is one of the most common elements and it consists of a nucleus and twenty six electrons per atom. If we only wanted to represent just electrons in a computer it would require three spatial coordinates and three values to represent momentum (or velocity) of each of a huge number of electrons. A basic single-precision floating-point format of one number is usually occupying 32 bits and taking into account memory size of present computers, a proper description of these electrons would not be possible for a larger system than a cube having sides of few nanometers. Therefore, developing efficient and reliable approximate methods like the DFT is of extreme importance.

An origin of the DFT may be found in 1960s, when the theorems of Hohenberg and Kohn were derived and Kohn-Sham equations introduced. Before that, approaches to calculate the wave function of atoms and solids had been proposed and developed, e.g., by Hartree [60, 61], Slater [62], Bloch [63], Dirac [64, 65], or Fock [66]. For the historical overview of the methods, we refer to [67].

In recent time, "beyond-DFT" methods [68, 69] become more popular because of increasing computational power and necessity to describe more sensitive effects like properties of strongly correlated or topologically nontrivial materials. For practical purposes, the DFT is used with the local-density approximation (LDA), which is an approximate method for a description of the exchange–correlation (XC) energy functional. It can be generalized to a form of the local spin-density approximation (LSDA), that includes electron spin or, e.g.,

with incorporating changes in the electron density like the generalized gradient approximations (GGA). Based on purposes of the calculations, the DFT is used in many computational codes with additional approximative tool like the atomic sphere approximation (ASA), the LMTO and Korringa–Kohn–Rostoker (KKR) methods for solving the single-particle Schrödinger equation. The CPA or supercell techniques are often used to describe disordered solids. Furthermore, more complex quantities including electrical transport properties can be computed based on electronic structure of materials.

For a description of *ab initio* methods, we mostly follow [12], [13], [70], [71], and [67]. For calculations presented in this thesis, the TB-LMTO formalism with the atomic sphere approximation (ASA) is used. Together with the CPA and the Kubo-Greenwood formula [72, 73], especially in the fully-relativistic framework [74], it represents an efficient and reliable framework for solid magnetic systems.

1.2.2 Many-electron systems

The time-dependent Schrödinger equation with a time variable t and the reduced Planck constant $\hbar$ gives a description of a system evolving in time:

$$i\hbar\frac{\mathrm{d}}{\mathrm{d}t}\left|\psi\right\rangle = \hat{H}\left|\psi\right\rangle \tag{1.13}$$

and for the stationary (time-independent) states, it simplifies to

$$\hat{H}\left|\psi\right\rangle = E\left|\psi\right\rangle \ . \tag{1.14}$$

A non-relativistic many-electron system is described by a Hamiltonian $\hat{H}$ in a form

$$\hat{H} = -\frac{\hbar^2}{2m}\sum_{i=1}^{N}\nabla_i^2 + \sum_{i=1}^{N}v(\mathbf{r}_i) + \frac{e^2}{4\pi\epsilon_0}\sum_{i<j}^{N}\frac{1}{r_{ij}} \tag{1.15}$$

and by the wave function $\psi(\mathbf{r}_1, s_1; \mathbf{r}_2, s_2; \ldots; \mathbf{r}_N, s_N)$ for N electrons with a position $\mathbf{r}_i$ and spin s_i for the $i-$th electron. The mass of electron is denoted m, its charge is e, and ϵ_0 is the vacuum permittivity. The distance between particles i and j is r_{ij} and E is the total energy. An external contribution to the potential $v(\mathbf{r})$ is usually assumed to be the Coulomb interaction between electrons and nuclei with charges eZ_J (Z_J is the number of protons of $J-$the nucleus):

$$v(\mathbf{r}_i) = -\frac{e^2}{4\pi\epsilon_0}\sum_J\frac{Z_J}{r_{iJ}}\,. \tag{1.16}$$

The notation $\sum_{i<j}$ in Eq. (1.15) is introduced to prevent double counting of the electron-electron interaction.

The Schrödinger equation, physical condition to minimalize energy of systems, and mathematical expression for the wave function of a many-body system in a form of the Slater determinant lead to an exact treatment of the Pauli exclusion principle in a form of Hartree-Fock equations [13] expressed as

$$\begin{aligned}&\left[-\frac{\hbar^2}{2m}\nabla_1^2 + v(\mathbf{r}_1) + \frac{e^2}{4\pi\epsilon_0}\sum_{i=1}^{N}\int\frac{\phi_i^*(\mathbf{r}_2)\phi_i(\mathbf{r}_2)}{r_{12}}\mathrm{d}^3\mathbf{r_2}\right]\phi_j(\mathbf{r}_1) - \\ &-\frac{e^2}{4\pi\epsilon_0}\sum_{i=1}^{N}\int\frac{\phi_i^*(\mathbf{r}_2)\phi_j(\mathbf{r}_2)}{r_{12}}\mathrm{d}^3\mathbf{r_2}\,\phi_i(\mathbf{r}_1) = E_j^{\lambda}\phi_j(\mathbf{r}_1)\,,\end{aligned} \tag{1.17}$$

where E_j^λ has a meaning of physical energy, but it mathematically corresponds to the Lagrange multiplier. Eq. (1.17) neglects correlation effects, it is solved by self-consistent methods leading to a description of the electronic structure of atoms or molecules, but it is computationally difficult to use for calculations of metallic solids [13].

To find a solution of the many-body system, theorems of Hohenberg and Kohn may be employed (we refer, e.g., to Ref. [13] for details). It results in a description of the system by the electron density $n(\mathbf{r})$ for the many-body wave function ψ of $N = \int n(\mathbf{r})\mathrm{d}^3\mathbf{r}$ particles given by

$$n(\mathbf{r}) = N \sum_{s_1,s_2,\ldots s_N} \int \cdots \int |\psi_s(\mathbf{r}, s_1; \mathbf{r}_2, s_2; \ldots \mathbf{r}_N, s_n)|^2 \, \mathrm{d}^3\mathbf{r}_2 \, \mathrm{d}^3\mathbf{r}_3 \, \ldots \, \mathrm{d}^3\mathbf{r}_N \,, \quad (1.18)$$

where s_i runs over two possible values of spin of the electron i and $\mathrm{d}^3\mathbf{r}_i$ are spatial integrations. We note that there is no integration over $\mathrm{d}^3\mathbf{r}$ and the final electron density is a function of just x, y, and z coordinates instead of a complex expression depending on $3N$ spatial variables. Within the Dirac bra-ket notation, Eq. (1.18) is

$$n(\mathbf{r}) = \langle\psi| \sum_i \delta(\mathbf{r} - \mathbf{r_i}) \, |\psi\rangle \,. \quad (1.19)$$

Based on functionals of the electron density, Walter Kohn and Lu Jeu Sham proposed in 1965 a method for numerical implementation of the DFT [75]. They introduced a system of non-interacting electrons generating the same density as a real system of interacting particles. It leads to the Kohn-Sham equations [13, 75] and the ground-state density (with the spin index omitted) is given by

$$n(\mathbf{r}) = \sum_{i=1}^{N} |\phi_i(\mathbf{r})|^2 \,, \quad (1.20)$$

where ϕ_i are called the Kohn-Sham orbitals. These orbitals are obtained as solutions of a one-electron Schrödinger equation with an effective (Kohn-Sham) potential $v_{\mathrm{eff}}[n](\mathbf{r})$. For a single electron, i.e., a particle moving in an effective field described by the Kohn-Shamn potential, the following holds

$$v_{\mathrm{eff}}[n](\mathbf{r}) = v(\mathbf{r}) + \frac{e^2}{4\pi\epsilon_0} \int \mathrm{d}^3\mathbf{r}_1 \frac{n(\mathbf{r}_1)}{|\mathbf{r}_1 - \mathbf{r}|} + \frac{\delta E_{\mathrm{xc}}[n]}{\delta n(\mathbf{r})} \,, \quad (1.21)$$

where $v(\mathbf{r})$ is an external potential and the last term in Eq. (1.21) is usually called the exchange-correlation potential

$$v_{\mathrm{xc}}[n](\mathbf{r}) = \frac{\delta E_{\mathrm{xc}}[n]}{\delta n(\mathbf{r})} \,. \quad (1.22)$$

The exchange-correlation potential is (together with the corresponding energy) the only unknown quantity in the Kohn–Sham approximation. The electron density with this potential is then given by a self-consistent solution of the Kohn-Sham equations.

Spin-polarized systems For clarity, the equations above were written without the spin index. When the spin-polarized case is studied, the electron density for the up-channel $n_+(\mathbf{r})$ may be different from the down one $n_-(\mathbf{r})$ and the total one is given by their sum

$$n(\mathbf{r}) = n_+(\mathbf{r}) + n_-(\mathbf{r})\,. \tag{1.23}$$

The partial spin-resolved densities are

$$n_\pm(\mathbf{r}) = \langle\psi| \sum_i \delta(\mathbf{r}-\mathbf{r}_i)\delta_{\pm,\sigma_i^z} |\psi\rangle\ , \tag{1.24}$$

where σ_i^z denotes the $z-$component of the spin operator (electron i).

In addition to the electron density, the spin density $\mathbf{m}(\mathbf{r})$ enters the effective potential $v_{\text{eff}}[n,\mathbf{m}](\mathbf{r})$. If the spins are oriented along the $z-$direction, i.e., $\mathbf{m} = (0,0,m)$, then the magnitude of the spin density is given by

$$m = \mu_B\,(n_+ - n_-) \tag{1.25}$$

and its direction coincides with that of the exchange magnetic field.

Equivalently to the non-magnetic case, $v_{\text{eff}}[n,\mathbf{m}](\mathbf{r})$ for a magnetic system is given in by the functional derivative of the energy functional with respect to the particle density [12]. The total Kohn-Sham Hamiltonian is then given by the original non-magnetic term with added magnetic contribution

$$\hat{H}_M = \boldsymbol{\sigma}\cdot\mathbf{B}_{\text{eff}}[n,\mathbf{m}]\,, \tag{1.26}$$

where $\boldsymbol{\sigma}$ is Pauli matrix and the effective magnetic field is [12, 76]

$$\mathbf{B}_{\text{eff}}[n,\mathbf{m}](\mathbf{r}) = \mu_B\mathbf{B}_{\text{ext}}(\mathbf{r}) + \frac{\delta E_{\text{xc}}[n,\mathbf{m}]}{\delta\mathbf{m}(\mathbf{r})}\,. \tag{1.27}$$

Here, μ_B is the Bohr magneton and $\mathbf{B}_{\text{ext}}$ is the external magnetic field.

Other methods Non-self-consistent approaches to the DFT also exist. They may be based, e.g., on the Harris functional which makes them less accurate but sufficient for many systems [77]. These methods are not discussed or used in this work any further.

1.2.3 Exchange-correlation potentials

Local density approximation The local density approximation (LDA) is an approach for determination of the exchange-correlation energy $E_{\text{xc}}[n]$.

The LDA is based on an assumption that the exchange–correlation energy functional depends only upon the value of the electronic density at each spatial point. The exchange-correlation energy per particle $\mathcal{E}_{\text{xc}}$ is given by

$$E_{\text{xc}}^{\text{LDA}}[n] = \int n(\mathbf{r})\mathcal{E}_{\text{xc}}[n(\mathbf{r})]\mathrm{d}^3\mathbf{r}\,; \tag{1.28}$$

obviously, $\mathcal{E}_{\text{xc}}$ contains contributions from both the exchange and correlation terms, as well as $E_{\text{xc}}[n]$ does. For a uniform electron gas with $n = n(\mathbf{r})$, the potential (1.22) becomes

$$v_{\text{xc}}^{\text{LDA}}[n] = \frac{\delta E_{\text{xc}}^{\text{LDA}}[n]}{\delta n(\mathbf{r})} = \mathcal{E}_{\text{xc}}[n(\mathbf{r})] + n(\mathbf{r})\left.\frac{\mathrm{d}\mathcal{E}_{\text{xc}}^{\text{LDA}}[n]}{\mathrm{d}n}\right|_{n=n(\mathbf{r})}\,. \tag{1.29}$$

The total exchange–correlation energy was reformulated in the term of the energy per particle, but the overall task has not been very simplified yet. To do that, it is useful to divide $\mathcal{E}_{\mathrm{xc}}[n]$ into an exchange part $\mathcal{E}_{\mathrm{x}}[n]$ and a correlation part $\mathcal{E}_{\mathrm{c}}[n]$

$$\mathcal{E}_{\mathrm{xc}}[n] = \mathcal{E}_{\mathrm{x}}[n] + \mathcal{E}_{\mathrm{c}}[n] \tag{1.30}$$

because the first one can be expressed as

$$\mathcal{E}_{\mathrm{x}}[n] = -\frac{3}{4}\left(\frac{3}{\pi}n(\mathbf{r})\right)^{1/3} . \tag{1.31}$$

Local spin-density approximation Spin-polarized systems with the different spin-up and spin-down electron densities are treated by the local spin-density approximation (LSDA). The difference between exchange-correlation interactions is related to an alignment of the spins to a configuration that may favor ferromagnetic state. In order to quantitatively describe magnetic systems, two electron densities for opposite spin channels (denoted as + and −) are used and the exchange-correlation potential becomes

$$v_{\mathrm{xc}}^{\mathrm{LSDA},\pm}[n_+, n_-](\mathbf{r}) = \frac{\delta E_{\mathrm{xc}}^{\mathrm{LSDA}}[n_+, n_-](\mathbf{r})}{\delta n_\pm(\mathbf{r})} , \tag{1.32}$$

where

$$E_{\mathrm{xc}}^{\mathrm{LSDA}}[n_+, n_-](\mathbf{r}) = \int n(\mathbf{r})\mathcal{E}_{\mathrm{xc}}[n_+, n_-](\mathbf{r})\mathrm{d}^3\mathbf{r} . \tag{1.33}$$

Both $v_{\mathrm{xc}}^{\mathrm{LSDA},\pm}[n_+, n_-](\mathbf{r})$ and $E_{\mathrm{xc}}^{\mathrm{LSDA}}[n_+, n_-](\mathbf{r})$ depend on both n_+ and n_-.

LDA+U One of the weaknesses of the LDA is a treatment of correlation effects between electrons. It is mostly seen for metals with partially filled d or f orbitals because these elements have a large energy difference between occupied states and the unoccupied ones. A commonly used attempt to remove this systematic error is LDA+U method where "U" comes from the standard Hubbard Hamiltonian, i.e., from its on-site repulsion term having the magnitude of the interaction usually denoted "U" [13, 78]. The full energy-dependent selfenergy is replaced by an energy independent non-local term coming from the screened Coulomb potential. To introduce the LDA+U, the total number of localized electrons in the d shell (for which the corrections are usually used) is N_d and it is given by the sum of orbital occupancies d_i:

$$N_d = \sum_i d_i . \tag{1.34}$$

The LDA+U energy E^{U} is obtained as the energy E^{LDA} with two corrections (exchange effects are neglected):

$$E^{\mathrm{U}} = E^{\mathrm{LDA}} - \frac{U}{2}N\left(N-1\right) + \frac{U}{2}\sum_{i\neq j} d_i d_j . \tag{1.35}$$

This form with the Hubbard term (last term on the right side of the previous equation) is chosen because now one obtains the orbital energies as

$$\mathcal{E}_i = \frac{\partial E}{\partial d_i} = \mathcal{E}^{\mathrm{LDA}} + U\left(\frac{1}{2} - d_i\right) , \tag{1.36}$$

which has an obvious interpretation: The occupied orbitals ($d_i = 1$) are shifted by $+U/2$ and the unoccupied ones by the same value with opposite sign. We note that U is now a strength of the interaction which is, especially because of practical reasons, considered to be a constant input parameter of many LDA+U first-principles codes. On the other hand, the U may be also obtained during self-consistent calculations as the energy difference corresponding to the changing number of localized electrons [13].

Generalized gradient approximation In general, the LDA underestimates the exchange energy and overestimates the correlation energy. To correct it, the energy may be expressed not only in terms of the electron density but also of its derivatives. This expansions is called the generalized gradient approximation (GGA) [79] and can be expressed as

$$E_{\mathrm{xc}}^{\mathrm{GGA}}[n] = \int n(\mathbf{r})\mathcal{E}_{\mathrm{xc}}[n(\mathbf{r}), \nabla n(\mathbf{r})]\mathrm{d}^3\mathbf{r} \tag{1.37}$$

or for the spin-polarized case

$$E_{\mathrm{xc}}^{\mathrm{GGA}}[n] = \int n(\mathbf{r})\mathcal{E}_{\mathrm{xc}}[n_+(\mathbf{r}), n_-(\mathbf{r}), \nabla n_+(\mathbf{r}), \nabla n_-(\mathbf{r})]\mathrm{d}^3\mathbf{r}\,. \tag{1.38}$$

1.2.4 Fully-relativistic DFT

Non-magnetic case The non-relativistic DFT presented so far gives reasonable results for a number of elements and phenomena; on the other hand, the relativistic theory is necessary for an investigation of heavier atoms or effects depending on a proper description of spin. Instead of the Schrödinger Eq. (1.14), the Dirac one is employed for these purposes [12]:

$$\left[c\,\boldsymbol{\alpha}\cdot\mathbf{p} + (\beta - I_4)\,mc^2 + V(\mathbf{r})I_4\right]\psi_i = E_i\psi_i\,. \tag{1.39}$$

In this notation, the wave function for one electron ψ_i is a bispinor containing a large ϕ and a small χ component

$$\psi_i = \begin{pmatrix} \phi \\ \chi \end{pmatrix}, \tag{1.40}$$

each of them having two components (one component for one spin). Therefore, the potential $V(\mathbf{r})$ is multiplied by the 4−dimensional unit matrix I_4. The 2×2 Pauli matrices $\boldsymbol{\sigma}$ are included in the matrix

$$\boldsymbol{\alpha} = \begin{pmatrix} 0 & \boldsymbol{\sigma} \\ \boldsymbol{\sigma} & 0 \end{pmatrix} \tag{1.41}$$

and $\mathbf{p} = -i\hbar\nabla$ is the standard momentum operator. The matrix β is composed of 2−dimensional unit matrices I_2

$$\beta = \begin{pmatrix} I_2 & 0 \\ 0 & -I_2 \end{pmatrix}, \tag{1.42}$$

where $\boldsymbol{\sigma}$ are Pauli matrices. The energy E does not include the rest energy of the electron.

For the relativistic case, the effective potential analogical to (1.21) is [12]

$$v_{\mathrm{eff}}(\mathbf{r}) = v(\mathbf{r}) + \frac{e^2}{4\pi\epsilon_0}\int \mathrm{d}^3\mathbf{r}_1 \frac{n(\mathbf{r}_1)}{|\mathbf{r}_1 - \mathbf{r}|} + \frac{\delta E_{\mathrm{xc}}[n]}{\delta n(\mathbf{r})}\,, \tag{1.43}$$

but we note that the electron density differs for the relativistic theory [12]. This effective potential together with the Dirac Eq. (1.39) is known as the Kohn-Sham-Dirac equations.

Spin-polarized case When an external magnetic field $\mathbf{B}(\mathbf{r})$ is taken into account, the Dirac Eq. becomes

$$\left[c\,\boldsymbol{\alpha}\cdot(\mathbf{p} - e\mathbf{A}(\mathbf{r})) + (\beta - I_4)\,mc^2 + V(\mathbf{r})I_4\right]\psi_i = E_i\psi_i \tag{1.44}$$

with the vector potential $\mathbf{A}(\mathbf{r})$ satisfying $\mathbf{B}(\mathbf{r}) = \nabla\times\mathbf{A}(\mathbf{r})$.

For practical purposes [12], the magnetic field due to exchange and correlation is usually taken into account by an additional Hamiltonian contribution

$$\hat{H}_{\mathrm{B}} = \beta\begin{pmatrix}\boldsymbol{\sigma} & 0\\ 0 & \boldsymbol{\sigma}\end{pmatrix}\cdot\mathbf{B}_{\mathrm{eff}}[n,\mathbf{m}](\mathbf{r})\,, \tag{1.45}$$

which then enters the Dirac Eq. (1.39) as a correction to the original Hamiltonian:

$$\left[c\,\boldsymbol{\alpha}\cdot\mathbf{p} + (\beta - I_4)\,mc^2 + V(\mathbf{r})I_4 + \hat{H}_{\mathrm{B}}\right]\psi_i = E_i\psi_i\,. \tag{1.46}$$

The effective potential is now dependent on $\mathbf{r}$ and also on the spin density $\mathbf{m}$, as well as other quantities, but (1.43) can be still used. The effective magnetic field now plays a role of an effective spin-dependent potential similarly to the non-relativistic case (1.27).

1.2.5 TB-LMTO technique

The tight-binding linear muffin-tin orbital (TB-LMTO) method with atomic sphere approximation and the multicomponent coherent potential approximation (CPA) [12] is used to obtain most of the results presented in this thesis. A complete description of the framework is beyond the scope of this work; therefore, we address the most important parts, relevant especially for the fully-relativistic calculations of electrical transport (see later Sec. 1.3.2), and for details we refer to [12, 74, 80–82].

The formalism may be used in both the non-relativistic and fully-relativistic approaches. In the former, the Schördinger equation is solved and quantum numbers $L = (l, m)$ label different solutions, whereas the Dirac equation and composed quantum numbers $\Lambda = (\kappa, \mu)$ are used in the latter. Numerically, dimensions of all the matrices are twice larger in the relativistic framework. For detailed description of differences, we refer to [12].

In the TB-LMTO approach with the CPA, we use the one particle Green's function $G(z)$

$$G(z) = \left(z - \hat{H}\right)^{-1} = \int_{-\infty}^{\infty}\frac{1}{z-t}\delta(t - \hat{H})\mathrm{d}t \tag{1.47}$$

for a complex variable z and we introduce $i0$ as an infinitesimally small imaginary value (necessary for an integration in the complex plane) to define

$$G_{\pm}(E) = G(E \pm i0)\,, \tag{1.48}$$

where E is real energy. The hat symbol over the Green's functions and other operators is omitted for brevity and to be consistent with literature [74, 80, 81].

In the orthonormal TB-LMTO approach, the fully-relativistic Hamiltonian for a spin-polarized system H^{orth} is [74]

$$H^{orth} = C + \left(\sqrt{\Delta}\right)^{+} S^{0} \left(1 - \gamma S^{0}\right)^{-1} \sqrt{\Delta}\,, \tag{1.49}$$

where the S^0 is the matrix of canonical structure constants and C, $\sqrt{\Delta}$, and γ are site-diagonal matrices of the potential parameters. The coordinates are represented by diagonal matrices $(X_\mu)_{\mathbf{R}Ls,\mathbf{R}'L's'} = X^{\mu}_{\mathbf{R}}\delta_{\mathbf{R}Ls,\mathbf{R}'L's'}$ (atoms located at the position $\mathbf{R}$, L is the angular momentum index, and s denotes spin index) and for the velocity (current) operators the following holds [74]

$$V_\mu = -i\left[X_\mu, H^{orth}\right] = \left(\sqrt{\Delta}\right)^{+} F^{-1} v_\mu \left(F^{+}\right)^{-1} \sqrt{\Delta}\,, \tag{1.50}$$

where $v_\mu = -i[X_\mu, S^\alpha]$, S^α are screened structure constants with screening constants $\alpha_{\mathbf{R},L}$ employed. For the F-matrices, $F = 1 + S^\alpha(\alpha - \gamma)$ holds.

The screened structure constants are given by

$$S^{\alpha} = S^{0}\left(1 - \alpha S^{0}\right)^{-1} \tag{1.51}$$

and the screened potential functions are

$$P^{\alpha}(z) = \left(\sqrt{\Delta}\,(z - C)^{-1}\left(\sqrt{\Delta}\right)^{+} + \gamma - \alpha\right)^{-1}. \tag{1.52}$$

The form of (1.51) and (1.52) implies that the LMTO technique treats structure constants (geometrical properties of a studied system) and potential functions (atomic parts, scattering properties) separately. The similar conclusion holds also for for the KKR method, whereas many other approaches employ combined forms of these properties.

We note that the effective velocity operators v_μ are non-random, whereas V_μ and $\sqrt{\Delta}$ are random. Only intersite hoppings are described by the velocity operators. For details of the notation, see Ref. [12]. The Green's function is then given by [74]

$$G(z) = \left(z - H^{orth}\right)^{-1} = \left(\sqrt{\Delta}\right)^{-1} F^{+}\left[\alpha - \gamma + g(z)F\right]\left[\left(\sqrt{\Delta}\right)^{+}\right]^{-1}, \tag{1.53}$$

where the auxiliary Green's function

$$g(z) = \left[P^{\alpha}(z) - S^{\alpha}\right]^{-1} \tag{1.54}$$

is more suitable for the numerical calculations because of its simpler form [12]. These relations are later used for electrical transport properties in Sec. 1.3.2.

1.2.6 Coherent potential approximation

The CPA is generally used to treat a substitutional disorder on a non-random lattice. In this thesis, it is also employed for the alloy analogy model (see later Sec. 2.1). Principles and description of the CPA are taken mainly from Ref. [12] and Ref. [82].

The primary aim of the CPA is to deal with distinguishable atomic species (component Q) on the same atomic positions (site $\mathbf{R}$). If they have concentrations $c^Q_{\mathbf{R}}$, occupation indices are $\eta^Q_{\mathbf{R}}$ ($\eta^Q_{\mathbf{R}} = 1$ if site $\mathbf{R}$ is occupied by atomic species Q and $\eta^Q_{\mathbf{R}} = 0$ otherwise), the configurational averaging and the single-site approximation result in the on-site block of the auxiliary Green's function in a form of

$$\bar{g}^{\alpha,Q}_{\mathbf{R},\mathbf{R}}(z) = \frac{1}{c^Q_{\mathbf{R}}} \left\langle \eta^Q_{\mathbf{R}} g^{\alpha}_{\mathbf{R},\mathbf{R}}(z) \right\rangle \tag{1.55}$$

and in the on-site blocks of the averaged auxiliary Green's functions

$$\bar{g}^{\alpha}_{\mathbf{R},\mathbf{R}}(z) = \sum_Q c^Q_{\mathbf{R}} \bar{g}^{\alpha,Q}_{\mathbf{R},\mathbf{R}}(z)\,. \tag{1.56}$$

A single impurity is assumed to be inside an effective medium described by the coherent potential functions $\mathcal{P}^{\alpha}(z)$ which is related to the complete average auxiliary Green's functions by

$$\bar{g}^{\alpha}_{\mathbf{R},\mathbf{R}'}(z) = \left[[\mathcal{P}^{\alpha}(z) - S^{\alpha}]^{-1} \right]_{\mathbf{R},\mathbf{R}'}\,, \tag{1.57}$$

where $\mathcal{P}^{\alpha}(z)$ is in general a non-random site non-diagonal matrix describing properties of effective, non-random atoms. The evaluation is simplified within the approximation of

$$\mathcal{P}^{\alpha}_{\mathbf{R},\mathbf{R}'}(z) = \mathcal{P}^{\alpha}_{\mathbf{R}}(z)\delta_{\mathbf{R},\mathbf{R}'}\,. \tag{1.58}$$

Site non-diagonal elements of a general $\mathcal{P}^{\alpha}(z)$ and local environment effects are neglected within the single-site approximation. For systems with a single sublattice (Bravais lattice), the on-site blocks in Eq. (1.57) are

$$\bar{g}^{\alpha}_{\mathbf{R},\mathbf{R}}(z) = \frac{1}{N} \sum_{\mathbf{k}} \left[\mathcal{P}^{\alpha}(z) - S^{\alpha}(\mathbf{k})\right]^{-1}\,, \tag{1.59}$$

where $\mathbf{k}$ denotes a vector from the Brillouin zone, N is the number of sites $\mathbf{R}$, and $S^{\alpha}(\mathbf{k})$ are given by the lattice Fourier transformation of real-space structure constants. For systems with several sublattices, a more general formula has to be used [12].

For practical numerical purposes, it is convenient to introduce the coherent interactor $\Omega^{\alpha}_{\mathbf{R}}(z)$ describing a coupling between the atomic site $\mathbf{R}$ with the auxiliary Green's function $\bar{g}^{\alpha}_{\mathbf{R},\mathbf{R}}$ to all the others

$$\Omega^{\alpha}_{\mathbf{R}}(z) = \mathcal{P}^{\alpha}_{\mathbf{R}}(z) - \left[\bar{g}^{\alpha}_{\mathbf{R},\mathbf{R}}(z)\right]^{-1}\,. \tag{1.60}$$

With the coherent interactor, we can writhe the CPA-condition in a form

$$\sum_Q c^Q_{\mathbf{R}} \left[P^{\alpha,Q}_{\mathbf{R}}(z) - \Omega^{\alpha}_{\mathbf{R}}(z)\right]^{-1} = \bar{g}^{\alpha}_{\mathbf{R},\mathbf{R}}(z)\,. \tag{1.61}$$

Eq. (1.59) and (1.61) can then be evaluated together to iteratively obtain their solutions.

Numerically, the coherent interactor is calculated self-consistently (iterations labeled by (n)) for all the sites $\mathbf{R}$ together with (1.59) to converge the coherent potential functions. It can be done in three iterative steps described by the following relations:

$$\mathcal{P}^{\alpha,(n)}_{\mathbf{R}}(z) = \left\{ \sum_{Q} c^{Q}_{\mathbf{R}} \left[P^{\alpha,Q}_{\mathbf{R}}(z) - \Omega^{\alpha,(n)}_{\mathbf{R}}(z) \right]^{-1} \right\}^{-1} + \Omega^{\alpha,(n)}_{\mathbf{R}}(z)\,, \tag{1.62}$$

$$\bar{g}^{\alpha,(n)}_{\mathbf{R},\mathbf{R}}(z) = \left\{ \left[\mathcal{P}^{\alpha,(n)}_{\mathbf{R}}(z) - S \right]^{-1} \right\}_{\mathbf{R},\mathbf{R}}\,, \tag{1.63}$$

and

$$\Omega^{\alpha,(n+1)}_{\mathbf{R}}(z) = \mathcal{P}^{\alpha,(n)}_{\mathbf{R}}(z) - \left[\bar{g}^{\alpha,(n)}_{\mathbf{R},\mathbf{R}}(z) \right]^{-1}\,. \tag{1.64}$$

When the potential functions $P^{\alpha,Q}_{\mathbf{R}}(z)$ are considered to be iteration-dependent, this approach can be combined with the LSDA self-consistent calculations [12].

Later introduced atomic displacements (Sec. 2.1) modify the potential functions $P^{\alpha,A}_{\mathbf{R}}$ before they are used to obtain the coherent potential functions $\mathcal{P}^{\alpha}_{\mathbf{R}}(z)$. Therefore, the atomic displacements are included purely in the CPA self-consistent approach, not in the self-consistent convergence of the potential functions within the LSDA, see Sec. 3.1 for details.

In studies of transport properties, a configuration averaging of a product of two Green's functions leads to the so-called vertex corrections, which can be also treated within the CPA, see Appendix of Ref. [82] for details. Generally, terms such as $\mathrm{Tr}\,\langle g(z_1)Ag(z_2)B\rangle$ containing auxiliary Green's function g with two energy arguments z_1 and z_2 and non-random matrices A and B are of interest. It can be approached by expressing an averaging as

$$\langle g(z_1)Ag(z_2)\rangle = \bar{g}(z_1)A\bar{g}(z_2) + \bar{g}(z_1)\Gamma(z_1,z_2)\bar{g}(z_2)\,, \tag{1.65}$$

where the first term on the right-hand side gives the coherent contribution and the second one results in the vertex corrections given by $\Gamma(z_1,z_2)$ in a form of

$$\Gamma(z_1,z_2) = \langle T(z_1)\bar{g}(z_1)A\bar{g}(z_2)T(z_2)\rangle\,. \tag{1.66}$$

Here, $T(z_1)$ and $T(z_2)$ denote the total T-matrices, which can be expressed by the single-site T-matrix, see Ref. [82] for details (including the CPA-like decoupling and employing the self-consistency conditions). After several mathematical steps, a result for the studied term is obtained:

$$\mathrm{Tr}\,\langle g(z_1)Ag(z_2)B\rangle = \mathrm{Tr}\,\{\bar{g}(z_1)A\bar{g}(z_2)B\} + \mathrm{Tr}\,\langle g(z_1)Ag(z_2)B\rangle_{\mathrm{vc}}\,. \tag{1.67}$$

For the explicit expression of the vertex-correction part $\mathrm{Tr}\,\langle g(z_1)Ag(z_2)B\rangle_{\mathrm{vc}}$, see Ref. [82].

1.3 Electrical transport

Electrical transport properties of solids are often described by formalism which was introduced by R. Kubo [72] and D.A. Greenwood [73] more than sixty years ago. The formalism was later improved, e.g., by Bastin et al. [83] or P. Středa [84]. Although it is a powerful framework, most of the *ab initio* studies employ this method only for zero temperature.

An approach for calculating electrical transport properties is described in this section; namely, we focus on the linear response theory and a material behavior connected to the conductivity tensor at zero temperature. An influence of the Fermi-Dirac distribution at finite temperatures is described in Sec. 2.3.3 and an approach for calculations of the spin-resolved electrical conductivity is shown in Sec. 2.4.

The linear response theory related to the electrical transport is introduced here because it is used in this thesis. We note that there are other approaches like the Drude theory or the Boltzman equation; moreover, different transport properties like heat transport may be studied [13].

1.3.1 Linear response theory

The linear response theory describes a system and its response to a small external perturbation as linear [13] and we first derive a general response that is later related to the electrical transport. The following notation is used:

- An investigated system is described by the Schrödinger equation (1.13).
- A time-independent Hamiltonian is $\hat{H}$.
- A time-dependent wave function of the perturbed system is $\bar{\psi}(t)$.
- An external perturbation is included in $\hat{H}^{\text{ext}}$.
- A perturbation is switched on in time t_0 ($\hat{H}^{\text{ext}} = 0$ for $t < t_0$).
- A studied observable of the system is represented by the operator $\hat{O}(t)$.
- A general operator $\hat{A}(t)$ satisfying $\hat{A}(t) = 1$ for $t \leq t_0$ is assumed.

For the perturbation, i.e., for $t > t_0$, the Schrödinger equation can be written in the form

$$i\hbar \frac{\partial}{\partial t} \left|\bar{\psi}(t)\right\rangle = \left[\hat{H} + \hat{H}^{\text{ext}}\right] \left|\bar{\psi}(t)\right\rangle . \tag{1.68}$$

For later, we set $\hbar = 1$. A solution of the previous equation may by assumed in a form

$$\left|\bar{\psi}(t)\right\rangle = e^{-i\hat{H}t} \hat{A}(t) \left|\bar{\psi}(0)\right\rangle \tag{1.69}$$

and employing an expansion of the perturbation ($\hat{H}^{\text{ext}}$ being a small perturbation of $\hat{H}$), we obtain an approximate relation for the wave function in the interaction representation (denoted by a subscript I)

$$\left|\bar{\psi}(t)\right\rangle = e^{-i\hat{H}t} \left|\psi(0)\right\rangle - i \int_{t_0}^{t} \hat{H}_I^{\text{ext}}(t') \left|\psi(0)\right\rangle \mathrm{d}t' + \cdots . \tag{1.70}$$

Because the wave function for $t = 0$ is the same in the Schrödinger, Heisenberg, and interaction representation, a small change of a general observable in the first order $\delta \left\langle \hat{O}(t) \right\rangle$ is

$$\delta \left\langle \hat{O}(t) \right\rangle = i \int_{t_0}^{t} \langle \psi_0 | \left[\hat{H}_I^{\text{ext}}(t'), \hat{O}_I(t) \right] | \psi_0 \rangle \, \mathrm{d}t' \,, \tag{1.71}$$

which is the basic relation for the linear response theory. For a detailed derivation we refer to [13].

In this thesis, we focus on the electrical transport properties. For this purpose, general Eq. (1.71) should be used to investigate a collective motion of particles (electrical current) in a presence of an electric field $\mathbf{E}_0$. The current is given by a summation over the moving particles with momentum $\mathbf{p}_i$, masses m_i, and charges e_i, i.e.,

$$\mathbf{j}(\mathbf{r}) = \frac{1}{2} \sum_i \frac{e_i}{m_i} \left[\mathbf{p}_i(\mathbf{r}) \delta \left(\mathbf{r} - \mathbf{r}_i \right) + \delta \left(\mathbf{r} - \mathbf{r}_i \right) \mathbf{p}_i(\mathbf{r}) \right] . \tag{1.72}$$

The Hamiltonian of the perturbation caused by the electric field

$$\mathbf{E}(\mathbf{r}, t) = \mathbf{E}_0 e^{i(\mathbf{q}\cdot\mathbf{r} - \omega t)} \tag{1.73}$$

with a corresponding vector potential $\mathbf{A}(\mathbf{r}, t)$ and the Coulomb gauge is

$$\hat{H}^{\text{ext}} = -\frac{1}{c} \int \mathbf{A}(\mathbf{r}, t) \cdot \mathbf{j}(\mathbf{r}) \mathrm{d}^3 r \tag{1.74}$$

or equivalently

$$\hat{H}^{\text{ext}} = \frac{i}{\omega} \mathbf{j}(\mathbf{q}) \cdot \mathbf{E}_0 e^{-i\omega t} \,. \tag{1.75}$$

In the relations above, $\mathbf{q}$ stands for a vector of the reciprocal space Eq. (1.75) was obtained from Eq. (1.74) by integration over the real-space variable, and it is expressed in terms of the Fourier component of the electrical current

$$\mathbf{j}(\mathbf{q}) = \sum_i \frac{e_i}{2m_i} \left(\mathbf{p}_i e^{i\mathbf{q}\mathbf{r}_i} + e^{i\mathbf{q}\mathbf{r}_i} \mathbf{p}_i \right) . \tag{1.76}$$

To introduce an induced current $\mathbf{J}(\mathbf{r}, t)$ (experimentally measured), we assume the carriers to be identical particles with a density n_0 in a volume Ω. We can then write

$$\mathbf{J}(\mathbf{r}, t) = \frac{e}{m} \sum_i \mathbf{p_i} \delta(\mathbf{r} - \mathbf{r_i}) = \frac{e}{m} \sum_i \langle \mathbf{p}_i \rangle \tag{1.77}$$

and in a presence of the vector potential this becomes

$$\mathbf{J}(\mathbf{r}, t) = \langle \mathbf{j}(\mathbf{r}) \rangle + i \frac{n_0 e^2}{m\omega} \mathbf{E}(\mathbf{r}, t) \,. \tag{1.78}$$

Within the linear response theory, the term given by the average of the current $\langle \mathbf{j}(\mathbf{r}) \rangle$ is proportional to the electric field, similarly to the second term in Eq. (1.78). The constant of proportionality is given by the Kubo formula. We note that the current in the absence of the perturbation is zero, which justifies a study of the first-order change $\delta \left\langle \hat{O}(t) \right\rangle$. For an investigation of electrical currents within the linear response theory, we employ Eq. (1.71) with the induced current $\mathbf{J}(\mathbf{r}, t)$

as the observable quantity (represented by $\hat{O}$) and the perturbation in the form of Eq. (1.74) or (1.75), i.e.,

$$\delta \langle \mathbf{j}_\mu(\mathbf{r},t)\rangle = i\int_{-\infty}^{t} \langle\psi_0|\left[\hat{H}_I^{\mathrm{ext}}(\mathbf{r},t'),\hat{j}_\mu(\mathbf{r},t)\right]|\psi_0\rangle\,\mathrm{d}t'\,, \tag{1.79}$$

where $\mu \in \{x,y,z\}$ (and later also ν) is a spatial coordinate. It is convenient to express time-dependent quantities in the interaction representation (for a unperturbed Hamiltonian $\hat{H}_0$ and general operator $\hat{O}(t) \to e^{i\hat{H}_0 t}\hat{O}e^{-i\hat{H}_0 t}$), which results in

$$\begin{aligned}\delta \langle \mathbf{j}_\mu(\mathbf{r},t)\rangle =& \frac{1}{\omega}\sum_\nu E_\nu(\mathbf{r},t)e^{-i\mathbf{q}\cdot\mathbf{r}} \\ &\cdot\int_{-\infty}^{t} e^{i\omega(t-t')}\langle\psi_0|\left[\hat{j}_\mu(\mathbf{r},t),\hat{j}_\nu(\mathbf{q},t')\right]|\psi_0\rangle\,\mathrm{d}t'\,.\end{aligned} \tag{1.80}$$

Electrical conductivity $\sigma_{\mu\nu}$, the coefficient of the proportionality between the electric field and the current ($\mathbf{j}(\mathbf{r},t) = \boldsymbol{\sigma}\mathbf{E}(\mathbf{r},t)$), is obtained after integration of Eq. (1.80) over the real space (a Fourier transformation: $\mathbf{r} \to \mathbf{q}$) and employing $\hat{j}_\mu(-\mathbf{q},t) = \hat{j}_\mu^+(\mathbf{q},t)$:

$$\sigma_{\mu\nu}(\mathbf{q},\omega) = \frac{1}{\omega}\int_{-\infty}^{t} e^{i\omega(t-t')}\langle\psi_0|\left[\hat{j}_\mu^+(\mathbf{q},t),\hat{j}_\nu(\mathbf{q},t')\right]|\psi_0\rangle\,\mathrm{d}t' + i\frac{n_0e^2}{m\omega}\delta_{\mu\nu}\,, \tag{1.81}$$

which is the Kubo formula for the electrical conductivity [13].

1.3.2 Static electrical transport

The form (1.81) of the Kubo formula may be used to calculate also frequency-dependent (optical) conductivities; however, it is not convenient for the TB-LMTO method with the CPA (the approach mostly used in this thesis). For such purposes, we will investigate a complex admittance $\chi_{\hat{A}\hat{B}}$ which is defined as a proportionality factor between the response of the system (observable $\hat{A}$) to a time-independent perturbation (operator $\hat{B}$); a possible time-dependence may be introduced in the relation of proportionality [13]. If we introduce a complex energy variable z, eigenfunctions $|m\rangle$ and eigenenergies E_m for a general operator (and, explicitly, second ones $|n\rangle$ and E_n), and matrix elements $A_{mn} = \langle m|\,\hat{A}\,|n\rangle$, then we obtain after performing contour integration in a complex plane (see Chapter 19 of [13] for details) the response function

$$\chi_{AB}(z) \approx \sum_{mn}\left\langle \frac{f(E_n)-f(E_m)}{z-E_n+E_m}B_{nm}A_{mn}\right\rangle\,. \tag{1.82}$$

A prefactor was omitted in Eq. (1.82) because its exact form depends on definitions of the matrix elements and physical quantities. The prefactor would also include normalization given by the volume of the primitive cell (V_0) and the number of cells in a big crystal with periodic boundary conditions (N). We note that the real part of z goes to zero for the DC conductivity. The brackets in Eq. (1.82) indicate an average over the sample including the configuration averaging [74, 80, 81, 83].

Employing Green's functions (1.47) and (1.48) with the TB-LMTO formalism introduced in Sec. 1.2.5, several identities for the Green's functions, and the limit of $z \to i0+$ (the plus sign denotes a positive value of the imaginary part), the following relation for the response is obtained:

$$\begin{aligned}\chi_{AB} = -2\sigma_0 \int_{-\infty}^{\infty} f(x) \mathrm{Tr} \Big\langle & A G'_+(x) \tilde{A} \left[G_+(x) - G_-(x)\right] \\ & - A \left[G_+(x) - G_-(x)\right] \tilde{A} G'_-(x) \Big\rangle \, \mathrm{d}x \,,\end{aligned} \tag{1.83}$$

where the Fermi-Dirac distribution is written as $f(E)$, the energy derivative is denoted by the prime, i.e., $G' = \frac{\mathrm{d}G(z)}{dz}$, and $\tilde{A} = -i[B, H]$ (a time derivative). The prefactor $\sigma_0 = e^2\hbar/(4\pi V_0 N)$ in (1.83) was chosen to be later consistent with expressions for the electrical conductivity. The static conductivity, obtained from Eq. 1.83 when the current operators ($A \to V$) are employed, was derived by A. Bastin et al. in 1971 [83]. Similarly, we will now use the coordinate operators X (perturbation B), the current operators V (observable A) and the H^{orth} containing the spin-orbit interaction; see Sec. 1.2.5 or Ref. [74] for details of the formalism. With the Green's functions defined by (1.53), the conductivity tensor is given by the Kubo-Bastin formula [81, 83]

$$\begin{aligned}\sigma_{\mu\nu} = -2\sigma_0 \int f(E) \mathrm{Tr} \Big\langle & V_\mu G'_+(E) V_\nu \left[G_+(E) - G_-(E)\right] \\ & - V_\mu \left[G_+(E) - G_-(E)\right] V_\nu G'_-(E) \Big\rangle \, \mathrm{d}E\end{aligned} \tag{1.84}$$

or in the terms of the auxiliary quantities [81]

$$\begin{aligned}\sigma_{\mu\nu} = -2\sigma_0 \int f(E) \mathrm{Tr} \Big\langle & v_\mu g'_+(E) v_\nu \left[g_+(E) - g_-(E)\right] \\ & - v_\mu \left[g_+(E) - g_-(E)\right] v_\nu g'_-(E) \Big\rangle \, \mathrm{d}E \,.\end{aligned} \tag{1.85}$$

The latter form is useful for configurational averaging within the CPA with the vertex corrections included [85].

1.3.3 Fermi-surface and Fermi-sea terms

The full conductivity tensor is calculated by employing the Kubo-Bastin formula which can be separated into [81]

$$\sigma_{\mu\nu} = \sigma_{\mu\nu}^{(1)} + \sigma_{\mu\nu}^{(2)} = \sigma_{\mu\nu}^{(1,\mathrm{coh.})} + \sigma_{\mu\nu}^{(1,\mathrm{v.c.})} + \sigma_{\mu\nu}^{(2)} \,, \tag{1.86}$$

where the $\sigma_{\mu\nu}^{(1)}$ term (in Ref. [81] called Fermi surface) can be separated into the coherent part $\sigma_{\mu\nu}^{(1,\mathrm{coh.})}$, and vertex corrections $\sigma_{\mu\nu}^{(1,\mathrm{v.c.})}$, and the $\sigma_{\mu\nu}^{(2)}$ term (Fermi sea [81]) is given by integration over the valence energy spectrum. The evaluation of vertex corrections $\sigma_{\mu\nu}^{(1,\mathrm{v.c.})}$ was formulated in the Appendix of Ref. [82].

The separation of the conductivity to the Fermi-surface and the Fermi-sea term is, technically, done by integrating Eq. (1.85) by parts. It results in the Fermi-surface

$$\begin{aligned}\sigma_{\mu\nu}^{(1)} = \sigma_0 \int f'(E) \mathrm{Tr} \big\langle & v_\mu g_+(E) v_\nu \left[g_+(E) - g_-(E)\right] \\ & - v_\mu \left[g_+(E) - g_-(E)\right] v_\nu g_-(E) \big\rangle \, \mathrm{d}E\end{aligned} \tag{1.87}$$

and the Fermi-sea

$$\sigma_{\mu\nu}^{(2)} = \sigma_0 \int f(E) \mathrm{Tr} \Big\langle v_\mu g_+(E) v_\nu g'_+(E) - v_\mu g'_+(E) v_\nu g_+(E) \\ - v_\mu g_-(E) v_\nu g'_-(E) + v_\nu g'_-(E) v_\nu g_-(E) \Big\rangle \, \mathrm{d}E \tag{1.88}$$

contributions separated [81]. The energy derivative of the Fermi-Dirac distribution, $f'(E)$ in the Fermi-surface term, goes to the Dirac delta-functions for zero temperature T; therefore the integration may be omitted and only the Green's functions at the Fermi energy $E = E_F$ remain

$$\sigma_{\mu\nu}^{(1)}(T=0) = \sigma_0 \mathrm{Tr} \left\langle v_\mu \left[g_+(E_F) - g_-(E_F) \right] v_\nu g_-(E_F) \right. \\ \left. - v_\mu g_+(E_F) v_\nu \left[g_+(E_F) - g_-(E_F) \right] \right\rangle \, , \tag{1.89}$$

which can be found also in [74]. The Fermi-sea term for zero temperature is written as a contour integral in the complex energy plane [81]

$$\sigma_{\mu\nu}^{(2)}(T=0) = \sigma_0 \int_{\mathcal{C}} \mathrm{Tr} \left\{ \left[v_\mu \bar{g}(z) v_\nu - v_\nu \bar{g}(z) v_\mu \right] \bar{g}(z) \mathcal{P}'(z) \bar{g}(z) \right\} \mathrm{d}z \, , \tag{1.90}$$

where $\bar{g}(z)$ denotes a configuration average of the $g(z)$ in the single-site CPA

$$\langle g(z) \rangle = \bar{g}(z) = \left[\mathcal{P} - S \right]^{-1} \, . \tag{1.91}$$

Here, $\mathcal{P}(z)$ is a nonrandom site-diagonal matrix of the potential functions and $\mathcal{P}'(z)$ is its energy derivative. Eq. (1.90), despite having formally a form of the coherent part of the conductivity tensor with vanishing vertex correction, contains $\mathcal{P}'(z)$ which has a form of the vertex correction ($gP'g$). The latter is related to the Ward identity for the particle number conservation and to the energy dependence of the averaged single particle Green's function [81]. For details about configurational averaging of the $\sigma_{\mu\nu}^{(2)}$ term we refer to Ref. [81].

We note that the $\sigma_{\mu\nu}^{(2)}$ term is antisymmetric and thus vanishes for the longitudinal conductivity. Moreover, it should be emphasised that the following quantities are invariant within the TB-LMTO method [81]:

- Total conductivity tensor $\sigma_{\mu\nu}$,
- the vertex corrections to the Fermi-surface term $\sigma_{\mu\nu}^{(1,\mathrm{v.c.})}$,
- the sum $\sigma_{\mu\nu}^{(1,\mathrm{coh.})} + \sigma_{\mu\nu}^{(2)}$, and
- the symmetric part of the coherent part of the Fermi-surface term, i.e., $\left(\sigma_{\mu\nu}^{(1,\mathrm{coh.})} + \sigma_{\nu\mu}^{(1,\mathrm{coh.})} \right) /2$.

The invariant properties of the Fermi-sea and Fermi-surface terms above described are essential for an investigation of the AHC, see bellow.

2. Development of methods

In the first two sections of this chapter we introduce general techniques for a description of disorder, i.e., atomic displacements and disordered magnetic moments. In principle, they can be employed to study various ranges of structural or magnetic fluctuations. Because we focus on a treatment of finite temperatures, Sec. 2.3 shows their connections to nonzero temperatures. Last but not least, an approach for treatment of a spin-polarized current within the linear response theory is shown.

2.1 Alloy analogy model within LMTO-CPA

The alloy analogy model (AAM) formally describes shifts of nuclei from their equilibrium positions (phonons) similarly to treatment of multicomponent alloys. The aim of this Section is to develop a transformation of the TB-LMTO potential functions to describe displacement of nuclei.

First, we describe basic principles of the AAM. Then, we present a short overview of similar techniques from literature and the rest of this Section describes a mathematical derivation of the AAM for the TB-LMTO method with the CPA.

Atoms in a studied bulk system are distributed in the whole sample, but to demonstrate their displacements, we choose an original reference frame O and a new one $\tilde{O} = O + \mathbf{u}$, where $\mathbf{u}$ stands for a displacement vector. The same notation (the tilde) is used also later to denote potential functions in the shifted origin. Fig. 2.1 schematically illustrate atomic displacements: the identical atoms form a 2D crystalline lattice (having only one sublattice) and they are displaced from their origin O to the new one $\tilde{O}$. Distances in Fig. 2.1 do not correspond to a real physical system, the scheme of the displacements is the same as in 3D bulk materials, and any of the nuclei can be displaced. We note that the same displacement is used for all of the atoms that are identical within the CPA (mathematically not distinguishable atoms at the same sublattice).

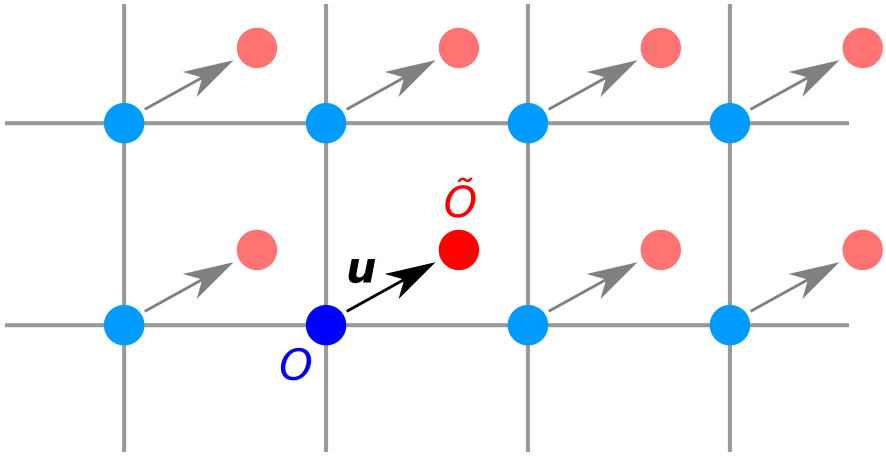

Figure 2.1: Atoms form a periodic lattice and all of the identical atoms with the origin O (blue) are displaced to the new one $\tilde{O}$ (red). The displacement vector $\mathbf{u}$ is the same for all of the identical atoms, but for clarity, only one of the atoms (dark blue and dark red) has the origins and the vector labeled.

Within the CPA, the originally identical atoms are considered to be distinguishable, similarly to a random alloy. Fig. 2.2 schematically shows an atom

on a single crystallographic position, which was taken four times (with nonzero arbitrary concentrations, see Eq. (1.56)). Each of the mathematically different atoms is displaced to a different direction characterized by the vector **u**, which is independent for the different atoms. We note that for the formalism, it is not important whether the atoms are physically identical (e.g., several atoms of Fe results again in pure Fe) or not (random alloys).

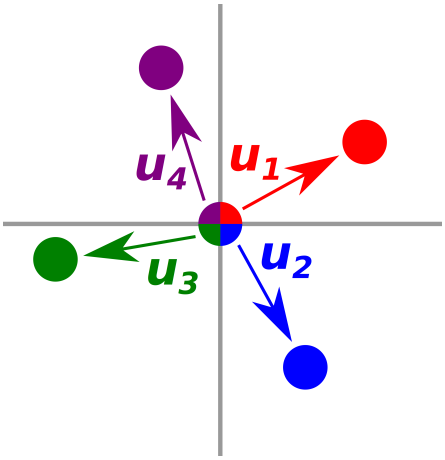

Figure 2.2: A single atom is treated by the CPA as several distinguishable ones and each of them may be displaced to any direction and with any magnitude. The transformation is done using the later derived Eq. (2.41) describing a change of scattering properties.

For a scheme describing technical implementation of the AAM within TB-LMTO with the CPA, see Sec. 3.1.

2.1.1 AAM – overview of literature

There are several ways how to deal with the lattice vibrations at finite temperatures. It can be approached using the Boltzmann formalism with the relaxation time approximation [86] or employing calculations of phonon properties [87, 88]. The model of frozen lattice displacements is often used in the calculations of transport properties. Atoms are moved randomly from their equilibrium positions in a perfect periodic crystal and the studied properties are calculated for this disordered system. The resulting quantity should be averaged over many configurations of random displacements of the atoms. The situation resembles a chemical disorder and because of this similarity, the AAM obtained its name [89].

The AAM has been recently implemented for a study of transport properties by several groups. Based on numerical codes they used, the AAM employs various techniques.

The CPA and the Korringa-Kohn-Rostoker (KKR) method with the Kubo-Bastin equation [29, 31, 89] For the description of the temperature-induced lattice vibrations, the AAM was introduced and worked out within the KKR Green's function formalism and the CPA [89]. Authors focused on the Gilbert damping parameter calculated via the Linear Response Formalism and

the Debye theory was used to assign temperature to the random thermal displacements of nuclei.

In Ref. [29], the AAM was used together with Monte Carlo simulations describing spin fluctuations to examine temperature dependent electrical resistivity and Gilbert damping. The KKR method with the CPA was used in that study to examine iron, nickel and copper from the first principles

Similarly to the electrical transport properties, also spectroscopic properties of solids may be obtained with the AAM [90].

Supercells with the TB-LMTO method and the Landauer-Büttiker formula [27, 32] The TB-LMTO method with the supercell technique was used in [91] to investigate Fe, Co and Ni and a dependence of the resistivity and Gilbert damping on the root-mean-square displacement of the nuclei. The Landauer-Büttiker formalism was employed for that purposes.

The supercell technique can also treat the spin disorder in the form of frozen random magnetic moments. The DLM state and the spin-disorder resistivity and the combined effect of the lattice displacement and of the spin disorder were studied in Fe and Gd [27].

A similar technique has also been used in a more recent study [92] where the calculated phonon spectra were connected to the displacement of nuclei in the supercell. This approach gives a very good agreement with experimental data for Cu, Pd, Pt, Fe and for random Ni-Fe alloys (permalloy).

Our approach based on the TB-LMTO method with the CPA numerical codes [1, 2, 4, 6] For all of the supercell techniques, it is necessary to perform numerically expensive averaging over random configurations realizing the studied system. The AAM-CPA is numerically more efficient, but the supercell AAM allows, at least in principle, e.g., to include correlated spin-fluctuations near the Curie temperature (the magnetic short-range order). Although this may be a huge disadvantage of the CPA, it does not usually cause any problems and it may be compensated by more detailed studies that are possible because of its effectiveness. It was shown especially in our studies focused on a description of systems, for which the AAM had not been employed before.

In Ref. [2], Ni and Cu-Ni alloys are treated by the fully-relativistic approach with a focus on the longitudinal resistivity and AHC. For similar systems, we also investigated the spin polarization of the electrical current [4] influenced by various alloying. Half-Heusler FM NiMnSb with both phonons and magnons was studied up to the Curie temperature [6].

2.1.2 Displacement matrix

Considering the TB-LMTO method where combinations of regular and irregular solutions of spherical Schrödinger equation (Laplace equation) are used for definition of LMTO orbitals [12], we may describe the homogeneous polynomials regular at zero by real spherical harmonics Y_L

$$J_L(\mathbf{r}) = J_l(r)Y_L(\hat{\mathbf{r}}), \tag{2.1}$$

where

$$J_l(r) = \frac{q}{2l+1}\left(\frac{r}{w}\right)^l \ . \tag{2.2}$$

In Eq. (2.1) and (2.2) $L = (l, m)$, $r = |\mathbf{r}|$, $\hat{r} = \mathbf{r}/r$, and w is a length scale. An arbitrary prefactor $q \neq 0$ (does not depend on L) has the value of $q = 1/2$ in Ref. [12].

Translation of the origin $J_L(\mathbf{r}) \to J_L(\mathbf{r} - \mathbf{u})$ can be performed using displacement matrices $D_{L'L}(\mathbf{u})$ described by the relation

$$J_L(\mathbf{r} - \mathbf{u}) = \sum_{L'} J_{L'}(\mathbf{r}) D_{L'L}(\mathbf{u}) \ ; \tag{2.3}$$

this treatment corresponds to a linear transformation of the coordinates and will be considered to be the implicit definition of the displacement matrices.

In order to describe the atomic displacements, the linear operators of the transformations must be known. For the displacement matrices defined in (2.3) the relation

$$D_{L'L}(\mathbf{u}) = 4\pi \sum_{L''}^{l=l'+l''} \frac{(-1)^{l''}(2l-1)!!C_{LL'L''}}{(2l'-1)!!(2l''+1)!!}\left(\frac{u}{w}\right)^{l''} Y_{L''}(\hat{\mathbf{u}}) \tag{2.4}$$

holds, where Gaunt coefficients $C_{LL'L''}$ are

$$C_{LL'L''} = \int Y_L(\hat{\mathbf{r}}) Y_{L'}(\hat{\mathbf{r}}) Y_{L''}(\hat{\mathbf{r}}) \ \mathrm{d}\Omega \, . \tag{2.5}$$

Employing (2.2), the displacement matrices may be expressed as

$$D_{L'L}(\mathbf{u}) = \frac{4\pi}{q} \sum_{L''}^{l=l'+l''} \frac{(-1)^{l''}(2l-1)!!C_{LL'L''}}{(2l'-1)!!(2l''-1)!!} J_{L''}(\mathbf{u}) \, . \tag{2.6}$$

Proof: Relation between the complex spherical harmonics $\mathcal{Y}_L(\hat{\mathbf{r}})$ for $L = (l, m)$ and the real ones is given by a unitary linear transformation

$$\mathcal{Y}_L(\hat{\mathbf{r}}) = \sum_{m'} A^{(l)}_{mm'} Y_{lm'}(\hat{\mathbf{r}}) \, , \tag{2.7}$$

where $A^{(l)}_{mm'}$ are some coefficients. For our purposes, it is not necessary to know their explicit form, we just need their property

$$\sum_m \left(A^{(l)}_{mm'}\right)^* A^{(l)}_{mm''} = \delta_{m'm''} \ . \tag{2.8}$$

Complex spherical harmonic functions create a basis with the relation of orthonormality

$$\int \mathcal{Y}^*_L(\hat{\mathbf{r}}) \mathcal{Y}_{L'}(\hat{\mathbf{r}}) \mathrm{d}\Omega = \delta_{LL'} \ ; \tag{2.9}$$

the plane wave $e^{i\mathbf{k}\cdot\mathbf{r}}$ in this space can be expand into this basis with the spherical Bessel functions $j_l(x)$ used as the coefficients of the series (Rayleigh Eq. [93]):

$$e^{i\mathbf{k}\cdot\mathbf{r}} = 4\pi \sum_L i^l j_l(kr) \mathcal{Y}^*_L(\hat{\mathbf{k}}) \mathcal{Y}_L(\hat{\mathbf{r}}) \ . \tag{2.10}$$

By using Eq. (2.7) and (2.8), the last identity can be recast into the form with real spherical harmonics:

$$e^{i\mathbf{k}\cdot\mathbf{r}} = 4\pi \sum_L i^l j_l(kr) Y_L(\hat{\mathbf{k}}) Y_L(\hat{\mathbf{r}}) \ . \tag{2.11}$$

Let us briefly show how to combine these equations in order do describe the displacement. The expansion of the spherical wave can be rewritten employing (2.11) and then we make a substitution $\mathbf{R} = \mathbf{r} - \mathbf{u}$ to simplify a notation of the new coordinate system:

$$\begin{aligned}
e^{i\mathbf{k}\cdot\mathbf{R}} &= e^{i\mathbf{k}\cdot(\mathbf{r}-\mathbf{u})} \\
&= 4\pi \sum_L i^l j_l(kR) Y_L(\hat{\mathbf{k}}) Y_L(\hat{\mathbf{R}}) \\
&= (4\pi)^2 \left(\sum_L i^l j_l(kr) Y_L(\hat{\mathbf{k}}) Y_L(\hat{\mathbf{r}}) \right) \left(\sum_{L'} i^{l'} j_{l'}(ku) Y_{L'}(\hat{\mathbf{k}}) Y_{L'}(-\hat{\mathbf{u}}) \right) \\
&= (4\pi)^2 \left(\sum_L i^l j_l(kr) Y_L(\hat{\mathbf{k}}) Y_L(\hat{\mathbf{r}}) \right) \left(\sum_{L'} (-1)^{l'} i^{l'} j_{l'}(ku) Y_{L'}(\hat{\mathbf{k}}) Y_{L'}(\hat{\mathbf{u}}) \right) \\
&= (4\pi)^2 \left(\sum_{L'} i^{l'} j_{l'}(kr) Y_{L'}(\hat{\mathbf{k}}) Y_{L'}(\hat{\mathbf{r}}) \right) \left(\sum_{L''} (-1)^{l''} i^{l''} j_{l''}(ku) Y_{L''}(\hat{\mathbf{k}}) Y_{L''}(\hat{\mathbf{u}}) \right) .
\end{aligned} \tag{2.12}$$

In the third step, we used

$$Y_L(-\hat{\mathbf{u}}) = (-1)^l Y_L(\hat{\mathbf{u}}) \tag{2.13}$$

and the last identity was obtained by changing summation indices.

Now, using Eq. (2.12), multiplying both sides of the equation by $Y_{\tilde{L}}(\hat{\mathbf{k}})$, integrating over $\hat{\mathbf{k}}$, considering orthonormality

$$\int Y_L^*(\hat{\mathbf{r}}) Y_{\tilde{L}}(\hat{\mathbf{r}}) \mathrm{d}\Omega = \delta_{L\tilde{L}} \tag{2.14}$$

and definition of Gaunt coefficients (2.5), one may get

$$i^l j_l(kR) Y_L(\hat{\mathbf{R}}) = 4\pi \sum_{L'L''} (-1)^{l''} i^{l'+l''} C_{LL'L''} j_{l'}(kr) Y_{L'}(\hat{\mathbf{r}}) j_{l''}(ku) Y_{L''}(\hat{\mathbf{u}}) \ . \tag{2.15}$$

These steps are obtained by algebraic substitutions, reorganizing the terms and dividing it by the part, which is same in the both sides of the equation.

Asymptotic behavior of the spherical Bessel function is

$$j_l(kr) \approx \frac{(kr)^l}{(2l+1)!!} \qquad \text{for} \quad kr \ll 1 \ . \tag{2.16}$$

Inserting the asymptotics for $kr \ll 1$ into Eq. (2.15), considering

$$C_{LL'L''} = 0 \qquad \text{for} \quad l > l' + l'' \tag{2.17}$$

and comparing the coefficients at the terms proportional to k^l on both sides of the equation, the following identity is obtained:

$$\begin{aligned}
&i^l \frac{R^l}{(2l+1)!!} Y_L(\hat{\mathbf{R}}) = \\
&= 4\pi \sum_{L'L'', l=l'+l''} (-1)^{l''} i^{l'+l''} C_{LL'L''} \frac{r^{l'}}{(2l'+1)!!} Y_{L'}(\hat{\mathbf{r}}) \frac{u^{l''}}{(2l''+1)!!} Y_{L''}(\hat{\mathbf{u}}) \ .
\end{aligned} \tag{2.18}$$

It can be further simplified when Eq. (2.2) is employed after dividing Eq. (2.18) by $2w^l = 2w^{l'+l''}$. Furthermore, imaginary unit cancels because of the same power of $l = l' + l''$. The final result corresponding to a translation of J_L is then

$$J_L(\mathbf{R}) = 4\pi \sum_{L'L'',l=l'+l''} (-1)^{l''} \frac{(2l-1)!!}{(2l''+1)!!} \; C_{LL'L''} \; \frac{J_{L'}(\mathbf{r})}{(2l'-1)!!} \left(\frac{u}{w}\right)^{l''} Y_{L''}(\hat{\mathbf{u}}) \; . \quad (2.19)$$

Eq. (2.4) for the transformation of the origin of the coordinates in the terms of matrix operation is the direct result of this identity. It is obtained when this relation is plugged into Eq. (2.3), both sides of the equation are compared and corresponding terms are cancelled. The conditions for l are taken into account once more and the desired transform is obtained.

2.1.3 Properties of the displacement matrix

The properties of the representation matrix given by Eq. (2.4) are following:

1. $D_{L'L}(\mathbf{u}) = 0$ for $l' > l$,
2. $D_{L'L}(\mathbf{u}) = \delta_{L'L}$ for $l = l'$,
3. $D_{L'L}(\mathbf{u})$ is a harmonic polynomial of a degree $l - l'$ for $l > l'$,
4. $D(\mathbf{0}) = \mathbb{1}$,
5. $D^{-1}(\mathbf{u}) = D(-\mathbf{u})$,
6. $D(\mathbf{u})D(\mathbf{v}) = D(\mathbf{v})D(\mathbf{u})$ (Physical interpretation: It does not depend on the order of displacements.), and
7. $D(\mathbf{u}+\mathbf{v}) = D(\mathbf{u})D(\mathbf{v})$ (Physical interpretation: Two displacements should be equivalent to the sum of them.).

2.1.4 Transformation of the potential functions

The previous sections describe the derivation of displacement matrices for the polynomials J_L related to the regular (at $r = 0$) solutions of the Laplace equation. The second kind of possible solution leads to polynomials regular in infinity ($r \to \infty$) and irregular at zero. A vector space can be also constructed using them, and the basis may by chosen in the following way:

$$K_l(\mathbf{r}) = K_l(r) Y_L(\hat{\mathbf{r}}) \; , \quad (2.20)$$

where

$$K_l(r) = q' \left(\frac{w}{r}\right)^{l+1} \quad (2.21)$$

with an arbitrary prefactor $q' \neq 0$ different from the previously introduced q; $q' = 1$ in Ref. [12]. The translation of the origin is given by a formula similar to the previous one, now in the terms of K_L:

$$K_L(\mathbf{r}-\mathbf{u}) = \sum_{L'} K_{L'}(\mathbf{r}) D_{LL'}(-\mathbf{u}) \; . \quad (2.22)$$

The sum above should be absolutely convergent for $u < r$ and this relation can be proven from the previous properties and the expansion (valid for $r + 2u < |\mathbf{r}'|$)

$$\frac{wqq'}{|\mathbf{r} - \mathbf{r}'|} = 4\pi \sum_L J_L(\mathbf{r}) K_L(\mathbf{r}') = 4\pi \sum_L J_L(\mathbf{r} - \mathbf{u}) K_L(\mathbf{r}' - \mathbf{u}) \ . \tag{2.23}$$

Once we have identities (2.3) and (2.22), we can describe a displacement of the potential functions, because these relations leads to translational invariance of the Wronskian relations

$$\{J_L, K_{L'}\} = -wqq'\delta_{LL'} \tag{2.24}$$

which is an analogy with Eq. (2.24) in [12].

Spin polarization must be assumed for many materials in order to get realistic results from the calculations. Let us introduce subscript $s = -\frac{1}{2}, \frac{1}{2}$ which labels spinors with quantum numbers $lms = Ls$. Then we can write for the solutions of the Schrödinger equation:

$$J_{Ls}(\mathbf{r}) = J_L(\mathbf{r})\chi_s \qquad \text{and} \qquad K_{Ls}(\mathbf{r}) = K_L(\mathbf{r})\chi_s \tag{2.25}$$

with

$$\chi_{s=+1/2} = \begin{pmatrix} 1 \\ 0 \end{pmatrix} \qquad \text{and} \qquad \chi_{s=-1/2} = \begin{pmatrix} 0 \\ 1 \end{pmatrix} \ . \tag{2.26}$$

All of the indices for the quantum numbers can be doubled to make the notation easy to understand:

$$L \to Ls \ . \tag{2.27}$$

In particular, the displacement matrices with spin are given be

$$D_{L's',Ls}(\mathbf{u}) = D_{L',L}(\mathbf{u})\delta_{s's} \ . \tag{2.28}$$

Relations for modifications of unscreened potential functions $P^0_{\mathbf{R}l}(E)$ used in the LMTO method are introduced in this section. Potential functions come from a solution of a single-site problem, they describe the properties of the individual atomic spheres and are required for the *ab initio* calculations.

Let N be a general index of quantum numbers

1. $N = L$ for non-relativistic and spin-less case and
2. $N = Ls$ if spin is taken into account (and also in the relativistic case).

For simplicity, the previously introduced (2.3) and (2.22) can be rewritten as

$$\tilde{J}_N = \sum_M D_{MN} J_M \tag{2.29}$$

$$\tilde{K}_N = \sum_M \left(D^{-1}\right)_{NM} K_M \tag{2.30}$$

with the inverse relations

$$J_N = \sum_M \left(D^{-1}\right)_{MN} \tilde{J}_M \tag{2.31}$$

$$K_N = \sum_M D_{NM} \tilde{K}_M \ . \tag{2.32}$$

Potential functions in the canonical (unscreened) LMTO representation and in the ASA are defined by Eq. (2.25) in [12]

$$P^0_{\mathbf{R}l}(E) = \frac{\{K_l(r), \varphi(r,E)\}}{\{J_l(r), \varphi(r,E)\}}|_{r=s_{\mathbf{R}}} \ , \tag{2.33}$$

where φ are radial amplitudes given by a solution of a radial Schrödinger equation and $s_{\mathbf{R}}$ is an atomic sphere radius[1]. In a general case, one has to use a matrix notation:

$$P^0_{M,N} = \sum_\Lambda \{K_M, \varphi_\Lambda\} \left[\{J, \varphi\}^{-1}\right]_{\Lambda,N} \tag{2.34}$$

and in a shorter form with matrix indices omitted

$$P^0 = \{K, \varphi\}\{J, \varphi\}^{-1} \ . \tag{2.35}$$

Labels Λ go through all linearly independent regular solutions of the single site problem [12]:

1. $\Lambda = L$ for the non-relativistic and spin-less calculations,
2. $\Lambda = \kappa\mu$ for the relativistic non-magnetic system, and
3. $\Lambda = l\mu\lambda$ in a general spin-polarized relativistic case.

Notation $\{A, B\}$ means a Wronskian given by elements $\{A_i, B_j\} = \{A, B\}_{i,j}$; A and B are general functions. In analogy with Eq. (2.34) and (2.35), it can be written with respect to displaced origin $\tilde{O} = O + \mathbf{u}$:

$$\tilde{P}^0_{M,N} = \sum_\Lambda \{\tilde{K}_M, \varphi_\Lambda\} \left[\{\tilde{J}, \varphi\}^{-1}\right]_{\Lambda,N} \tag{2.36}$$

$$\tilde{P}^0 = \{\tilde{K}, \varphi\}\{\tilde{J}, \varphi\}^{-1} \ . \tag{2.37}$$

Since the displacement matrices $D_{L'L}(\mathbf{u})$ are real, see (2.4), we may combine the equations above in order to get Wronskians for the shifted origin:

$$\{J_N, \varphi_\Lambda\} = \sum_M \left(D^{-1}\right)_{MN} \{\tilde{J}_M, \varphi_\Lambda\} \ , \quad \{J, \varphi\} = \left(D^{-1}\right)^T \{\tilde{J}, \varphi\} \ , \tag{2.38}$$

$$\{K_N, \varphi_\Lambda\} = \sum_M D_{NM} \{\tilde{K}_M, \varphi_\Lambda\} \ \text{ and } \quad \{K, \varphi\} = D\{\tilde{K}, \varphi\} \ . \tag{2.39}$$

When we plug the Wronskians to each other, we get

$$P^0 = D\{\tilde{K}, \varphi\} \left[\left(D^{-1}\right)^T \{\tilde{J}, \varphi\}\right]^{-1} = D\{\tilde{K}, \varphi\}\{\tilde{J}, \varphi\}^{-1} D^T \ . \tag{2.40}$$

Definition of potential functions can be used now and we finally get

$$P^0 = D(\mathbf{u}) \tilde{P}^0 D^T(\mathbf{u}) \ . \tag{2.41}$$

[1]The radius determines the region where the atomic sphere approximation is used

Let us remind, that P^0 is in the original coordinates and corresponds to the ideal crystalline lattice, whereas $\tilde{P}^0$ describes the potential function with respect to the displaced origin. Since we investigate the single-site problem and use the ASA, the potential functions $\tilde{P}^0$ are spherically symmetric, in contrast to P^0.

Unscreened potential functions may be modified to a new origin by Eq. (2.41); for the transformation to the screened representation (functions P^α) one has to use

$$P^\alpha = P^0 \left(1 - \alpha P^0\right)^{-1} \ . \tag{2.42}$$

Unscreened P^0 can be obtained in the numerical codes for the electrical transport in the same way as P^α if $\alpha = 0$ is used. The computational order is following:

1. Set $\alpha = 0$ and get $\tilde{P}^0$,
2. transform $\tilde{P}^0$ to P^0 using (2.41),
3. calculate P^α with (2.42) and use it for the following numerical steps.

Green's functions, conductivity etc. are then calculated in the original way with the new P^α and with the screened structure constants (S^α) of the ideal crystalline lattice.

2.1.5 Fermi-sea term

To evaluate the Fermi-sea term within the fully-relativistic LMTO approach and related properties, derivatives of the potential functions with respect to the complex energy z are needed, see Eq. (27) in Ref. [81]. With the same notation as above, it holds

$$\frac{\mathrm{d}P^\alpha}{\mathrm{d}z} = \left(1 - P^0\alpha\right)^{-1} \frac{\mathrm{d}P^0}{\mathrm{d}z} \left(1 - \alpha P^0\right)^{-1} \ . \tag{2.43}$$

Proof: Eq. (2.43) is a direct result of the energy derivative combined with Eq. (2.42):

$$\begin{aligned} \frac{\mathrm{d}P^\alpha}{\mathrm{d}z} =& \frac{\mathrm{d}P^0}{\mathrm{d}z} \left(1 - \alpha P^0\right)^{-1} + P^0 \left(1 - \alpha P^0\right)^{-1} \alpha \frac{\mathrm{d}P^0}{\mathrm{d}z} \left(1 - \alpha P^0\right)^{-1} = \\ &= \left(1 + \left(1 - P^0\alpha\right)^{-1} P^0\alpha\right) \frac{\mathrm{d}P^0}{\mathrm{d}z} \left(1 - \alpha P^0\right)^{-1} = \\ &= \left(1 - P^0\alpha\right)^{-1} \left(1 - (P^0\alpha - P^0\alpha)\right) \frac{\mathrm{d}P^0}{\mathrm{d}z} \left(1 - \alpha P^0\right)^{-1} . \end{aligned} \tag{2.44}$$

The derivatives of the unscreened potential functions are then transformed by the energy-independent displacement matrix D similarly to P^0 in Eq. (2.41), specifically

$$\frac{\mathrm{d}P^0}{\mathrm{d}z} = D(\mathbf{u}) \frac{\mathrm{d}\tilde{P}^0}{\mathrm{d}z} D^T(\mathbf{u}) \ . \tag{2.45}$$

For practical purposes, the first step of the numerical approach is an evaluation of $\tilde{P}^0$ and of its energetic derivative from the LMTO potential parameters, which is then used in both Eq. (2.41) and (2.45). Similar numerical approaches hold for the matrix inversions $\left(1 - P^0\alpha\right)^{-1}$ and $\left(1 - \alpha P^0\right)^{-1}$, that are also computed only once. Therefore, obtaining the Fermi-sea term for the displaced nuclei is numerically almost the same as calculating the standard Fermi-surface term.

2.2 Models of magnetic disorder

The total magnetic moment decreases with increasing temperature for ferromagnetic (FM) materials, see Sec. 1.1.3. It is caused by fluctuating magnetic moments which occur also in systems with different magnetic properties (ferrimagnets, antiferromagnets). To describe these phenomena, two models of magnetic disorder were assumed: (i) the uncompensated disordered local moments and (ii) tilting of the moments. The second one is more general, but both describe only a "static fluctuation" using an averaging within the CPA. If not stated otherwise, for description of magnetic behavior we use local magnetic moments per atom.

Uncompensated disordered local moments The disordered local moment (DLM) approach [94, 95] is based on a description of a paramagnetic (PM) state as a system consisting of uncorrelated magnetic moments (randomly oriented spins). The magnetic moments are aligned in one direction in an undistorted FM state, they start to fluctuate with increasing temperature and the high-temperature limit (beyond the Curie temperature) of the system is described by the moments heading (randomly) to any direction. In the paramagnetic state, the energy of temperature-induced fluctuations of magnetic moments is larger than the energy necessary to sustain the magnetic order.

Not only electronic structure, but also a two-particle quantity such as electrical conductivity can be for a system without the spin-orbit interaction described within the CPA [96, 97]. Therefore, a material having magnetic moments in all of the directions is mathematically equivalent to a system with the same total magnetization (equal to zero) but with the moments heading only in two opposite directions. This description of the high-temperature limit of the system in the form of paramagnetic (antiferromagnetic) structure simplifies the description of the magnetically disordered materials.

The DLM approach was used, e.g., to examine Heusler alloys [96] or spin fluctuations in Fe and Ni [98]. Dependence of physical quantities on the magnetization, and consequently on temperature, cannot be obtained within this model because the total magnetization is equal to zero (PM state). This high-temperature limit may be used to extrapolate the spin-disorder resistivity ρ^{SD} from the electrical transport properties influenced by a combined effect of phonons and magnons. Same extrapolation could be done for measured data, the ρ^{SD} than has a clear interpretation (coming from a pure influence of magnetic disorder) and calculated ρ^{SD} agrees with experimental results. It was proven in studies incorporating both phonons and the DLM: Fe [1], Ni [2], and iron at extreme conditions [3].

The uncompensated DLM (uDLM) model [20, 99, 100] examines systems between the FM state and the PM one (DLM). Magnetic disorder is treated similarly to substitutionaly disordered alloys having two components of identical atoms with magnetic moments heading to opposite directions. Concentration of atoms "A" having the opposite moments (x_{A^-}) ranges from zero (FM) to 0.5 (DLM). Total magnetic moment is given by a sum of the two components $M(x_{\mathrm{A}^+}) + M(x_{\mathrm{A}^-})$ with $x_{\mathrm{A}^+} = 1 - x_{\mathrm{A}^-}$ (concentration of original atoms) and $M(x_{\mathrm{A}^+})$ having opposite sign (direction) than $M(x_{\mathrm{A}^-})$.

The total magnetization monotonically decreases from its maximal value (for $x_{\mathrm{A}^-} = 0$) to the minimal ($M = 0$ for $x_{\mathrm{A}^-} = 0.5$). The direct dependence of

the magnetization on temperature is not obtained even by this model, but its decrease with x_{A^-} may be connected to experimentally known data describing $M(T)$ [34]. It results to the dependence $x_{\mathrm{A}^-}(T)$ and, ultimately, to temperature dependence of other physical quantities such as electrical transport properties.

Because local moments of some elements within the DLM method may collapse to zero (e.g., Ni), we also employed the fixed-spin moment (FSM) method [101, 102], see Sec. 4.3.2 or Ref. [5]. The FSM method prescribes values of the local moments and their final value is obtained by minimizing the free energy and stabilized by the magnetic entropy effects [3, 103, 104]. The application of the DLM-FSM method applied on random fcc Ni-Fe alloys is presented in Sec. 4.3.2.

Tilting of magnetic moments Magnetic disorder in real systems would more likely consist of fluctuations of magnetic moments around their equilibrium positions. Changing directions of magnetization within the uDLM, even for small x_{A^-}, requires lot of energy and it would be better to describe low-energy magnetic fluctuations by another model.

For these purposes, we introduce a model that is based on tilting several (n) moments of the same atom and on the same crystalographic position. It is done within the CPA, similarly to the DLM approach, and a concentration of the original atom (for a given crystalographic position) is equally divided among these n atoms. Sum of the concentrations equals to the concentration of the single original atom in the FM alignment. In the framework of noncolinear magnetism, the moments of the new "virtual" atoms are chosen to head to different directions respecting a symmetry of the material; moreover, they head symmetrically with respect to the original direction. A similar model was also employed within the TB-LMTO method with the CPA and supercells [32].

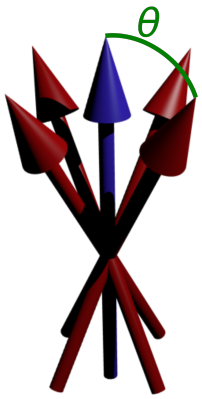

Figure 2.3: Tilting of magnetic moments from a single equilibrium direction (blue) the four new ones (red). Increasing angle of tilting θ corresponds to rising temperature with a limit $\theta = \pi/2$ representing states at and above the Curie temperature.

For our purposes, $n = 4$ is sufficient and the new moments lie on a cone around the original direction. The cone is parametrized by a vertex angle θ: $\theta = 0$ for FM and $\theta = \pi/2$ for PM (or DLM with moments in the plane perpendicular

to moments in the DLM state), see Fig. 2.3. Mathematically, an alloy was constructed by substituting magnetic atoms oriented along the z-direction by the four magntic moments tilted by the Euler angle θ from the z-axis symmetrically in the four directions x, y, $-x$, and $-y$; the four directions are parametrized by the Euler angle $\phi \in \{0.0, 0.5\pi, 1.0\pi, 1.5\pi\}$.

In principle, any number of directions may by used; moreover, different directions could be chosen with different weights (different concentrations of components for the random alloy). This could be employed, e.g., when probability distribution of magnetic moments (and their magnitudes and directions) on temperature is known. Complex methods like Monte-Carlo simulations give such data [29]. Much simpler approach is based on varying the angle θ to obtain $M(\theta)$ dependence and then, similarly to the uDLM method, experimental or other data of $M(T)$ are used to obtain θ angle (being parameter of further calculations) as a function of temperature, see Sec. 2.3.2.

2.3 Description of nonzero temperatures

The previous sections introduced methods for a description of atomic displacements or magnetic disorder. These effects play an important role for a study of finite-temperature phenomena, but a proper implementation is needed to describe the specific values of the temperature. The modification of the potential functions (Sec. 2.1) can be used to displace nuclei, but the magnitudes and directions of the displacement vectors $\mathbf{u}$ must be used as input parameters; it holds similarly for the fluctuation of the magnetic moments (Sec. 2.2, parameters θ or x_{A^-}). Strictly speaking, necessity of the input parameters is not consistent with the philosophy of the first-principles calculations, which should be done "from the beginning" without additional assumptions or special models. Methods for obtaining the parameters by *ab inito* techniques exist, e.g., calculating phonon spectra [92] or Monte-Carlo simulations [29], but their inclusion is beyond the scope of this work and models like the Debye theory of fitting of experimental data are sufficient for our purposes.

2.3.1 Displacements of atoms at finite temperatures

Magnitudes of displacements: Debye theory The directions and magnitudes of the random displacement vectors must correspond to the temperature T of the system. Let us define the mean square displacement

$$\left\langle u^2 \right\rangle = \frac{1}{N} \sum_{i=1}^{N} |\mathbf{u}_i|^2, \tag{2.46}$$

where N is the number of displacement vectors. Considering three spatial dimensions, the Debye theory then leads to (e.g. [105, 106])

$$\left\langle u^2 \right\rangle = \frac{9\hbar^2}{M k_B \Theta_D} \left(\frac{D_1(\tau)}{\tau} + \frac{1}{4} \right), \tag{2.47}$$

where

$$\tau = \frac{\Theta_D}{T} \quad \text{and} \quad D_n(x) = \frac{n}{x^n} \int_0^x \frac{t^n}{e^t - 1} \mathrm{d}t. \tag{2.48}$$

Here $D_n(x)$ is known as the Debye function ($n = 1, 2, 3, ...$), $\hbar$ is the reduced Planck constant, M is the atomic mass, k_B is the Boltzmann constant and Θ_D denotes the Debye temperature. The last term in the bracket (i.e., $1/4$) is important especially for low temperatures and; therefore, can be often neglected.

We note that the Debye theory represents a simplified model for the magnitudes of the atomic displacements that is valid, e.g., only for atoms having identical masses. On the other hand, the Debye theory is also used by other authors [29–32] with good results and we obtained agreement with experimental data even for Cu-Ni [4] and Co-Ni random alloys and for more complex systems like NiMnSb [6, 9], see Sec. 4.3 and 5.1.

A ratio of masses for the Cu-Ni alloy is $[m(\mathrm{Cu}) : m(\mathrm{Ni}) \approx 1 : 0.92]$, i.e., the atoms are very similar. NiMnSb has $[m(\mathrm{Ni}) : m(\mathrm{Mn}) : m(\mathrm{Sb}) \approx 1 : 0.93 : 2.07]$; therefore, a proper choice of atomic displacements was investigated for two cases: a) the magnitudes identical for each atoms or b) the magnitudes scaled according to atomic masses [9]. For this system, we have found deviations of order 5 %

for $\sqrt{\langle u^2 \rangle} = 0.20$ and $0.25\,a_\mathrm{B}$. Compared to other possible uncertainties, e.g., a difference between *spd*- vs. *spdf*-basis or chemical impurities in samples, the error is small and may be usually neglected.

The magnitudes of the displacements coming from the Debye theory are not directly connected to the number of phonons (in the system at given temperature). Therefore, phenomena like the Bloch T^5 law [22, 23] or other more complex effects (see Sec. 1.1.3) are omitted. Similarly, differences between the Debye and Bloch–Grüneisen temperatures [107, 108] are neglected. We also consider phonons to be described by the single value of the mean-square displacement and no difference between optical phonons and acoustics phonons is taken into account. For the proper description of temperatures far bellow the Debey temperature, it would be necessary to assume lower amount of phonons, which would lead to lower root-mean-square displacements. Such a complex behavior is observed, e.g., in data obtained by VASP code (see later Fig. 2.6), but the effects may be neglected for an investigation of a wide range of temperatures.

Although the Debye theory gives reasonable results for many materials, it is still a model having many limitations. For example, it was derived with assumptions that the integrated density of states is proportional to $3n$ (n = the number of atoms in the unit cell) and that the dispersions of phonons may be described by phase velocities [15, 109, 110]. The assumptions are supported by the numbers of freedom related to the oscillators (atoms) and isotropic character of studied systems. A complete revision of the assumptions and the validity of the Debye theory is beyond the scope of this thesis, but we note that a discussion of different approximations is included in many material-specific studies. While the $3n$ factor and the Debye theory holds reasonably for iron [111], it must be modified, e.g., for cubic $KMgF_3$ perovskite [112]. The Debye theory is used or discussed also by other authors employing the AAM [27, 29, 31, 32, 92].

Last but not least, the Debye temperature may be temperature-dependent quantity which is related to an expansion of lattice constants and an interpretation of experimental data [113]. No comprehensive study of the assumptions and the validity of the Debye theory has been found, but for simpler systems like Fe it agrees with experimental literature [111]. If not stated otherwise, in this thesis we use the Debye formula from the quantum averaging (2.47). For simplicity, we neglect the zero-temperature fluctuations (the 1/4 term).

Directions of displacements The nuclei must be displaced in a way which corresponds to stochastic motions of particles. There are two kinds of approaches: The first method defines N directions regularly distributed around the origin and lying on a sphere with a radius equal to the magnitude of the displacement. In this case, the directions are well defined and it is easy to reproduce them; on the other hand, they may not correspond to the random thermal movement. The second approach constructs N (pseudo-)random directions of the vectors with the given magnitude. Furthermore, not only random directions, but also random magnitudes having defined mean values and dispersions can be used. Advantages and disadvantages are opposite to the first approach: it is hard to reproduce the directions, but it describes the stochastic movement in a better way. Both methods should give the same results for large N.

Since we are focused on metals with cubic symmetry (FCC or BCC), one

can choose $N = 8$ in the first method and set the directions pointing along the body diagonals of the cube; to be specific, we are talking about the vectors $(1,1,1)$, $(1,1,-1)$, $(1,-1,1)$, $(1,-1,-1)$, $(-1,1,1)$, $(-1,1,-1)$, $(-1,-1,1)$ and $(-1,-1,-1)$. Let us mark this set of the vectors as XYZ. To study an influence of an asymmetry of the displacements, we denote the set $\{(0,1,1)$, $(0,1,-1)$, $(0,-1,1)$, $(0,-1,-1)$, $(1,0,1)$, $(1,0,-1)$, $(-1,0,1)$, $(-1,0,-1)\}$ as XZ. Let us denote the resistivity ρ for these sets as ρ_{XYZ} and ρ_{XZ}.

Fig. 2.4 shows the electrical resistivity as a function of the root-mean-square displacement $\sqrt{\langle u^2 \rangle}$. The corresponding temperature was calculated for each displacement using Eq. (2.47), see secondary horizontal axes on the graphs. The detailed knowledge of the temperature as a function of the displacement is not perfectly clear at present. It may influence a comparison with experimental data which are usually presented as a $\rho(T)$ dependence; the same conversion was used for data from [29]. The term $1/4$ in the bracket of Eq. (2.47) was omitted in the conversion (in order to get $\rho = 0$ for $T = 0$), this leads to an error of 7 % at $\sqrt{\langle u^2 \rangle} = 0.15\, a_\mathrm{B}$ and lesser than 2 % for $\sqrt{\langle u^2 \rangle} > 0.23\, a_\mathrm{B}$ (a_B is the Bohr radius). The error given by the Debye model is estimated to 5 %.

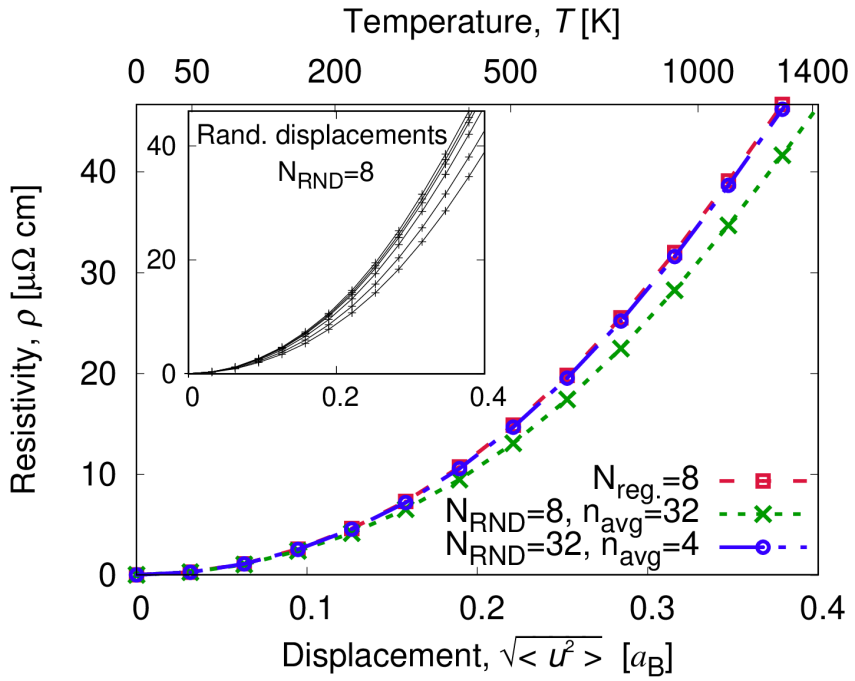

Figure 2.4: Dependence of the resistivity on the numerical parameters: directions (random RND and regularly distributed XYZ) and number N of the displacement vectors for FM iron. The inset graph shows the dispersions for different configurations of random displacement vectors.

The input parameters of the calculations include also directions of the displacement vectors. We present Fig. 2.4 (resistivity of FM iron) to illustrate the dependence of the resistivity on the directions of the displacement. Our results exhibit only negligible dependence on directions of the displacements if they were distributed regularly around an origin. It even does not depended on the number N of directions (it has been examined for $8 \leq N \leq 32$; this does not hold for the

random vectors), see Fig. 2.4 for $\rho_{XYZ} = \rho_{XZ}$ (the two curves overlap). These vectors were scaled to correspond to the given $\sqrt{\langle u^2 \rangle}$ and we generated several (K) configurations of random vectors for each N. The data $\rho_{RND,N=8}$ for $N = 8$ correspond to the arithmetic mean over $K = 32$ independent configurations. If we use $N = 32$ random directions, the vectors are apparently randomly distributed to all directions and the resistivity $\rho_{RND,N=32}$ overlaps with ρ_{XYZ} already if the mean value from $K = 4$ configurations is taken. The scatter of the resistivity values for different configurations of random vectors for $N = 8$ is displayed in the inset of Fig. 2.4.

Directions of displacements in tetragonal CuMnAs Various tests were performed to verify that a choice of atomic displacements does not influence results. Here we show data from one of the tests, i.e., for tetragonal CuMnAs (see details in Sec. 5.2) with a ratio of the lattice constants $c/a = 1.65$ [114]. We calculated electrical resistivities for the two following choices of the directions (summarized in Fig. 2.5):

1. The directions were the same as for the previously mentioned cubic systems, i.e., pointing along the body diagonals of a cube. This set of displacements is labeled as "cubic" in Fig. 2.5.

2. The displacement vectors headed towards the body diagonal of the tetragonal cell, i.e., they were scaled by the factor c/a with respect to the cubic structure (labeled "tetragonal").

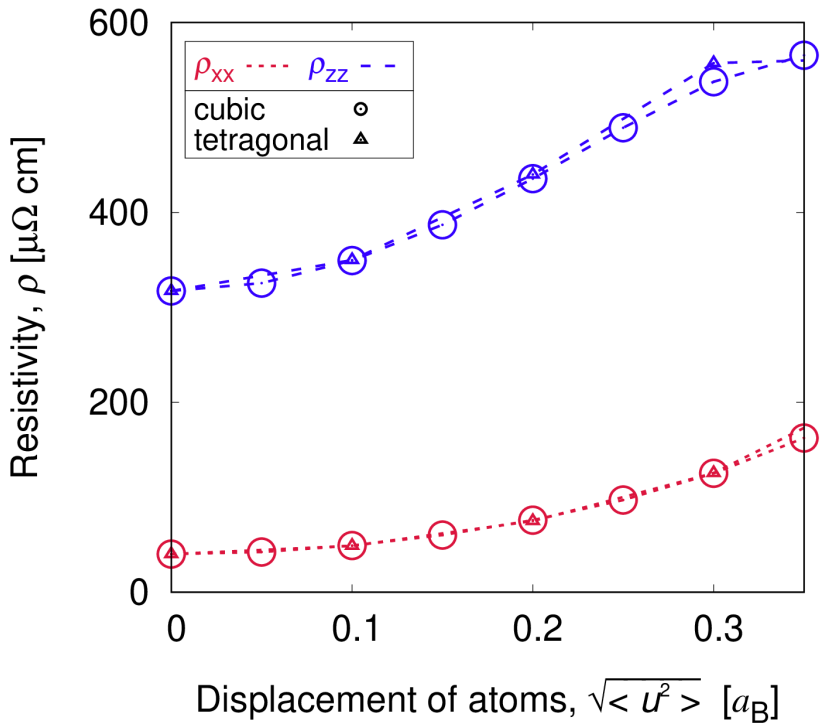

Figure 2.5: Both ρ_{xx} (red dotted lines) and ρ_{zz} (blue dashed lines) are identical for the cubic (circles) and tetragonal (triangles) directions of the displacements in tetragonal CuMnAs.

Although the directions differ, the magnitudes may be easily compared and they are shown on the horizontal axis in Fig. 2.5. The in-plane ρ_{xx} and out-of-plane ρ_{zz} resistivities are almost identical for both choices ("cubic" and "tetragonal"). This justifies employing the AAM even if the proper directions of the displacements are not perfectly known.

More accurate determination of the atomic displacements Modern techniques like atomistic simulations can give more accurate results for both the magnitudes and directions of the displacements at finite temperatures. While the magnitudes can be obtained analytically from the Debye theory, the simulations are numerically expensive. They are necessary when the Debye approximation fails; two such conditions were met.

Firstly, employing Eq. (2.47) and the AAM results in electrical resistivities that agree with experimental data for many transition metals and alloys, see Chapter 4. On the other hand, the identical approach does not work for copper, silver, and gold. It was assumed that the inaccuracy is caused by the less localized valence s and p orbitals (compared to d shells) [1], but it was later found that the error comes from the Debye theory. The VASP (and phonopy) package within the scalar-relativistic approach was used to obtain temperature-depended values of $\sqrt{\langle u^2 \rangle}$ for different materials. The magnitudes agree with the Debey theory for metals that were well described also without VASP but differ two or three times for Cu, Ag, and Au – previously problematic elements.

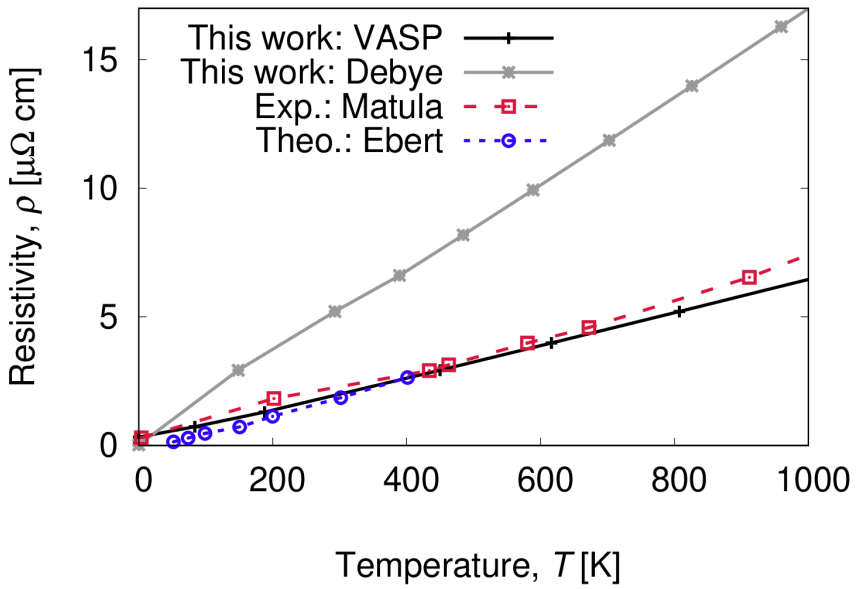

Figure 2.6: Obtained results compared with both experimental data [115] and calculations [29] reveals a huge error coming for the Debye theory for Cu while the root-mean-square displacement from the VASP package agree perfectly.

Resistivity of Cu as a function of temperature is shown in Fig. 2.6. The experimental data [115] were, naturally, measured as a function of temperature, our results calculated as $\rho(\sqrt{\langle u^2 \rangle})$ and converted to the temperature-dependence by (i) the Debye theory and (ii) VASP displacements. The magnitudes of the

displacements are not shown on the secondary horizontal axis because they differ for the approaches. Authors of the theoretical study [29] also employ the Debye theory, but their results agree with the same experimental data (and our results with VASP). Our VASP- and Debye-results differ by the same factor and we note that it is the same number coming from the degrees of freedom (see the previously discussed limitations of the Debye theory). On the other hand, Ref. [29] also shows data for Fe and Ni (also without the factor of 3 in the Debye theory) that agree with our calculations (both Debye- and VASP-based). A source of the disagreement remains unclear.

Secondly, for the conditions of the Earth's core, see Sec. 4.5. Iron and iron-based alloys were studied at high pressure (350 GPa) and high temperature (5000–6000 K). The Debye theory describes only the ambient conditions and for the root-mean-square displacements obtained for standard pressure and 5500 K were $\sqrt{\langle u^2 \rangle} = 0.82\, a_\mathrm{B}$. On the other hand, finite temperature *ab initio* molecular dynamics (AIMD) within the VASP code results in $\sqrt{\langle u^2 \rangle} = 0.59\, a_\mathrm{B}$ [116].

Atomic displacements: Thermal expansion and spin-orbit interaction With VASP software we also checked an influence of thermal expansion and the spin-orbit interaction on magnitudes of the displacements. Fcc-Pt was chosen for this purpose because both phenomena could be important. For an influence of the spin-orbit see Fig. 4.3 showing electrical resistivity and a correction of 20 % caused by this effect (at 1000 K). An expansion of the lattice parameter increased a volume by 3.4 % (1000 K), which agrees with the measured volumetric thermal expansion being about 3 % [117].

Root-mean-square displacements for 1000 K was obtained:

- Scalar-relativistic without thermal expansion: $\sqrt{\langle u^2 \rangle} = 0.2648\, a_\mathrm{B}$,
- spin-orbit interaction without thermal expansion: $\sqrt{\langle u^2 \rangle} = 0.2623\, a_\mathrm{B}$, and
- scalar-relativistic with thermal expansion: $\sqrt{\langle u^2 \rangle} = 0.2644\, a_\mathrm{B}$.

These corrections correspond to 0.9 and 1.5 %, respectively. The thermal expansion for Ag results in the correction of 1.9 %.

Because both effects were found to be negligible within the whole relevant temperature range (1000–2000 K); the corrections to the magnitudes of the displacements are neglected in the rest of the thesis.

2.3.2 Fluctuations of magnetic moments

An increase of both the angle of tilting θ and concentration of moments with the opposite direction x_{A^-} (Sec. 2.2) monotonously decreases the total magnetization of a ferromagnetic system. The same happens when temperature increases towards the Curie point, see Fig. 1.3; therefore, θ and x_{A^-} can be unambiguously connected to the temperature below T_C.

Authors of [29] employ Monte-Carlo simulations in a combination with fitting the experimental data to obtain the connections between the directions of the moments and the temperature. This approach is beyond the scope of this work; on

the other hand, measured temperature-depended magnetization $M(T)$ is available for many systems and by fitting $M(\theta)$ or $M(x_{\mathrm{A}^-})$ the dependences $T(\theta)$ and $T(x_{\mathrm{A}^-})$ (or inverse ones) may be obtained. With this approach, perfect agreement of our calculated electrical resistivity and experimental data from literature was obtained for ferromagnetic Fe and Ni (not published)and NiMnSb [6, 9], see Sec. 4.2.

To demonstrate this approach, we present Fig. 2.7, where the dependence of the energy difference $E - E_0$ from the undistorted ferromagnetic NiMnSb (E_0) on the spin magnetic moment μ_s (local moment per atom) is shown; μ_s is the average of all local magnetic spin moments projected onto the direction of the original magnetization. The disordered PM state corresponds to $\mu_s = 0$ while

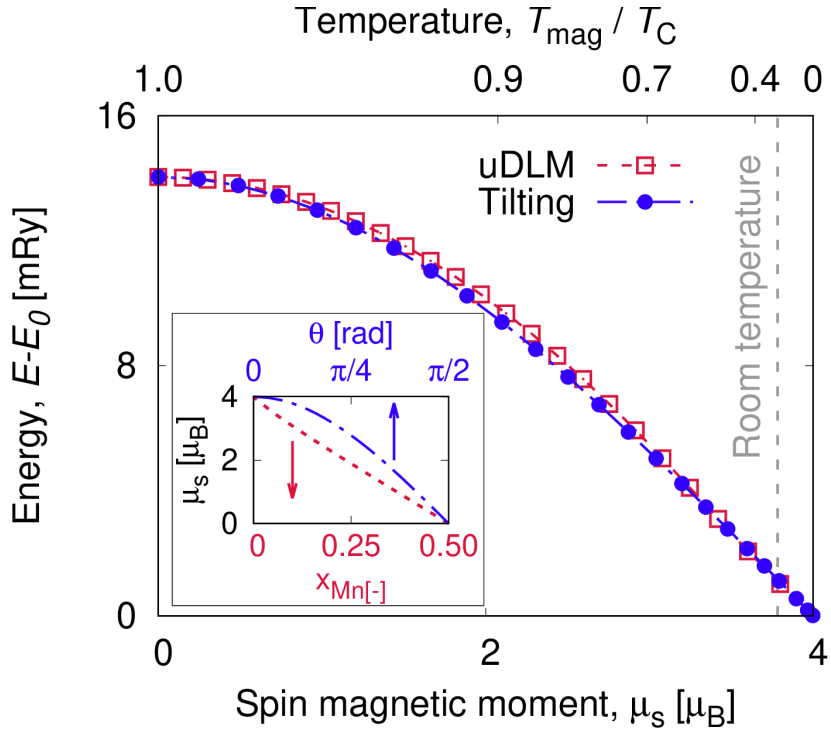

Figure 2.7: For stoichiometric NiMnSb, the uDLM (red dashed lines with squares) and the tilting (blue dot-dashed lines with circles) models give the same total energy (E) from the undistorted state (E_0) as a function of the magnetic moment μ_s. Temperature T_{mag} (top horizontal axis) obtained by fitting approximate formula [34] to the experimental magnetization data [118]. Inset: The spin magnetic moment as a function of model parameters x_{Mn^-} or θ.

the undistorted system has $\mu_s = 4\mu_B$. With increasing θ or x_{Mn^-} the total magnetization of stoichiometric NiMnSb decreases from $M = 4.0\mu_B$ per formula unit (local moments are $m_{\mathrm{Ni}} = 0.26\mu_B$, $m_{\mathrm{Mn}} = 3.75\mu_B$, $m_{\mathrm{Sb}} = -0.05\mu_B$, and the empty-sphere moment $m_{\mathrm{empty}} = 0.08\mu_B$) to zero. Almost identical parabolic-like dependences $E(\mu_s)$ are obtained for both models, which can be understood in terms of the classical Heisenberg Hamiltonian (note that μ_s is proportional to $\cos\theta = 1 - 2x_{\mathrm{Mn}^-}$). The equivalence of both models of the magnetic disorder for the $E(\mu_s)$ does not hold for the transport properties, see Sec. 5.1. We fitted the measured magnetization [118]; both the zero- and Curie-temperature limits were fixed. The Bloch $T^{3/2}$ law is approximately valid up to temperatures of

$T_C/3$ [118]; however, with this more advanced formula [34] we reproduced the magnetization satisfactorily for T_{mag} from 0 to to $T_C = 730$ K. This temperature scale is depicted in Fig. 2.7 on the top horizontal axis. The experimentally observed change of saturation magnetization is about 10 % of the original value at the room temperature [118–120], which corresponds to $x_{\mathrm{Mn^-}} \approx 0.04$ or $\theta \approx 0.14\pi$. We note that the experimental data [118] are available only up to 300 K; beyond this temperature the extrapolation based on the approximate equation obtained from [34] is used.

The electrical transport properties with included spin-fluctuations are shown in Sec. 4.2 and 5.1.

2.3.3 Fermi-Dirac distribution

Transport properties in our first principles calculations are obtained using the linear response theory and Kubo formula [72, 73], see Sec. 1.3. The Fermi-Dirac distribution $f(E)$ in the Eq. (1.87) is usually assumed to describe conditions of the zero temperature. For such case the following holds

$$\frac{\partial f(E)|_{T=0}}{\partial E} = -\delta(E - E_F)\,, \tag{2.49}$$

which effectively cancels out the integration over the energy variable in Eq. (1.87). The integration may become of significant importance for larger temperatures, i.e. for the case when the derivative of the Fermi-Dirac function has a larger support or the density of states is an odd function around the Fermi level E_F. The conductivity tensor is then

$$\sigma_{\mu\nu}^{\mathrm{int.}} = -\int_{-\infty}^{\infty} \mathrm{d}E\, \sigma_{\mu\nu}^{0}(E) \frac{\partial f(E)}{\partial E} \tag{2.50}$$

where $\sigma_{\mu\nu}^{0}(E)$ is the zero temperature conductivity obtained for $T = 0$ with an assumption of (2.49).

The effect of the broadened Fermi-Dirac distribution may be investigated whenever the electrical conductivity is calculated; e.g., also for the temperature-depended spin-polarized conductivity. We note that the inclusion of this phenomenon is computationally expensive because the $\sigma_{\mu\nu}^{0}(E)$ must be calculated for a wide range of energies. It was found that twenty or more energy points (depending on the shape of $\sigma_{\mu\nu}^{0}(E)$) are needed to obtain negligible error within the numerical integration. On the other hand, the corrections for the resistivities given by the temperature-depended Fermi-Dirac distribution were obtained in the orders of a few percent, see Sec. 4.4; therefore, it was not applied for more advanced studies.

2.4 Spin-resolved electrical transport

In this Section, a formalism and an approach for treatment of the spin-resolved conductivity is introduced. It is used to evaluate the spin polarization of the electrical current, which characterizes an efficiency of the longitudinal electrical transport for electrons with opposite spin quantum numbers. The spin-nonconserving term is also defined.

Electrical transport properties within the linear response theory are calculated by employing Eq. (1.85). The TB-LMTO method neglects electron motion inside the Wigner-Seitz cells, the velocity operators describe only intersite hoppings [80], and the resulting effective velocity operators are spin-independent. Therefore, the coherent part of the conductivity tensor (obtained from the configurationally averaged auxiliary Green's functions $\bar{g}^s_\pm(E)$) may be projected onto the spin-up and spin-down directions for the spin indices $s =\uparrow$ and $s =\downarrow$, respectively.

The polarization of the spin-resolved currents

$$P_\mu = \frac{\sigma^{\mathrm{coh},\uparrow}_{\mu\mu} - \sigma^{\mathrm{coh},\downarrow}_{\mu\mu}}{\sigma^{\mathrm{coh},\uparrow}_{\mu\mu} + \sigma^{\mathrm{coh},\downarrow}_{\mu\mu}} \tag{2.51}$$

describes a quality of the spin-dependent transport [4, 45, 121]. The polarization equals one for an ideal halfmetal (with exactly one of the spin-channels insulating); if both channels are identical, e.g., for nonmagnetic materials, $P = 0$.

In the relativistic treatment of the transport, strictly speaking, one cannot define the spin-resolved currents precisely because of nonzero spin-flip contribution to the total conductivity (spin-nonconserving term)

$$\sigma^{\mathrm{coh,flip}}_{\mu\mu} = \sigma^{\mathrm{coh}}_{\mu\mu} - \sum_{s=\uparrow,\downarrow} \sigma^{\mathrm{coh},s}_{\mu\mu} \,. \tag{2.52}$$

The spin-flip contribution was found to be small compared to the total (coherent) conductivity for the Cu-Ni alloy in a wide range of magnetic moments [4]. On the other hand, the spin-flip contribution is essential, e.g., for the Ni-rich NiFe alloys [74]. Calculating the coherent part of the conductivity tensor projected onto the spin-up and spin-down directions for the spin indices $s =\uparrow$ and $s =\downarrow$, respectively, is a sufficient approximation for halfmetals. The projected conductivity is then

$$\begin{aligned} \sigma^{\mathrm{coh},s}_{\mu\nu} = \sigma_0 \int_{-\infty}^{\infty} \mathrm{d}E\, f'(E_F)\, \mathrm{Tr} \Big\{ & v_\mu \bar{g}^s_+(E_F) v_\nu \left[\bar{g}^s_+(E_F) - \bar{g}^s_-(E_F) \right] \\ & - v_\mu \left[\bar{g}^s_+(E_F) - \bar{g}^s_-(E_F) \right] v_\nu \bar{g}^s_-(E_F) \Big\} \,, \end{aligned} \tag{2.53}$$

where $\bar{g}^s_\pm(E)$, and v_μ are averaged spin-resolved Green function and velocity operator, respectively, expressed in the auxiliary form suitable for the numerical implementation within the relativistic TB-LMTO formalism after performing the configurational averaging. A real-energy variable is denoted E and $f'(E)$ is the energy derivative of the Fermi-Dirac distribution. To simplify the notation, $g_\pm(E) = g(E \pm i0)$ is used. In Eq. (2.53), $\sigma_0 = e^2/(4\pi V_0 N_0)$ depends on the charge of the electron e, on the volume of the primitive cell V_0, and on the number of cells N_0 in a large finite crystal with periodic boundary conditions. If there was no spin-orbit interaction (in the two-current model [122]) the sum $\sigma^{\mathrm{coh},\uparrow}_{\mu\mu} + \sigma^{\mathrm{coh},\downarrow}_{\mu\mu}$ would correspond to the total coherent conductivity.

To investigate an influence of the spin-flip term of the coherent conductivity and vertex corrections, the formula with the total conductivity $\sigma_{\mu\mu}^{\text{tot.}}$ in the denominator was also used

$$P_\mu = \frac{\sigma_{\mu\mu}^{\text{coh},\uparrow} - \sigma_{\mu\mu}^{\text{coh},\downarrow}}{\sigma_{\mu\mu}^{\text{tot.}}} \,. \tag{2.54}$$

The relations above do not explicitly dependent on temperature. We note that the effect of broadened Fermi-Dirac distributions (at finite temperatures) on the polarization P_μ can be obtained similarly to corrections of the total conductivity, see Sec. 2.3.3.

2.5 Properties and limitations of the AAM

Many effects may be responsible for disagreement of experimental literature or theoretical data of other authors with our results from the AAM. Apart from the standard TB-LMTO method with the ASA and CPA, the most important of them which may play a role for different systems are:

- Chemical impurities in measured systems are usually not precisely known.
- Changes in lattice constants due to temperature are neglected similarly to usually omitted changes caused by alloying.
- Correlations between atomic displacements for neighboring atoms are neglected within the CPA.
- Correlations between magnetic fluctuations for neighboring atoms are neglected within the CPA.
- The relaxation of the one-electron potentials due to the displacements are not taken into account for our implementation of the AAM.
- Directions of magnetic moments for both the uDLM approach and tilting model are fixed.
- The Debye theory holds only for small magnitudes of displacements, the Debye temperatures are often not exactly known, and the magnitudes of displacements should differ for atoms with different masses.
- Magnetic disorder is compared to experimental data of the total magnetization, but neither tilting of the moments nor uDLM approach is perfect.

Some of the described limitations are not directly caused by the AAM but by its implementation within TB-LMTO-CPA or by employing other techniques. Therefore, they could be removed by different approaches, e.g., molecular simulations instead of the Debye theory, but it goes beyond the scope of this thesis.

Despite of these limitations of the AAM, it is still a powerful framework. We tested the approach on many systems and it agrees well with experimental results or theoretical data of other authors, see Chapter 4. On the other hand, these limitations must be taken into account during each interpretation of the results.

2.6 Summary of the results

In this Chapter, the methods of our finite-temperature calculations were introduced. The main outcomes are the following:

- The technique for the treatment of the atomic displacements within the TB-LMTO method with the CPA was derived. Mathematically, it can be used for the transformation of any potential function, but an application of the approach remains for the later chapters.
- Two models of the magnetic disorder were described, i.e., the DLM (and uDLM) method and the approach of tilting of the local moments. They can be used to decrease the total magnetization of a magnetic system.
- The relations between finite temperature and both the atomic displacements and spin fluctuations were discussed.
- The spin-resolved electrical conductivities and the spin-polarization of the electrical current were introduced.

3. Details of numerics and applications

This section focuses on technical aspects of the AAM, i.e., on its implementation within the TB-LMTO approach with the CPA. First, a modification of the numerical codes which leads to an incorporation of the atomic displacements is described. Then, numerical properties of our methods are discussed together with examples of numerical expenses. For both the physical and mathematical descriptions, see Sec. 2.1.

3.1 Scheme of finite-temperature calculations

Methods and quantities related to finite temperatures and their implementation within our formalism (TB-LMTO method, CPA) are schematically shown in Fig. 3.1. Atomic displacements described in Sec. 2.1 were included in numerical codes evaluating electrical transport properties and properties of electronic structure (black text in Fig. 3.1 in green rectangles); however finite temperatures are related to more steps of our methods.

In the first step of the standard ($T = 0$) framework, the potential functions P are self-consistently calculated within LSDA, see Sec. 1.2.5 for the notation or Ref. [12] for details. They are then used to obtain the coherent potential functions $\mathcal{P}$ for the CPA. From converged $\mathcal{P}$, the Green's functions and, consequently, electrical transport or electronic properties are then calculated. This approach would be described in Fig. 3.1, if "Atomic displacements" were omitted.

The inclusion of atomic displacements is shown in Fig. 3.1 in the bottom part related to the "Atomic displacements" and the modified sections of calculations are labeled by black text. It differs from zero temperature in the transformation of the potential functions (2.41), i.e., P (previously converged for $T = 0$ within the LSDA) are modified and then used to obtain $\mathcal{P}$ employed in the CPA. This means that the effect of the displacements on the self-consistent electronic structure (TB-LMTO potential functions) is neglected similarly to other finite-temperature studies [27, 29, 31, 32]. Despite this approximation, the AAM within the TB-LMTO gives results that agree with experimental data, see later sections.

Fluctuations of magnetic moments, caused by finite temperatures or other effects, can be included in the the self-consistent calculations of P. Both the uDLM approach or tilting of the moments (Sec. 2.2) are included from the beginning similarly to, e.g., the geometry of a studied system.

We emphasize that Fig. 3.1 shows a simplified structure of our framework. For example, a geometry may be specified by varying a lattice constant and searching for energy minimum or there are not many atomistic simulations that could deal with both magnons and phonons on the same level. Similarly, "Atomic displacements" may be considered as results of the atomistic simulations or inputs for the following calculations.

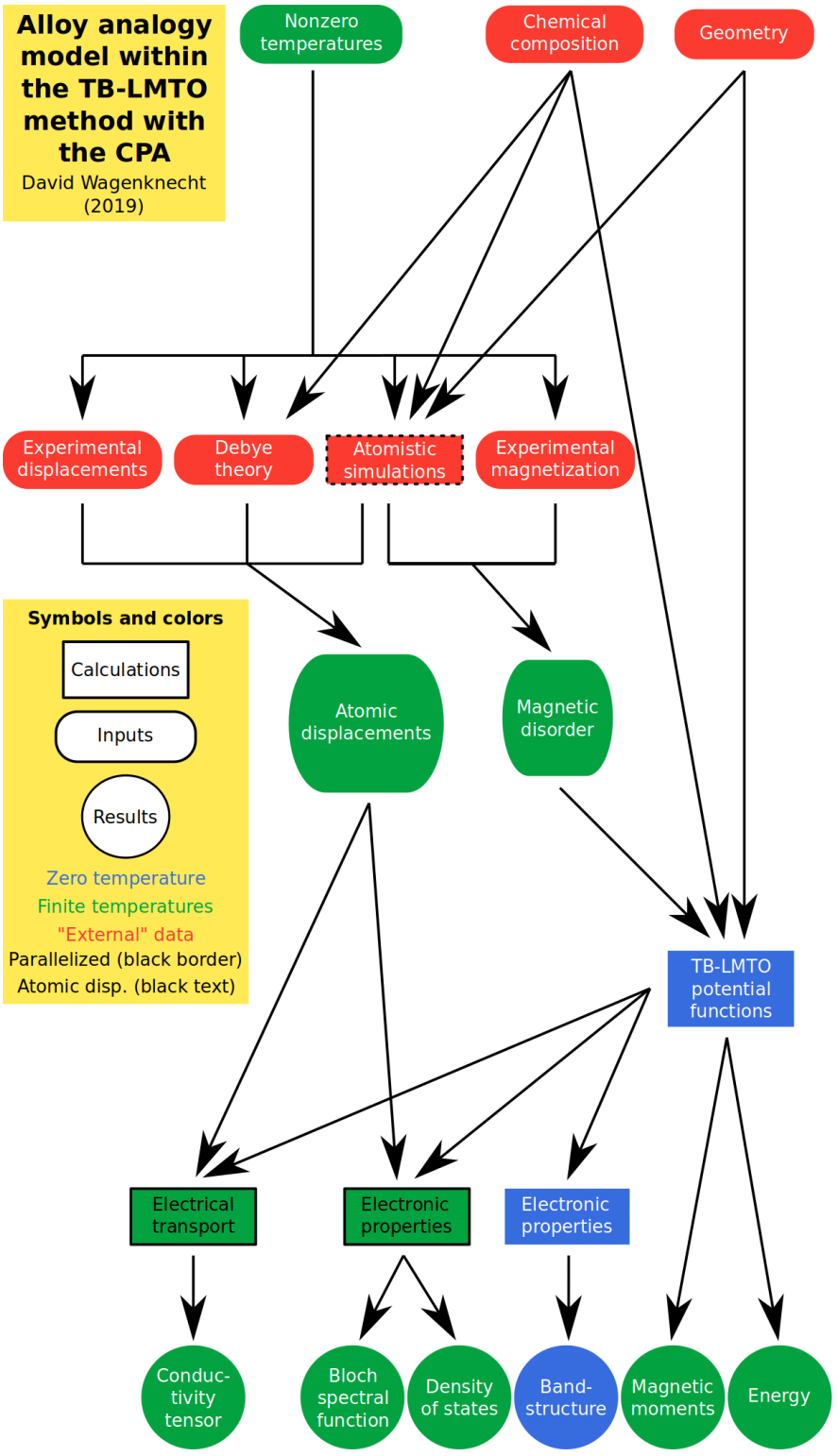

Figure 3.1: Illustration scheme of the AAM within the TB-LMTO approach with the CPA. Finite-temperature topics related to this thesis are marked by green and parts modified because of the atomic displacements are labeled by black text.

3.2 Numerical details

3.2.1 Formalism and employed frameworks

Basic physical approximations If not stated otherwise, the fully-relativistic TB-LMTO method with the atomic sphere approximation and the CPA [12] is used in this thesis, see Chapter 1. For the parametrization of the local density functional, the Vosko-Wilk-Nusair exchange-correlation potential [123] is employed.

Most of the calculations neglect Hubbard U. For a fully-relativistic LSDA+U scheme with nonzero U for d-orbitals of Mn, see Sec. 5.1 with Ref. [6] and Sec. 5.2 with Ref. [11].

Electrical transport properties are investigated by the linear response theory with the Kubo-Bastin formula [74] introduced in Sec. 1.3.2. CPA-vertex corrections [82] are included and for more complicated systems, especially NiMnSb (Sec. 5.1), the Fermi-sea contributions [81] to the total conductivity tensor are taken into account. We note that the only intersite hoppings are described by the velocity operators [80]. A small imaginary part of energy of 10^{-5} Ry is added for numerical purposes (the CPA-self-consistency and the evaluation of the Green's functions). The model of finite relaxation time is obtained by increasing this value; e.g., see Fig. 5.7.

The alloy analogy model (AAM) is used for treatment of finite temperatures with both the atomic displacements (phonons) [1, 2, 4] and magnetic fluctuations (magnons) [6], see Sec. 2.1 for details. For most cases, the magnitudes of the displacements are connected to the temperatures by the Debye theory [105, 106]. The fluctuations of moments are treated by the disordered local moment (DLM) approach [94–97] or with a model assuming tilting of the moments [6, 32]. The atomic displacements are given in units of the Bohr radius $a_{\mathrm{B}} = 0.529$ Å.

Input data required by the AAM Although the TB-LMTO framework with the CPA is an *ab initio* method, i.e., it calculates results "from the beginning", parameters such as chemical compositions or geometries are often taken over from literature. For finite temperatures, displacements (especially their magnitudes) and magnetization are also obtained by other means than from the full *ab initio* approaches. For most of the results, we employ the quantum averaging resulting in the Debye formula (2.47) with the zero-temperature fluctuations omitted (the 1/4 term). To acquire results completely "from the beginning", both sets of parameters could be taken from atomistic simulations; however, it represents a difficult task, that is beyond the scope of this thesis and is not directly connected to the implementation of the displacements or magnetic fluctuations within the TB-LMTO method. To focus on the implementation, we obtained most of the magnitudes of the displacements by the Debye theory, see Sec. 2.3, which was for simple systems compared to experimental data [111]. The Debye theory may not be correct for more complex systems. Similarly, temperature-dependent magnetization was obtained by fitting experiments, see Sec. 2.2 or later 5.1.

LMTO basis: *spd* vs. *spdf* Because of the summation over the quantum number L, linear transformation given by Eq. (2.41) the *spdf*-basis has to be

employed for nonzero temperatures even for transition-metal based systems [1–4, 6]; see also later Fig. 4.3. The necessity of the *spdf*−basis is the main reason which makes calculations with atomic displacements numerically more expensive than the zero-temperature studies. Examples of CPU-times for fully relativistic *spdf*−calculations without the Fermi-sea term are later given in Fig. 3.2; analogical calculations of NiMnSb with the *spd*−basis (usually performed for residual resistivities) are about ten times numerically cheaper (than the *spdf*−basis) and inclusion of the Fermi-sea term (*spdf*−basis) is about two times more expensive (than the *spdf*−basis only with the Fermi-surface term).

We studied the effect of including the f-orbitals in the basis. Very often TB-LMTO studies neglect an influence of the the f-orbital without proper justification; however, the proper inclusion of f-orbitals might influence the calculation results. For comparison of the influence of the TB-LMTO basis on the AHC see later Fig. 5.10. It should be noted that a larger basis within the TB-LMTO approach does not imply a better accuracy.

3.2.2 Numerical precision and expenses

Numerical precision To achieve a reliability of the numerical approaches, all of the TB-LMTO potential functions were obtained by a self-consistent calculation that converged at least to thirteen digits (of the total energy value).

The number of necessary $k-$points for calculations of electrical transport significantly depends on investigated systems. The imaginary part of the selfenergy is larger, when impurities, phonons, magnons or multiple sublattices are present. Then, for a larger imaginary part of the energy, a sampling of the Brillouin zone may be of lower density (lesser number of $k-$points) compared to ordered materials. Typical number of necessary $k-$points is approx. 300^3 for cubic systems. All of the presented calculations were checked for different number of the $k-$points and the final results are influenced by the finite number of the $k-$points lesser than 1 %.

A numerically expensive part of the DOS calculations comes from the evaluating of a large number (hundreds) energy points. Only a few thousands $k-$points are needed for the DOS. In contrast, Bloch spectral functions are usually evaluated for a few energies and a fine $k-$space mesh. Last but not least, calculating bandstructures requires negligible time compared to other numerical codes.

Numerical parallelization and computational limitations Although the *spdf*-basis is employed for the AAM, the TB-LMTO approach with the CPA still represents a numerically efficient framework. To use the AAM for multi-sublattice systems, we have parallelized the numerically most expensive sections of our codes. In Fig. 3.1, parallelized parts of the approaches are marked by black border. Because of these two aspects, our investigations of half-Heusler NiMnSb (four sublattices) [6] and antiferromagnetic CuMnAs (six or eight sublattices) represent studies of electrical transport in the most complex solids described at nonzero temperatures so far.

Most of our *ab initio* calculations were performed on a single node with multiple threads. Technically speaking, it was done only with OpenMP (Open Multi-Processing) library without MPI (Message Passing Interface). This framework

results in the best efficiency of our multi-thread programs and it is easier to implement than MPI. Although MPI can be used as well, similarly to hybrid MPI-OpenMP, running several instances of the codes (each of them on different node) is more suitable and efficient for our purposes.

The numerically most expensive part is usually the integration over the Brillouin zone that can be divided into any number of threads; other parts of the codes are parallelized as well. The high performance computing (HPC) is successfully used with our approaches, i.e., we have experience with Metacentrum and IT4Innovations resources. With the HPC, an almost ideal performance indicator *resources_used.cpupercent* is achieved. It says how much of CPU-time is used for parallelized calculations, i.e., how much faster is the code if it is run with n_{th} threads. The maximal value corresponds to the number of the threads. With the AAM, the factor is larger than $0.9n_{\mathrm{th}}$ for tasks with a prevalent numerical integration over the Brillouin zone (electrical transport properties) and even larger than $0.99n_{\mathrm{th}}$ for calculating density of states.

Examples of computational expenses To compare numerical expenses for different systems, we performed finite-temperature electrical transport calculations with the same numerical codes with the OpenMP parallelization (24 threads) on the HPC Salomon cluster of IT4Innovations national supercomputing center (Czech Republic, Ostrava). The Fermi-sea term was omitted in the statistics and following values do not include time necessary for the self-consistent calculation of the TB-LMTO potential functions that does not depend on the inclusion of the displacements.

CPU-times for different number of $k-$points in the Brillouin zone (BZ) n_{BZ} for bcc Fe with the *spdf*$-$basis summarized in Tab. 3.1 show only negligible dependence on magnitudes of the displacements $\sqrt{\langle u^2 \rangle}$ or magnetic disorder (tilting angle θ). The fitted linear dependence on n_{BZ} is depicted in Fig. 3.2. Zero-temperature calculations with the *spdf*$-$basis are approximately four to five times more expensive than with the *spd*$-$basis.

Table 3.1: CPU-time in hours for bcc Fe calculated with 24 threads in the *spdf*$-$basis linearly depends on the number of $k-$points in the Brillouin zone n_{BZ}, but it is independent on parameters of finite temperatures.

		Number of points in the BZ, n_{BZ}			
$\sqrt{\langle u^2 \rangle}[a_{\mathrm{B}}]$	θ	$4 \cdot 10^6$	$32 \cdot 10^6$	$108 \cdot 10^6$	$256 \cdot 10^6$
0.0	0.0 π	19.0	54.1	150	338
0.0	0.1 π	18.6	53.8	150	335
0.2	0.0 π	17.2	52.7	148	334
0.2	0.1 π	17.9	52.9	149	336

Numerical expenses increase especially for multi-sublattice systems. Converged results for NiMnSb are obtained for $\gtrsim 1.6 \cdot 10^6$ $k-$points ($\approx$ 340 CPU-hours). It is possible to perform even more precise integration over the Brillouin zone; however, the expenses increase significantly, see Fig. 3.2. For comparison, AFM CuMnAs (six sublattices) with $n_{BZ} = 8 \cdot 10^6$ requires (640 ± 75) CPU-hours, whereas only (386 ± 154) CPU-hours is needed with the *spd*$-$basis (zero temperature); the statistics was performed on 21 different possible impurities. One can

see also Fig. 3.2, where errorbars are given by the standard deviations that were obtained from calculations with displacements and relevant chemical impurities (see Chap. 5). The errorbars may be also influenced by running the codes on different machines (different hardware configurations). For these more complex systems, CPU-time may slightly depend on the magnitudes of the displacements ($\approx 10\,\%$ of the CPU-time); however, there is no obvious function describing this dependence and some larger magnitudes may be even numerically cheaper than smaller ones.

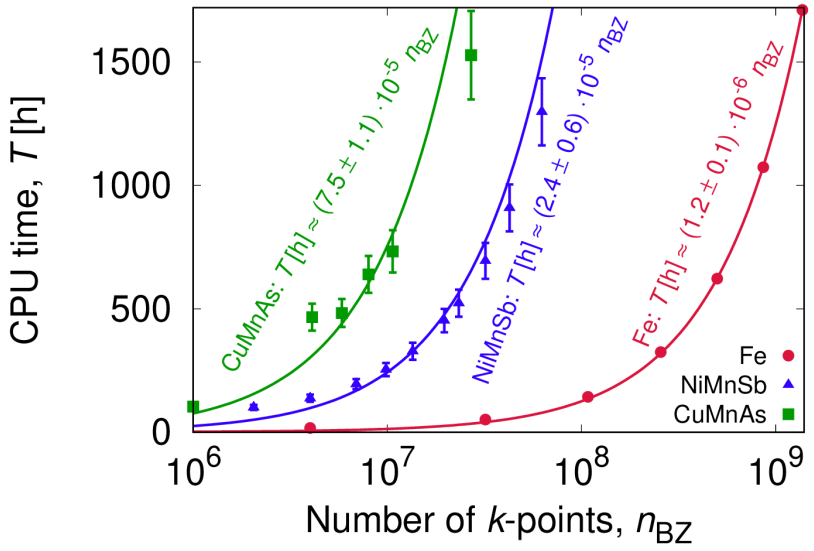

Figure 3.2: CPU-time dependence on n_{BZ} was fitted by the linear function and plotted in the logarithmic scale for bcc Fe (red circles), half-Heusler NiMnSb (blue triangles) and tetragonal CuMnAs (green squares). Errorbars for Fe are negligible. All calculations were performed for the *spdf*−basis and $U = 0$.

Requirements of RAM are usually relatively modest. The above mentioned calculations of Fe and CuMnAs used 960 MB and 21 GB RAM, respectively; a consumption of virtual memory is about two times larger. Standard deviations of these values are less than 1 %.

3.3 Summary of the results

In this Chapter we described the technical details of the novel *ab initio* approaches, as well as we discussed numerical aspects of the employed methods. The most important results are:

- The AAM can be implemented within the previously used and tested TB-LMTO method with the CPA. Technically, the implementation is based on the modification of the potential functions P, while most of the other algorithms remain unchanged.

- Because of the transformation of the potential function, the $spdf-$basis must be used instead of the standard $spd-$basis. From the numerical point of view, this is the most important drawback because it increases dimensions of the employed matrices and, consequently, the CPU-time.

- The numerical efficiency of the AAM within the CPA is almost independent on the number of displaced atoms or tilted magnetic moments.

- With standard numerical resources, we have enumerated even temperature-dependent electrical transport properties in AFM CuMnAs with six sublattices (eight if the empty spheres are used to fill empty space between atoms). We consider even more complex systems to be treatable by the AAM.

- The structure of our numerical codes allows the perfect CPU-parallelization. The numerical most expensive parts consist of the integration over the Brillouin zone or similar loops; therefore, their steps can be evaluated independently.

4. Electrical transport at finite temperatures

4.1 Pure transition metals

Transition metals without chemical disorder represent ideal candidates for testing of novel *ab initio* frameworks, i.e., implementation of the AAM within the TB-LMTO method with the CPA. Both the experimental values and theoretical data of other authors are available in literature, which can be used to compare with our novel results. Moreover, there are several nonmagnetic metals as well as metals with nonzero local magnetic moments. According to atomic masses, relativistic effects may be taken into account or neglected, but the masses are identical in a whole system (without chemical disorder), which simplifies a selection of the atomic displacements. Because of the many different properties but a relatively easy description, we choose the pure transition metals to the first systems for finite-temperature studies. The Fermi-sea term was omitted during the studies presented in this Section.

4.1.1 Cubic systems

Introduction Among the pure transition metals, cubic systems are the most simple ones, at least when transition metals are compared by number of atoms and complexity of atomic displacements described by the AAM. We focus on BCC and FCC structures. The structure is chosen for each metal according to its common occurrence in nature; however, some of them are allotropes: For example, Fe at ambient pressure has the BCC lattice ($\alpha-$iron) up to $T \approx 1200$ K, FCC above this temperature ($\gamma-$iron), and again BCC structure close to the melting point ($\delta-$iron, approx. 1700–1800 K). At finite temperatures, each of the distinguishable atoms in the cubic structures were displaced along [111] direction of the crystalline structure, see Sec. 2.3 for details.

Figures in this section for materials with neglected magnetic disorder show the electrical resistivity as a function of the root-mean-square displacement $\sqrt{\langle u^2 \rangle}$. The corresponding temperature was calculated for each displacement using Eq. (2.47), see secondary horizontal axes on the graphs. It may influence a comparison with experimental data, which are usually presented as a $\rho(T)$ dependence; the same conversion was used for data in Ref. [29]. The error given by the Debye model is estimated to 5 %.

Most of the results presented here were published in [1] and [4]. Even for scalar-relativistic approximation we obtain an agreement with literature. This approach does not allow an investigation of more complex phenomena such as galvanomagnetic properties (anisotropic magnetoresistance, anomalous Hall effect). On the other hand, present results show good agreement with experimental data. Therefore, the scalar-relativistic method is good approximation that shows an applicability of the alloy analogy model implemented within the TB-LMTO formalism.

Electrical resistivities Temperature dependent resistivity for some of the transition metals is presented in Fig. 4.1–4.3. Our calculations, which took into account only lattice vibrations, are for these metals in good agreement with both different calculations and experimental results. Underestimation of measured values is often related to unknown disorder in real samples. It is clearly visible in

Fig. 4.1, where the nonzero experimental residual resistivity corresponds to a difference between measured data and calculated results in the whole temperature range. Moreover, different samples have different resistivities, see experimental values in Fig. 4.1 or 4.2.

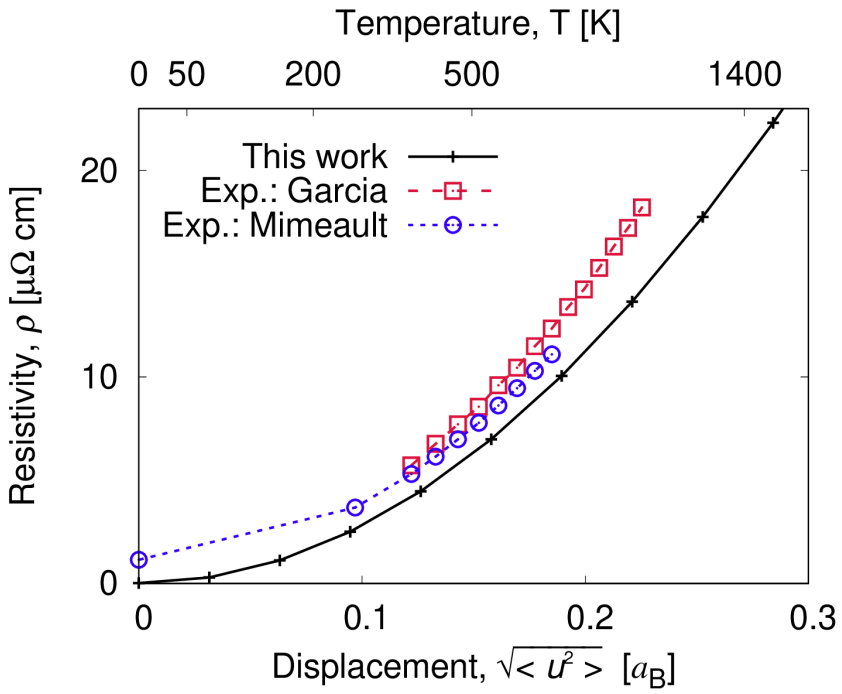

Figure 4.1: Our scalar-relativistic results for Rh (solid line) are compared with experimental data [124, 125]; the difference is almost identical for each displacements and it corresponds to the residual resistivity.

We also investigated stoichiometric Pd (Fig. 4.2), but the correction given by the full Dirac approach is obtained much smaller than the change of resistivity due to phonons. A discrepancy between measured values is larger than a difference from the calculated data; therefore we consider our results to agree well with measurements.

Now we focus examination of fully-relativistic effects on nonmagnetic pure metals with a strong spin-orbit interaction, i.e., platinum and palladium. Fig. 4.3 – left shows the dependence of electrical resistivity on displacements of atoms for platinum. The obtained theoretical results are in good agreement with both experimental data and calculations of other authors. Errorbars show an uncertainty (approx. five to ten percents of the resistivity) of the displacement–temperature conversion caused by a discrepancy of the Debye temperature presented in literature. Experimental data were taken from Ref. [126]. The difference between the scalar-relativistic calculations and fully-relativistic ones is expected for a heavy element such platinum. It was found to be much smaller or negligible for Fe, Co, Ni or Cu. We obtain the agreement with experiments also for palladium, which is not shown here.

The results shown in Fig. 4.1–4.3 are satisfactory, whereas calculations for copper (see Fig. 2.6 and Sec. 2.3) do not agree with experimental data unless

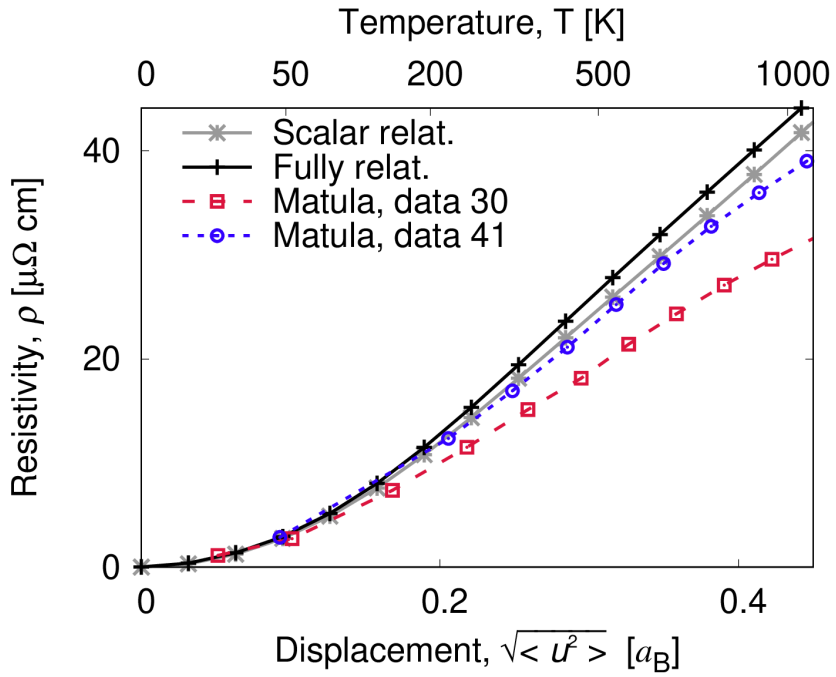

Figure 4.2: Scalar and fully-relativistic calculations of Pd are in good agreement with experimental data [115] and the relative difference between the scalar-relativistic and the fully-relativistic calculation is the same (5 %) in the whole calculated temperature range.

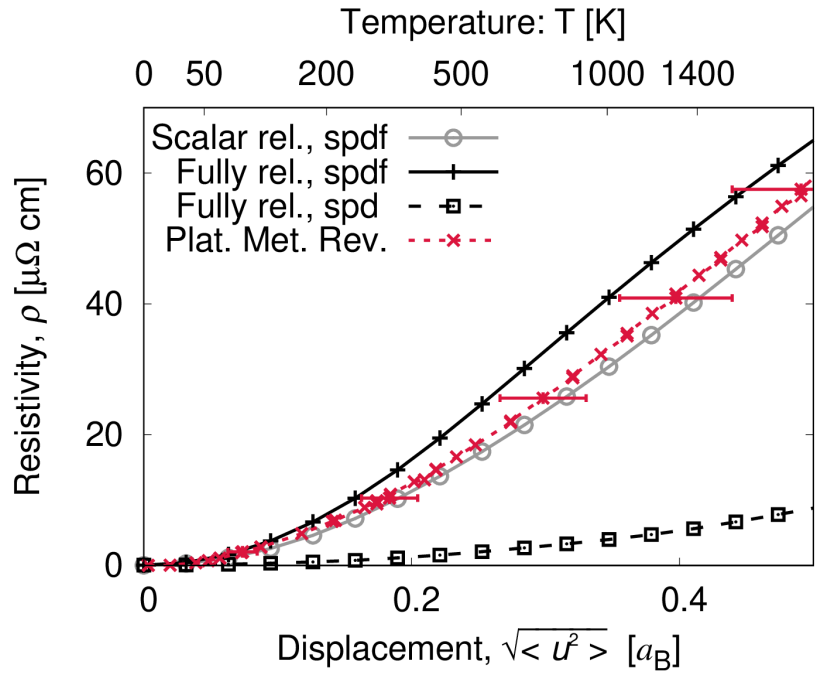

Figure 4.3: Electrical resistivity calculated with the scalar-relativistic and the fully-relativistic approach for platinum. Results are compared with experimental data [126] and the errorbars are given by the displacement–temperature conversion.

VASP software with the phonopy package is employed (see previously shown Fig. 2.6).

Anomalous Hall effect The fully-relativistic results for the electrical resistivity are almost the same as the scalar-relativistic ones. It is not surprising for Ni because of its small spin-orbit coupling which, however, the fully-relativistic calculations are indispensable for all galvanomagnetic phenomena, such as the anomalous Hall effect (AHE).

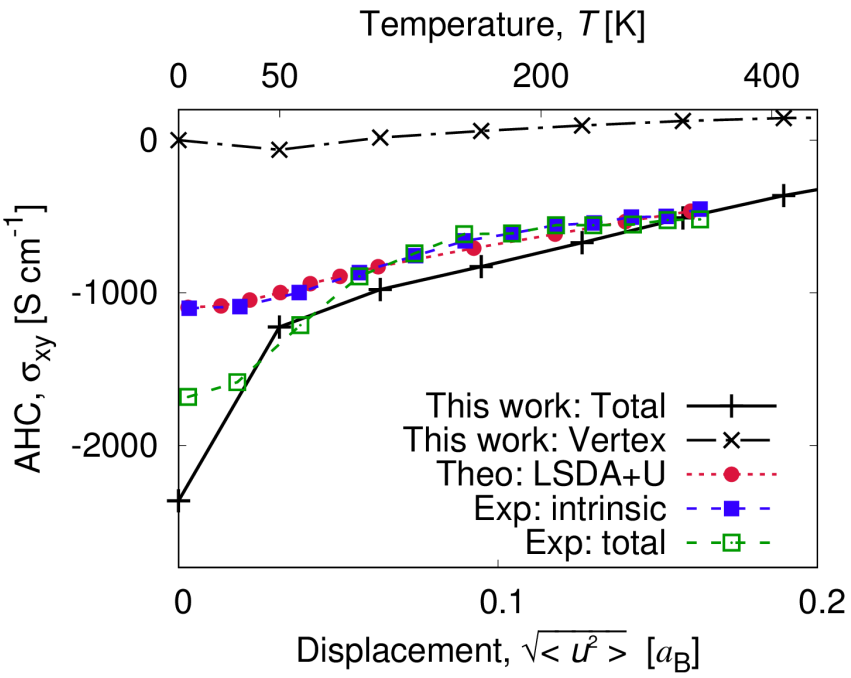

Figure 4.4: Anomalous Hall conductivity of Ni, experimental and other theoretical data are taken from [31] and [127].

Our temperature-dependent calculations for stoichiometric Ni incorporating only phonons which describe both the paramagnetic and ferromagnetic state agree with data of other authors; see later Fig. 4.9 presenting also an inclusion of the magnetic fluctuations. Without the magnetic disorder, the FM state is well described up to the room temperature. The AHE for pure Ni within this temperature range is presented in Fig. 4.4. Our data exhibit good agreement to both theoretical and experimental results, especially for the coherent part of the anomalous Hall conductivity corresponding to the so-called intrinsic contribution. The difference between the KKR values and the presented LMTO data is significant especially at zero temperature and it mainly comes from the LSDA+U approach in the KKR technique [31] in contrast to the pure LSDA in our scheme. The incoherent (vertex) part, equivalent to the extrinsic contribution to the AHE, is very small even at the room temperature. The total AHE is several orders of magnitude smaller than diagonal elements of the conductivity tensor; therefore, it is much more sensitive to numerical methods and other approximations. The obtained calculated data prove the reliability of our approach.

Calculated AHC for Fe is later shown in Tab. 4.6 with included influence of the Fermi-Dirac distribution at high temperatures.

4.1.2 Hexagonal systems

Hexagonal Co, Ru, and Os show anisotropy between electrical transport properties in the in-plane direction (σ_{xx}) and the perpendicular one (σ_{zz}); therefore, it can be used to verify validity of the AAM for non-cubic systems. Moreover, the anisotropy is one of the basic physical properties and as such it deserves a detailed study. It has also a potential application in novel spintronic memories which are often based on multi-sublattice materials or layered structures [59, 128]. Because of our *ab initio* framework, different phenomena like a role of the spin-orbit interaction may be studied. The AAM and finite temperatures were used as a scattering mechanism, which leads to finite conductivities for metals without chemical disorder [10]. For the anisotropy induced by the hexagonal structure of random alloys see later Sec. 4.3.3.

The fully-relativistic calculations of electrical transport properties with eight directions of atomic displacements respecting the symmetry of materials were employed. Experimental Debye temperatures for Co (445 K [129]), Ru (550 K [130]), and Os (467 K [130]) were used. We also assumed experimental lattice constants: $a = 2.503$ Å and $c = 4.058$ Å for Co [131], $a = 2.270$ Å and $c = 4.274$ Å for Ru [132], and $a = 2.432$ Å and $c = 4.315$ Å for Os [133].

Good agreement with literature (Ref. [134] for Co and [130] for Ru and Os) was obtained for resistivities with atomic displacements (without spin fluctuations and impurities), see Fig. 4.5. Omitting chemical impurities and magnetic disorder is probably the reason why theoretical data underestimate experimental values. Results for hexagonal Co with magnetic disorder are shown in Sec. 4.2.3. The deviations may be also caused by neglecting correlation between atomic displacements of the different atoms.

A strong dependence of the anisotropy on the magnetic state was observed for Co, compare the FM state in Fig. 4.5 (a) with the nonmagnetic (NM) one in Fig. 4.5 (b). For the first one, $\rho_{xx} < \rho_{zz}$ which agrees with experimental data, whereas the second one gives $\rho_{xx} > \rho_{zz}$. For Ru and Os (both are also NM), also $\rho_{xx} > \rho_{zz}$ holds. The difference in the anisotropy can be related to the spontaneous FM order of Co and the role of a different number of valence electrons is of minor importance. The anisotropy of FM Co is opposite with respect to Ru and Os and the effect was explained on the basis of the strong itinerant ferromagnetism of Co [10].

To estimate the effect of the spin-orbit interaction on transport properties, we employed also the scalar-relativistic approach. The trends are similar to the fully-relativistic method and the differences in resistivities are up to ≈ 10 %, see Tab. 4.1 for finite temperature given by phonons ($\sqrt{\langle u^2 \rangle} = 0.2\, a_{\mathrm{B}}$). The anisotropies ($\rho_{xx}/\rho_{zz}$) are almost identical for both approaches. It can be concluded that the spin-orbit interaction has only a small influence on the studied anisotropy of longitudinal resistivity.

In the two-current model [43], the total conductivity is obtained as a sum of two conductivities for opposite spin channels (majority spin $\uparrow$ and minority spin $\downarrow$). Scalar-relativistic results (in terms of resistivities) for these two channels are

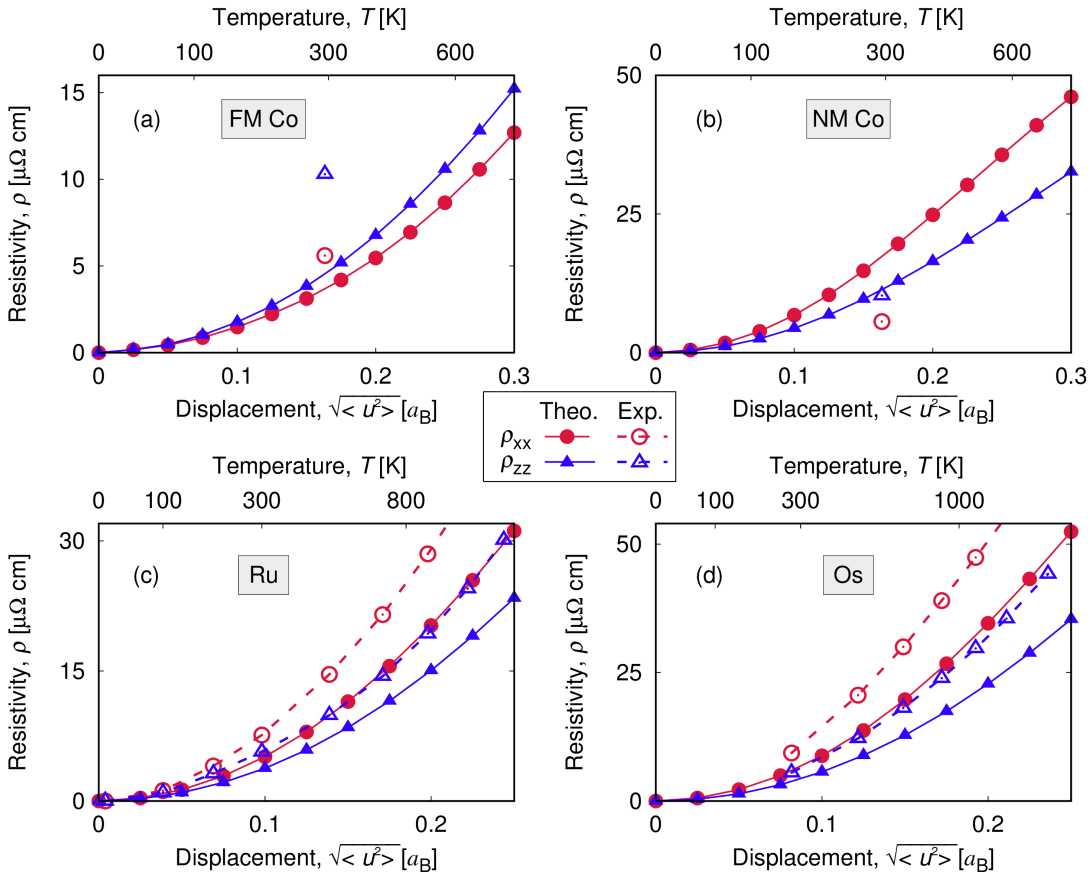

Figure 4.5: Fully-relativistic calculations (solid lines, full symbols) with only phonons included. Data for FM Co (a) show an opposite anisotropy than for NM Co (b); for both Ru (c) and Os (d) the anisotropy is the same ($\rho_{xx} > \rho_{zz}$). Experimental data (dashed lines, empty symbols) are obtained from Ref. [134] for Co and from Ref. [130] for Ru and Os. ρ_{xx} is shown by the red circles, ρ_{zz} by the blue triangles.

also presented in Tab. 4.1. The resistivity of the minority spin channel is more then ten times larger than the resistivity of the majority channel; therefore, the electrical current is given and characterized mainly by the spin-↑ carriers. The majority channel has almost the same anisotropy ρ_{xx}/ρ_{zz} as the FM case, while the minority one is similar to the NM system. It leads to the conclusion that the anisotropy in the real FM Co is caused by the strong spin dependence of the resistivity. It also agrees with the difference in the electronic structure in FM Co (not shown here): the Fermi level of the majority valence band is in the $sp-$like states (above the $d-$band) and the broad $sp-$band implies high velocities of electrons. On the other hand, the minority $d-$band is not completely filled and this narrow band determines smaller velocities than the $sp-$one.

Although experimental data of resistivities are underestimated, the anisotropy (σ_{xx}/σ_{zz}) is described correctly, see Table 4.2 for two selected temperatures of Ru and Os. For both materials and in the whole calculated temperature range ($\sqrt{\langle u^2 \rangle} < 0.4\, a_B$), $\sigma_{xx} > \sigma_{zz}$, which agrees with experimental data.

Table 4.1: Calculated resistivities for $\sqrt{\langle u^2 \rangle} = 0.2\,a_{\mathrm{B}}$ without magnetic disorder give $\rho_{xx}/\rho_{zz} < 1$ only for FM Co and its spin-up channel and the anisotropy is almost identical in both the scalar and fully-relativistic approaches. The majority and minority channel in the two-current model are denoted by $\uparrow$ and $\downarrow$, respectively.

	Scalar-relativistic			Fully-relativistic		
	ρ_{xx} $[\mu\Omega\,\mathrm{cm}]$	ρ_{zz} $[\mu\Omega\,\mathrm{cm}]$	ρ_{xx}/ρ_{zz}	ρ_{xx} $[\mu\Omega\,\mathrm{cm}]$	ρ_{zz} $[\mu\Omega\,\mathrm{cm}]$	ρ_{xx}/ρ_{zz}
Co FM	5.33	6.02	0.89	5.46	6.77	0.81
Co FM $\uparrow$	5.71	6.87	0.83	-	-	-
Co FM $\downarrow$	80.1	49.0	1.63	-	-	-
Co NM	24.2	15.9	1.52	24.8	16.5	1.50
Ru	19.8	14.8	1.34	20.2	15.1	1.34
Os	30.5	20.5	1.49	34.6	22.8	1.52

Table 4.2: Calculated electrical resistivities ($\rho^{\mathrm{calc.}}$, scalar-relativistic) of hexagonal Ru and Os underestimate measured data ($\rho^{\mathrm{exp.}}$) [130], but the anisotropy ρ_{xx}/ρ_{zz} is obtained correctly. Magnitudes of atomic displacements (calculated values) correspond to the temperatures (experimental data) in the same columns.

		Ruthenium		Osmium	
Calc.	$\sqrt{\langle u^2 \rangle}\,[a_{\mathrm{B}}]$	0.13	0.23	0.10	0.20
	$\rho_{xx}^{\mathrm{calc.}}[\mu\Omega\,\mathrm{cm}]$	7.97	25.5	8.80	34.6
	$\rho_{zz}^{\mathrm{calc.}}[\mu\Omega\,\mathrm{cm}]$	5.88	19.0	5.67	22.8
	$\rho_{xx}^{\mathrm{calc.}}/\rho_{zz}^{\mathrm{calc.}}$	1.35	1.34	1.56	1.52
Exp.	T [K]	450	1200	400	1200
	$\rho_{xx}^{\mathrm{exp.}}[\mu\Omega\,\mathrm{cm}]$	12.9	38.9	15.7	51.5
	$\rho_{zz}^{\mathrm{exp.}}[\mu\Omega\,\mathrm{cm}]$	8.82	27.3	9.27	32.6
	$\rho_{xx}^{\mathrm{exp.}}/\rho_{zz}^{\mathrm{exp.}}$	1.46	1.42	1.69	1.58

4.2 Transition metals with magnetic disorder

In this Section we describe finite-temperature behavior of transition metals with the magnetic disorder (Sec. 2.2) taken into account. First, only the fluctuations of the magnetic moments described by the DLM approach are presented. Then, the combined effect of the atomic displacements and spin fluctuations for Ni and Fe is shown to give good agreement with experimental data. Last but not least, the Matthiessen's rule for phonons and magnons is discussed for hexagonal Co.

4.2.1 Pure metals: Disordered local moments

Spin disorder, giving important contribution to electrical transport properties, especially for magnetic materials, can be described in the most simple approximation by the DLM state. The resistivity in the PM state of iron with nonzero local moments treated by the DLM approach is shown in Fig. 4.6. Measured values of the spin-disorder resistivity at zero temperature vary from 77 to 100 $\mu\Omega$ cm and the calculated ones are $(129 \pm 1)\,\mu\Omega$ cm [27]. Our extrapolations from high-temperature limit ($T > 1000\,\mathrm{K} \approx T_C$) to $T = 0$ give $(89 \pm 1)\,\mu\Omega$ cm; the uncertainty is given only by the fit.

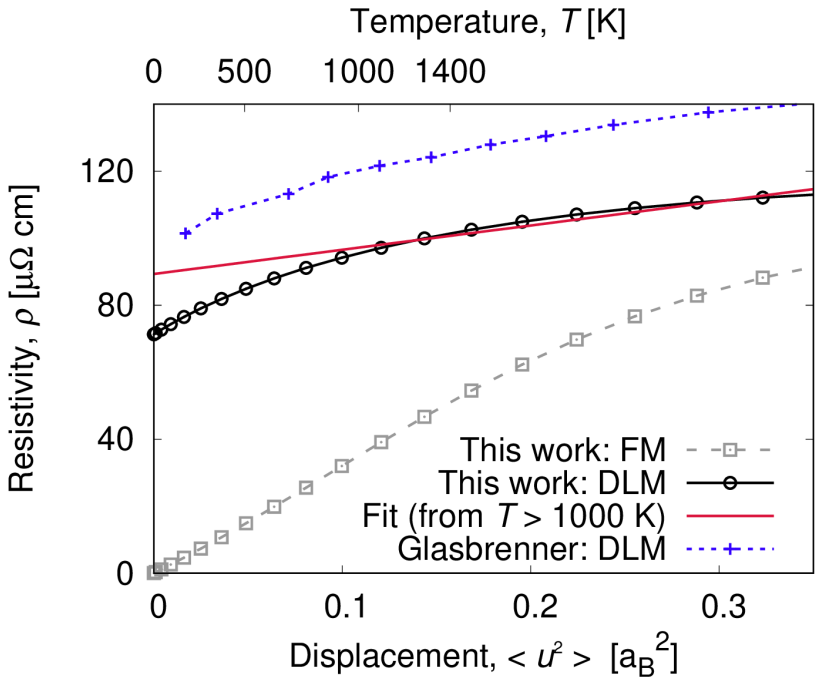

Figure 4.6: Calculated electrical resistivity of iron in the FM state (without magnetic disorder) and in the DLM approach. Obtained results are compared with [27] and the spin-disorder resistivity of $(89 \pm 1)\,\mu\Omega$ cm was obtained by extrapolation from $T > 1000$K.

The combined effect of spin disorder and displaced nuclei has recently been studied for iron and gadolinium [27] using the DLM state. A straightforward application of this procedure for nickel is not possible because the Ni magnetic moment in the DLM state collapses. In the present study, the DLM state was

obtained for a fixed magnetic moment of 0.42 μ_B according to [96, 97], and [98], which corresponds to the value at the Currie temperature (632 K).

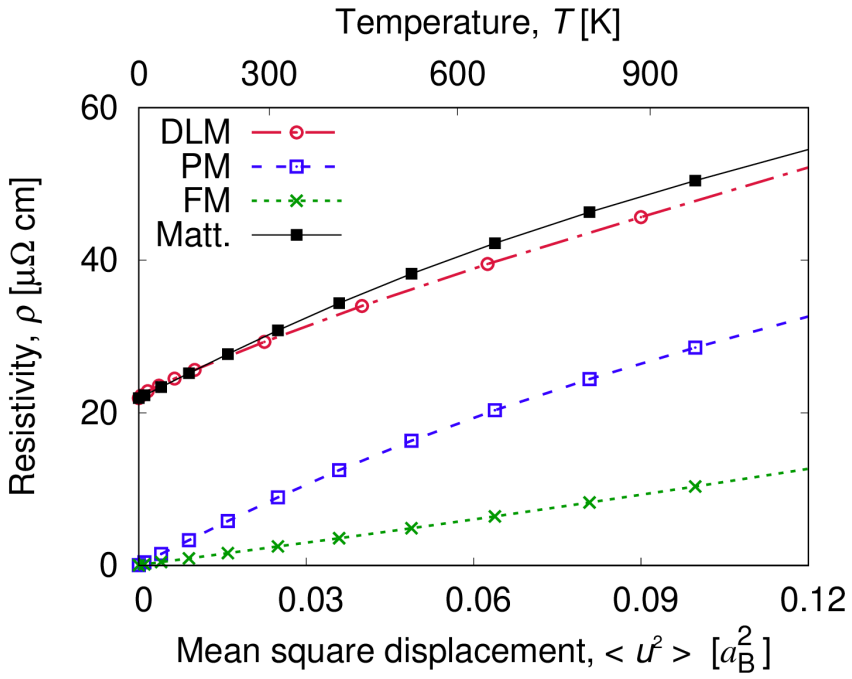

Figure 4.7: Scalar-relativistic calculations of nickel: Comparison of resistivity for ferromagnetic (FM), paramagnetic (PM), disordered local moment (DLM) state, and values resulting from the Matthiessen's rule (Matt.). The presented dependence on the mean square displacement indicates linear behavior of the resistivity at high temperatures.

The temperature-dependent electrical resistivity in the DLM state of Ni calculated by the scalar-relativistic approach is shown in Fig 4.7; for comparison the values in the PM (with zero Ni magnetic moment) and FM states (Fig. 4.9) are shown as well. The spin disorder resistivity (resistivity in the DLM state without atomic displacements) is $\rho_{SD} = 21.9\ \mu\Omega\,\mathrm{cm}$, which is in good agreement with previous results [96]. This value is close to the resistivity extrapolated to zero temperature by a linear function from the high-temperature limit, which amounts to $\rho_{extrap} = (25.8 \pm 0.2)\ \mu\Omega\,\mathrm{cm}$ (the error comes from the uncertainty of the fit). The relative difference of both values is smaller than the differences reported for iron and gadolinium [27]. This feature reflects the validity of the Matthiessen's rule within the present model with spin fluctuations corresponding to high temperatures (above the critical temperature) similarly to Ref. [27]. This rule assumes additivity of the resistivity contributions due to the spin disorder and the phonons, as documented in Fig. 4.7 by the Matthiessen's resistivity $\rho_{Matt.}(T) = \rho_{PM}(T) + \rho_{SD}$, which is very close to the values of $\rho_{DLM}(T)$.

4.2.2 Pure metals: Tilting of magnetic moments

The model of tilting magnetic moments (Sec. 2.2) was employed to describe electrical resistivity of Fe and Ni with both the atomic displacements and magnetic

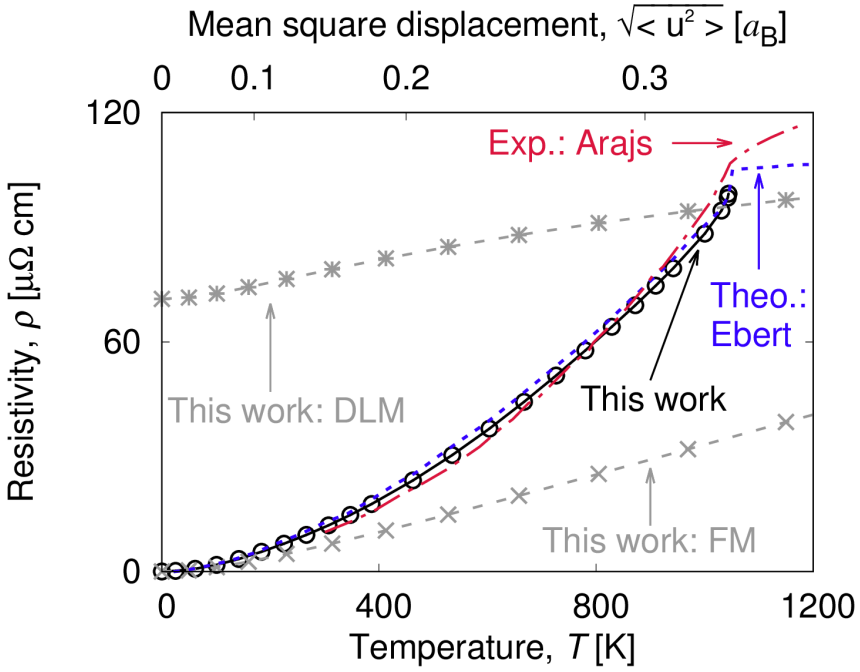

Figure 4.8: Our calculations with magnetic disorder (black solid line with circles) agree with both experimental (red dash-dotted line) [135] and theoretical (blue dotted line) [29] data. Low-temperature limit (the FM state, only phonons) and the high-temperature one (DLM state with phonons) are shown by gray dashed lines.

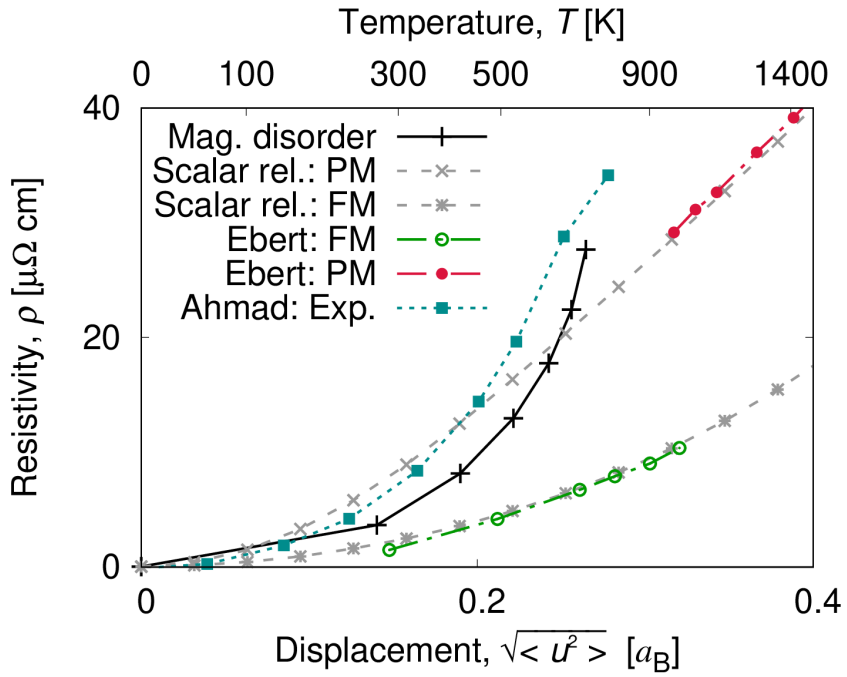

Figure 4.9: An agreement with the measured temperature dependence of the electrical resistivity for nickel [136] (blue full squares) is obtained for our calculations with combined effect of magnons and phonons (solid black line with crosses). Without the magnetic disorder, our FM (gray stars) and PM (gray crosses) data also agree with literature (green empty and red full circles) [29].

disorder. Each (physical) atom was taken into account (within the CPA) thirty two times: eight times because of the displacements and each of them with four different directions of the magnetic moments. We note that it had almost no influence on the numerical expenses (compared to undistorted Fe), see Sec. 3.2. If necessary, chemical impurities can be included in the framework as well. The moments were tilted from the z axis to the directions of the x, $-x$, y, and $-y$ axes by the angle θ. Increasing the tilting angle θ decreased the overall magnetization M of the system because the moments compensated each other. Different angles were than connected to the temperature using a simple analytical formula presented in [34]. The Debye theory was employed to obtain magnitudes of the atomic displacements for the given temperatures. Our fully-relativistic transport calculations then agreed perfectly with measured ([135] and [136]) or calculated [29] resistivities of iron and nickel, see Fig. 4.8 and 4.9, respectively.

4.2.3 Hexagonal Co: Tilting of magnetic moments

Here we describe study of hexagonal Co with magnetic disorder described by the model of tilted moments. For electrical transport of the hexagonal metals without the magnetic disorder see Sec. 4.1.2.

The magnetic disorder is described by the moments tilted to twelve angles equidistantly distributed over $[0, 2\pi]$ (around the direction of the original magnetization). The decreased magnetization was mapped to experimental data by a simple model described in Ref. [34].

Tab. 4.3 presents resistivities in hcp Co influenced by both the spin fluctuations and atomic displacements. Although the magnetic disorder results in the opposite anisotropy with respect to phonons, the overall ρ_{xx}/ρ_{zz} is dominated by the second effect. We note that the influence of these phenomena is comparable to chemical impurities, see later Sec. 4.3.3. The parameters chosen for data in Tab. 4.3 roughly correspond to the room temperature ($\sqrt{\langle u^2 \rangle} = 0.175\, a_{\mathrm{B}}$, $\theta = 0.045\pi$) and the Curie temperature of Co is about four times larger but despite that, the Matthiessen's rule is violated by ~ 30 %. We note that the comparable conditions (room-temperature parameters, same methods) for Fe give the violation of the Matthiessen's rule only by ~ 7 %.

Table 4.3: Calculated resistivities in Co within the fully-relativistic framework for $\sqrt{\langle u^2 \rangle} = 0.175\, a_{\mathrm{B}}$ and $\theta = 0.045\pi$ show the small influence of the spin fluctuations (ρ^{sf}) compared to phonons (ρ^{ph}) and the violation of the Matthiessen's rule (combined effect of phonon and magnons is denoted $\rho^{\mathrm{ph,sf}}$ while the bare sum is shown in the last row).

	$\rho_{xx}[\mu\Omega\,\mathrm{cm}]$	$\rho_{zz}[\mu\Omega\,\mathrm{cm}]$	ρ_{xx}/ρ_{zz}
ρ^{ph}	4.19	5.19	0.81
ρ^{sf}	0.95	0.72	1.31
$\rho^{\mathrm{ph,sf}}$	7.20	8.06	0.89
$\rho^{\mathrm{ph}} + \rho^{\mathrm{sf}}$	5.14	5.91	0.87

4.3 Alloys

Our implementation of the AAM successfully describes pure transition metals without chemical impurities; therefore, alloys of these metals represent the next logical step for testing of the framework. There are several new properties that we take into account: (i) Atoms have nonidentical masses, which complicates the selection of atomc displacements; (ii) different chemical compositions may be used to vary magnetic moments of a studied system; and (iii) the electrical resistivity is nonzero even at $T = 0$ (the residual resistivity). Similarly to the pure metals, we focus on electrical transport properties and, despite these new effects, our calculated results agree with literature for most of the systems.

4.3.1 Random Cu-Ni and Co-Ni alloys

Random Co-Ni and Cu-Ni alloys are perfect candidates to study the electrical conductivity and anomalous Hall conductivity at finite temperatures. Depending on composition, the magnetic moment changes significantly and almost linearly when plotted as a function of number of electrons, see Fig. 4.10. We note that Co has 27 electrons, 28 correspond to Ni, and Cu is characterized by 29 electrons. The virtual crystal approximation (VCA) describes random alloys as pure metals with non-integer nuclear charge, whereas the CPA takes into account real concentrations of the true alloy species.

The anomalous Hall effect is extremely dependent on the magnetization of the system; therefore, we plot a comparison of the AHC for the VCA and CPA in Fig. 4.11. Both approaches agree qualitatively and give identical results for the pure elements. For future study, we focus on the Cu-Ni and Co-Ni alloys with different compositions, i.e., different magnetic moments. In this section, only phonons are taken into account as the temperature-induced disorder. The magnetic fluctuations could be incorporated similarly to Ni (Sec. 4.2) or to complex NiMnSb (Sec. 5.1).

The electrical resistivities of ferromagnetic $Cu_{0.01}Ni_{0.99}$ and PM (with zero Ni magnetic moments) $Cu_{0.99}Ni_{0.01}$ random alloys are shown in Fig. 4.12. The relation between displacement and temperature is not presented here because the Debye temperatures differ a lot, as well as the conversions. For instance, the maximal displacement $\sqrt{\langle u^2 \rangle} = 0.2\ a_\mathrm{B}$ corresponds approximately to 350 K for $x = 0.99$ and to 120 K for $x = 0.01$. The experimental data [137] are measured as a temperature dependence. Therefore, the comparison of the theory and experiment may be influenced by the validity of the Debye theory and reliability of the Debye temperatures. The increasing difference for higher displacements between the experimental values and theoretical results for $Cu_{0.01}Ni_{0.99}$ is caused by the spin disorder omitted in the theory similarly to the case of pure nickel (see Fig. 4.9). Small differences between the calculated and measured electrical resistivity, visible even at zero temperature, are probably caused by imperfections of the experimental samples.

In the present treatment of binary alloys, the same magnitudes of the displacements for both elements have been assumed even though their chemical nature and atomic masses differ (the mass difference for Cu-Ni alloy is approximately 3 %). The same simplification has been used in previous CPA [29] and supercell

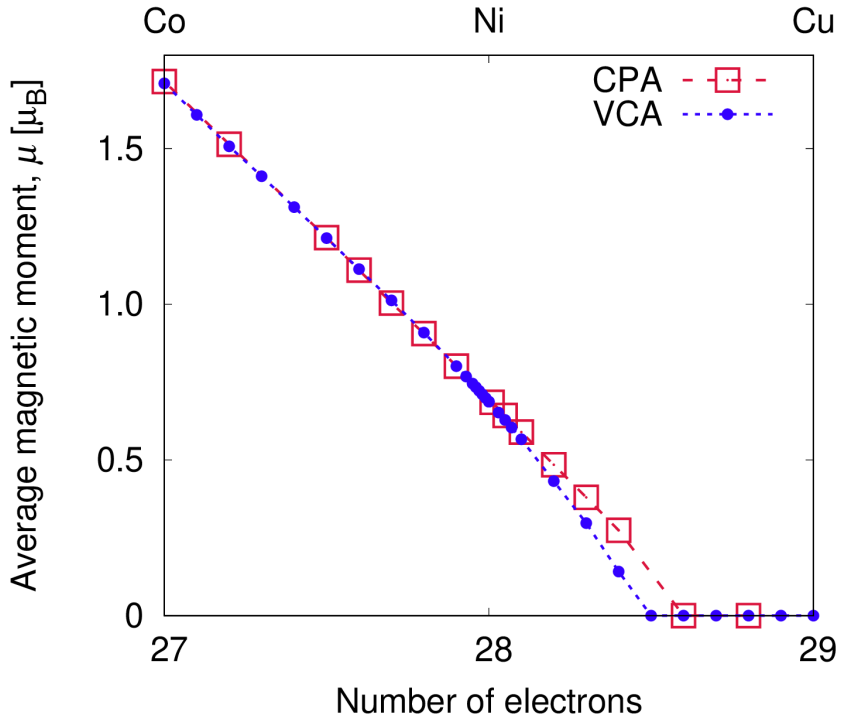

Figure 4.10: The average magnetic moment per atom of the Co-Ni and Cu-Ni random alloys decreases almost linearly with the number of electrons in both the virtual crystal (red squares) and coherent potential (blue circles) approximations.

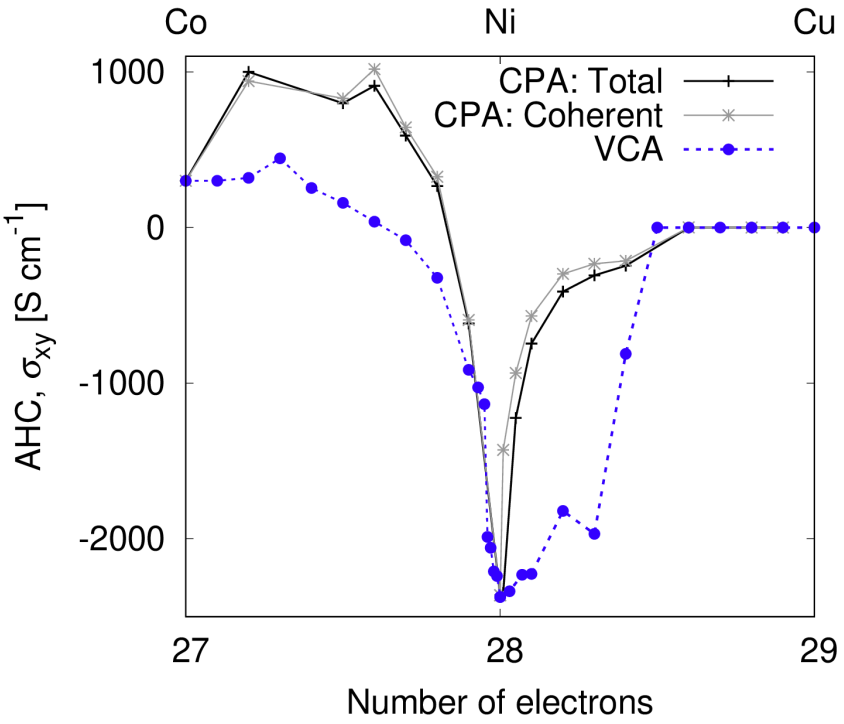

Figure 4.11: Although the scattering properties are not described properly by the virtual crystal approximation (blue circles) for non-integer number of electrons, the AHC qualitatively agrees with the more advanced CPA (black line: total AHC; gray stars: coherent part).

[92] studies. Simple improvements accounting for the mass difference have been suggested [138] but the obtained corrections are so small (changes of resistivities by a few percents) that we do not show these results here. The most general tool to remove this approximation seems to be the *ab initio* molecular dynamics, which could provide more realistic values of the displacements for both alloy species; however, this goes beyond the scope of this thesis.

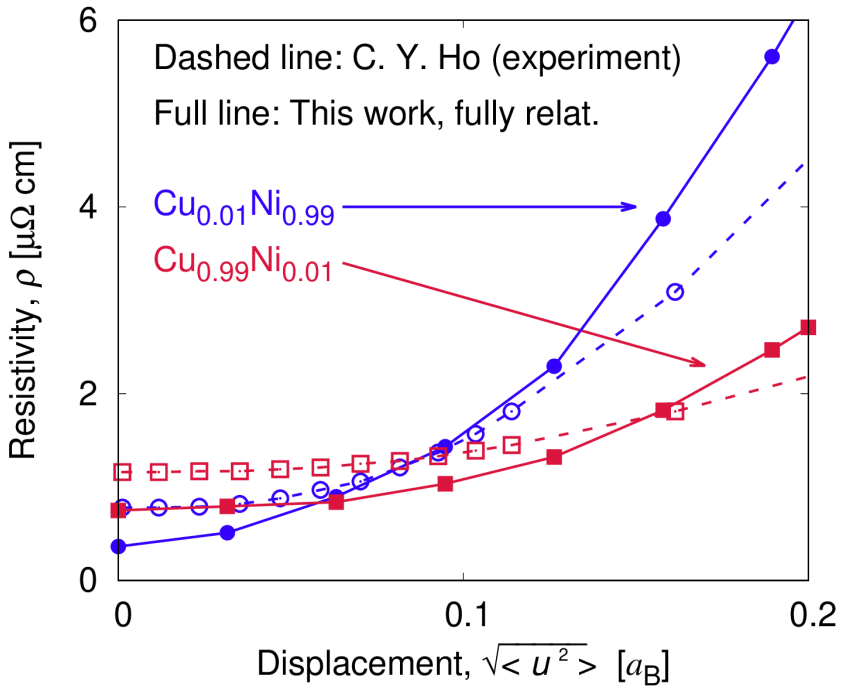

Figure 4.12: Fully-relativistic calculation (the solid line) of electrical resistivity for $Cu_{1-x}Ni_x$ compared with experimental values (dashed lines) [137]. The bottom curve showing theoretical data (red, squares) is for $x = 0.01$ and the top one (blue, circles) for $x = 0.99$.

The calculated results for concentrated Cu-Ni alloys are summarized in Fig. 4.13. The data reflect a transition between the FM Ni-rich alloys and the PM Cu-rich systems. It should be noted that this trend is solely due to the varying local moment of Ni atoms, whereas the Cu local moment is negligible for all concentrations.

The change of the longitudinal conductivity with the temperature (from $T = 0$ to the room conditions) is usually larger than an effect coming from chemical disorder in a dilute limit or from vertex corrections of the conductivity. This is demonstrated in Fig. 4.14 – left for Ni-rich Cu-Ni alloys. The electrical conductivity has a decreasing trend when the atoms are displaced, similarly to the decrease coming from increasing chemical disorder; both effects increase electron scattering. Similarly to the case of pure platinum, the incoherent part of the conductivity is significantly smaller than the total conductivity.

The scalar-relativistic approach gives reasonable agreement with the full Dirac method for the longitudinal conductivities; however, the fully-relativistic treatment is necessary to describe galvanomagnetic phenomena, such as the anomalous Hall effect (AHE). The AHE is described by the nondiagonal elements of the con-

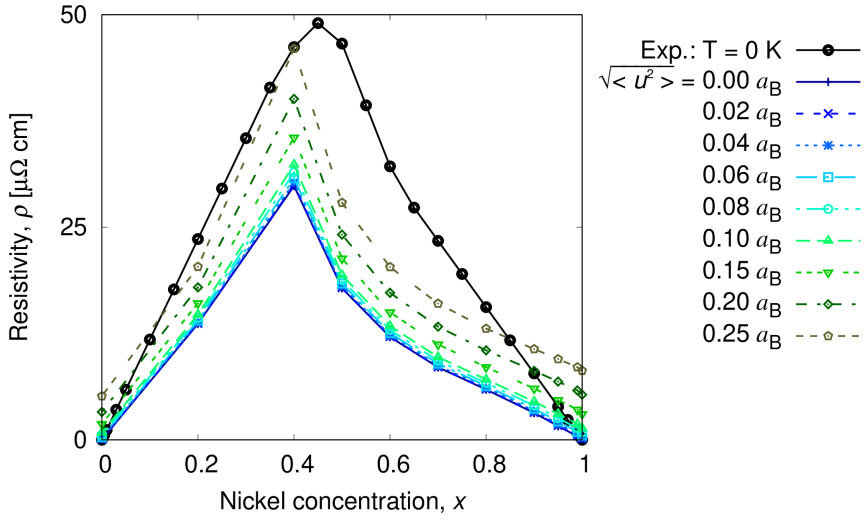

Figure 4.13: Electrical resistivity compared with experimental data [137] for zero temperature for $Cu_{1-x}Ni_x$ alloy as a function of nickel concentration.

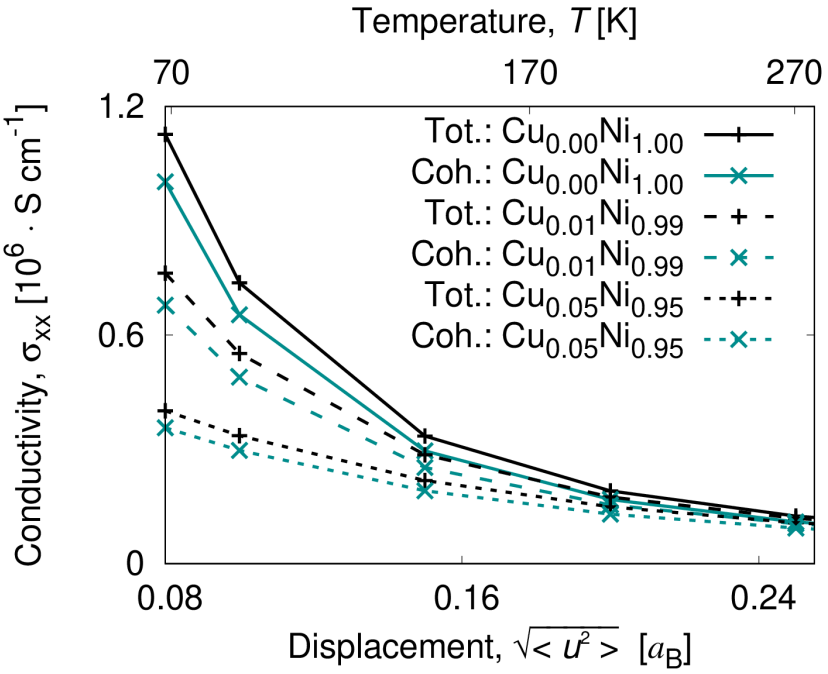

Figure 4.14: Temperature dependence of total and coherent electrical conductivity for Cu-Ni alloy, phonons only. Conversion between the displacements and temperature (secondary horizontal axis) was obtained for pure Ni.

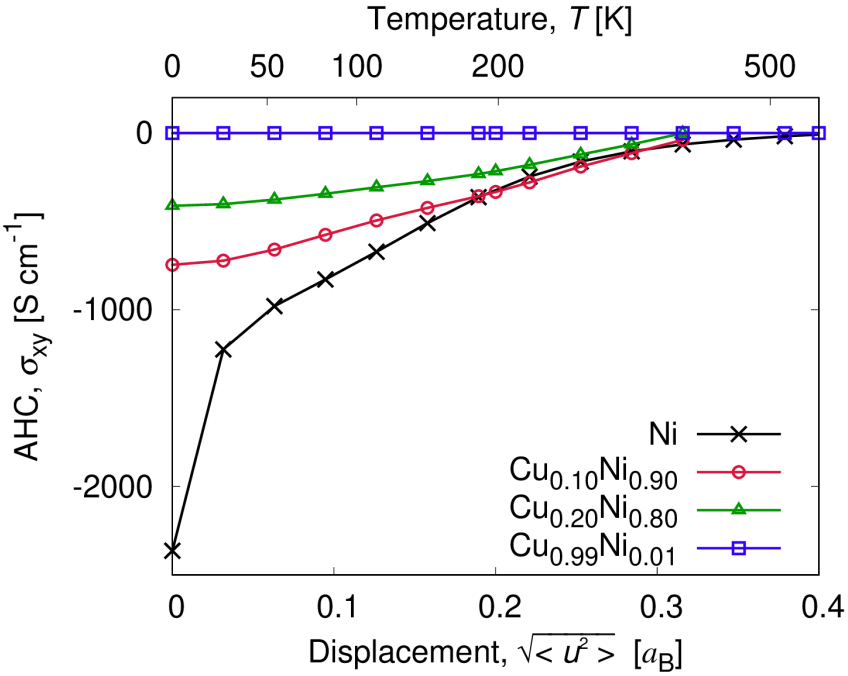

Figure 4.15: Anomalous Hall conductivity for Cu-Ni alloy, phonons only. Conversion between the displacements and temperature (secondary horizontal axis) was obtained for pure Ni.

ductivity tensor, which are several orders of magnitude smaller than the diagonal ones. Agreement of calculated results with data from literature proves reliability of our method. Such agreement for pure nickel was documented in Ref. [2] (see also Sec. 4.1.1) and here we present the calculated AHE results for the Cu-Ni alloy, see Fig. 4.15 – right. For all alloys studied, the anomalous Hall conductivity (AHC) decreases monotonically with the increasing magnitude of atomic displacements.

With increasing copper content, the AHC decreases as well due to decreasing average magnetic moment per atom (from 0.68 μ_B for pure Ni to 0.64 μ_B for $Cu_{0.05}Ni_{0.95}$, which is in good agreement with experiment [139, 140]). An exception was obtained for very low concentrations of copper ($\lesssim 1\%$), where the coherent part is responsible for higher AHC (compared to pure nickel) for displacements $\sqrt{\langle u^2 \rangle} \gtrsim 0.02\, a_\mathrm{B}$ and the vertex part for lower displacements. Data for higher concentration of copper were also obtained (not shown here); the AHE is almost negligible for more than 20 % of copper, but it cannot be included in one figure because of the displacement–temperature conversion that dramatically differs for different compositions.

Our results for the AHC of Co-Ni random alloy with atomic displacements are presented in Fig. 4.16. The magnetic moment of the random Co-Ni alloy increases with increasing Co concentration (see Fig. 4.10) and the also the AHE depends on Co content. This trend is independent on the magnitudes of atomic displacements. The magnetic disorder is not assumed for these calculations because the Curie temperature of Ni is higher than 600 K and it increases with

increasing Co content.

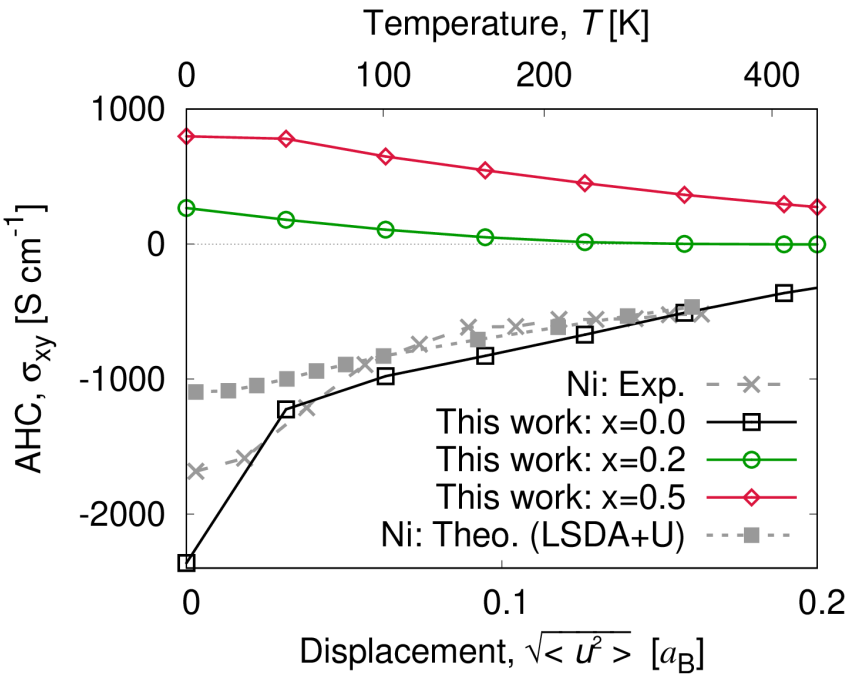

Figure 4.16: Calculated anomalous Hall effect (solid lines) of Co_xNi_{1-x} is compared with theoretical calculations using LSDA+U [31] (dotted line) and experimental data [127] (dashed line) for pure Ni. The dependence on Co concentration, x, is not monotonic with increasing amount of Co; on the other hand, increasing temperature monotonically decreases the AHC. Conversion between the displacements and temperature (secondary horizontal axis) was obtained for pure Ni.

4.3.2 Random Ni-Fe alloys

In Ref. [5] we focused on random fcc Ni-Fe alloys and their resistivities influenced by the spin disorder. The spin-disorder resistivity (SDR) above the Curie temperature was approached from the point of view of residual resistivities described by the DLM approach. Moreover, the fixed-spin moment (FSM) method was extended for two independent magnetic moments and the paramagnetic state was determined by minimizing the corresponding free energy [5]. The SDR was obtained from experiments by extrapolating the high-temperature resistivities (see schematic Fig. 1.1). Ni-Fe has many appropriate experimental data available, but a comprehensive *ab initio* study was missing. Last but not least, longitudinal spin fluctuations on Ni make the alloy even more theoretically interesting.

The alloy was described within the CPA as a four-component system with two directions of magnetic moments (pointing upwards ↑ and downwards ↓) and the concentration of components x: $Ni^{\uparrow}_{(1-x)/2}$, $Ni^{\downarrow}_{(1-x)/2}$, $Fe^{\uparrow}_{x/2}$, $Fe^{\downarrow}_{x/2}$. Because the local moment of Ni within the DLM approach collapses to zero for some cases, it was stabilized by the FSM method [101, 102]. The magnetic entropy effects [3, 103, 104] stabilized the local moments. The minimization of the free energy included the randomness of the directions and longitudinal spin fluctuations, but

the employed entropy (we used $S \propto \ln(1+m)$, where S is the entropy and m denotes local moments) is still under discussion; see Ref. [5] for more details and the Appendix of this Reference for a description of the extension to the two local moments.

The local moments slightly depend on spaces between Fe atoms and Ni ones and to describe it correctly, we used space-filling spheres which had the identical radii for both components. We investigated moments for $x \leq 0.5$ where the alloys had the fcc structure: The moments decrease weakly with increasing Fe concentration, the dependence is almost linear and it reproduces experimental data [141]. For this range of the magnetic moments, the calculated SDR also agreed with measurements [142], but the DLM-FSM method (instead of just DLM) must have been used for the better agreement (especially for $x = 0.0$). We refer to the published results [5] for more information and figures.

The presence of two spin channels (electrical conductivity) may lead to a violation of the Matthiessen's rule [44], but the experimental acquirement of the SDR assumes its validity. Therefore, we investigated a possibility to sum contributions given by different scattering mechanisms, i.e., impurities, atomic displacements, and spin fluctuations (described by the DLM-FSM method). Results of the scalar-relativistic calculations of the electrical resistivities are presented in Fig. 4.17 and 4.18 for $x = 0.50$ and $x = 0.25$, respectively. Data are shown up to large (not physical) magnitudes of displacements and the Curie temperature for both composition corresponds to $\sqrt{\langle u^2 \rangle} \approx 0.35\, a_{\mathrm{B}}$.

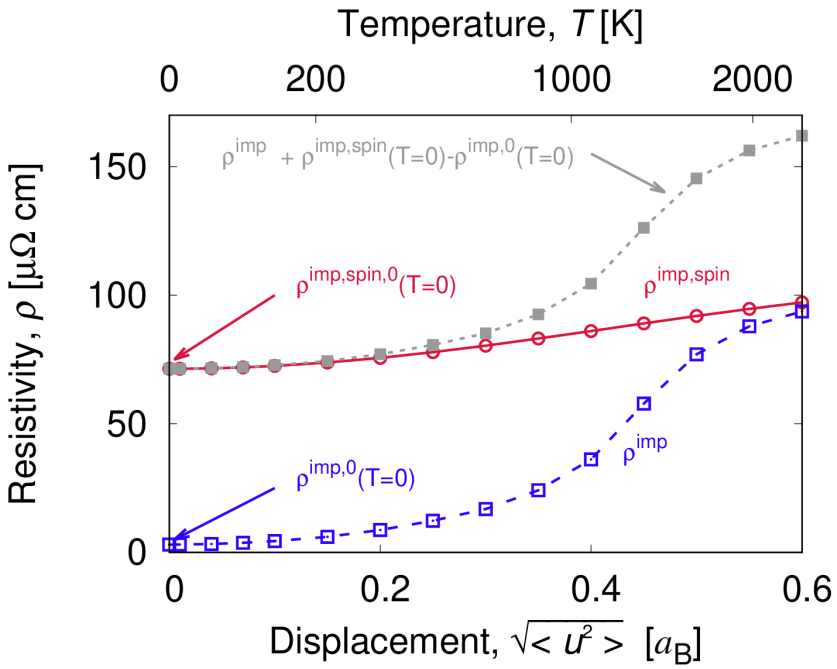

Figure 4.17: Electrical resistivity of $Ni_{0.50}Fe_{0.50}$ with included phonons and chemical disorder (blue dashed line with empty squares) has similar trend to the values with spin fluctuations (red solid line with circles). The Matthiessen's rule is violated for larger displacements (sum of contributions is shown by the dotted gray line with full squares; see text for detailed description).

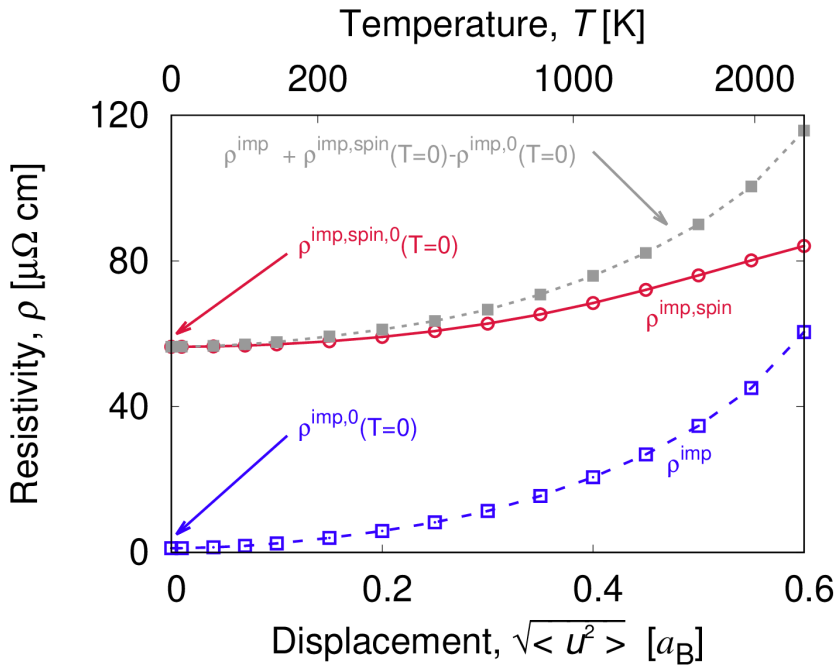

Figure 4.18: For $Ni_{0.75}Fe_{0.25}$, the electrical resistivity differs from the one for an alloy with equal concentrations (Fig. 4.17) especially in the data for the system included phonons and chemical disorder (blue dashed line with empty squares). Results for the spin fluctuations (red solid line with circles) are shifted by the different SDR. Sum of the contributions based on the Matthiessen's rule are shown by the dotted gray line with full squares; see text for detailed description.

In both Fig. 4.17 and 4.18, the gray dotted lines show resistivities that would correspond to the Matthiessen's rule for the phononic and magnonic contributions. It was obtained as the sum of the temperature-depend resistivity calculated only with phonons and impurities (ρ^{imp}) with the magnetic contribution at zero temperature. Because we study random alloys, the magnetic contribution at $T = 0$ is given by the DLM resistivity without the contribution of impurities, i.e., $\rho^{\mathrm{imp,spin}}(T = 0) - \rho^{\mathrm{imp,0}}(T = 0)$. For the relevant region of temperatures ($T \lesssim 1000$ K), the Matthiessen's rule is violated only slightly; larger deviation is observed for $x = 0.50$ than for $x = 0.25$. If the calculations are extended to higher temperatures (larger magnitudes of displacements), the Matthiessen's rule does not hold anymore; see Fig. 4.17 and 4.18.

4.3.3 Hexagonal random alloys

An effect of finite temperatures (phonons and magnons) on anisotropy of transition metals (Co, Ru, and Os) was shown in Sec. 4.1.2. Both the atomic displacements and spin fluctuations lead to finite conductivities; here we show an influence of chemical disorder on the anisotropy, see also Ref. [10] for details. We focus on electrical transport in random equiatomic Os-Ru alloy and Co-rich Co-Ni and Co-Ni-Fe alloys: a) $Co_{0.85}Ni_{0.15}$ is a stable (around room temperatures) binary alloy [143], b) $Os_{0.50}Ru_{0.50}$ is stable at high temperatures [143], and c) $Co_{0.84}Fe_{0.08}Ni_{0.08}$ is a hypothetical alloy with the same number of electrons as Co.

The resistivities ρ_{xx} and ρ_{zz} and their anisotropy ρ_{xx}/ρ_{zz} behave similarly to pure Co, Ru, and Os (Sec. 4.1.2), see Tab. 4.4 for the fully-relativistic results. It means that the impurities represent scattering mechanisms comparable to atomic displacements or magnetic fluctuations. The particular scattering mechanism is of minor importance for the anisotropy (of resistivities) with respect to the presence of a spontaneous FM order.

Although the behavior is similar for phonons, magnons, and impurities, we emphasize that the first two effects are always present in the finite-temperature measurements and their contributions are hardly distinguishable. On the other hand, the chemical composition may be used to tune the resistivities and the anisotropy ρ_{xx}/ρ_{zz}.

Table 4.4: Calculated resistivities in hexagonal alloys ($T = 0$) show a large importance of magnetism on the anisotropy. For comparison, data for pure Co with $\sqrt{\langle u^2 \rangle} = 0.2\,a_\mathrm{B}$ are stated, see Tab. 4.1 for more results.

	$\rho_{xx}[\mu\Omega\,\mathrm{cm}]$	$\rho_{zz}[\mu\Omega\,\mathrm{cm}]$	ρ_{xx}/ρ_{zz}
Co FM	5.46	6.77	0.81
Co NM	24.8	16.5	1.50
$Co_{0.85}Ni_{0.15}$ FM	0.67	0.85	0.78
$Co_{0.85}Ni_{0.15}$ NM	12.0	9.53	1.26
$Co_{0.84}Fe_{0.08}Ni_{0.08}$ FM	1.91	2.18	0.88
$Co_{0.84}Fe_{0.08}Ni_{0.08}$ NM	11.6	8.95	1.30
$Os_{0.50}Ru_{0.50}$	3.98	2.86	1.39

4.4 Influence of the Fermi-Dirac distribution

In Sec. 2.3.3, we described a possible influence of the Fermi-Dirac distribution at finite temperatures to the electrical transport properties. Here we examine Pt and Pd, which are ideal candidates for this study because of the large change of the density of states (DOS) around the Fermi level. The described effect is small and similar negligible influence was obtained also for Co, Fe, and Rh (not shown here). It justifies omitting this phenomenon for other calculations.

The energy dependent conductivity appearing in Eq. (2.50) is shown in Fig. 4.19 for Pd and in Fig. 4.20 for Fe. Energy ranges were determined by the Fermi-Dirac distribution and chosen in the way that the contribution to the original isotropic conductivity $\sigma_0(E_F)$ given by the Fermi-Dirac distribution was

$$\left|\frac{\partial f(E)}{\partial E}\right| > 10^{-5} \tag{4.1}$$

for each studied temperature.

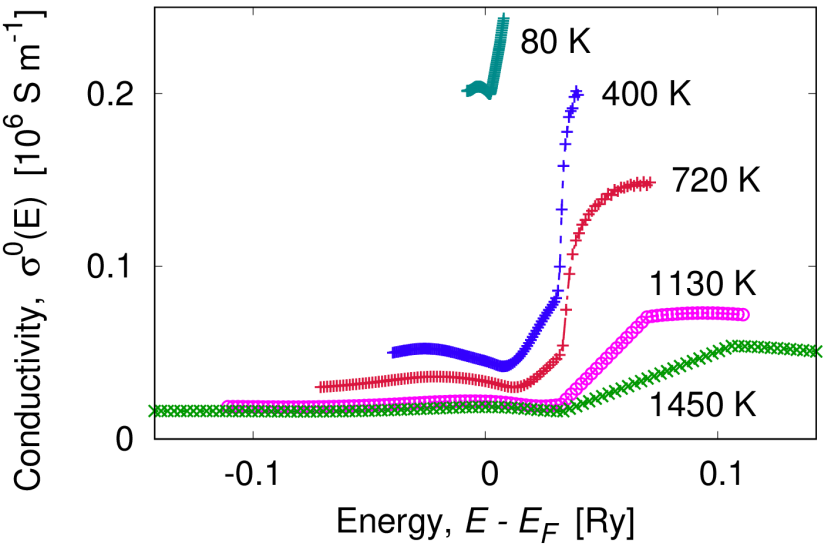

Figure 4.19: Electrical conductivity $\sigma^0(E)$ for Pd is dependent on the energy $E - E_F$, but its integrated value does not differ much from $\sigma^0(E = E_F)$; therefore, the correction obtained using (2.50) is small.

In Tab. 4.5 (Pd) and 4.6 (Fe) we present corrections to the resistivities (denoted Resist.). The correction for the lowest investigated temperature of Pd (T=80 K) is below our numerical precision; therefore, it is not presented. Original values (calculated with zero-temperature Fermi-Dirac distribution) are denoted by the superscript "0" and the quantities calculated with Eq. (2.50) have the superscript "int."

The larger corrections in Fe compared to Pd are caused by the shape of the energy-dependent conductivities (Fig. 4.19 vs. 4.20), which could be traced back to different shapes of the DOS around the Fermi level (not shown here). Obtained corrections for the AHC (Tab. 4.6) have the same orders of magnitudes as for the

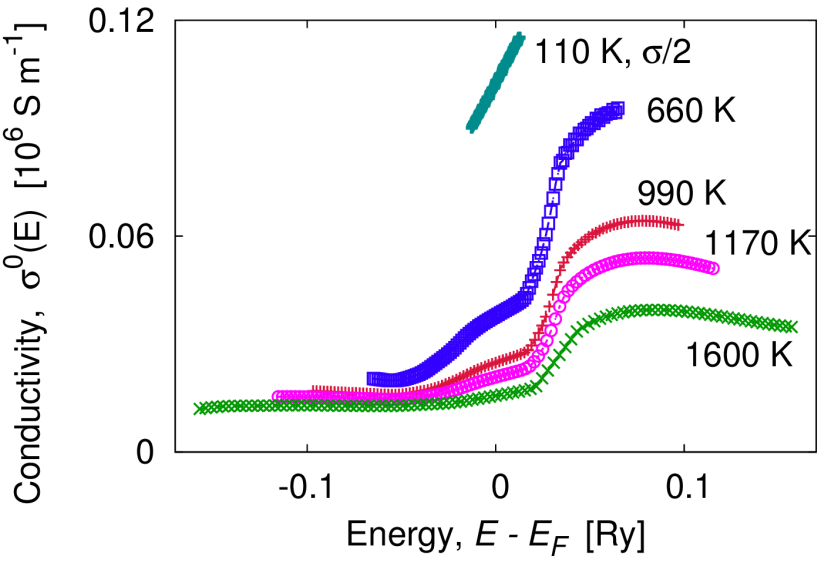

Figure 4.20: Electrical conductivity $\sigma^0(E)$ for FM Fe is strongly dependent on the energy $E - E_F$. The conductivity for $T = 110$ K is divided by two.

resistivities. It is caused by the relative corrections being similar for all elements of the conductivity tensor.

Table 4.5: Corrections to the electrical resistivity of Pd caused by the temperature-dependent Fermi-Dirac distribution are negligible.

	T [K]	400	720	1130	1450
	$\sqrt{\langle u^2 \rangle}$ [a_B]	0.284	0.379	0.474	0.537
Resist.	ρ^0 [$\mu\Omega$ cm]	22.1	29.9	45.8	53.9
	$\rho^{\mathrm{int.}}$ [$\mu\Omega$ cm]	22.1	30.0	46.6	55.1
	Correct. [%]	<0.1	0.2	1.9	2.3

In Sec. 4.5 we focus on the electrical transport at extreme conditions in the Earth's core. For temperature of 6000 K, the corrections to the electrical resistivities caused by the Fermi-Dirac distributions for iron were obtained [3]: nonmagnetic Fe results in 1.6 % and DLM Fe results in 2.7 %. We note that these corrections hold for high pressure (350 GPa); therefore, they can be hardly compared to values in Tab. 4.6. On the other hand, these small numbers justify omitting the effect of the Fermi-Dirac distribution in the rest of this thesis.

Table 4.6: FM iron: Corrections caused by the temperature-dependent Fermi-Dirac distribution are larger than for Pd (Tab. 4.5) and they are similar for the resistivities and the AHC.

	T [K]	110	660	990	1170	1600
	$\sqrt{\langle u^2 \rangle}$ [a_B]	0.126	0.284	0.347	0.379	0.442
Resist.	ρ^0 [$\mu\Omega$ cm]	4.85	26.1	39.7	47.2	62.7
	$\rho^{\mathrm{int.}}$ [$\mu\Omega$ cm]	4.88	26.4	39.9	47.1	60.7
	Correct. [%]	0.6	0.9	0.5	-0.4	-3.2
AHC	σ^0_{xy} [10^4 S m^{-1}]	5.85	5.21	4.89	4.70	4.35
	$\sigma^{\mathrm{int.}}_{\mathrm{xy}}$ [10^4 S m^{-1}]	5.81	5.14	4.72	4.49	4.04
	Correct. [%]	-0.7	-1.4	-3.2	-4.5	-7.8

4.5 Extreme conditions in the Earth's core

In other parts of this thesis, we focused on ambient conditions, i.e., on temperatures up to the melting point and the standard pressure. This Section describes extreme conditions of the Earh's core. It may be surprising, but our formalism works even for these conditions and the results were published in [3] and [8].

For the purpose of this topic (conditions in the Earth's core), the spin fluctuations are incorporated as the DLM state, which reproduces well high temperatures (about 5500 K). The Wigner-Seitz radius r_{ws} is assumed to correspond to a volume reduction to 60 % (bcc lattice constant 2.418Å, r_{ws} = 2.25 a_B, pressure of 350 GPa) with respect to the ambient case. The identical r_{ws} was used for all compositions of the iron-based alloys, which should be a good approximation for a low amount of impurities. For ambient conditions (r_{ws} = 2.66 a_B), the resistivity is almost the lowest (among the investigated values), while the assumed high-pressure conditions result in two times larger (this factor holds for $\sqrt{\langle u^2 \rangle} = 0.5\, a_\mathrm{B}$), see Fig. 4.21 that was obtained only for the change of the volume without additional conditions on magnetic moments. We note that the magnetic moment collapses to zero for $r_{ws} \lesssim 2.3$ a_B (Fig. 4.22).

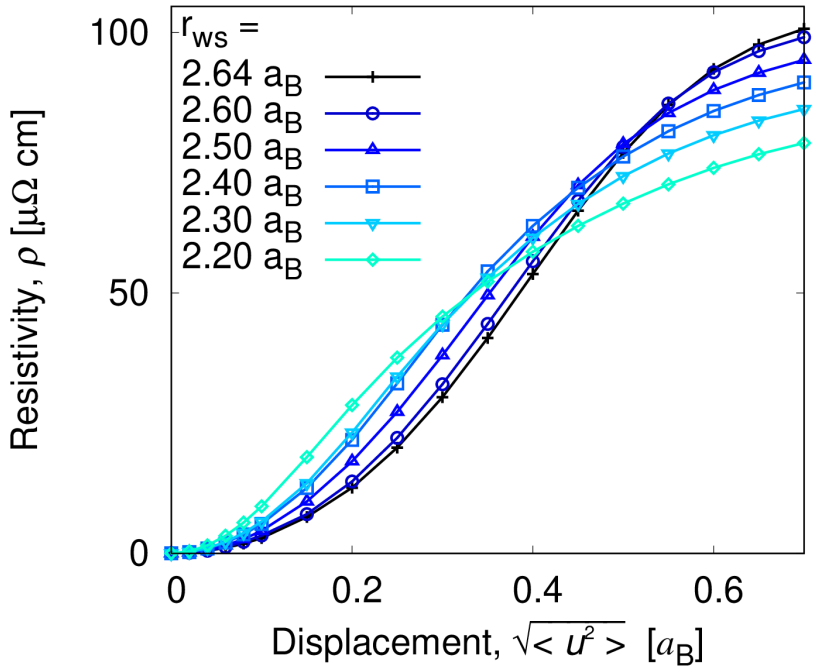

Figure 4.21: NM Fe within the scalar-relativistic framework and without the magnetic disorder changes its electrical transport with the decreasing Wigner-Seitz radius.

The Debye theory cannot be expected to give accurate magnitudes of displacements for the extreme temperature and pressure. (The Debye temperature for ambient conditions of 477 K was used.) Fortunately, the Earth's core was previously studied by the VASP code employing *ab initio* molecular dynamics (AIMD) [116]. Results from this work are compared to the Debye model in Tab.

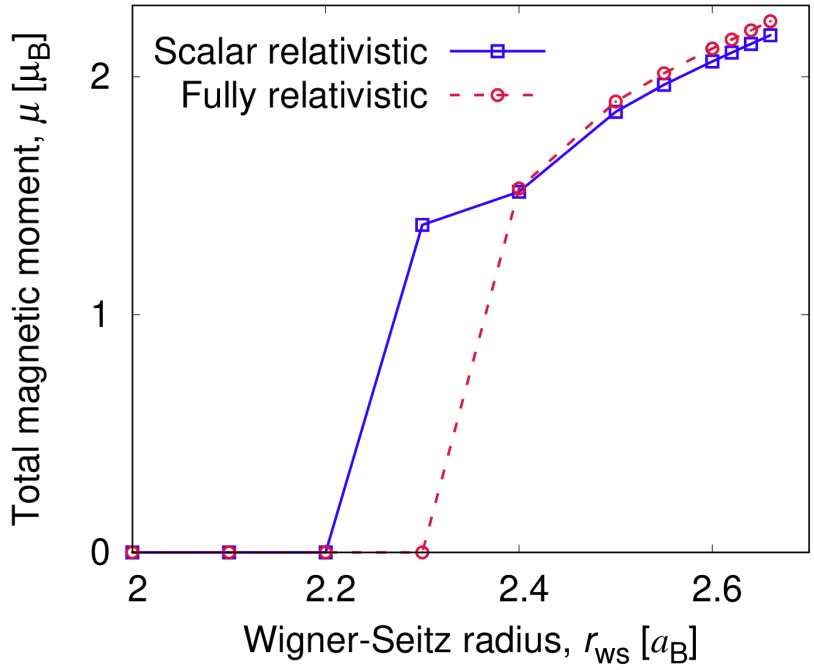

Figure 4.22: The local average magnetic moment per atom of Fe decreases with the decreasing Wigner-Seitz radius.

4.7; because of the high difference, data from the molecular dynamics were used for our purposes.

Table 4.7: Root-mean-square displacements obtained for high temperatures from the Debye theory compared to [116]

Temperature, T [K]	Displacement, $\sqrt{\langle u^2 \rangle}[a_B]$	
	Martorell [116]	Debye ($\Theta_D = 477$ K)
2000	0.31	0.49
5500	0.59	0.82
6500	0.68	0.89
7000	0.80	0.92

A pioneering work of Ref. [3] and [8] was based on considering the spin disorder in Fe and Fe-based alloys in the Earth's core. Although they are magnetic (at ambient conditions), previous studies neglected that. It was shown that the magnetic entropy allows an existence and stabilizes robust local moments of order from 1.1 to 1.3 μ_B for temperatures 5000-6000 K. It was calculated using (i) the combination of the disorder local moment and fixed spin moment methods or (ii) the classical model of local spin fluctuations; for details see Ref. [3]. The spin-disorder resistivity for the relevant conditions was found to be about 20 $\mu\Omega$cm, which agrees perfectly with calculations using molecular dynamics [144]. A scattering on phonons was found to be several times larger. However, the effects are not additive, see later a discussion of Fig. 4.23.

Fig. 4.23 shows a behavior of pure iron and random $Fe_{85}Ni_{0.15}$ alloy at the Earth's core conditions for magnetic disorder both incorporated and neglected.

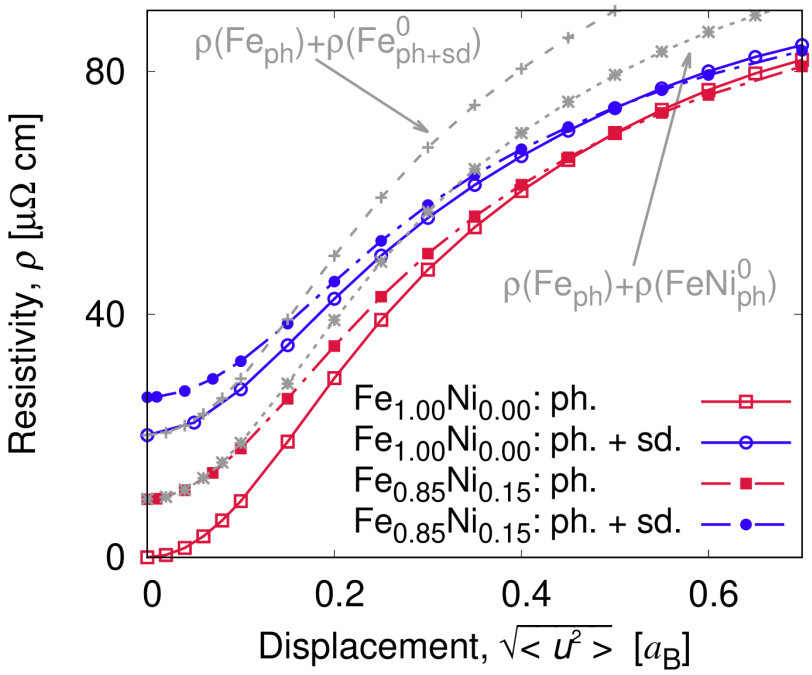

Figure 4.23: A comparison of electrical resistivity at Earth's core conditions for iron (empty symbols) and $Fe_{85}Ni_{0.15}$ alloy (full symbols) without and with magnetic disorder (squares and circles, respectively) results in a violation of the Matthiessen's rule for both the spin disorder (dashed gray line with crosses) and impurities (dotted gray lines with stars).

A difference in resistivities is getting smaller for increasing magnitudes of the displacements, which implies a violation of the Matthiessen's rule, i.e., an additivity of scattering contributions coming from different effects (impurities, phonons, spin disorder). The gray dotted and dashed lines showing the validity of the Matthiessen's rule in Fig. 4.23 are obtained similarly to the previously shown Fig. 4.17 and 4.18: they present a sum of the temperature-dependent resistivity for pure iron with the zero-temperature value for iron with the spin fluctuations and Ni-Fe alloy without the spin disorder, respectively. If all of the scattering mechanisms (phonons, magnetic disorder, impurities) are taken into account, then the Matthiessen's rule overestimates the resistivity for $\sqrt{\langle u^2 \rangle} = 0.59\, a_{\mathrm{B}}$ by 30 % (100 vs. 77 $\mu\Omega\,$cm).

For a summary of resistivities for Fe with different chemical impurities, see Fig. 4.24. Fe random alloys with different content of Ni, O, S, and Si are shown in Fig. (a), (b), (c), and (d), respectively; Fig. (e) compares the resistivities for 15 % of impurities. All of the results were obtained for the high-pressure systems with $r_{ws} = 2.25$ a$_B$. While the Fe-Ni alloy is almost independent on amount of Ni, the large dependence is obtained for other elements, especially for S and Si.

We note that the resistivities of alloys are shown as functions of $\sqrt{\langle u^2 \rangle}$. The conversion between the displacements and temperature may differ for different alloys because the Debye theory cannot be reliably used for these conditions and investigation similar to [116] is beyond the scope of this thesis. Moreover, an

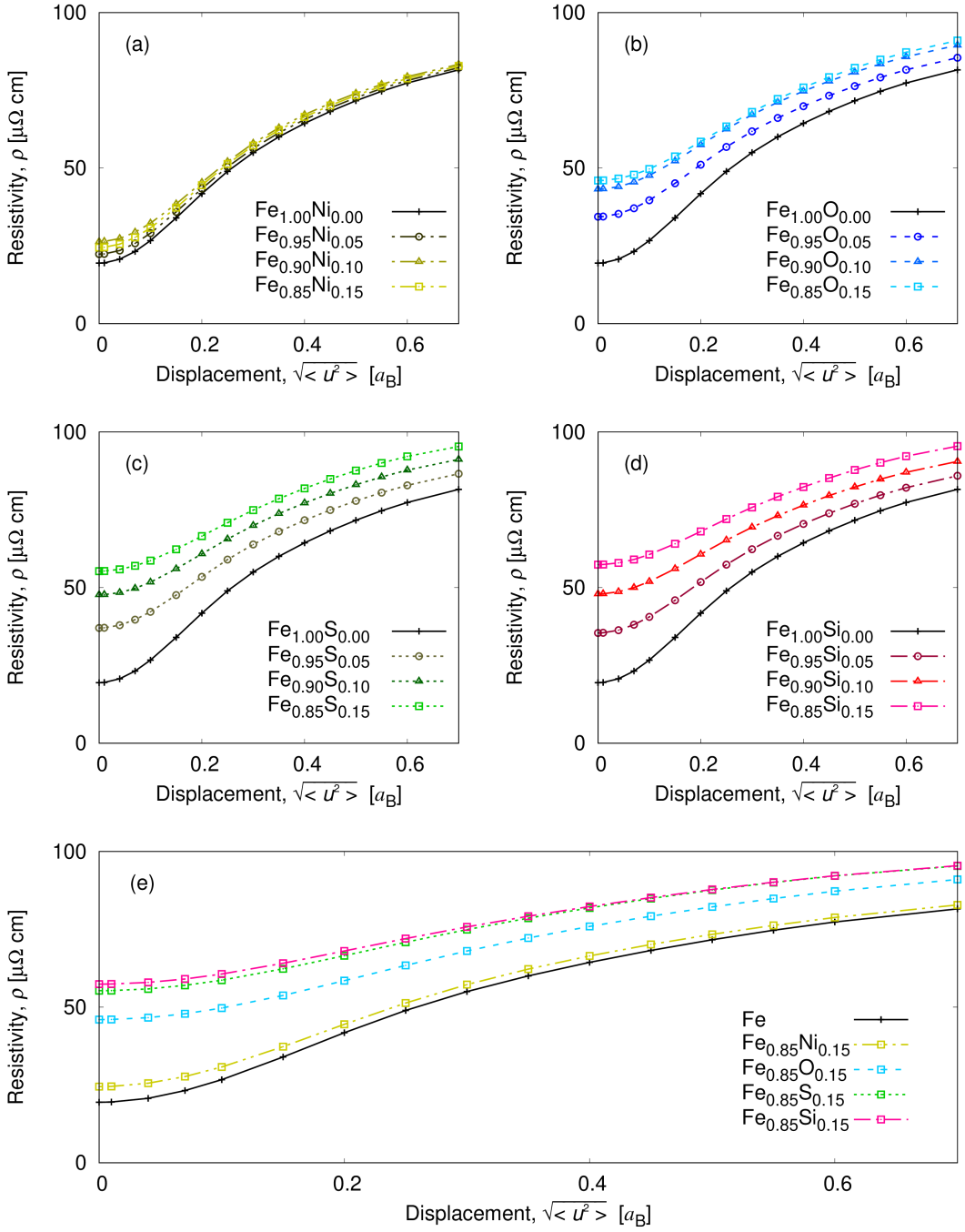

Figure 4.24: Electrical resistivity of alloys at Earth's core conditions ($r_{ws} = 2.25$ a$_B$ with included chemical disorder, lattice vibrations, and spin-disorder exhibit for all impurities (Ni – Fig. (a), O – (b), S – (c), Si – (d)) similar metallic-like behavior even for high magnitudes of the displacements; for comparison see Fig. (e).

ideal framework that would give a proper $\sqrt{\langle u^2 \rangle}(T)$ dependence with all of the important phenomena (finite temperatures with magnetic disorder, high pressure, etc.) included is still missing. Therefore, Fig. 4.24 (e) does not states that the temperature-dependent resistivities of the Fe-S and Fe-Si alloys are identical.

4.6 Spin-resolved transport

Not only the longitudinal resistivity and the AHC may be studied by the linear response theory, but also the (longitudinal) spin-resolved electrical conductivity (Sec. 2.4) may be examined. It is the central topic of this Section and we focus on both the nonmagnetic and magnetic systems. Some of the results presented here were published [4], but the tested robustness of the approach was also used for NiMnSb [6, 9], which is a much more difficult system (see later Sec. 5.1).

4.6.1 Platinum

The spin-resolved coherent and incoherent (vertex) parts of the longitudinal conductivity for platinum are displayed in Fig. 4.25. As can be seen, the vertex part of the conductivity is small for all displacements. Therefore, the coherent contribution corresponds almost exactly to the total conductivity. Moreover, both spin-up and spin-down coherent conductivities are identical, as they should be for a nonmagnetic system, and their sum is almost equal to the total coherent conductivity, which makes the spin-flip contribution to the conductivity negligible. One can conclude from Fig. 4.25 that the combined effect of the vertex corrections and the spin-flip contribution leads to a difference that is much smaller than errors related to experimental values (comparison of calculated and measured data or imperfections of samples).

No difference between the spin-up channel and the spin-down one were expected and it leads to zero polarization (not shown here) of the spin-resolved electrical current. Therefore, Pt is not interesting for our future studies, but it showed the reliability and accurateness of our approach.

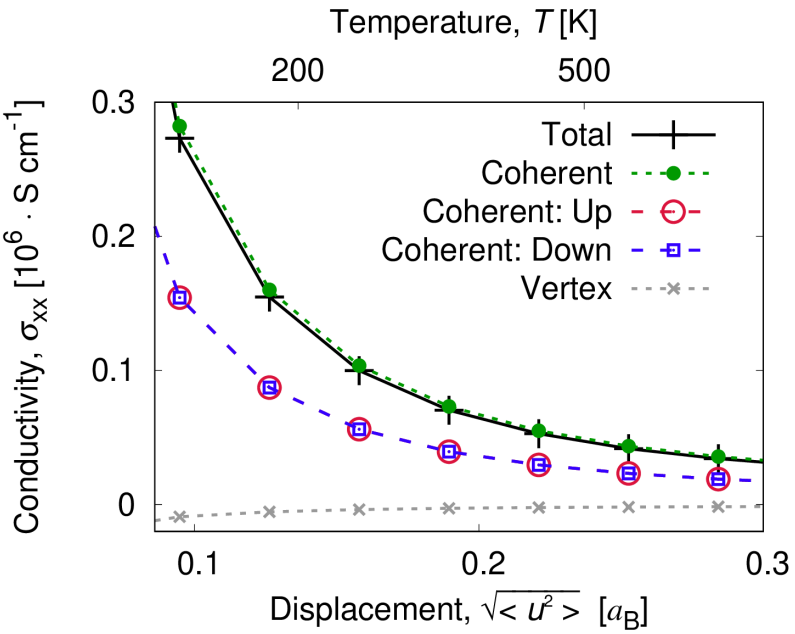

Figure 4.25: Electrical conductivity of Pt separated to the (spin-resolved) coherent and vertex contributions; difference between spin-up and spin-down channels is negligible.

4.6.2 Cu-Ni random alloys

The nonmagnetic system, as well as Pt, is obtained for the Cu-Ni alloy having its composition close to Cu, see Fig. 4.10. By varying the composition, pure Ni with magnetic moment of $\mu = 0.69\mu_B$ is obtained. It makes the Cu-Ni system a perfect candidate for investigation of the spin-resolved conductivity.

First, we discuss the combined effect of atomic displacements and chemical disorder on the spin-resolved conductivities for the random $Cu_{1-x}Ni_x$ alloys. The spin-resolved coherent conductivities and the incoherent (vertex) conductivity for pure nickel are displayed in Fig. 4.26 and, compared to Pt, they have nonidentical spin-up and spin-down channels. The spin polarizations of the current P for pure Ni and $Cu_{0.05}Ni_{0.95}$ alloy are shown in Fig. 4.27. For all FM Cu-Ni alloys, the polarization P is positive, which reflects a higher conductivity in the majority (spin-up) channel than in the minority (spin-down) one. For pure Ni, the spin-up conductivity is almost exactly three times larger than the spin-down one in the entire interval of displacement magnitudes, which results in $P \approx 0.5$. Both features are strongly modified by Cu alloying: the spin polarization is enhanced and its value decreases with increasing $\sqrt{\langle u^2 \rangle}$ because the spin-up conductivity decreases faster than the spin-down one.

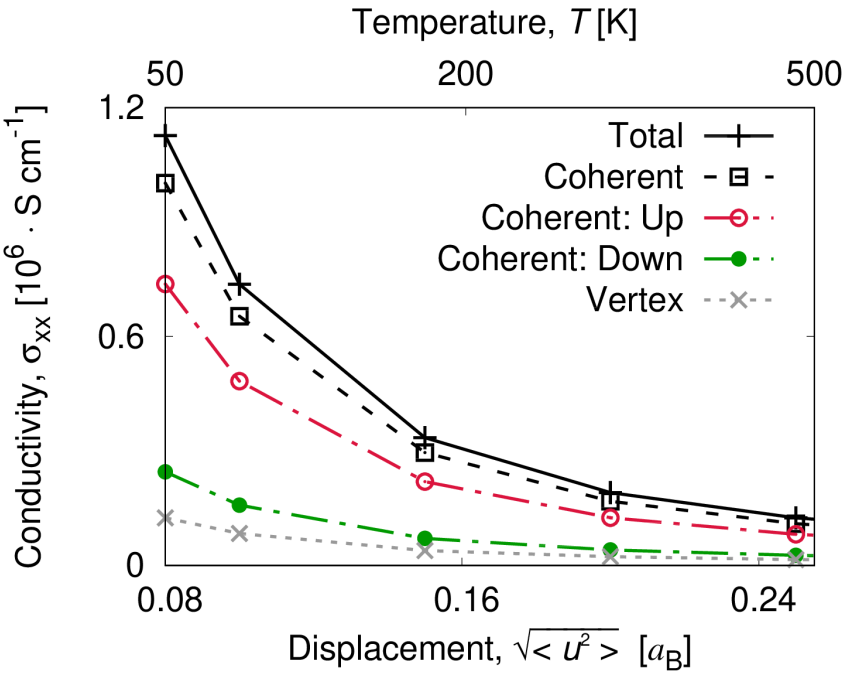

Figure 4.26: Electrical conductivity of nickel separated to the (spin-resolved) coherent and vertex contributions.

The conductivity of cubic ferromagnets is anisotropic. It gives rise to the anisotropic magnetoresistance effect. In this work, magnetization was chosen to be in z-direction, which leads to two different longitudinal conductivities, $\sigma_{xx} = \sigma_{yy}$ and σ_{zz}. One can see that the anisotropy of the polarization P is rather weak in the studied range of displacements for both systems (Fig. 4.27).

The calculated concentration dependence of the residual resistivity agrees

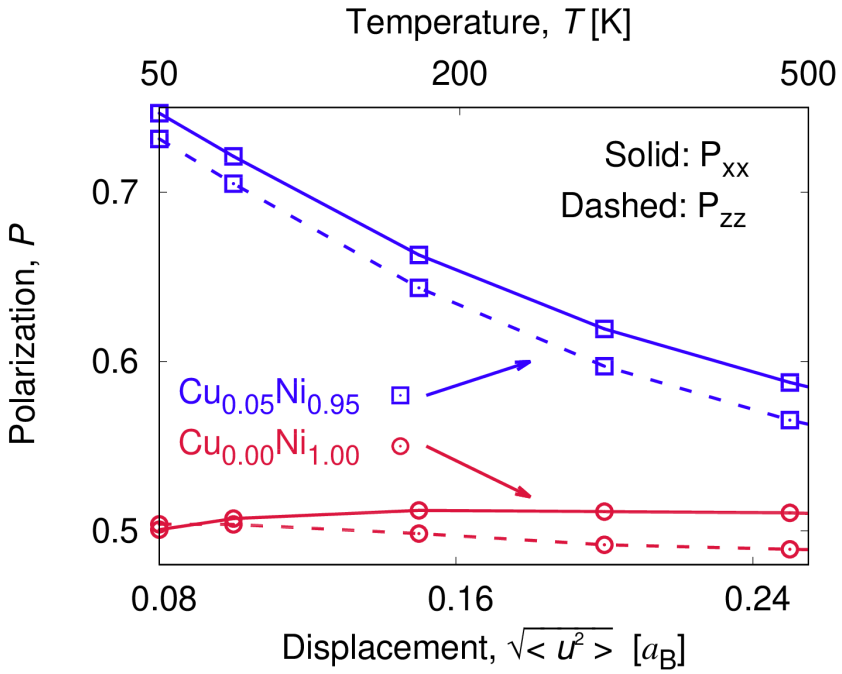

Figure 4.27: Polarization of the coherent conductivities for pure nickel (circles) and $Cu_{0.05}Ni_{0.95}$ alloy (squares); dashed lines: current in the direction of magnetization (P_{zz}), solid lines: current in the plane perpendicular to magnetization (P_{xx}).

qualitatively with the experiment [137]; the maximum resistivity is found at the critical concentration for the disappearance of ferromagnetism (see Fig. 4.13). The inclusion of atomic displacements leads to an increase of the resistivity in all cases, in contrast to the spin polarization P which decreases with increasing $\sqrt{\langle u^2 \rangle}$ (Fig. 4.28).

The concentration trend of the spin polarization is not monotonic. Vanishing P is obtained for PM alloys in full analogy with nonmagnetic platinum. In FM $Cu_{1-x}Ni_x$ alloys with $x \geq 0.5$, the polarization exhibits strongly positive values ($P \gtrsim 0.5$), which is surprising if we take into account the strong variation of the alloy magnetization in this concentration range (Fig. 4.28). Note that the calculated magnetizations for $x = 0.5$ and $x = 1$ differ more than by a factor of three. The high stability of the polarization P with respect to the atomic displacements has been obtained with the assumption of a perfect FM order, i.e., with neglected temperature-induced magnetic fluctuations. It can be expected that the polarization of the current will be reduced by these spin fluctuations; however, their inclusion goes beyond the scope of the present study.

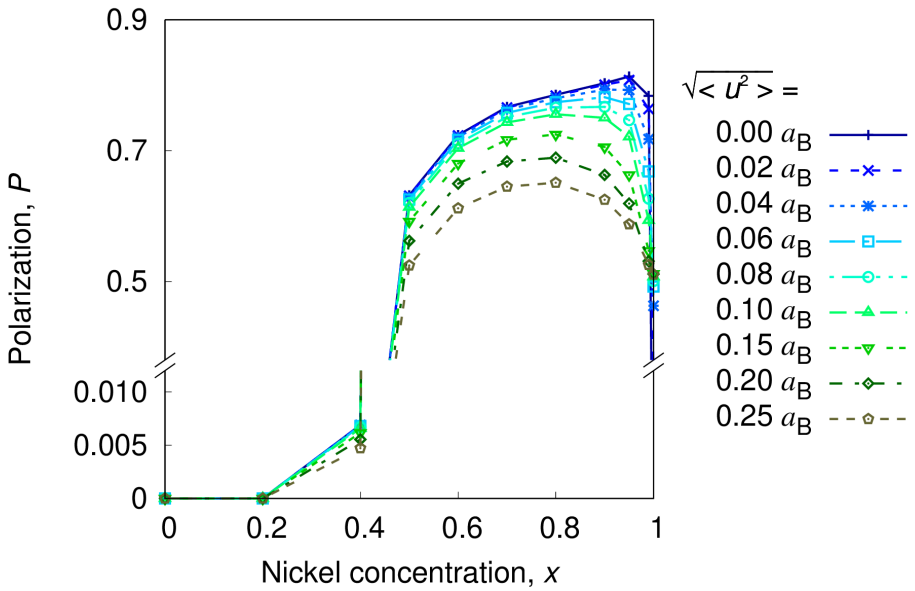

Figure 4.28: Polarization of the spin current calculated for $Cu_{1-x}Ni_x$ alloy as a function of nickel concentration.

4.7 Summary of the results

This Chapter showing calculations of electrical transport at finite temperatures summarizes data for a wide range of materials. Most of the presented systems were also used to test the AAM and its implementation. The attention should be paid especially to these results:

- Temperature-dependent electrical transport of nonmagnetic pure transition metals such as Pt or Pd can be straightforwardly described by the AAM. For magnetic systems (Fe and Ni), the agreement with experimental data is obtained after inclusion of spin fluctuations; the experimental magnetization is used for this purposes.

- The binary random alloys can be described with the approximation of identical displacements for atoms with different masses. It was tested especially on Co-Ni a Cu-Ni alloys, which significantly change their magnetic moments depending on the chemical composition.

- For simplicity, most of the examined systems have a cubic structure, but we also successfully employed the AAM for the purposes of hexagonal systems, i.e., Co, Ru, Os, and their alloys. The finite-temperature phenomena are used as one of the scattering mechanisms and in addition to their influence on the transport, we focus on explaining the magnetic state and anisotropy of the resistivities.

- The role of the broadened Fermi-Dirac distribution (within the linear response theory) is small and may be neglected for most of the studies.

- Not only standard systems and ambient conditions may be described by the AAM, but also the conditions of the Earth's core were successfully studied.

- Because of spintronic applications, we investigated also the spin-resolved electrical transport, especially in Cu-Ni alloys.

5. Comprehensive study of selected materials

5.1 NiMnSb

In this section we present results for half-Heusler NiMnSb compound [6, 9]. Because the AAM was successfully applied to transition metals and binary alloys, we then focused on simulating the temperature dependence of conductivity, AHC, and spin polarized conductivity of this prototypical half-metalic system.

In contrast to so far investigated materials within AAM, half-metallic ferromagnet [36] NiMnSb is more complicated in terms of two magnetic sublattices with ferromagnetic and antiferromangetic exchange interactions and a wide range of possible structure defects with similar formation energies [145]. This makes it difficult to compare calculations and experiment. On the other hand, NiMnSb has been intensively studied for over 25 years including AHC and electric resistance [26, 146–148], which makes it good for testing of new *ab initio* methods. Moreover, novel spintronics effects such as room-temperature spin-orbit torque in strained NiMnSb may be observed due to Dresselhaus symmetry [41]. NiMnSb has large Curie temperature of 730 K [147], it makes it an ideal candidate for spintronic applications for which our investigation and knowledge of temperature-dependent transport properties are essential.

Half-metallic NiMnSb NiMnSb has the cubic crystal structure $C1_b$ and the experimental lattice constant $a_{\text{latt.}} = 5.927$ Å is used [147]. Without chemical disorder, NiMnSb consists of four FCC sublattices Ni-Mn-empty-Sb equidistantly shifted along [111] direction, see Fig. 5.1. The empty sublattice denotes interstitial sites, i.e., empty positions in the half-Heusler lattice which would be occupied in the full-Heusler structure. We investigate Mn-rich and Ni-rich alloys with substitutional disorder, i.e., systems with sublattices $(\text{Ni}_{1-y}\text{Mn}_y)$-Mn-empty-Sb and Ni-$(\text{Mn}_{1-y}\text{Ni}_y)$-empty-Sb, respectively, with $y \in [0, 0.2]$. Notation $\text{Ni}_x\text{Mn}_{2-x}\text{Sb}$ with x from 0.8 (Mn-rich) to 1.2 (Ni-rich) is used for brevity.

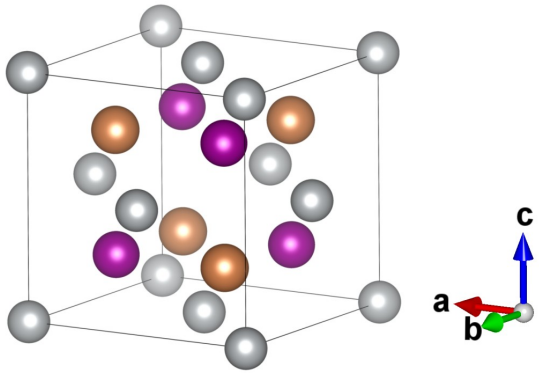

Figure 5.1: FCC $C1_b$ structure of half-Heusler NiMnSb: Ni, Mn, and Sb atoms are shown by the grey, violet, and bronze (orange) colors, respectively. Created with [149].

These defects are consistent with literature [41] and they have low formation energies [145]: 0.49 and 0.92 eV per formula unit for Mn- and Ni-rich case, respectively. Lower formation energies were obtained for Ni- and Mn-atoms occupying the interstitial crystallographic positions (0.20 eV and 0.73 eV per formula

unit, respectively), but our calculated resistivity as a function of temperature significantly underestimates experimental values for these systems.

NiMnSb is half-Heusler ferromagnet known for the presence of states only for one spin at the Fermi level [150, 151]. The measured value of the spin polarization of the electrical current is from 45 to 58 % [119, 148, 152, 153] at low temperatures and about 50 % at room temperature [154]; spin polarized photoemission experiments show the spin polarization of the emitted electrons about 50 % at 300 K [155]. The polarization of the ballistic transport for correlated electrons about 50 % was calculated for Au–NiMnSb–Au heterostructures by the SMEAGOL DFT code [156].

In previous reports, the Debye temperature was theoretically estimated to be between 250 and 300 K [26], measured $(312 \pm 5)\,\mathrm{K}$ [157] or 322 K [158] and calculated 327 K [159] and 270 K [160]. We used $\Theta_D = 320\,\mathrm{K}$ (see later Fig. 5.7); the above scatter in Debye temperature values leads to approx. 10 % error in the root-mean-square displacement $\sqrt{\langle u^2 \rangle}$. The best agreement between experimental data [26, 148, 161] as concerns the slope of the calculated temperature dependence of the resistivity is obtained for $\Theta_D = 350\,\mathrm{K}$ and 2 % Ni-rich NiMnSb.

The TB-LMTO method (both LSDA and LSDA+U) was previously used to estimate the Curie temperature, exchange interactions, magnon spectra, and magnetic moments in $Ni_{2-x}MnSb$ alloys [162, 163]. A saturation magnetization of NiMnSb is changing only slightly (by 5 to 10 %) from zero to room temperature [118–120] and the magnetic moments were investigated by a polarized neutron diffraction [146]. Treating NiMnSb within LDA+U (for temperature $T = 0$) results only in a small correction to magnetic moments [99, 163].

Computational details The mesh of $150 \times 150 \times 150$ k-points in the Brillouin zone was used for transport calculations if not specified otherwise. Smaller numbers of k-points as for, e.g., pure metals, are required because of a large self-energy term originating from chemical or temperature disorder. Increasing the mesh to 200^3 k-points leads to a correction of 0.05 % for the isotropic resistivity.

NiMnSb has $[m(\mathrm{Ni}) : m(\mathrm{Mn}) : m(\mathrm{Sb}) \approx 1 : 0.93 : 2.07]$; therefore, a proper choice of atomic displacements was investigated for two cases: (a) the magnitudes identical for each atom or (b) scaled according to atomic masses. The TB-LMTO approach assumes empty spheres at the empty positions in the half-Heusler lattice which would be occupied in the full-Heusler lattice. The potential functions of the empty sphere may be (i) formally displaced like other nuclei or (ii) independent on atomic shifts. We have tested all four possibilities, i.e., combinations of models (a) and (b), and (i) and (ii) above. We have found deviations in the isotropic resistivities of the order of 5% by assuming $\sqrt{\langle u^2 \rangle} = 0.20\,a_\mathrm{B}$ and $0.25\,a_\mathrm{B}$, where a_B is the Bohr radius. This value should be considered as a systematic error of the AAM (later shown by error bars in Fig. 5.7). In the following sections, identical magnitudes of the displacements are assumed for all atoms. Each atom was assumed to have eight different directions of displacements (within the CPA) uniformly distributed around its equilibrium position.

5.1.1 Electronic structure at zero and finite temperatures

Chemical disorder at zero temperature The magnetic moment of the stoichiometric NiMnSb is $m = 4.0\mu_B$ per formula unit, which agrees well with the half-metallic character (the Fermi level in the minority gap), with its integer number of electrons per formula unit, and it is in good agreement with experimental data [146] and previous calculations [41, 99]. In Fig. 5.2 we show the average moment, local magnetic moments, as well as local Mn- and Ni-impurity magnetic moments on Ni- and Mn-sublattices, respectively. Local moments per atoms for the stoichiometric system are $m_{\mathrm{Ni}} = 0.26\mu_B$, $m_{\mathrm{Mn}} = 3.75\mu_B$, $m_{\mathrm{Sb}} = -0.05\mu_B$, and $m_{\mathrm{empty}} = 0.08\mu_B$; for 10 % Ni-rich $m_{\mathrm{Ni}} = 0.20\mu_B$, $m_{\mathrm{Mn}} = 3.69\mu_B$, $m_{\mathrm{Sb}} = -0.07\mu_B$, $m_{\mathrm{empty}} = 0.06\mu_B$, and $m_{\mathrm{impurity}} = -0.64\mu_B$; and for 10 % Mn-rich $m_{\mathrm{Ni}} = 0.24\mu_B$, $m_{\mathrm{Mn}} = 3.68\mu_B$, $m_{\mathrm{Sb}} = -0.05\mu_B$, $m_{\mathrm{empty}} = 0.08\mu_B$, and $m_{\mathrm{impurity}} = -1.88\mu_B$ (the m_{empty} denotes moment induced on empty spheres at the interstitial positions). Both Mn and Ni impurities tend to couple antiferromagnetically and thus decrease the net moment with increasing disorder; however, the main reason for the moment reduction is slightly different for the Mn- and Ni-rich systems: In the former one, Mn atoms on the Ni sublattice have opposite directions of the magnetic moments with respect to Mn atoms on their own sublattice and the sum of all the moments decreases with increasing concentration of antiparallel Mn moments. For the Ni-rich case, the concentration of Mn atoms having large moment decreases and they are replaced by Ni having moments much smaller (five to thirty times, see Fig. 5.2); moreover, with the antiparallel orientation.

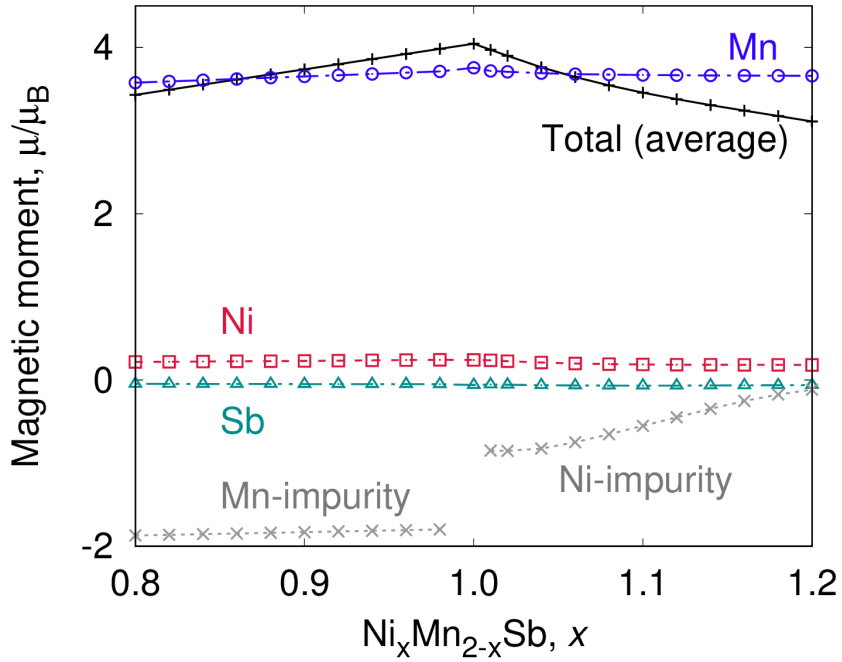

Figure 5.2: Total averaged magnetic moment (per formula unit) of Ni- and Mn-rich NiMnSb and spin magnetic moments of individual atoms for zero temperature. The Ni/Mn-impurity dataset presents the local magnetic moments of Ni and Mn atom placed on the crystallographic position of the second atom.

Magnetic disorder at finite temperatures We investigate the influence of magnetic disorder on the electrical transport within the uDLM approach and the model of tilted local moments. For detailed description of the approaches, see Sec. 2.2.

The mean-field alloy was constructed by substituting a given site occupied by a single local moment oriented along the z-direction by 4 different local moments tilted by the Euler angle θ from the z-axis symmetrically in the four directions x,y,$-x$, and $-y$ and parametrized by the second Euler angle $\phi \in \{0.0\pi, 0.5\pi, 1.0\pi, 1.5\pi\}$. Four directions are sufficient for our case. This approach interpolates between fully-ordered spin ferromagnetic (FM) state ($T = 0$ K) and fully disordered spin state (DLM, T above the Curie temperature). Attempts to make descriptions of magnetic disorder more realistic were published [29, 32, 33], but a fully *ab initio* theoretical estimate of temperature-dependence of total magnetization $M_{\mathrm{tot}}(T)$ can be also rather inaccurate because it employs the classical Boltzmann statistics (Monte Carlo) method (see the discussion in quaternary Heusler alloys [20]).

We aim to estimate only the strength of the magnetic disorder contribution relative to the contribution from phonons and chemical disorder. The order of magnitude is determined from the energy difference between the disordered DLM state and the FM ground state which amounts to $\Delta E \approx 12$ mRy (0.16 eV) per formula unit. In such approximation, room temperature disorder roughly corresponds to $\phi = 0.10\pi$. A comparison to an experimentally observed change of the saturation magnetization [118–120] would give $\phi = 0.15\pi$. The use of experimental $M_{\mathrm{tot}}(T)$, if available, may be a better choice, but, in general, an accurate relation of the tilting angle as a function of the temperature is missing.

With increasing θ or $x_{\mathrm{Mn^-}}$, the total magnetization of stoichiometric NiMnSb decreases from $M = 4.0\mu_B$ per formula unit to zero. The total energy E as a function of the spin magnetic moment μ_s is displayed in Fig. 2.7, where the disordered PM state corresponds to $\mu_s = 0$ while the undistorted system has $\mu_s = 4\mu_B$; μ_s is the average of all local magnetic spin moments projected onto the direction of the original magnetization. The equivalence of uDLM and tilting models of the magnetic disorder for the $E(\mu_s)$ dependence cannot be extended to the transport properties, see later. The fit of the temperature-dependent magnetization by the measured one was described in Sec. 2.3.2. Based on the fit, spin disorder is not dominant at the room temperature, but it gives a major contribution close to the Curie temperature.

Density of states and Bloch spectral function The spin-resolved densities of states (DOS) of the studied system are displayed in Fig. 5.3. The stoichiometric NiMnSb is the half-metal as it is indicated by the DOS in Fig. 5.3 (b). Our results are in agreement with literature [99]. The influence of atomic displacements slightly broadens peaks in the DOS (see Fig. 5.3 for 540 K) but the DOS around the Fermi level is almost the same. The half-metallic character is thus preserved even at nonzero temperatures.

The behavior of Ni-rich and Mn-rich samples differs significantly. Mn atoms on Ni sublattice preserve the half-metallic character of the alloy, see Fig. 5.3 (a), while Ni atoms on the Mn sublattice give a nonzero DOS at the Fermi level (Fig. 5.3 (d) and later Fig. 5.4). This leads to an increase of the conductivity. Later

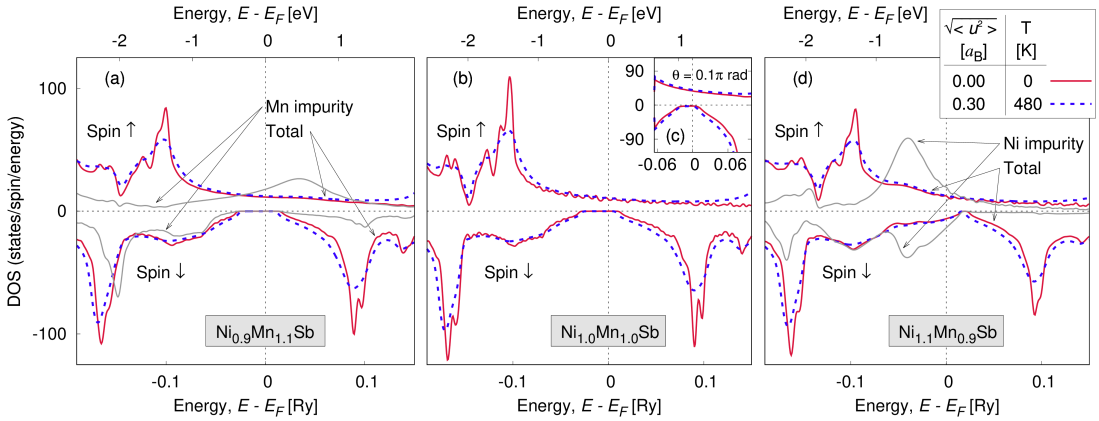

Figure 5.3: Temperature and alloying disorder dependence of the half-metallicity in NiMnSb. Atomic concentrations are used as weights of the local DOS and data for impurities (Mn and Ni). (a) The 10 % Mn-rich NiMnSb preserves the half-metallic character for all of the considered atomic displacements. Mn-impurity virtual bound state forms in the majority spin-channel. (b) Stoichiometric NiMnSb exhibits the half-metallic band-gap also at the room temperature. Inset (c) shows that magnetic disorder (tilted magnetic moments with $\theta = 0.1\pi$) has almost no influence on DOS, especially in the minority channel. (d) The 10 % Ni-rich NiMnSb is no longer half-metal and the states around E_F are almost independent on temperature.

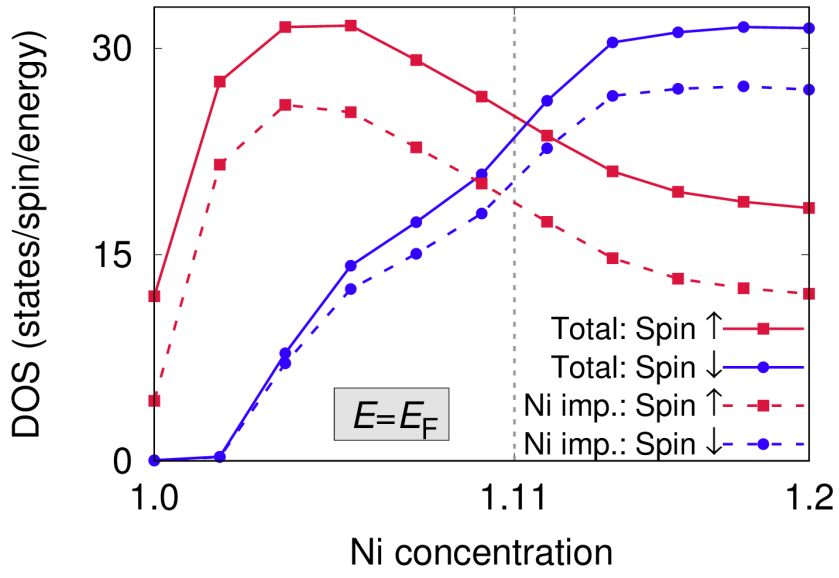

Figure 5.4: Total DOS at the Fermi level (solid lines) as well as the local DOS for Ni impurities (dashed lines) are increasing with higher substitution of Mn atoms by Ni. The spin-up states (red lines, squares) are dominant for less than 10 %, after 12 % the spin-down states (blue lines, circles) prevail. The total DOS (sum of the spin channels, not shown here) increases monotonically.

presented electrical transport calculations are in agreement with these changes. The inset (Fig. 5.3 (c)) shows a minor influence of the magnetic disorder (tilting of moments with $\theta = 0.1\pi$) on the DOS of stoichiometric NiMnSb at both zero and finite temperature ($T \approx 220$ K).

Fig. 5.4 presents the DOS at the Fermi level for the Ni-rich NiMnSb. The negligible DOS in the minority channel is preserved for small amount (up to 2 %) of Ni impurities. With increasing Ni concentration, the difference between spin-up and spin-down DOS is getting smaller. They become equal at approx. 11 % of impurities and the spin-down states are dominant after this value.

The electronic structure can be also visualized by using the spin-resolved Bloch spectral functions $\mathcal{A}^s(\mathbf{k}, E)$ [12], where $s \in \{\uparrow, \downarrow\}$ is the spin index, $\mathbf{k}$ is a reciprocal-space vector and E is the electron energy. For 6, 10, and 14 % of Ni-rich NiMnSb, we plot in Fig. 5.5 the Bloch spectral function for $E = E_F$ and in Fig. 5.6 the energy-dependent spin-resolved Bloch spectral function along the $L - \Gamma - X$ path in the reciprocal space.

We observe that at 10 % of Ni impurities in the Ni-rich system new minority-spin bands smeared due to disorder emerge at the Fermi surface (region marked by the violet circle in Fig.5.6 (b)), also visible for 14 % but absent for 6 %. These bands may be responsible for the AHC slope change, Fig. 5.11, where we observe smearing out of the spin-down band at the Γ point and emergence of more spectral weights at around the X point for the critical Ni disorder. See also Fig. 5.5 for $k_z = 0$ and total DOS at the Fermi level in Fig. 5.4.

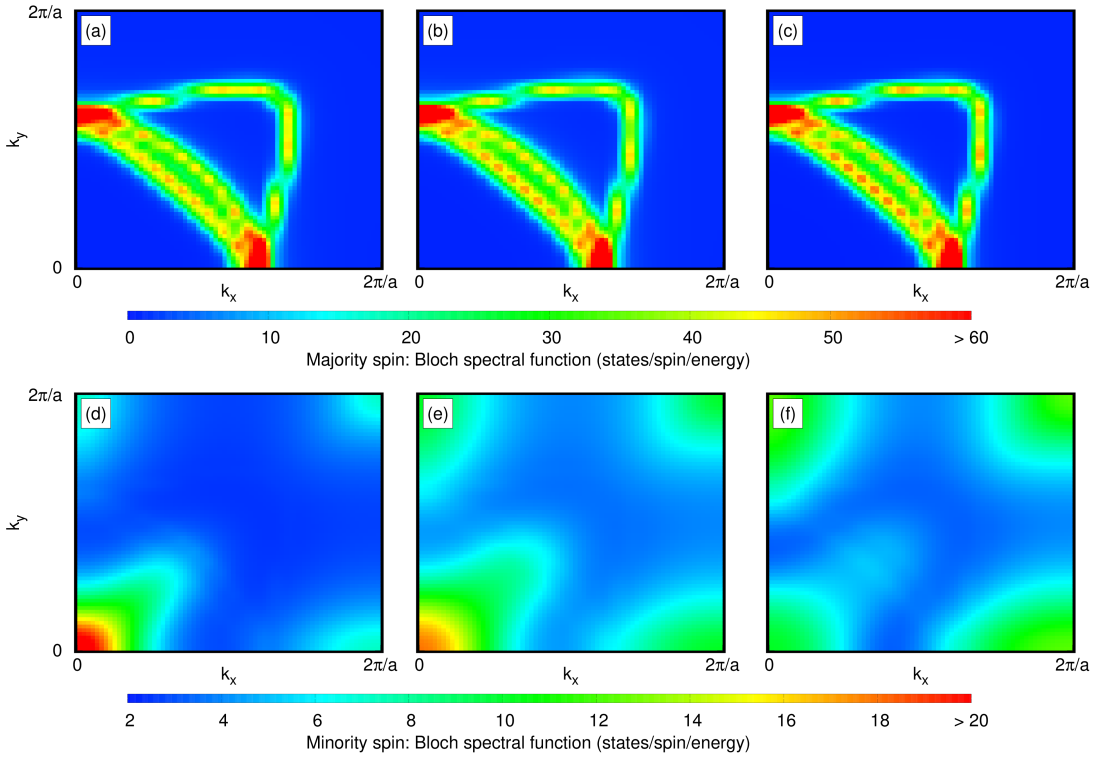

Figure 5.5: Bloch spectral functions displayed for the Fermi level and $k_z = 0$ for the majority spin (a), (b), and (c) and the minority one (d), (e), and (f); (a) and (d) for $Ni_{1.06}Mn_{0.94}Sb$, (b) and (e) for $Ni_{1.10}Mn_{0.90}Sb$, and (c) and (f) for $Ni_{1.14}Mn_{0.86}Sb$.

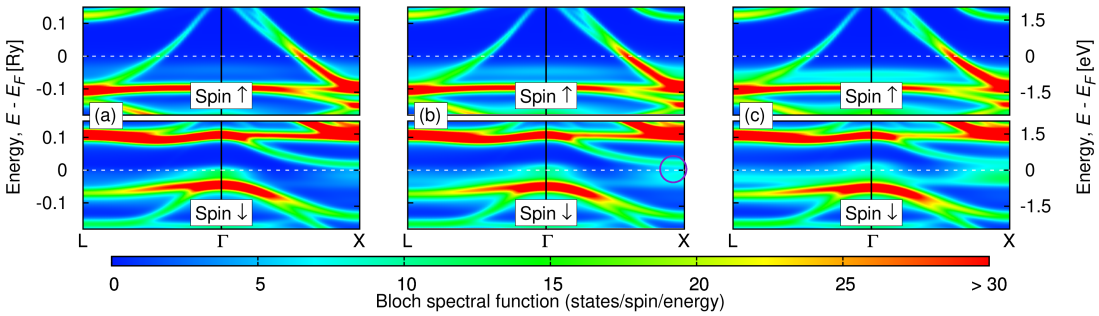

Figure 5.6: Bloch spectral functions of (a) $Ni_{1.06}Mn_{0.94}Sb$, (b) $Ni_{1.10}Mn_{0.90}Sb$, and (c) $Ni_{1.14}Mn_{0.86}Sb$ for spin-up (upper panels) and spin-down (lower panels) channels.

5.1.2 Temperature dependent resistivity and AHC

Chemical disorder and phonons NiMnSb has almost linear dependence of the resistivity on temperature (from 100 to 300 K), which indicates that phonons are the most important scattering mechanism [147]. Calculated temperature dependence of the resistivity and the anomalous Hall effect (resistivity ρ_{xy}) are shown in Fig. 5.7. The results are in agreement with experimental data; measured resistivities are taken from Refs. [26] and [161], and experimental ρ_{xy} was obtained by combining Refs. [147] and [161]. The quadratic (nonlinear) behavior of electrical resistivities as a function of temperature is important especially for low temperatures ($T \lesssim 100\,\mathrm{K}$) and experimental resistivities exhibit only a small deviation from the quadratic form [118]. The residual resistivity and the weak influence of magnons are in agreement with other studies [26, 41, 161]. It is consistent with the high Curie temperature, resulting in a weak influence of magnetic disorder and it also agrees with the DOS showing a negligible influence of the magnetic disorder on the number of carriers at the Fermi level (Fig. 5.3 (c)).

The comparison of calculated and measured ρ and ρ_{xy} indicates that the presence of the Mn-rich phase in real samples is unlikely because an increasing presence of additional Mn atoms dramatically increases both the resistivity and ρ_{xy} at the zero temperature and, moreover, slopes of these quantities as a function of temperature are much higher than the measured counterparts [146, 147], see Fig. 5.7. The calculated transport properties as a function of Ni impurity are non-monotonic, both the resistivity and ρ_{xy} have maxima around a 10 % Ni-rich sample. The measured residual resistivity could correspond to a presence of additional Ni atoms on the empty atomic sites (unoccupied positions of the half-Heusler structure); however, the calculated results contradict the experimental data that exhibit much steeper temperature dependence of both the resistivity and the ρ_{xy} for these defects.

Comparing our theoretical results with data from literature (especially Ref. [147] and [161]), the best mutual agreement is obtained for Ni-rich sample with 1 to 2 % of Mn atoms replaced by Ni; we note that the exact composition and chemical disorder in the experimental samples is unknown. In real samples, a wide range of different defects may occur, but a systematic investigation of the huge number of different combinations of such defects goes beyond the scope of this study.

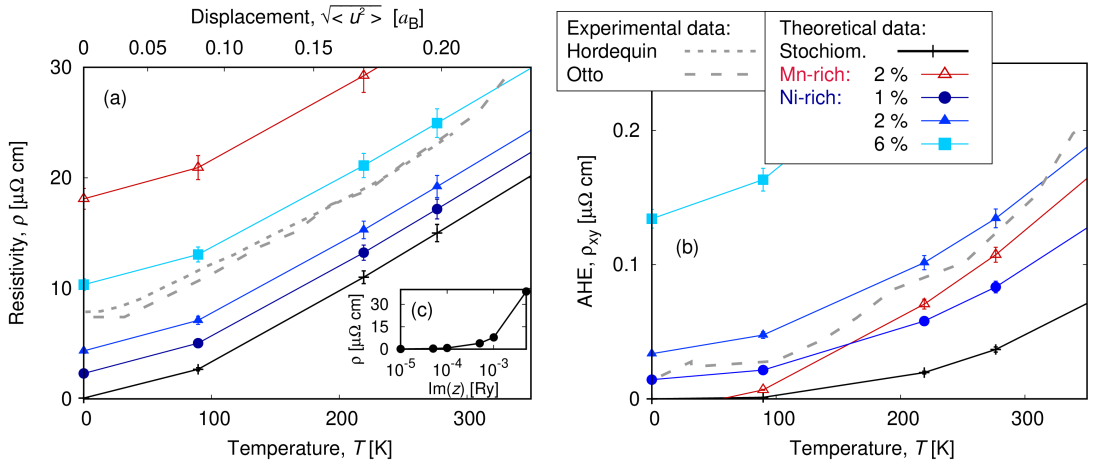

Figure 5.7: (a) The isotropic resistivity and (b) anomalous Hall effect (ρ_{xy}) of Ni- and Mn- rich NiMnSb monotonously increase with increasing temperature. Experimental results [26, 147, 161] agree with our theoretical data obtained for Ni-rich case with low concentration of impurities. (c) The model of FRT (stoichiometric NiMnSb) for an unknown disorder qualitatively agrees with calculated data at nonzero temperature.

Magnetic disorder up to room temperature In calculations including the magnetic disorder that corresponds to room temperature, transport properties differ less than by 1 % when only Mn moments are tilted or when moments of all atoms are tilted. It is caused by a dominant contribution to the total moment from Mn atoms. The influence of magnetic disorder on the electrical resistivity for the stoichiometric NiMnSb is negligible up to room temperature as can be seen in Tab. 5.1. The experimentally observed [118–120] decrease of saturation magnetization of 10 % for room temperature leads to $3.6\mu_B$ (the same decrease from the original value of $4.0\mu_B$). For theoretical magnetic disorder ($\theta = 0.14\pi$) which corresponds to the same change, we obtained electrical resistivity between $\rho = 17\ \mu\Omega\,\mathrm{cm}$ and $\rho = 25\ \mu\Omega\,\mathrm{cm}$ (see the caption of Tab. 5.1). It is in perfect agreement with experimental values of $\rho = 23\ \mu\Omega\,\mathrm{cm}$.

The small influence of magnetic disorder (predicted by both models) on electrical transport properties agrees with literature [161] and it is supported by negligible influence on the DOS at the Fermi level, see the inset in Fig. 5.3 for $\theta = 0.1\pi$ The calculated weak dependence of the resistivity on magnetic disorder justifies neglecting magnetic disorder in further discussion for $T \lesssim 300\,\mathrm{K}$. The uDLM model has the same dependence of the energy difference (of the disordered state from the undistorted one) on the total magnetization, but the resistivity increases faster than with the tilting model, see later Fig. 5.8.

Chemical impurities decrease the total magnetic moment similarly to the pure magnetic disorder. If the scattering properties are considered as a function of the alloy magnetization, results obtained by the different scattering mechanisms (magnetic disorder and chemical impurities) quantitatively agree with each other.

Magnetic disorder close to Curie temperature The combined influence of phonons and magnons on the resistivity is shown in Fig. 5.8 (a) and (b) for stoichiometric NiMnSb; the case without displacements ($T_{\mathrm{ph}} = 0$) described

Table 5.1: Pure NiMnSb: Isotropic resistivity (in $\mu\Omega\,\mathrm{cm}$, ten rows and three columns in the right bottom block of the Table) for different magnitudes of displacements ($\sqrt{\langle u^2\rangle}$) and tilting angles ($\theta$) are almost identical to the aligned moments ($\theta = 0$). Empty values in the Table were smaller than the numerical accuracy. The room temperature roughly corresponds to $\sqrt{\langle u^2\rangle} \approx 0.21\,a_\mathrm{B}$ for $\Theta_D = 300\,\mathrm{K}$ (between the two bold values) and the experimental decrease of saturation magnetization is up to 10 % (to $3.6\mu_B$) [118–120].

Tilting angle, θ	Total mag. moment	Displacement, $\sqrt{\langle u^2\rangle}$		
		0.00 a_B	0.20 a_B	0.25 a_B
0.00π	4.04 μ_B	-	15.0	23.4
0.01π	4.04 μ_B	-	15.0	23.4
0.04π	4.01 μ_B	-	15.0	23.5
0.07π	3.93 μ_B	0.20	15.2	23.6
0.10π	3.82 μ_B	0.47	15.6	24.0
0.14π	3.58 μ_B	1.38	**16.7**	**25.2**
0.20π	$3.16\mu_B$	6.47	22.4	31.8
0.30π	$2.25\mu_B$	42.5	59.3	68.3
0.40π	$1.17\mu_B$	120	133	140
0.50π	$0.00\mu_B$	173	180	184

within both the *spd*−basis and *spdf*−basis gives almost identical results. For both models, the low- and high-temperature limits are identical and the contribution of phonons is similar (at given magnetic temperature).

The Matthiessen's rule (total resistivity is the additive sum of the phonon and spin-disorder contributions; see Fig. 5.8 (c) for the tilting model) is violated, especially in the highly-disordered region. For the tilting model with $\theta = \pi/2$ and $\sqrt{\langle u^2\rangle} = 0.40\,a_\mathrm{B}$, $\rho_\mathrm{mag} = 173\,\mu\Omega\,\mathrm{cm}$, $\rho_\mathrm{ph} = 59\,\mu\Omega\,\mathrm{cm}$ (together $\rho_\mathrm{mag} + \rho_\mathrm{ph} = 232\,\mu\Omega\,\mathrm{cm}$), whereas combined effect gives $\rho_\mathrm{mag+ph} = 200\,\mu\Omega\,\mathrm{cm}$. Similar conclusions were obtained for the uDLM model.

The resistivity ρ as a function of μ_s (the orbital magnetization is approx. 1 % of the μ_s) shown in Fig. 5.8 (d) is useful for a comparison of both models of the magnetic disorder (similarly to Fig. 2.7 for the total energy E). Although $E(\mu_s)$ obtained by both models is practically the same, the resistivities differ appreciably. The difference in ρ is the highest for μ_s between $1.5\mu_B$ and $3.0\mu_B$, which is caused by the difference in $\mu_s(x_{\mathrm{Mn}^-})$ and $\mu_s(\theta)$ dependences, see inset of Fig. 2.7. Both models are similar for the undistorted system ($T \to 0$, i.e., $x_{\mathrm{Mn}^-} \to 0$ or $\theta \to 0$) and smaller moments ($T \to T_c$, i.e., $x_{\mathrm{Mn}^-} \to 0.5$ or $\theta \to \pi/2$). The obtained ρ values indicate that the spin-flip in the uDLM model represents a stronger scattering mechanism than the tilting of moments around their equilibrium direction.

In Tab. 5.2 we present comparison of experimental data [147] with both models of magnetic disorder. Each value (at the given temperature) is obtained by the proper combination of atomic displacements (Debye theory) and magnetic disorder. Except regions of low ($\mu_s \to 4\mu_B$) and high ($\mu_s \to 0$) disorder, the

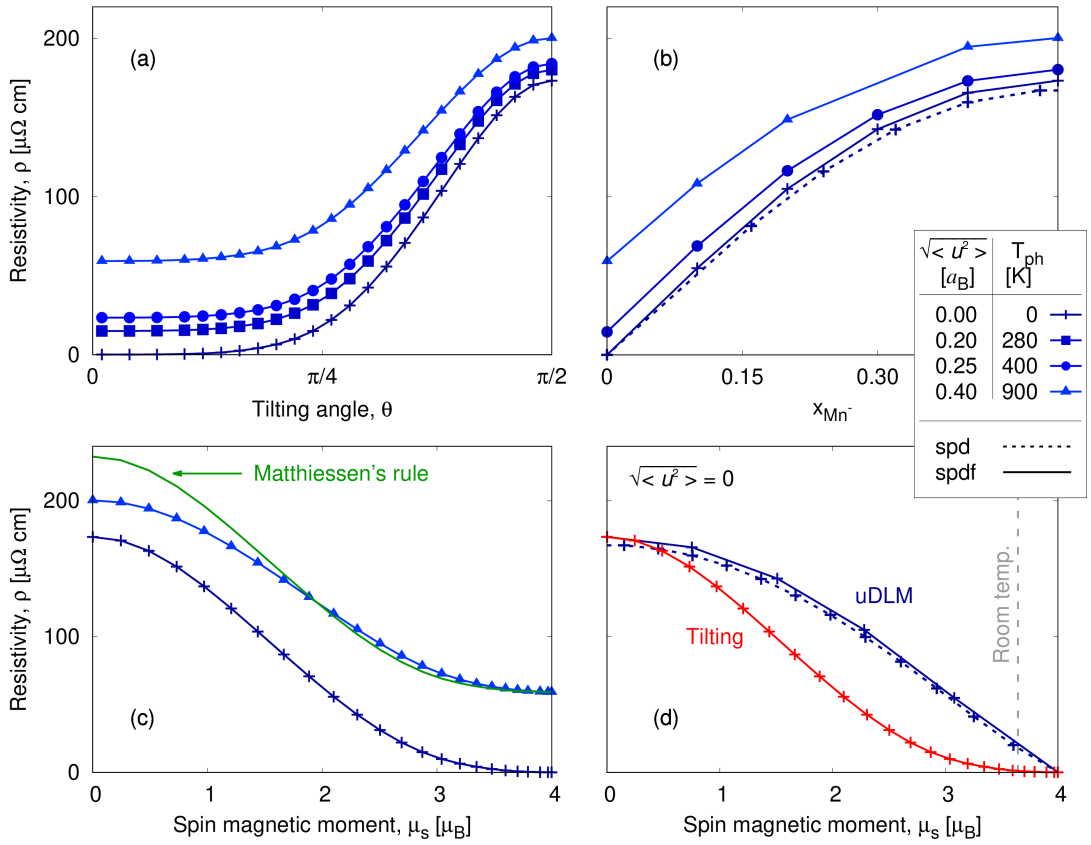

Figure 5.8: FM and PM resistivity is the same for the tilting (a) and uDLM (b) approach. The phononic contribution is also similar, but the resistivity as a function of parameters θ or x_{Mn^-} differs significantly. (c) The contributions to the resistivity due to pure spin-disorder (croses for $\sqrt{\langle u^2 \rangle} = 0\,a_{\mathrm{B}}$), and combined effect of spin-disorder and phonons (triangles for $\sqrt{\langle u^2 \rangle} = 0.40\,a_{\mathrm{B}}$) are shown. The sum of spin-disorder and phonon-contributions (Matthiessen's rule) is shown by the green line indicating its violation with increasing temperature (decreasing magnetic moment). The disagreement between both models in $\rho(\mu_s)$ is the largest between $1.5\mu_B$ and $3.0\mu_B$ (d). The temperature T_{ph} is obtained via the Debye theory assuming only phonons and the μ_s decreases due to the magnetic disorder.

uDLM model overestimates experimental data and the resistivities obtained by the tilting approximation. The overestimation is approx. 80 % at 500 K, while the tilting approach gives an error lower than 6 % up to 600 K.

The maximally disordered state corresponding to $T = T_C$ is parametrized by $\sqrt{\langle u^2 \rangle} = 0.38\,a_{\mathrm{B}}$ ($T_{\mathrm{ph}} = 730$ K) and $\theta = \pi/2$ or $x_{\mathrm{Mn}^-} = 0.5$ ($T_{\mathrm{mag}} = 730$ K). Both models result in the same resistivity for this state of 197 $\mu\Omega\,$cm, which is about 70 % larger than the measured value (116 $\mu\Omega\,$cm). We note that resistivity at the Curie point may be reduced by employing the LSDA+U scheme with nonzero Hubbard U for d-orbitals of Mn atoms, e.g., for $U = 0.10$ Ry and $U = 0.15$ Ry, the tilting model yields 117 $\mu\Omega\,$cm and 96 $\mu\Omega\,$cm, respectively. For $U \neq 0$, values of (nonzero) magnetic moments also slightly change (increase by five to ten percents) compared to $U = 0$ used in this work; therefore detailed investigation is beyond

Table 5.2: The tilting model gives better agreement with experimental data [147]. For each temperature, the appropriate magnitude of atomic displacements was assumed (Debye theory), as well as corresponding values of measured θ and x_{Mn^-} (parameters obtained by the fit of measured $M(T)$ dependence [118] are also shown).

	Exp. [147]	Tilting		uDLM	
T [K]	ρ [$\mu\Omega$ cm]	θ	ρ [$\mu\Omega$ cm]	x_{Mn^-}	ρ [$\mu\Omega$ cm]
500	48	0.22π	48	0.10	88
600	68	0.27π	72	0.17	91
695	97	0.36π	131	0.28	136

the scope of this study.

Qualitative description of the AMR by the FRT model The FRT model corresponds to the spin- and orbital independent scatterings, which is technically realized by adding a finite imaginary constant (Im z) to the Fermi energy in corresponding Green functions in the Kubo-Bastin equation. The FRT model assumes zero vertex corrections and does not allow to separate out the phonon and spin-disorder contributions to the conductivity tensor. For the total resistivity obtained by the FRT model, see Fig. 5.7 (c). The calculated negative AMR (given be Eq. (1.12)) sign for Hall bars oriented along the [110] directions within the FRT is consistent with previous estimates of AMR in NiMnSb [41], i.e., $\rho(\mathbf{m} \parallel \mathbf{j}) < \rho(\mathbf{m} \perp \mathbf{j})$, where ρ is the longitudinal resistivity and $\mathbf{j}$ the electric current. Remarkably the AMR value is well described within the FRT applied in combination of the 10% Ni-rich disorder. Our calculated value changes from $\left(\rho_{\mathbf{m}\parallel E[110]} - \rho_{\mathbf{m}\perp E[110]}\right) / \left(\rho_{\mathbf{m}\parallel E[110]} + \rho_{\mathbf{m}\perp E[110]}\right) = -1.6\%$ (for Im $z = 10^{-5}$ Ry corresponding to low temperatures) to -0.3 % (roughly to the room temperature residual resistivity values, Im $z = 3 \cdot 10^{-3}$ Ry), while the experiment shows AMR of -0.08 % [41]. The sign of the AMR is the same as in Mn-doped GaAs and opposite to the typical transition metal ferromagnets Ni, Co, and Fe.

5.1.3 Anomalous Hall effect mechanism

We calculated the $\sigma_{xy}^{(1)}$ and $\sigma_{xy}^{(2)}$ contributions to the anomalous Hall effect at zero temperature. In Fig. 5.9 we show the separation of the AHC into $\sigma_{xy}^{(1)}$ and $\sigma_{xy}^{(2)}$ contributions; for a detailed analysis of the contributions see later Fig. 5.10. We observe a strong dependence of the AHC magnitude on the type of disorder. In general, the AHC is much larger for the Ni-rich system ($\sigma_{xy} \sim 10^3$ S/cm) than for the Mn-rich NiMnSb ($\sigma_{xy} \sim 10^1$ S/cm). Both the Mn and Ni rich cases show the same positive sign of the AHC in agreement with experimental literature [26, 41, 161]; an exception of a small negative AHC is found for the 2 % Mn-rich material due to large negative vertex corrections. For concentrations of chemical impurities going to zero (dilute limit), the divergent behavior of the vertex part of the total AHC is observed for both the Mn-rich and Ni-rich cases. Similar behavior is obtained in binary transition-metal alloys due to the skew-scattering mechanism [164].

In Fig.5.10 we show the comparison between *spd*−basis and *spdf*−basis for

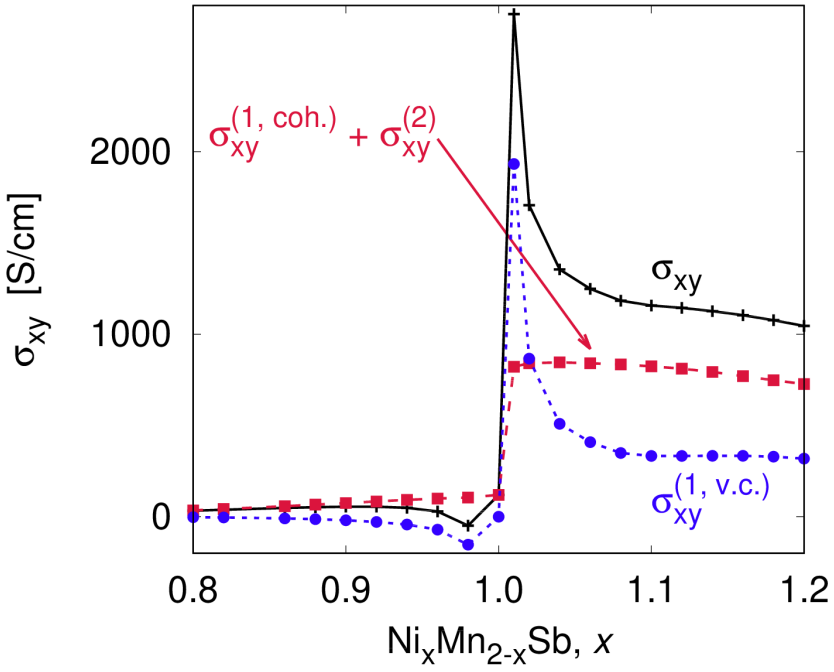

Figure 5.9: Negative sign of the calculated ($T = 0$) total AHC σ_{xy} (black solid line) was observed only for $Ni_{0.98}Mn_{1.02}Sb$, which is caused by a small contribution of the intrinsic term (red dashed line with squares) but dominant vertex corrections (blue dashed line with circles).

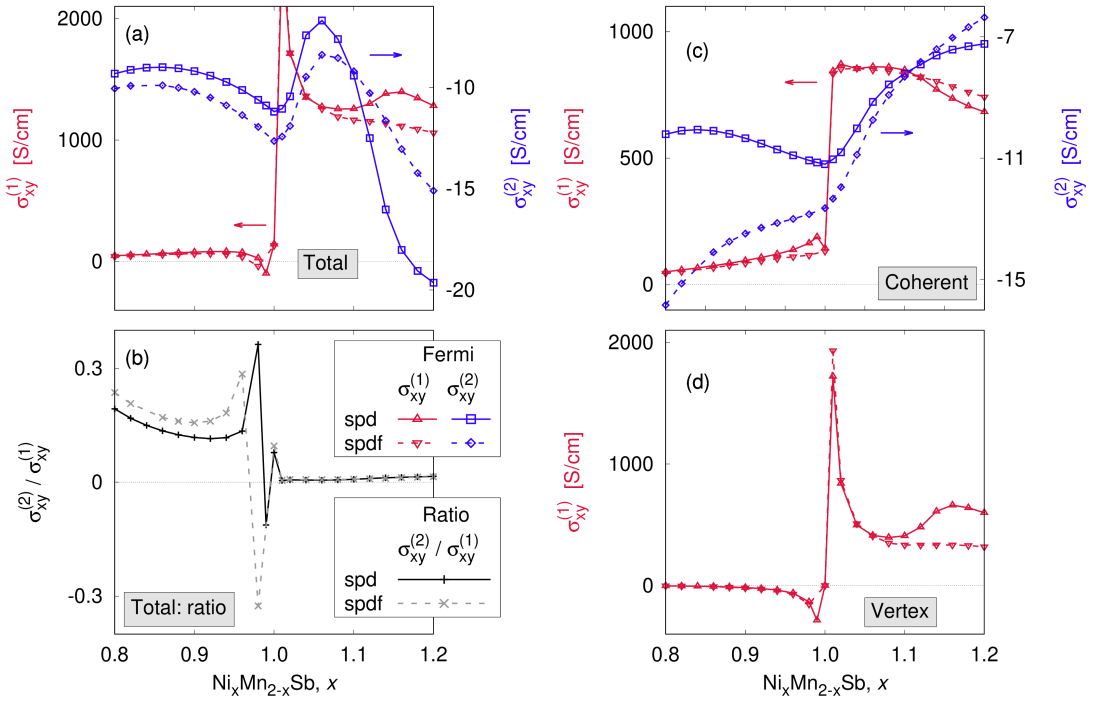

Figure 5.10: $\sigma_{xy}^{(1)}$ (left axes, red lines) and $\sigma_{xy}^{(2)}$ (right axes, blue lines) contribution to anomalous Hall effect in NiMnSb calculated in the formalism of the *spd*- (solid lines) and *spdf*-basis (dashed lines): (a) Total conductivity, (b) ratio between $\sigma_{xy}^{(2)}$ and surface terms, (c) coherent conductivity, (d) vertex conductivity.

T=0. The importance of $f-$orbitals for zero-temperature calculations increases with the larger chemical disorder. Moreover, it presents different mathematical contributions to the total AHC (Fig.5.10 (a)) with varying ratio between the Fermi-surface term and Fermi-sea term (Fig.5.10 (b)): the coherent and vertex parts (Fig.5.10 (c) and (d)). Discussion of the contributions obtained within the TB-LMTO approach is given in Sec. 1.3. The total value of the AHC (compare Fig. 5.9 and 5.10) is given by the sum of $\sigma_{xy}^{(1)}$ and $\sigma_{xy}^{(2)}$ terms. The major contribution comes from the former one which is about two orders of magnitude larger than $\sigma_{xy}^{(2)}$, see Fig. 5.10. This justifies omitting $\sigma_{xy}^{(2)}$ in the temperature-dependent calculations. While the concentration dependence of $\sigma_{xy}^{(1,\mathrm{coh})}$ consists of two linear parts (one in the Mn-rich region, the second one for the Ni-rich system), $\sigma_{xy}^{(1,\mathrm{v.c.})}$ diverges for small concentrations of impurities. The small magnitude of the Fermi sea term allows us to neglect the $\sigma^{(2)}$ term in the temperature study of the AHC by the alloy analogy model which substantially speed up our calculations.

In Fig. 5.11 (a), nonmonotonic behavior of the resistivity in the Ni-rich region is displayed and compared to increasing resistivity for increasing Mn impurities in the Mn-rich system; this trend is independent on temperature. In panels (b, d) we present the anomalous Hall versus longitudinal conductivity dependence for both the Mn-rich and Ni-rich calculations.

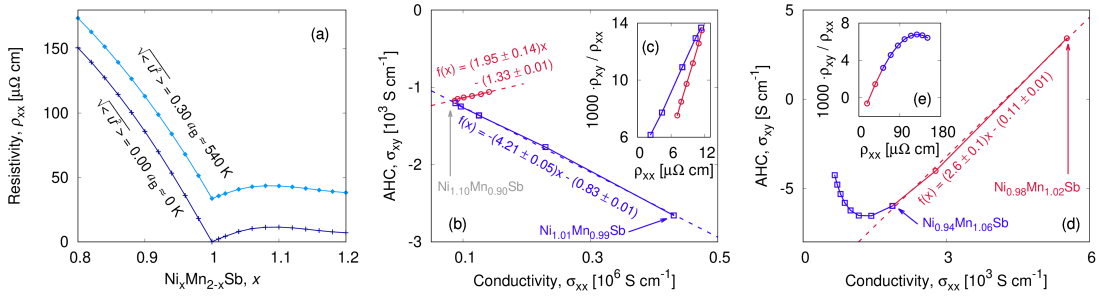

Figure 5.11: Total resistivity (a) for zero and finite (540 K) temperature is monotonic in the Mn-rich region, but it has a maximum in the Ni-rich case at 10 % and 8 % of Ni impurities for T = 0 and 540 K, respectively. Zero temperature AHC plotted as a function of the total conductivity has (b) two piecewise linear parts for the Ni-rich NiMnSb, one having a negative slope (fitted from 1, 2, 4, 6, 8, and 10 % of Ni) and the second with a positive slope (10, 12, 14, 16, 18, and 20 % of Ni). The parts are distinguishable when the resistivity for the same data is plotted (c). The same dependence in the Mn-rich region (d) exhibits a linear (2, 4, and 6 % of Mn impurities) and a nonmonotonic (8, 10, 12, 14, 16, 18, and 20 % of Mn) behavior; a ratio of resistivities (e) show a smooth transition between both parts.

A linear fit of the dependences is shown in Fig. 5.11 (b, d). In the insets (Fig. 5.11 (c,e)) we show also the experimentally relevant anomalous Hall angle ρ_{xy}/ρ_{xx} obtained by the full inversion of the conductivity tensors (instead of the usually used approximation $\rho_{xy} \sim \sigma_{xy}/\sigma_{xx}^2$). A part of the Ni-rich branch belongs to a rather high conductivity regime (10^5 S/cm) and follows linear dependence $\sigma_{xy} \sim \sigma_{xx}$ signaling the dominating extrinsic, skew-scattering mechanism of the AHC [37, 165]. In contrast, the behavior of Mn-rich system with higher conductivities is non-monotonic but different from a power dependence reported in literature

[37]. It is rather linear for larger conductivities (small Mn disorder below 6 %), where the AHC is influenced by the disorder [165], see Fig.5.11 (d).

Interestingly for Ni-rich branch around ∼10 %, the slope of the AHC as a function of σ_{xx} changes sign. It signals multiband character of the transport (Fig.5.11 (b)), see also Fig. 5.5 and its description. As long as the Friedel sum rule [37, 166] can be applied, the change of the AHC sign can be attributed to the change of the dominating spin channel at the concentration of ∼10 % Ni-rich (Fig. 5.4).

We note that the half-metal and multi-band character of the transport in NiMnSb can be responsible for notably different behavior than that generally reported in metals. For metals, only one slope exists (variations of disorder are typical on the level of a few percents) and it is difficult to achieve more than one conductivity regime [37, 165].

5.1.4 Spin-resolved electrical conductivity

To obtain maximal efficiency of the spin-polarized currents, their polarization P should approach unity and both the spin-flip part (of the coherent conductivity) and the vertex part (of the total conductivity) should be negligible. Ni-rich NiMnSb has ten or more times larger conductivity of the majority channel than similar concentration of the Mn-rich material and, unlike the minority channel, it strongly depends on temperature (especially Ni-rich), see Fig. 5.12.

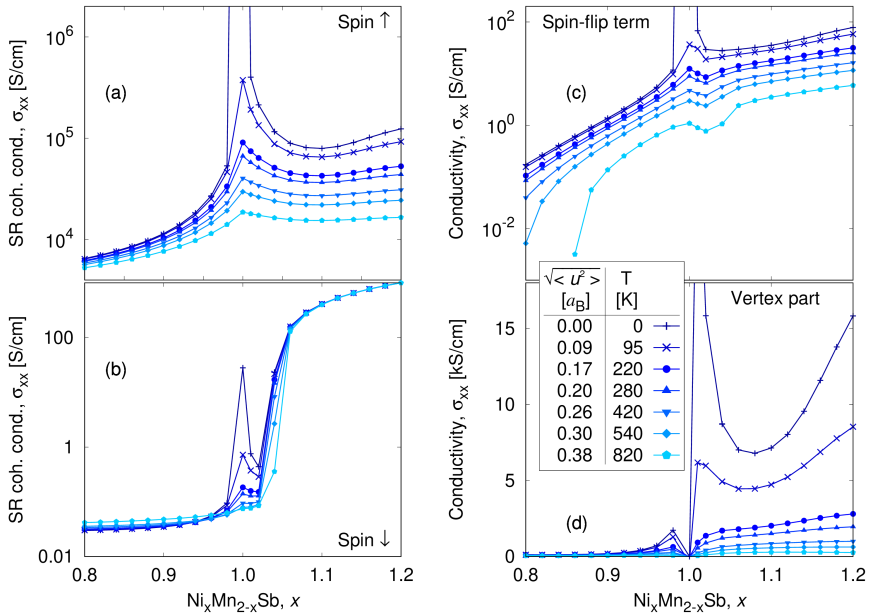

Figure 5.12: The spin-resolved in-plane (perpendicular to the magnetization) coherent conductivity for the majority channel (a) differs by several orders of magnitude for the Mn- and Ni-rich cases. On the other hand, the conductivity for the minority channel (b) is almost independent of the temperature, except of extreme displacements in the Mn-rich case. Both the spin-flip term (c) and vertex part of the conductivity (d) are larger for the Ni-rich system than in the Mn-rich region.

The spin-resolved conductivity is crucial for spintronic applications, but its

measurement is difficult. The total conductivity is the largest (infinitely high) for stoichiometric NiMnSb with resistivity going to zero. For most of the impurities and temperatures, the conductivity of the majority spin channel is at least two orders of magnitude larger than the vertex contribution and about four orders of magnitude larger than the spin-flip term (Fig. 5.12). The spin-flip term (Fig. 5.12 (c)) and the vertex contributions (Fig. 5.12 (d)) are at least three orders of magnitude smaller than the conductivity of the majority channel. These features justify the simple definition of the spin polarization of the current in terms of the coherent majority and minority conductivities in Eq. (2.54).

The Mn impurities do not destroy the half-metallic character of the system while the Ni impurities lead to nonzero density of minority carriers at the Fermi level (Fig. 5.3). It leads to the spin polarization that is almost unity for the Mn-rich case (for all temperatures) and in the Ni-rich region it decreases with increasing impurity concentration or increasing temperature, see Fig. 5.13. However, even at room temperature and in the Ni-rich case, $P > 0.9$, which ensures highly polarized electrical current. The influence of the spin-flip term and vertex contributions on the polarization P is small, see Fig. 5.12, which justifies employing Eq. (2.54). Influence of the spin-flip term and vertex contributions is obtained by comparing the P calculated by Eq. (2.51) and (2.54). The major difference is caused by the temperature-nonmonotonic behavior of the vertex part.

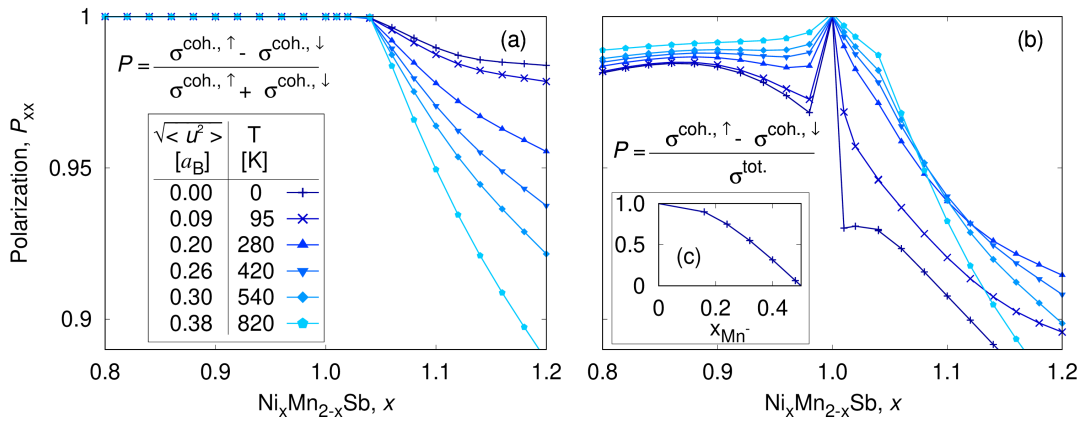

Figure 5.13: The polarization defined by Eq. (2.51) for the in-plane direction is almost unity for the Mn-rich NiMnSb (small total conductivity), see Fig. (a). The polarization calculated with the total conductivity (Eq. 2.54) is similar (Fig. (b)), which is caused by the small but temperature-dependent spin-flip and vertex terms.

For any magnitude of atomic displacements, other scattering mechanisms (uDLM, tilting of moments, chemical disorder) result in spin-up conductivities about five orders of magnitude higher than the spin-down conductivity in a region of small disorder, see Fig. 5.14 (a) and (b) for the stoichiometric NiMnSb described by the tilting model. The difference is getting smaller with decreasing total magnetic moment and it vanishes in the PM state ($\theta = \pi/2$ in the tilting model).

The uDLM model causes larger conductivity of the minority channel (larger DOS in the minority channel at the Fermi level) with increasing x_{Mn^-}. The mag-

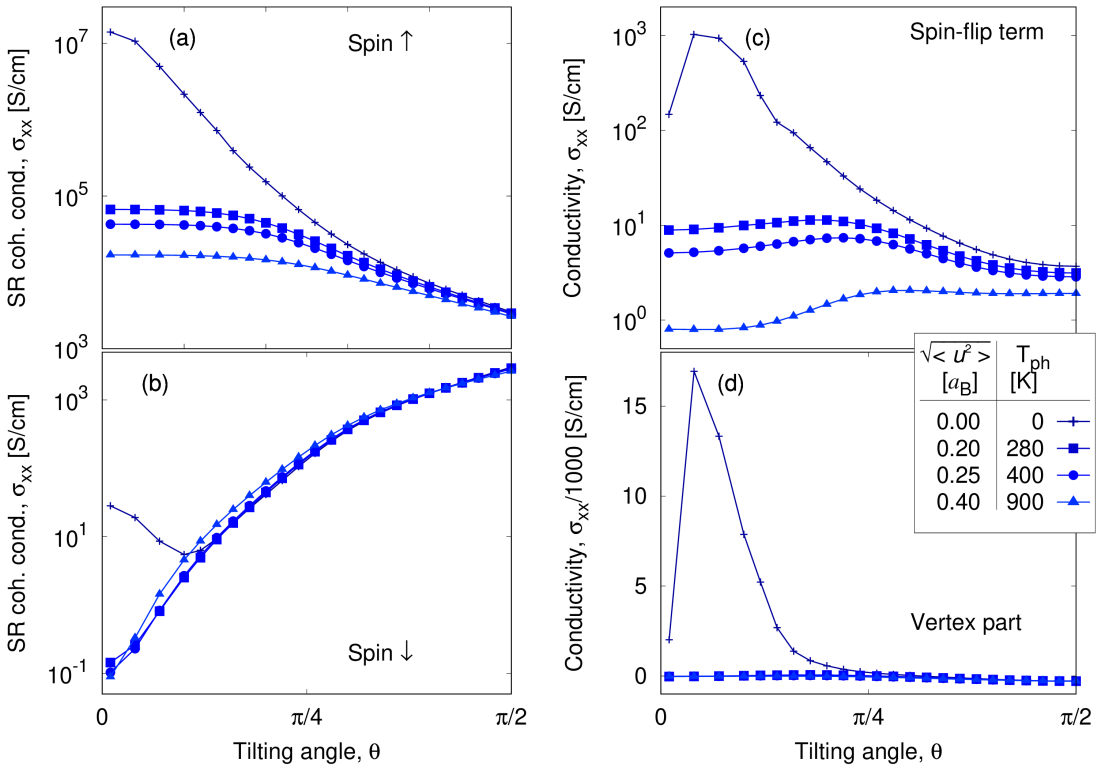

Figure 5.14: For $\theta \to 0$, electrical conductivity of the spin-up channel (a) is more than five orders of magnitude larger than that of the spin-down channel (b). No chemical impurities are assumed; therefore, the conductivity diverges without any disorder ($\theta = 0$, $\sqrt{\langle u^2 \rangle} = 0$). Both conductivities are the same for the PM state ($\theta = \pi/2$). The spin-flip term (c) and the vertex corrections (d) are of minor importance (as compared to the dominating spin-up conductivity).

netic disorder is dominant close to the Curie temperature, Fig. 5.15, where spin fluctuations lead to $P = 0$, which could not be achieved by phonons themselves. For room temperature ($x_{Mn[-]} < 0.04$), $P > 0.98$ and the decrease is even smaller for the model of tilted moments.

In the region with high polarization of the spin polarized current ($\theta < \pi/4$), see also Fig. 5.15, the spin-flip term and the vertex part of the total conductivity (Fig. 5.14 (c) and (d)) are smaller than the spin-up conductivity. Except of vertex corrections for $T_{\mathrm{ph}} = 0$, the difference is at least three orders of magnitude. The magnitude of vertex corrections is always the highest for small, but nonzero disorder and they are about ten times smaller for the uDLM approach compared to the tilting model.

Because of the half-metallic character of NiMnSb, the small spin-flip term, and negligible vertex corrections, the spin-polarization of the electric current is well defined; it is shown in Fig. 5.15. The value of P is almost unity for the perfect system (note that $P = 1$ holds exactly for half-metallic systems without spin-orbit interaction) and it is monotonously decreasing towards the Curie temperature ($P = 0$ for $\mu_s = 0$). We predict the polarization to be larger than 90 % for realistic combination of disorders at room temperature. None of the phenomena (magnons, phonons, chemical disorder) is dominant and all of them decrease the polarization by a few percents. The experimental values of $P \sim 50$ % [119, 148,

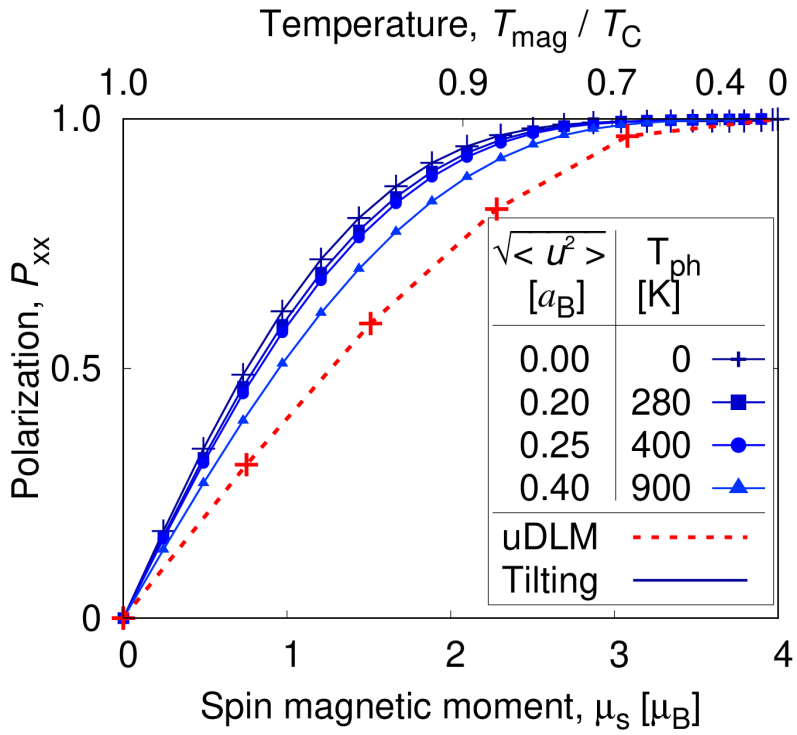

Figure 5.15: Both models give correct polarization for FM and PM ($P = 1$ and 0, respectively) NiMnSb without magnetic, but dependences $P(\mu_s)$ are different. The phonons taken into account for the tilting model have smaller influence on the polarization than the magnetic disorder.

152–155] could be explained by more complex combination of various types of disorder or, e.g., by strain in the samples.

We focused on systems similar to samples from literature (about 1 to 2 % Ni-rich), but experimental $P(T)$ was measured with a wide range of samples: 44 % for a free surface of a bulk material with $M_S = 3.6\mu_B$ [153], 45 % for a thin film with $M_S = 4.0\mu_B$ [148], 45 % for bulk NiMnSb with $M_S = 3.6\mu_B$ [119], 58 % for thin films [152], and from 20 to 50 % depending on temperature in polycrystalline samples [155]. Saturation magnetization $M_S < 4.0\mu_B$ indicated disordered samples, but the disorder is unknown, which makes it hard to reproduce. The discrepancy is not caused by the magnetic disorder [6]. It is dominant close to the Curie temperature, where spin fluctuations lead to $P = 0$; the zero polarization cannot be achieved by phonons themselves. For room temperature, the decrease of the polarization caused by the magnetic disorder is negligible, i.e., $P > 0.98$ for $\theta \approx 0.14\pi$.

We also investigated the polarization anisotropy. Similarly as the small AMR (difference between σ_{zz} and $\sigma_{xx} = \sigma_{yy}$ is around 0.25%), the polarization P_{zz} is almost the same as $P_{xx} = P_{yy}$. The polarization for Mn- and Ni-rich cases with impurities occupying the empty crystallographic position of the Heusler structure was also calculated. The Ni atoms on interstitial positions behave similarly to the Ni-rich system with Mn atoms substituted by Ni impurities; on the other hand, for the 20 % Mn-rich case with access Mn in the interstitial positions, $P(0\text{ K}) \approx 91$ % and $P(400\text{ K}) \approx 87$ %. This demonstrates a strong dependence of the polarization on the kind of chemical disorder.

5.2 CuMnAs

Tetragonal CuMnAs is an antiferromagnetic (AFM) material with the Néel temperature about $T_N = 480$ K [167]. It represents an interesting material not only because of AFM spintronic applications [47, 48, 57–59, 167] but also because of novel phenomena related to basic science. Moreover, unique bulk samples of tetragonal CuMnAs were prepared in our department, therefore, our *ab initio* calculations and experimental measurements of electrical transport were used to support each other [11].

AFM CuMnAs can be found with an orthorhombic and tetragonal structure. The former is more common for bulk samples, but the latter, usually existing only in thin layers, is more interesting for spintronic applications, e.g., because of demonstrated electrical switching [58]. For an overview of possible structures, see Ref. [19].

5.2.1 Formalism and computational details

This study is focused on tetragonal AFM CuMnAs, its orthorhombic phase is neglected. Both geometry and lattice constants corresponding to previous literature (structure "II" in Ref. [114]) are used for all compositions and temperatures: lattice parameters of bulk P4/nmm CuMnAs are $a = b = 3.82$ Å and $c = 6.318$ Å. See also Fig. 5.16 with shown AFM magnetic moments of Mn atoms. We note that there is a huge discrepancy in reported compositions and lattice parameters for the bulk CuMnAs [19]. For additional information regarding thin films, bulk systems, and applications related to the structure of CuMnAs, we refer to [47, 58] and [167].

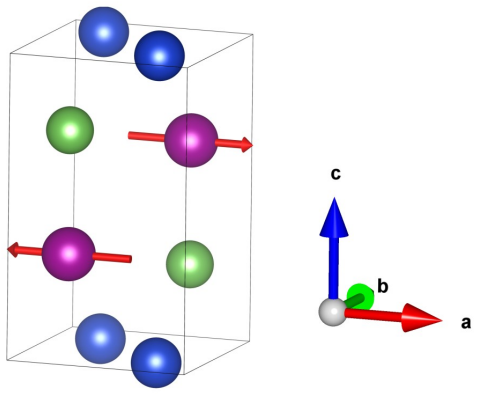

Figure 5.16: AFM P4/nmm structure of CuMnAs: Cu, Mn, and As atoms are shown by blue, violet, and green color, respectively. The opposite in-plane AFM moments on Mn atoms are denoted by red arrows. Created with [149].

To determine the most appropriate structure, we theoretically examined tetragonal CuMnAs with different lattice parameters. Most of the results depend only slightly on reasonable small (a few percents) changes of the lattice parameters [19]; therefore, they are omitted in the future sections. Because of the TB-LMTO method, we have also tried to formally (mathematically) place LMTO empty spheres in empty crystallographic positions. Specifically, two spheres were

assumed with coordinates $[0, 0, 0.5]$ and $[0.5, 0.5, 0.5]$ with respect to the atomic unit shown in Fig. 5.16. The influence of the spheres was neglected in results presented in this thesis.

Electronic structure and electrical transport properties may by influenced strongly by chemical composition; therefore, non-stoichiometric CuMnAs with impurities should be investigated. For simplicity, impurities ("imp") occupying "host" sublattices are later denoted as $\mathrm{imp}_{\mathrm{host}}$. In this notation, "vac" stands for vacancies, i.e., empty TB-LMTO spheres with radii identical to original atoms. Based on experimental data [19] and formation energies [114], we focused especially on Cu-rich samples (As sublattices unchanged) with $\mathrm{Cu}_{\mathrm{Mn}}$. Magnetic impurities of Mn atoms on Cu and As sublattices ($\mathrm{Mn}_{\mathrm{Cu}}$ and $\mathrm{Mn}_{\mathrm{As}}$, respectively) were assumed to be in the DLM state. Concentrations of impurities are stated per formula unit.

A mesh of at least $8 \cdot 10^6$ $k-$points was used for transport calculations, which is sufficient because of the complexity of the system; increasing it to thirteen millions, obtained corrections are smaller than one percent of the resistivity.

Atomic displacements ($\sqrt{\langle u^2 \rangle}$, later shown in the Bohr radius a_{B}), were connected to temperature by the Debye theory with zero-temperature fluctuations omitted similarly to [2, 4, 29]. Because of absence of experimental data for the Debye temperature Θ_D for tetragonal CuMnAs, we used $\Theta_D = 274$ K measured for an orthorhombic sample [168].

5.2.2 Electronic structure

The electronic structure of tetragonal AFM CuMnAs was unclear for a long time, but the GGA+U calculations of the bandstructure with the Hubbard 1.7 eV seem to correspond to data from ellipsometry [169]. In Fig. 5.17, we present bandstructures (left panels) and total DOS (right panels) to compare calculations employing the *spd*−basis (top Figures) with the *spdf*−data (three bottom rows). All of the results agree qualitatively with literature [169, 170].

In the bandstructure, the most important differences can be found around the X, Γ, and M points in bands close to the Fermi energy E_F. Similar behavior is found for the *spdf*−basis and for the *spd*−case (not shown here in details). At the X-point, a conduction band lies on the Fermi level for 0.10 Ry, while it is above and bellow this energy for 0.15 Ry and 0.00 Ry, respectively. Bands at the Γ−point bellow the Fermi level ($E \approx E_F - 0.05$ Ry) exhibit different splitting for 0.00 Ry and $U \neq 0.00$ Ry but the examined parameters almost unchange these bands closer to the Fermi level. The bottom of the conduction band at the M-point is above the Fermi level for 0.00 Ry and it moves bellow this energy for the increasing U.

Comparing electronic structures obtained by the two different bases, the largest difference is at the M-point, i.e., the bottom of the conduction band is much closer to $E = E_F$ for the *spd*−calculations than for the *spdf*−ones. This characteristic may be responsible for the Fermi level being much closer to the increased DOS above this energy for the smaller basis, compare Fig. 5.17 (e) vs. Fig. 5.17 (h). The Fermi level is located in a (nonzero) minimum of the total DOS. With increasing U, the minimum gets closer to zero value of DOS and the energy range (with small value of the total DOS) is broadened, see Fig. 5.17 (f)–(h).

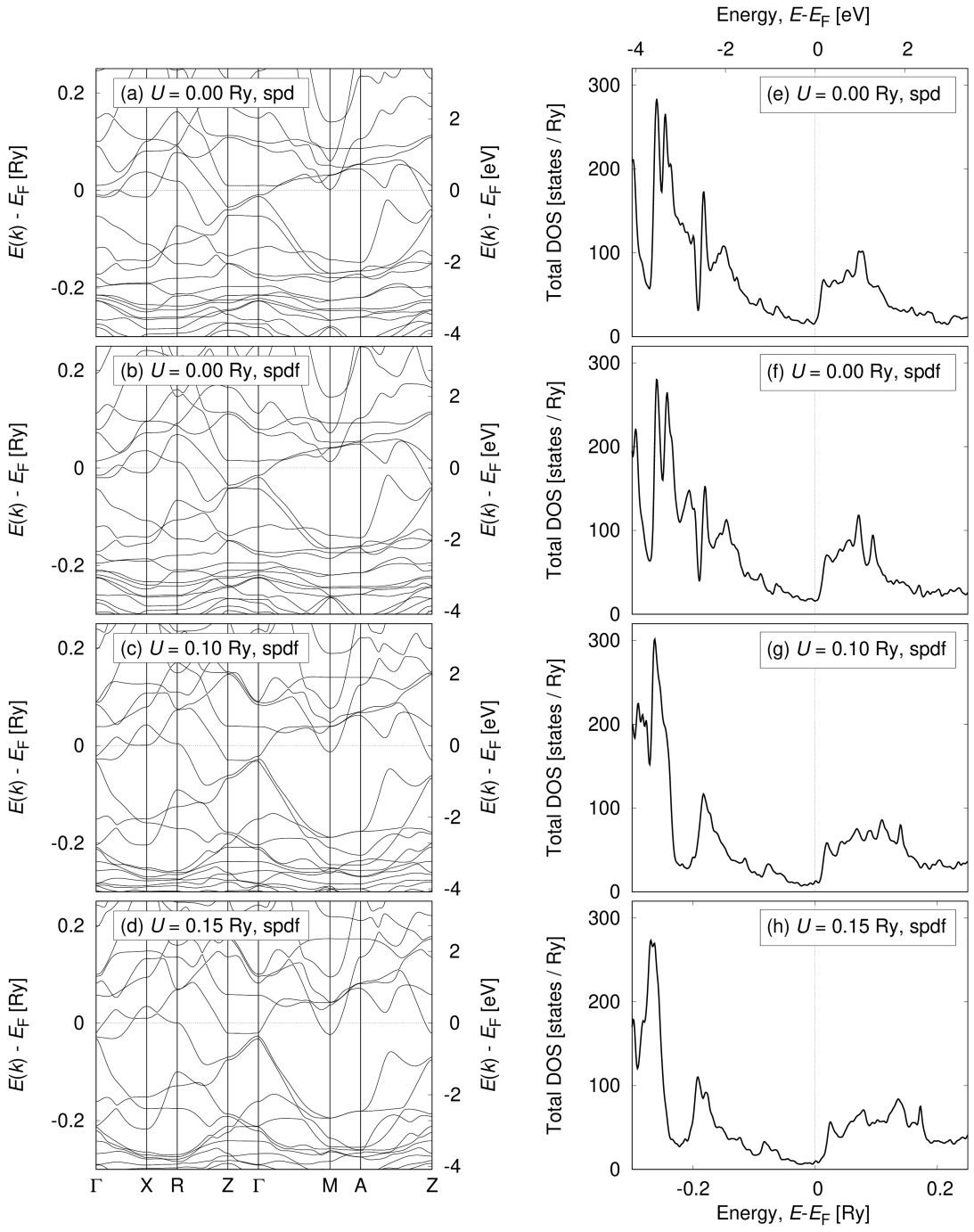

Figure 5.17: Bandstructures (a)–(d) and total DOS (e)–(h) of CuMnAs depend on the employed basis, see Figs. (a) and (e) for the *spd*−basis and the rest for the *spdf*−one. States around the Fermi level are also influenced by the Hubbard U: Figs. (a), (b), (e), and (f) are obtained for 0.00 Ry; (c) and (g) for 0.10 Ry; and (d) and (h) for 0.15 Ry.

To understand the ground-state electronic structure of CuMnAs and to get its proper description within our TB-LMTO method, many calculations with different parameters were performed. Results presented here are for conditions which have the best agreement with literature [19, 169, 170]. However, the electronic structure does not lead to precise determination of these parameters, e.g., the Hubbard parameter for a real system may range from 0.00 Ry to $U \approx 0.20$ Ry.

Table 5.3: Mn local spin magnetic moment (in μ_B) of a single atom in the AFM state depends much more on employed U than on concentration of Cu_{Mn} impurities. Both AFM (opposite) Mn atoms have the same magnitude of the moments.

	Cu_{Mn} concentration			
U [Ry]	0 %	2 %	5 %	10 %
0.00	3.71	3.71	3.72	3.73
0.10	4.08	4.08	4.07	4.07
0.15	4.20	4.20	4.20	4.19
0.20	4.30	4.30	4.30	4.29

For the realistic parameters, i.e., for $U \leq 0.20$ Ry, Wigner-Seitz radius of $r_{ws} = 2.9144\, a_B$ (1.542 Å), and a chemical disorder observed in experiments ($Cu_{Mn} \lesssim 10$ %), we examined DOS (not shown here) and local spin magnetic moments (see Tab. 5.3). Although all local moments in the AFM state compensate each other, the local magnetic moments of Mn atoms are large. They depend much more on the Hubbard U (almost linearly) than on the concentration of impurities. Induced moments on other atoms are about hundred times smaller, as well as Mn orbital moments.

5.2.3 Canting of magnetic moments

To describe CuMnAs with noncollinear magnetic moments, the local magnetic moments of Mn atoms (in the $a - b$ crystallographic plane, see Fig. 5.16) were rotated towards each other, while still being in the same plane. For verification of our method, not only the Mn moments were canted but we also investigated systems where all of the moments were canted (including induced moments). These two approaches lead to almost identical results for both the electronic structure and resistivities.

We use a nomenclature of "the canting angle" even for large deviations of the magnetic moments from their original directions. In AFM materials, the canting usually describes a small deviation of the moments caused by an antisymmetric form of exchange coupling and resulting canting angles of about 1° [171]; see Ref. [172] for canted AFM moments in half-Heusler CuMnSb with observed angles of 11°. Here we consider canting of moments due to an external magnetic field which is described, e.g., in [47] and see the same reference for an illustration of the canting caused by the local spin-transfer torque.

The canting angle of $\phi = 0$ corresponds to the AFM state and for $\phi \neq 0$, all of the magnetic moments were canted towards the same direction. For example, if two opposite AFM moments are along $-a$ and $+a$ direction, then the increasing

ϕ rotates both moments towards the $+b$ direction. The angle of $\phi = \pi/2$ results in FM CuMnAs.

Complementary to Tab. 5.3, in Fig. 5.18, we present values of local magnetic moments of a single Mn atom for disordered (Fig. 5.18 (a)) and stoichiometric (Fig. 5.18 (c)) CuMnAs for different orientations of Mn moments in the $a - b$ plane. Panel (a) shows the Mn local magnetic moments, while (c) contains a

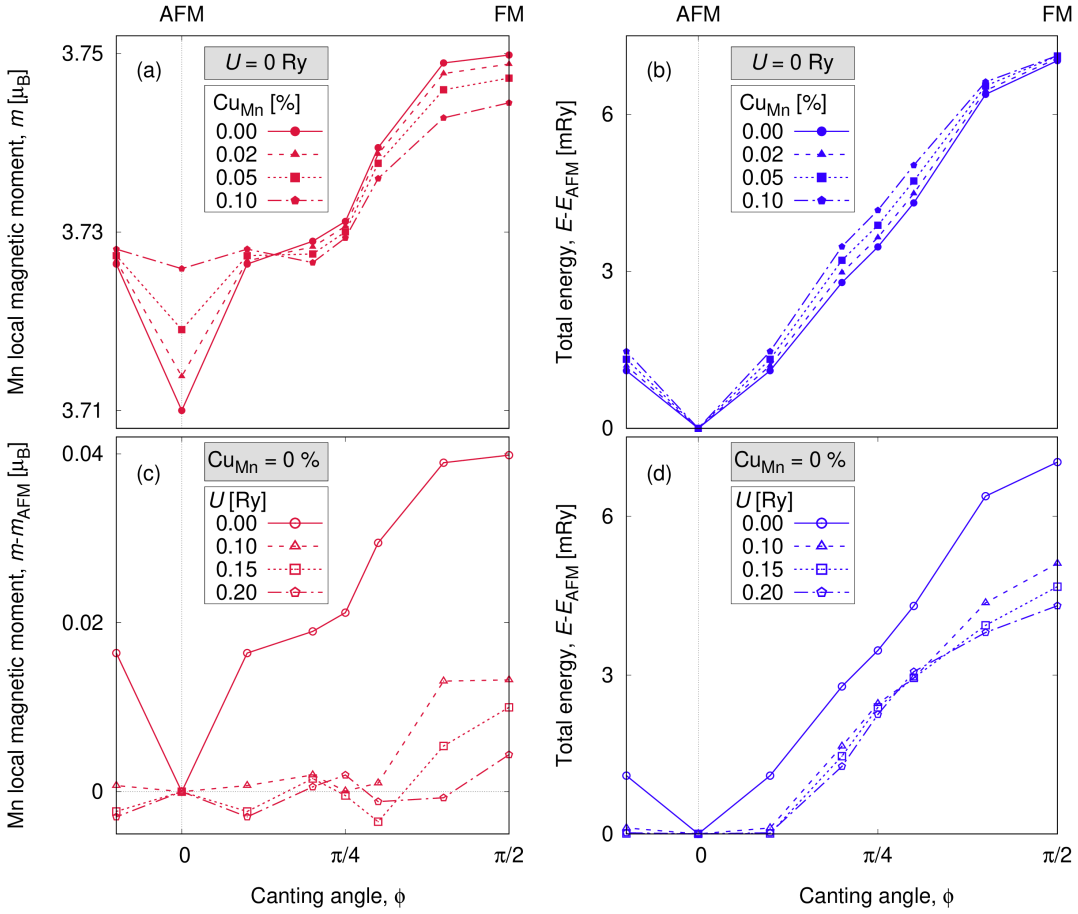

Figure 5.18: For 0.00 Ry ((a) and (b), full symbols) and stoichiometric CuMnAs without impurities ((c) and (d), empty symbols), the local spin Mn magnetic moments ((a) and (c), red lines) and energy difference per formula unit from the AFM state ((b) and (d), blue lines) are symmetric with respect to the AFM state ($\phi = 0$) and except of the moments for $U > 0$ Ry, the dependencies have a sine-like shape.

change of the moment from the corresponding AFM state (shown in Tab. 5.3). Fig. 5.18 also shows an energy difference of the given state (with canted moments) from the AFM one. For each concentration of the Cu_{Mn} impurity (Fig. 5.18 (b)) and Hubbard U (Fig. 5.18 (d)), the differences are calculated from the corresponding AFM state. All data are expressed per formula unit, calculated with the *spd*−basis and obtained by the full Dirac apporach. The following conclusions can be made: (i) Both the magnetic moment and energy difference have the sine-like dependence on the canting angle ($m \sim \sin\phi$ and $E \sim \sin\phi$) and they have a minimum for $\phi = 0$. This dependence of the moments is less obvious for nonzero U. (ii) The AFM state is preferred for each of the impurities and

values of U. (iii) The influence of various U is more important than canting of the angles. For example, energies per formula unit for the AFM ground states with 0.00 Ry and 0.10 Ry differ by approx. 100 mRy. (iv) The behavior is symmetrical for opposite angles of tilting ($-\phi$ and $+\phi$).

Both the magnetic moments and energy differences are almost independent on the employed basis (the *spd*−basis vs. *spdf*−one) or for the systems with empty LMTO spheres placed on interstitial positions. For the scalar relativistic approach, the energy difference is about two times smaller than for the fully relativistic one.

Motivated by possible experimental data, we investigated also a possibility of the moments to be canted by an external magnetic field. For this purpose, we roughly compared energy of the magnetic field with the energy difference for CuMnAs with canted moments. Experimentally accessible fields of approx. 10 T could be able to cant the moments by $\phi \lesssim 0.3\pi$. This value is important for the future analysis of changes in resistivities.

5.2.4 Residual resistivities

The *spdf*−basis is used for later presented temperature-dependent calculations and the full Dirac approach is necessary for proper inclusion of magnetism. Therefore, we calculated residual resistivities for defects presented in Ref. [114] to compare these approaches with the scalar-relativistic formalism employed in that study. Both the *spdf*−basis and fully-relativistic method increase resistivities for most of the impurities with respect to *spd*−basis and scalar relativistic approach. The increase is large especially for disorder with As atoms (impurities with large formation energies), see Tab. 5.4 for details.

Table 5.4: While the fully-relativistic results with the *spd*-basis represent small corrections (approx. 10 %) to the scalar-relativistic resistivities, employing the *spdf*-basis influences ρ_{zz} even by 45 % (As_{Mn}). Formation energies and scalar-relativistic ρ_{xx} are stated in [114]; resistivities (in $\mu\Omega\,$cm) were calculated for 5 % of impurities. 0.00 Ry was used for all of the calculations. The last row (Cu↔Mn) shows data for a swap of 5 % Cu and Mn atoms.

	Formation	Scalar-rel., *spd*		Fully-rel., *spd*		Fully-rel., *spdf*	
Defect	energy [eV]	ρ_{xx}	ρ_{zz}	ρ_{xx}	ρ_{zz}	ρ_{xx}	ρ_{zz}
Vac_{Mn}	−0.16	36	155	32	154	31	184
Vac_{Cu}	−0.14	12	44	12	54	16	79
Mn_{Cu}	−0.03	111	171	115	203	112	263
Cu_{Mn}	0.34	24	122	22	130	23	131
Cu_{As}	1.15	107	273	109	377	121	481
As_{Cu}	1.73	94	219	98	257	114	359
As_{Mn}	1.79	113	262	124	240	141	476
Mn_{As}	1.92	122	151	130	270	147	423
Vac_{As}	2.18	174	203	182	246	210	306
Cu↔Mn	-	124	267	123	304	120	393

The variance of results obtained by different approaches is related to the complexity of CuMnAs. Especially differences between the calculations with two

different bases should be considered as systematic uncertainties of our methods. Although the differences are even about 30 %, trends are preserved.

If it were possible to cant or rotate local magnetic moments by external magnetic field, it should be also possible to observe a change of electrical transport properties. In Sec. 5.2.3, we discussed local magnetic moments and energy differences from the AFM state for CuMnAs with canted local magnetic moments. Based on an estimation of the magnetic field and its strength, the experimentally achievable canting angle is between $\phi = 0.1\pi$ and $\phi = 0.3\pi$; therefore, the FM state cannot be obtained.

In Fig. 5.19 (fully relativistic, *spd*−basis), we show residual resistivities for CuMnAs with canted magnetic moments and Cu_{Mn} impurities. The FM state, although it is not energetically preferred, has the lowest resistivities. The non-monotonic behavior and maxima around $\phi \approx 0.25\pi$ correspond to angles, where non-monotonic behavior of the magnetic moments is observed, see Sec. 5.2.3. The in-plane resistivities ρ_{xx} (Fig. 5.19 (a)) are about five times smaller than the resistivities along the fourfold axis ρ_{zz} (Fig. 5.19(b)) and this anisotropy is similar for the different impurities.

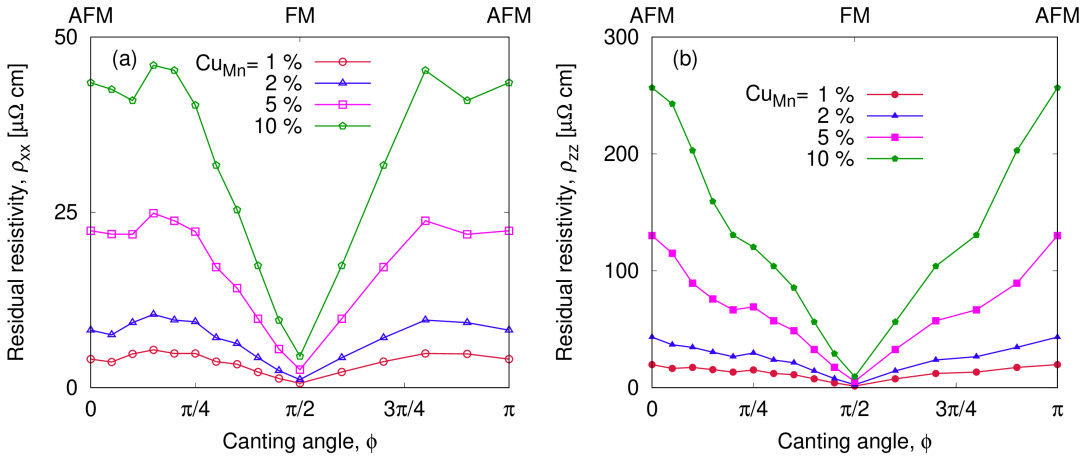

Figure 5.19: Mn magnetic moments of CuMnAs were canted in the $a-b$ plane (of the crystal structure) from the antiparallel (AFM) direction towards each other, so that the canting angle of $\phi = \pi/2$ corresponds to the parallel (FM) state and $\phi = \pi$ is again the AFM state. Residual resistivities (a) $\rho_{xx} = \rho_{yy}$ and (b) ρ_{zz} are shown for 1, 2, 5, and 10 % of Cu_{Mn} by circles, triangles, squares, and pentagons, respectively.

To verify a symmetrical behavior of resistivities with respect to the rotated moments, we plot the residual resistivity of a (hypothetical) FM system in Fig. 5.20 (fully relativistic, *spd*−basis). The magnetic moments were placed into parallel directions and together rotated by the angle ϕ in the $a-b$ crystallographic plane. For CuMnAs with 5 % of Cu_{Mn}, changes in both in-plane and out-of-plane resistivities are negligible. The data are symmetrical with respect to $\phi = 0$ and $\phi = \pi/4$.

The analysis with the canted magnetic moments was verified for CuMnAs without chemical disorder but within the finite relaxation time model. Results similar to Fig. 5.19 were obtained for six different values of the imaginary part of the self-energy (increased by up to 10^{-3} Ry). Zero-temperature results pre-

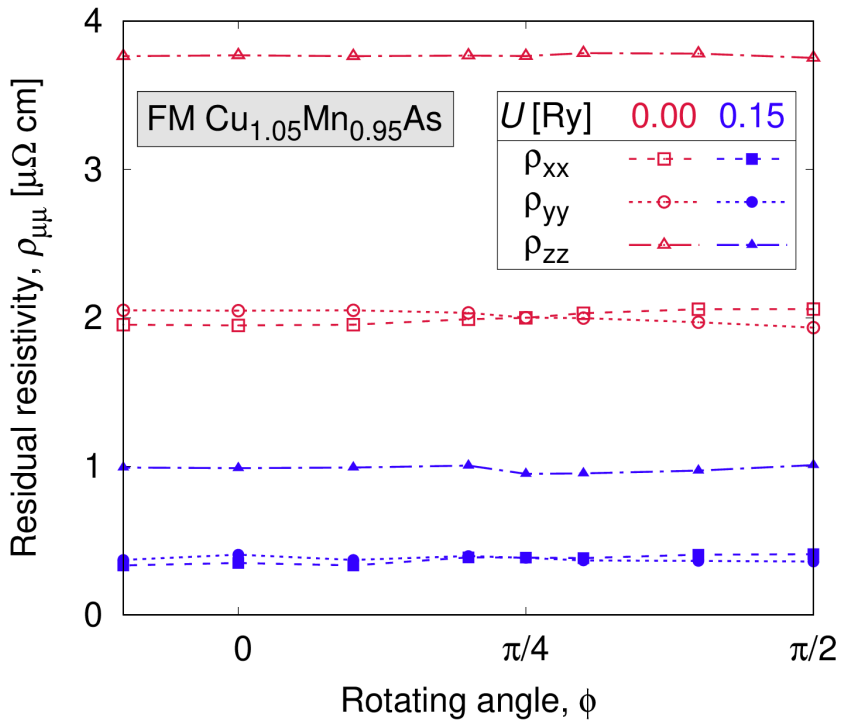

Figure 5.20: CuMnAs with 5 % of Cu_{Mn} was assumed to be in the FM state (Mn moments parallel) and all of them were rotated in the $a-b$ plane (of the crystal structure), so that $\phi = \pi/2$ corresponds to the perpendicular direction with respect to the original one. Residual resistivities ρ_{xx}, ρ_{yy}, and ρ_{zz} are denoted by the dashed, dotted and dash-dotted lines, respectively. 0.00 Ry is shown by red lines with empty symbols, 0.15 Ry by blue lines with full symbols.

sented above for the canted and rotated magnetic moments were obtained with the *spd*−basis. The same examination of the residual resistivities was performed also with the *spdf*−basis and obtained values are almost the same. Moreover, the *spdf*−basis and atomic displacements let to a dependence of the (finite-temperature) resistivities on the canting angle comparably to Fig. 5.19. This leads to the conclusion, that different scattering mechanisms (impurities, phonons, and FRT model) behave equivalently.

5.2.5 Finite-temperature resistivities

Finite temperatures influence material behavior and spintronic devices operating at real-life conditions; therefore, they should be taken into account during investigations of relevant materials. Moreover, understanding temperature-dependent phenomena and contributions of different effects may be crucial from a point of view of basic science. In this Section, electrical transport in CuMnS influenced by finite temperatures is discussed.

Atomic displacements and chemical impurities Calculated finite-temperature longitudinal resistivities for AFM CuMnAs with 5 %, 10 %, and 15 % of Cu_{Mn} are shown in Fig. 5.21 and both vac_{Mn} and vac_{Cu} are shown in Fig. 5.22. The uncertainty in the Debye temperature and a presence of atoms with different

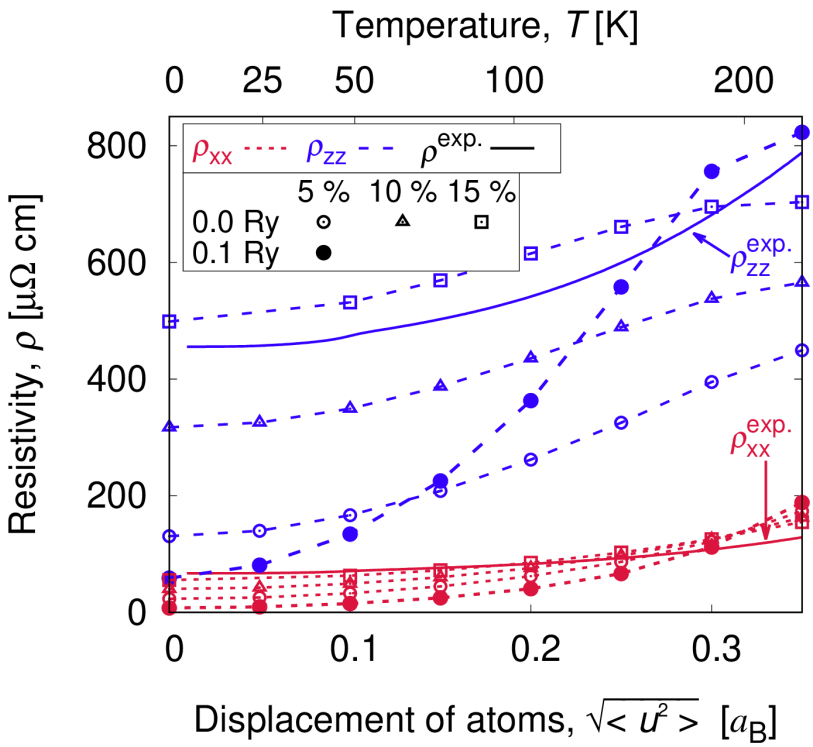

Figure 5.21: Calculated resistivities in the in-plane (red dotted lines) and $z-$direction (blue dashed lines) with 0.00 Ry (empty symbols) for 5 % (circles), 10 % (triangles) and 15 % (squares) Cu_{Mn} are compared with experimental data [11] (full lines). The slope of $\rho(T)$ agrees with measurements, which does not hold for 0.1 Ry (full circles for 5 % of Cu_{Mn}).

masses lead to a conversion between temperatures and atomic displacements that is not reliable; therefore, a dependence on $\sqrt{\langle u^2 \rangle}$ is primarily used for theoretical data.

Without the Hubbard U, a temperature dependence of resistivity (Fig. 5.21) is similar to measured data and differences between the measured values and calculated results are almost independent on temperatures. From all of the investigated impurities, resistivities for Cu_{Mn} in a concentration between 10 % and 15 % show the best correspondence to experimental data. Although nonzero U leads to an improvement in the electronic structure [169], calculated $\rho(T)$ for 0.10, 0.15 and 0.20 Ry contradicts measurements, see Fig. 5.21 for the first value.

A slope of $\rho(T)$, which agrees with experiments, is obtained also for vac_{Mn} and vac_{Cu}, see Fig. 5.22; however, calculated data underestimate measurements even for 15 % of vacancies. For most of the examined defects, the residual resistivity may be tuned by changing concentrations of the impurity (the dependence on the concentration is almost linear for Cu_{Mn} and Mn_{Cu}). We calculated temperature-dependent resistivities for all of the defects stated in Tab. 5.4 and the slopes of $\rho(T)$ extremely differ for individual impurities, but they are almost independent on their concentrations. Based on these data, we consider: (i) Cu_{Mn}, vac_{Cu}, and vac_{Mn} to be realistic, (ii) Mn_{Cu} not present in the real samples ($\rho(T)$ almost constant), and (iii) impurities with As atoms having a low probability to be observed. This agrees with probabilities given by the formation energies [114]. It should be emphasized that this could not be obtained without the inclusion of

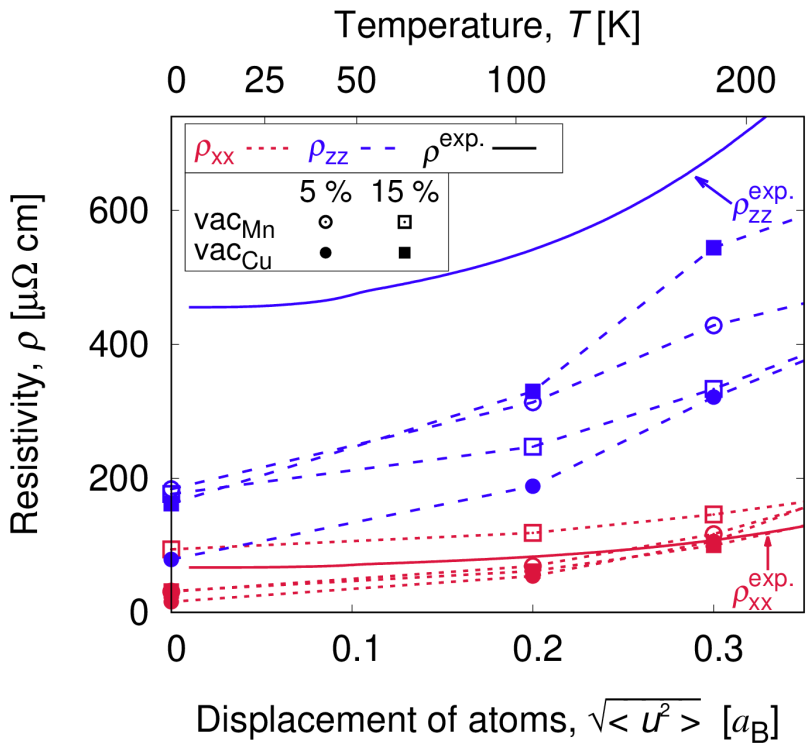

Figure 5.22: Calculated resistivities (0.00 Ry) in the in-plane (red dotted lines) and $z-$direction (blue dashed lines) agree qualitatively with experimental data [11] (full lines) for Mn (empty symbols) or Cu (full symbols) replaced by vacancies. The temperature-dependent behavior is similar for both 5 % (circles) and 15 % (squares) of impurities.

the atomic displacements.

If the Matthiessen's rule holds, i.e., the total resistivity is given by a sum of contributions for different scattering mechanisms, the measured resistivities of the Cu-rich samples may be obtained for 10 % of Cu atoms moved to Mn sublattices (10 % vacancies on Cu positions, 10 % Cu atoms on Mn positions, and 10 % Mn atoms missing). We investigated combined effects of these two impurities but the resistivities are not additive, see Fig. 5.23 for a comparison with Fig. 5.21 and 5.22. It can be concluded, that the Matthiessen's rule does not hold for combinations of most of the chemical defects, atomic displacements, and spin fluctuations.

Magnetic disorder Significant underestimation of experimental data [11] observed for high temperatures ($T \gtrsim 200$ K) is attributed to the magnetic disorder ($T_N = 480$ K [167]). The AAM may describe also disordered spins (see Sec. 4.2 or Refs. [6, 32]), but their proper inclusion is beyond the scope of this study. Therefore, we present results only for $\sqrt{\langle u^2 \rangle} \leq 0.35\, a_\mathrm{B}$ (approx. $T < 230$ K), where the major contribution comes from phonons. Table 5.5 shows results for CuMnAs with magnetic disorder and possible impurities. The high-temperature measured values may be compared with a sum of several contribution: a) residual resistivities for 10 % $\mathrm{Cu_{Mn}}$ ($\rho_{xx} = 40\,\mu\Omega$cm, $\rho_{zz} = 317\,\mu\Omega$cm), b) DLM state with 10 % $\mathrm{Cu_{Mn}}$ ($\rho_{xx} = 249\,\mu\Omega$cm, $\rho_{zz} = 513\,\mu\Omega$cm), and c) an extrapolation of the

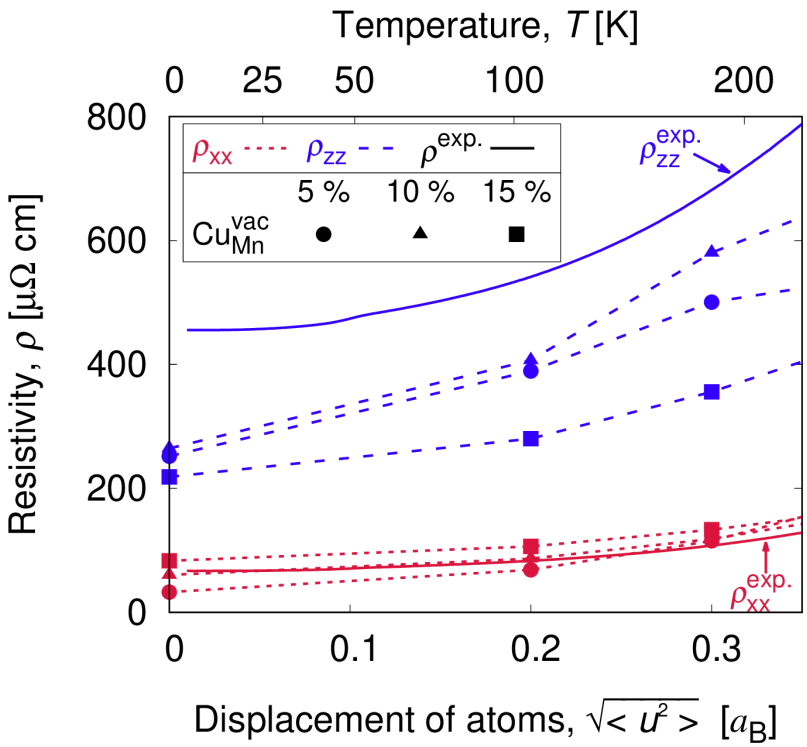

Figure 5.23: Calculated resistivities (0.00 Ry) in the in-plane (red dotted lines) and $z-$direction (blue dashed lines) for a combined effect of $\mathrm{vac_{Cu}}$ and $\mathrm{Cu_{Mn}}$ for concentrations of both impurities 5 % (circles), 10 % (triangles), and 15 % (squares) underestimate the experimental data [11]. Comparing these data with with results presented in Fig. 5.22, invalidity of the Matthiessen's rule for different impurities is obtained. Moreover, they are not monotonic with respect to the concentrations.

phonon contribution from $\sqrt{\langle u^2 \rangle} \leq 0.35\, a_\mathrm{B}$ (Fig. 5.21) to $\sqrt{\langle u^2 \rangle} \approx a_\mathrm{B}$. All of the mechanisms together result in $\rho_{xx} = 459\,\mu\Omega$cm and $\rho_{zz} = 1218\,\mu\Omega$cm. Considering a huge uncertainty in impurities and previously shown overestimation of resistivities in NiMnSb given by the Matthiessen's rule [6], it is in good agreement with experiments (400 K).

Anisotropy of resistivities Large anisotropy of resistivities is observed in experimental samples and the anisotropy are also different for various impurities assumed in the calculations. In bulk tetragonal samples, measured anisotropy ρ_{zz}/ρ_{xx} is 6.8, 6.6, and 5.9 for 0, 100, and 300 K, respectively [11]. We show the calculated anisotropies in Tab. 5.6 for the same defects as in Tab. 5.4. In addition, data for nonzero Hubbard U are presented. In general, nonzero U increases the anisotropy and for some of the defects even twice or more, see, e.g., Cu-Mn swap and $\mathrm{Mn_{Cu}}$. On the other hand, differences between the employed basis (*spd* vs. *spdf*) are not so large and the scalar-relativistic data for $U = 0.0$ Ry are similar to the fully-relativistic results (with the same parameters).

Comparing all data, i.e., anisotropies, residual resistivities, and temperature-dependent resistivities, especially $\mathrm{Vac_{Mn}}$, $\mathrm{Vac_{Cu}}$, $\mathrm{Mn_{Cu}}$, and $\mathrm{Cu_{Mn}}$ are preferable to be present in real samples. These are also the defect having low formation energies [114].

Table 5.5: The best high-temperature agreement for ρ_{xx} is obtained with 10 % of Cu_{Mn}; however, the huge measured anisotropy is not reproduced by the DLM state without phonons (0.00 Ry, *spdf*−basis).

	ρ_{xx} [$\mu\Omega$cm]	ρ_{zz} [$\mu\Omega$cm]
Measured at 200 K [11]	103	656
Measured at 300 K [11]	150	885
Measured at 400 K [11]	224	1119
Stoichiometric DLM	276	489
DLM with 5 % Mn_{Cu}	280	437
DLM with 10 % Cu_{Mn}	249	513

Temperature-depend resistivities for $U = 0.0$ Ry mostly preserve the anisotropy observed for the residual resistivity, while $U = 0.1$ Ry causes huge increase of ρ_{zz} with temperature (relative change of ρ_{xx} is smaller), see Fig. 5.21 or other previous figures for examples.

Table 5.6: Anisotropy of resistivities for CuMnAs calculated with 5 % of impurities depends especially on the defect and a value of the Hubbard parameter. The second row shows a value of U in Ry.

	Scalar rel., *spd*	Fully rel., *spd*		Fully rel., *spdf*	
Defect	0.00 Ry	0.00 Ry	0.10 Ry	0.00 Ry	0.10 Ry
Vac_{Mn}	4.31	4.81	7.02	5.94	8.84
Vac_{Cu}	3.67	4.50	6.23	4.94	8.52
Mn_{Cu}	1.54	1.77	5.17	2.35	6.12
Cu_{Mn}	5.08	5.91	5.09	5.70	7.48
Cu_{As}	2.55	3.46	6.85	3.98	7.97
As_{Cu}	2.33	2.62	4.74	3.15	5.66
As_{Mn}	2.32	1.94	3.43	3.38	3.84
Mn_{As}	1.24	2.08	5.51	2.88	9.59
Vac_{As}	1.17	1.35	4.80	1.46	5.48
Cu↔Mn	2.15	2.47	4.96	3.28	6.20

5.3 Summary of the results

Our finite-temperature calculations of electrical transport properties in prototypical half-Heusler NiMnSb alloy agree with experimental data from literature. The main conclusions of our study are:

- Both the longitudinal and anomalous Hall resistivities of the Ni-rich system (especially for 1 to 2 % of Ni atoms on the Mn sublattice) agree with measured data and also the sign of AMR is consistent with experimental literature.

- The combination of magnons and phonons reproduces fairly well the experimental resistivity even at high temperatures. It is not achieved by a bare contribution of one of the two effects and the Matthiessen's rule is valid for temperatures up to about 650 K, but it is violated by about 16 % at the Curie point (730 K).

- The effect of the Fermi-sea contribution to the AHC is generally weak although it is stronger for the Mn-rich case. The AHE in Ni-rich NiMnSb is dominated by the $\sigma^{(1)}$ part ("integration over the Fermi sheets") of the conductivity, while for the Mn-rich case, the $\sigma^{(2)}$ ("complex integration over the valence spectrum") term represents a sizable contribution of the order of 20 %. Qualitatively different behavior of the AHC was observed for the Mn- and Ni-rich systems.

- Both models of the magnetic disorder yield the same dependence of the total energy on the alloy magnetization, but the tilting model is more realistic for a description of electrical transport. The uDLM model overestimates the influence of spin fluctuations on the electrical resistivity.

- The calculated spin-current polarization is typically greater than 0.9 at room temperature for studied concentrations of the impurities and its behavior correlates with the half-metallic-like character (small amount of states in the minority channel). Its values overestimate available experimental data and the calculations indicate the possibility to influence current spin polarization by tuning chemical composition.

AFM CuMnAs with six sublattices is probably the most complex system for which the AAM was employed to study the finite-temperature electrical transport properties. Despite that, the formalism was used successfully and no physical limitations were found. The following conclusions can be made:

- Obtained electronic structure is in agreement with literature and based on the bandstructure or total DOS, the correct Hubbard U cannot be precisely determined. The correct symmetry with respect to the canted and rotated magnetic moments is obtained.

- Without the temperature dependence, the zero-temperature (residual) resistivity could be ambiguously ascribed to several different chemical impurities. Our calculated temperature-dependent resistivity agrees with experimental data for approx. 10 % Cu atoms on the Mn sublattices; a combination of various chemical defects is also possible. The high-temperature

DLM ρ_{xx} agrees with experimental data, but the measured increase in ρ_{zz} is not reproduced by the DLM state.

- Calculated resistivities, which we obtained for nonzero Hubbard parameters, increase much faster (probably not realistically) with temperature than experimental values. Therefore, our results show that $U = 0.00\,\mathrm{Ry}$ gives the best agreement with experiments.

- Although the numerical expenses of the finite-temperature calculations are higher for CuMnAs compared to materials with a lower number of sublattices, the AAM can be probably used even for more complex materials.

Conclusions

This thesis is focused on theory of spin-dependent transport in magnetic solids. For the purposes of both describing novel physical phenomena and studying materials relevant for spintronics, we have implemented the AAM within *ab initio* numerical codes based on the relativistic TB-LMTO method and the CPA. This first-principles framework opened possibilities to investigate an influence of finite temperatures for a wide range of materials, even those with nontrivial magnetic structures. Because knowledge of electrical transport properties in these materials is essential for electronic applications, the conductivity (or resistivity) influenced by atomic displacements and fluctuations of magnetic moments was studied. Moreover, due to spintronic applications, part of the results describes also the spin disorder and spin polarization of electrical current. The aims of this thesis (which are stated in the Introduction) are now addressed in details and then possibilities for further studies are described.

Implementation of the AAM within the TB-LMTO method with the CPA The AAM describing atomic displacements was successfully developed (Sec. 2.1) and incorporated (Chapter 3) within the *ab initio* TB-LMTO method with the CPA. Both physical and numerical properties of the model were tested to verify its robustness and efficiency. Although the AAM has a number of limitations (Sec. 2.5), it was found to be suitable and usable for many systems. This thesis is focused on magnetic and spintronic materials; therefore, especially electrical transport in transition metals and their alloys (both random and nonrandom) was described and most of the results agree well with literature (Chapter 4). Because the framework is numerically cheap, compared to other similar techniques, it can be used even for complex systems and it allows one to efficiently describe the combined effect of different finite-temperature phenomena or scattering mechanisms on electrical transport (Sec. 2.3).

Realistic description of finite temperatures The AAM was used to approximate phonons and two models of magnetic disorder (uncompensated disorder local moments, tilting of magnetic moments) were employed to treat magnetic solids at finite temperatures. Moreover, the effect of the broadened Fermi-Dirac distribution (entering the linear response theory for $T > 0$) was investigated, found to be small (Sec. 4.4), and, therefore, neglected in most of the calculations. For the description of phonons, directions of displacements are of minor influence (Sec. 2.3.1). The magnitudes of the displacements were mostly obtained from the Debye theory; more proper values were taken from the VASP software or the high-temperature simulation of molecular dynamics could be also used (Sec. 2.3.1) but these advanced methods were not necessary for most of the systems. Similarly, the total magnetization as a function of temperature was obtained from literature and used as an input parameter (Sec. 4.2); although it can be obtained by *ab initio* techniques which, however, would be beyond the scope of this thesis. The presented formalism was successfully used to describe even extreme conditions in the Earth's core (Sec. 4.5).

Study of spintronic materials influenced by various types disorder The developed and tested formalism can be not only used to reproduce data from literature but also to predict behavior of novel systems and relevant material properties. For purposes of spintronic applications, the spin-resolved electrical conductivity was examined for systems with different chemical composition and magnetization and the studied materials were also disordered by finite temperatures (Sec. 4.6). Techniques previously tested on pure metals and random alloys (Chapter 4) were then applied on half-Heusler NiMnSb alloy (Sec. 5.1) and antiferromagnetic CuMnAs compound (Sec. 5.2). Both of them are multisublattice alloys, they can be influenced by various impurities, and the composition is not exactly known in experimental samples. Not only do the finite-temperature resistivities agree with experimental data, but our data also helped to identify the possible defects.

For half-Heusler NiMnSb, important spintronic phenomena such as the spin polarization of electrical current were investigated. Moreover, contributions of atomic displacements and spin fluctuations at $T > 0$ to the scattering mechanisms were examined and the influence of electronic structure on transport properties, both the longitudinal conductivity and anomalous Hall conductivity, was discussed.

In tetragonal CuMnAs, both the electronic structure and electrical resistivities were studied. This antiferromagnetic material is important because of a wide range of spintronic applications; therefore, we focused on its chemical composition, non-collinear magnetic moments, and a role of temperature. Above that, hypothetical cases such as ferromagnetic CuMnAs were investigated.

Although we have shown that our approaches to finite-temperature effects are suitable for many purposes, there are still open topics that could be addressed in future studies. From a technical point of view, various simplifying assumptions were employed. It could be improved or replaced by more advanced techniques. For example, instead of the Debye theory or fitting of measured temperature-dependent magnetization, *ab initio* methods could lead to more accurate results. This thesis is focused especially on the longitudinal electrical transport and anomalous Hall conductivity, but there are other phenomena that could be described by the linear response theory on an equal footing such as the Gilbert damping, spin Hall effect, and spin-orbit torques. We introduced a formalism and methods to deal with finite-temperature phenomena, however a complete combination of different scattering mechanisms (impurities, phonons, and magnons) are beyond our capabilities. Above that, the AAM could be combined with other temperature-dependent effects such as a change of geometry (dependence of lattice parameters on temperature). Last but not least, even more complex materials than CuMnAs and advanced systems such as layered structures could be examined.

Bibliography

[1] D. Wagenknecht, I. Turek, and K. Carva, in *WDS'15 Proceedings of Contributed Papers - Physics*, edited by J. Šafránková and J. Pavlů (Matfyzpress, 2015) pp. 42–47, ISBN: 978-80-7378-311-2.

[2] D. Wagenknecht, K. Carva, and I. Turek, IEEE Transactions on Magnetics **53**, 517 (2017).

[3] V. Drchal, J. Kudrnovský, D. Wagenknecht, I. Turek, and S. Khmelevskyi, Physical Review B **96**, 024432 (2017).

[4] D. Wagenknecht, K. Carva, and I. Turek, Proceedings of SPIE **10357**, 10357 (2017).

[5] V. Drchal, J. Kudrnovský, D. Wagenknecht, and I. Turek, Physical Review B **98**, 134442 (2018).

[6] D. Wagenknecht, J. Kudrnovský, L. Šmejkal, K. Carva, and I. Turek, Journal of Magnetism and Magnetic Materials **474**, 517 (2019).

[7] V. Drchal, J. Kudrnovský, I. Turek, D. Wagenknecht, and S. Khmelevskyi, Solid State Phenomena **289**, 185 (2019).

[8] V. Drchal, J. Kudrnovský, D. Wagenknecht, and I. Turek, Journal of Magnetism and Magnetic Materials **475**, 767 (2019).

[9] D. Wagenknecht, L. Šmejkal, Z. Kašpar, J. Sinova, T. Jungwirth, J. Kudrnovský, K. Carva, and I. Turek, Submitted to PRB (March 2019) .

[10] D. Wagenknecht and I. Turek, In preparation: Anisotropy of resistivity in hexagonal late transition metals and their alloys .

[11] J. Volný, D. Wagenknecht, I. Turek, J. Železný, K. Výborný, and K. Uhlířová, In preparation: Electrical transport properties of bulk tetragonal CuMnAs .

[12] I. Turek, V. Drchal, J. Kudrnovský, M. Šob, and P. Weinberger, *Electronic structure of disordered alloys, surfaces and interfaces*, 1st ed. (Kluwer Academic Publishers, Boston, MA, USA, 1997).

[13] A. Gonis, *Theoretical materials science: Tracing the electronic origins of materials behavior* (Materials Research Society, Warrendale, PA, USA, 2000).

[14] J. Coey, *Magnetism and Magnetic Materials*, Magnetism and Magnetic Materials (Cambridge University Press, 2010).

[15] C. Kittel, *Introduction to solid state physics* (Wiley, 1986).

[16] R. O'Handley, *Modern Magnetic Materials: Principles and Applications* (Wiley, 1999).

[17] A. Ramirez, Annual Review of Materials Science **24**, 453 (1994).

[18] F. Gerhard, C. Schumacher, C. Gould, and L. W. Molenkamp, Journal of Applied Physics **115**, 094505 (2014).

[19] K. Uhlířová, E. Duverger-Nédellec, R. Colman, J. Volný, B. Vondráčková, and K. Carva, Journal of Alloys and Compounds **771**, 680 (2019).

[20] S. K. Bose, J. Kudrnovský, V. Drchal, and I. Turek, Physical Review B **82**, 174402 (2010).

[21] W. Schreiner, D. Brandão, F. Ogiba, and J. Kunzler, Journal of Physics and Chemistry of Solids **43**, 777 (1982).

[22] J. M. Ziman, *Electrons and phonons: The Theory of transport phenomena in solids*, International series of monographs on physics (Clarendon Press, Oxford, 1960).

[23] N. Ashcroft and N. Mermin, *Solid State Physics*, HRW international editions (Holt, Rinehart and Winston, 1976).

[24] F. Brouers and M. Brauwers, Journal de Physique Lettres **36**, 17 (1975).

[25] N. Wiser, Contemporary Physics **25**, 211 (1984).

[26] C. Hordequin, D. Ristoiu, L. Ranno, and J. Pierre, The European Physical Journal B - Condensed Matter and Complex Systems **16**, 287 (2000).

[27] J. K. Glasbrenner, B. S. Pujari, and K. D. Belashchenko, Physical Review B **89**, 174408 (2014).

[28] G. Shen, W. Sturhahn, E. Alph, J. Zhao, T. Tollenner, V. Prakapenka, Y. Meng, and H.-R. Mao, Physics and Chemistry of Minerals **31**, 353 (2004).

[29] H. Ebert, S. Mankovsky, K. Chadova, S. Polesya, J. Minár, and D. Ködderitzsch, Physical Review B **91**, 165132 (2015).

[30] S. Mankovsky, D. Ködderitzsch, G. Woltersdorf, and H. Ebert, Physical Review B **87**, 014430 (2013).

[31] D. Ködderitzsch, K. Chadova, J. Minár, and H. Ebert, New Journal of Physics **15**, 053009 (2013).

[32] A. Starikov, Y. Liu, Z. Yuan, and P. Kelly, Physical Review B **97**, 214415 (2018).

[33] B. Skubic, J. Hellsvik, L. Nordström, and O. Eriksson, Journal of Physics: Condensed Matter **20**, 315203 (2008).

[34] M. D. Kuz'min, Physical Review Lett. **94**, 107204 (2005).

[35] P.-W. Ma, S. L. Dudarev, and J. S. Wróbel, Physical Review B **96**, 094418 (2017).

[36] R. A. de Groot, F. M. Mueller, P. G. v. Engen, and K. H. J. Buschow, Physical Review Lett. **50**, 2024 (1983).

[37] N. Nagaosa, J. Sinova, S. Onoda, A. H. MacDonald, and N. P. Ong, Rev. Mod. Phys. **82**, 1539 (2010).

[38] W. Döring, Annalen der Physik **424**, 259 (1938).

[39] S. Zhang and S. Zhang, Journal of Applied Physics **115**, 17C703 (2014).

[40] J. Kudrnovský, V. Drchal, and I. Turek, Journal of Superconductivity and Novel Magnetism **30**, 1367 (2017).

[41] C. Ciccarelli, L. Anderson, V. Tshitoyan, A. J. Ferguson, F. Gerhard, C. Gould, L. W. Molenkamp, J. Gayles, J. Železný, L. Šmejkal, Z. S. Yuan, F. Freimuth, and T. Jungwirth, Nature Physics **12**, 855–860 (2016).

[42] A. W. Rushforth, K. Výborný, C. S. King, K. W. Edmonds, R. P. Campion, C. T. Foxon, J. Wunderlich, A. C. Irvine, P. Vašek, V. Novák, K. Olejník, J. Sinova, T. Jungwirth, and B. L. Gallagher, Physical Review Lett. **99**, 147207 (2007).

[43] I. A. Campbell, A. Fert, and R. Pomeroy, Philosophical Magazine **15**, 977 (1967).

[44] A. Fert and I. A. Campbell, Physical Review Lett. **21**, 1190 (1968).

[45] I. Žutić, J. Fabian, and S. Das Sarma, Rev. Mod. Phys. **76**, 323 (2004).

[46] X. Li and J. Yang, National Science Review **3**, 365 (2016).

[47] T. Jungwirth, X. Marti, P. Wadley, and J. Wunderlich, Nature Nanotechnology **11**, 231–241 (2016).

[48] E. V. Gomonay and V. M. Loktev, Low Temperature Physics **40**, 17 (2014).

[49] A. Manchon, H. Koo, J. Nitta, S. Frolov, and R. Duine, Nature materials **14**, 871 (2015).

[50] M. König, S. Wiedmann, C. Brüne, A. Roth, H. Buhmann, L. Molenkamp, X. Qi, and S. Zhang, Science **318**, 766 (2007).

[51] N. Kiyohara, T. Tomita, and S. Nakatsuji, Physical Review Applied **5**, 064009 (2016).

[52] C. Suergers, Nature Electronics **1**, 154 (2018).

[53] J. Sinova, S. Valenzuela, J. Wunderlich, C. H. Back, and T. Jungwirth, Rev. Mod. Phys. **87**, 1213 (2015).

[54] Y. Pershin, N. Sinitsyn, A. Kogan, A. Saxena, and D. Smith, Applied Physics Letters **95**, 022114 (2009).

[55] L. Šmejkal, R. González-Hernández, T. Jungwirth, and J. Sinova, arXiv preprint arXiv:1901.00445 (2019).

[56] S. Bhatti, R. Sbiaa, A. Hirohata, H. Ohno, S. Fukami, and S. Piramanayagam, Materials Today **20**, 530 (2017).

[57] J. Železný, H. Gao, K. Výborný, J. Zemen, J. Mašek, A. Manchon, J. Wunderlich, J. Sinova, and T. Jungwirth, Physical Review Lett. **113**, 157201 (2014).

[58] P. Wadley, B. Howells, J. Železný, C. Andrews, V. Hills, R. P. Campion, V. Novák, K. Olejník, F. Maccherozzi, S. S. Dhesi, S. Y. Martin, T. Wagner, J. Wunderlich, F. Freimuth, Y. Mokrousov, J. Kuneš, J. S. Chauhan, M. J. Grzybowski, A. W. Rushforth, K. W. Edmonds, B. L. Gallagher, and T. Jungwirth, Science **351**, 587 (2016).

[59] S. Bodnar, L. Šmejkal, I. Turek, T. Jungwirth, O. Gomonay, J. Sinova, A. Sapozhnik, H. Elmers, M. Klui, and M. Jourdan, Nature Communications **9**, 348 (2018).

[60] D. R. Hartree, Mathematical Proceedings of the Cambridge Philosophical Society **24**, 89–110 (1928).

[61] D. R. Hartree, Mathematical Proceedings of the Cambridge Philosophical Society **24**, 111–132 (1928).

[62] J. C. Slater, Physical Review **34**, 1293 (1929).

[63] F. Bloch, Zeitschrift für Physik **57**, 545 (1929).

[64] P. Dirac, Proceedings of the Royal Society of London A: Mathematical, Physical and Engineering Sciences **123**, 714 (1929).

[65] Mathematical Proceedings of the Cambridge Philosophical Society **25**, 62–66 (1929).

[66] V. Fock, Zeitschrift für Physik **61**, 126 (1930).

[67] R. O. Jones, Rev. Mod. Phys. **87**, 897 (2015).

[68] J. M. Tomczak, P. Liu, A. Toschi, G. Kresse, and K. Held, The European Physical Journal Special Topics **226**, 2565 (2017).

[69] H. Jiang, R. I. Gomez-Abal, P. Rinke, and M. Scheffler, Physical Review B **82**, 045108 (2010).

[70] P. Strange, *Relativistic Quantum Mechanics: With Applications in Condensed Matter and Atomic Physics*, Religious Studies; 47 (Cambridge University Press, 1998).

[71] E. Kryachko and E. Ludeña, Physics Reports **544**, 123 (2014).

[72] R. Kubo, Journal of the Physical Society of Japan **12**, 570 (1957).

[73] D. A. Greenwood, Proceedings of the Physical Society **71**, 585 (1958).

[74] I. Turek, J. Kudrnovský, and V. Drchal, Physical Review B **86**, 014405 (2012).

[75] W. Kohn and L. J. Sham, Physical Review **140**, A1133 (1965).

[76] P. Strange, J. Staunton, and B. Gyorffy, Journal of Physics C: Solid State Physics **17**, 3355 (1984).

[77] J. Harris, Physical Review B **31**, 1770 (1985).

[78] J. Hubbard, Proceedings of the Royal Society of London A: Mathematical, Physical and Engineering Sciences **276**, 238 (1963).

[79] J. Perdew, Physical Review B **33**, 8822 (1986).

[80] I. Turek, J. Kudrnovský, V. Drchal, L. Szunyogh, and P. Weinberger, Physical Review B **65**, 125101 (2002).

[81] I. Turek, J. Kudrnovský, and V. Drchal, Physical Review B **89**, 064405 (2014).

[82] K. Carva, I. Turek, J. Kudrnovský, and O. Bengone, Physical Review B **73**, 144421 (2006).

[83] A. Bastin, C. Lewiner, O. Betbeder-Matibet, and P. Nozieres, Journal of Physics and Chemistry of Solids **32**, 1811 (1971).

[84] P. Středa, Journal of Physics C: Solid State Physics **15**, L717 (1982).

[85] I. Turek, Physical Review B **93**, 245114 (2016).

[86] K. Shirai and K. Yamanaka, Journal of Applied Physics **113**, 053705 (2013).

[87] P. B. Allen, T. P. Beaulac, F. S. Khan, W. H. Butler, F. J. Pinski, and J. C. Swihart, Physical Review B **34**, 4331 (1986).

[88] S. Y. Savrasov and D. Y. Savrasov, Physical Review B **54**, 16487 (1996).

[89] H. Ebert, S. Mankovsky, D. Ködderitzsch, and P. J. Kelly, Physical Review Lett. **107**, 066603 (2011).

[90] H. Ebert, J. Braun, J. Minár, and S. Mankovsky, in *Multiple Scattering Theory for Spectroscopies*, edited by D. Sébilleau, K. Hatada, and H. Ebert (Springer International Publishing, Cham, 2018) pp. 339–344.

[91] Y. Liu, A. A. Starikov, Z. Yuan, and P. J. Kelly, Physical Review B **84**, 014412 (2011).

[92] Y. Liu, Z. Yuan, R. Wesselink, A. Starikov, M. van Schilfgaarde, and P. Kelly, Physical Review B **91**, 220405 (2015).

[93] R. Mehrem, Applied Mathematics and Computation **217**, 5360 (2011).

[94] J. Staunton, B. L. Gyorffy, A. J. Pindor, G. M. Stocks, and H. Winter, Journal of Physics F: Metal Physics **15**, 1387 (1985).

[95] B. Gyorffy, A. Pindor, J. Staunton, G. Stocks, and H. Winter, Journal of Physics F: Metal Physics **15**, 1337 (1985).

[96] J. Kudrnovský, V. Drchal, I. Turek, S. Khmelevskyi, J. K. Glasbrenner, and K. D. Belashchenko, Physical Review B **86**, 144423 (2012).

[97] V. Drchal, J. Kudrnovský, and I. Turek, EPJ Web of Conferences **40**, 11001 (2013).

[98] A. V. Ruban, S. Khmelevskyi, P. Mohn, and B. Johansson, Physical Review B **75**, 054402 (2007).

[99] J. Kudrnovský, V. Drchal, I. Turek, and P. Weinberger, Physical Review B **78**, 054441 (2008).

[100] J. Kudrnovský, V. Drchal, and I. Turek, Physical Review B **92**, 224421 (2015).

[101] K. Schwarz and P. Mohn, Journal of Physics F: Metal Physics **14**, L129 (1984).

[102] V. L. Moruzzi, P. M. Marcus, K. Schwarz, and P. Mohn, Physical Review B **34**, 1784 (1986).

[103] A. V. Ruban, S. Khmelevskyi, P. Mohn, and B. Johansson, Physical Review B **75**, 054402 (2007).

[104] A. V. Ruban, A. B. Belonoshko, and N. V. Skorodumova, Physical Review B **87**, 014405 (2013).

[105] E. F. Skelton and J. L. Katz, Physical Review **171**, 801 (1968).

[106] G. Ouyang, Z. M. Zhu, W. G. Zhu, and C. Q. Sun, The Journal of Physical Chemistry C **114**, 1805 (2010).

[107] M. Fuhrer, Physics **3**, 256805 (2010).

[108] M. Al-Jalali and S. Mouhammad, International Journal of Pure and Applied Mathematics **102**, 233 (2015).

[109] P. Debye, Annalen der Physik **344**, 789 (1912).

[110] M. Shubin and T. Sunada, Pure and Applied Mathematics Quarterly **3**, 745 – 777 (2006).

[111] E. Owen and E. Evans, British Journal of Applied Physics **18**, 611 (1967).

[112] I. G. Wood, K. S. Knight, G. D. Price, and J. A. Stuartd, Journal of Applied Crystallography **35**, 291 (2002).

[113] S. Pati, R. Jat, S. Mukerjee, and S. Parida, Physica B: Condensed Matter **484**, 42 (2016).

[114] F. Máca, J. Kudrnovský, P. Baláž, V. Drchal, K. Carva, and I. Turek, Journal of Magnetism and Magnetic Materials **474**, 467 (2019).

[115] R. A. Matula, Journal of Physical and Chemical Reference Data **8**, 1147 (1979).

[116] B. Martorell, L. Vočadlo, J. Brodholt, and I. Wood, Science **342**, 466 (2013).

[117] R. Edsinger, M. Reilly, and J. Schooley, Journal of Research of the National Bureau of Standards **91**, 333 (1986).

[118] S. Gardelis, J. Androulakis, P. Migiakis, J. Giapintzakis, S. K. Clowes, Y. Bugoslavsky, W. R. Branford, Y. Miyoshi, and L. F. Cohen, Journal of Applied Physics **95**, 8063 (2004).

[119] L. Ritchie, G. Xiao, Y. Ji, T. Y. Chen, C. L. Chien, . Zhang, J. Chen, Z. Liu, G. Wu, and X. X. Zhang, Physical Review B **68**, 104430 (2003).

[120] S. Ren, J. Gao, X. Jiang, G. Ji, W. Zou, F. Zhang, and Y. Du, Journal of Alloys and Compounds **384**, 22 (2004).

[121] D. Orgassa, H. Fujiwara, T. C. Schulthess, and W. H. Butler, Physical Review B **60**, 13237 (1999).

[122] N. Mott, Advances in Physics **13**, 325 (1964).

[123] S. H. Vosko, L. Wilk, and M. Nusair, Canadian Journal of Physics **58**, 1200 (1980).

[124] V. J. Mimeault and R. S. Hansen, The Journal of Chemical Physics **45**, 2240 (1966).

[125] E. Y. Garcia and D. G. Loffler, Journal of Chemical & Engineering Data **30**, 304 (1985).

[126] J. M. Plc, Johnson Matthey Technology Review **28**, 164 (1984).

[127] L. Ye, Y. Tian, X. Jin, and D. Xiao, Physical Review B **85**, 220403 (2012).

[128] F. Máca, J. Mašek, O. Stelmakhovych, X. Martí, H. Reichlová, K. Uhlířová, P. Beran, P. Wadley, V. Novák, and T. Jungwirth, Journal of Magnetism and Magnetic Materials **324**, 1606 (2012).

[129] F. Kuang, X. Kuang, K. S.y., and A. Mao, Physica B: Condensed Matter **441**, 72 (2014).

[130] J. W. Arblaster, Johnson Matthey Technology Review **60**, 179 (2016).

[131] F. Ono and H. Maeta, J. Phys. Colloques **49**, C8 (1988).

[132] J. W. Arblaster, Johnson Matthey Technology Review **57**, 127 (2013).

[133] J. W. Arblaster, Johnson Matthey Technology Review **57**, 177 (2013).

[134] H. Masumoto, H. Saito, and M. Kikuchi, Journal of the Japan Institute of Metals **30** (1966).

[135] S. Arajs and R. V. Colvin, Physica status solidi (b) **6**, 797 (1964).

[136] H. M. Ahmad and D. Greig, J. Phys. Colloques **35**, C4 (1974).

[137] C. Ho, W. Ackerman, K. Wu, T. Havill, R. Bogaard, R. Matula, S. Oh, and H. James, J. Phys. Chem. Ref. Data **12**, 183 (1983).

[138] J. Baijal and U. Baijal, Physics Letters **23**, 67 (1966).

[139] T. Hicks, Journal of Physics F: Metal Physics **7**, 481 (1977).

[140] Y. Cheng, Y. Zheng, X. Huang, K. Zhong, Z. Chen, and Z. Huang, Rare Metals **31**, 130 (2012).

[141] G. Blaise and M. Cadeville, Physical Review B **36**, 545 (1975).

[142] S. U. Jen and S. S. Liou, Journal of Applied Physics **85**, 8217 (1999).

[143] L. H. Bennett, T. B. Massalski, J. Murray, and H. Baker, *Binary alloy phase diagrams* (Metals Park, Ohio : American Society for Metals, 1986) "Alloy phase diagram master grid" in pocket.

[144] M. Pozzo and D. Alfè, SpringerPlus **5**, 256 (2016).

[145] B. Alling, S. Shallcross, and I. A. Abrikosov, Physical Review B **73**, 064418 (2006).

[146] C. Hordequin, E. Lelievre-Berna, and J. Pierre, Physica B: Condensed Matter **234**, 602 (1997), proceedings of the First European Conference on Neutron Scattering.

[147] M. Otto, R. Van Woerden, P. Van der Valk, J. Wijngaard, C. Van Bruggen, C. Haas, and K. Buschow, Journal of Physics: Condensed Matter **1**, 2341 (1989).

[148] W. Branford, S. Roy, S. Clowes, Y. Miyoshi, Y. Bugoslavsky, S. Gardelis, J. Giapintzakis, and L. Cohen, Journal of Magnetism and Magnetic Materials **272**, E1399 (2004), proceedings of the International Conference on Magnetism (ICM 2003).

[149] K. Momma and F. Izumi, Journal of Applied Crystallography **44**, 1272 (2011).

[150] M. I. Katsnelson, V. Y. Irkhin, L. Chioncel, A. I. Lichtenstein, and R. A. de Groot, Rev. Mod. Phys. **80**, 315 (2008).

[151] R. A. de Groot, F. M. Mueller, P. G. v. Engen, and K. H. J. Buschow, Physical Review Lett. **50**, 2024 (1983).

[152] R. J. Soulen, J. M. Byers, M. S. Osofsky, B. Nadgorny, T. Ambrose, S. F. Cheng, P. R. Broussard, C. T. Tanaka, J. Nowak, J. S. Moodera, A. Barry, and J. M. D. Coey, Science **282**, 85 (1998).

[153] S. K. Clowes, Y. Miyoshi, Y. Bugoslavsky, W. R. Branford, C. Grigorescu, S. A. Manea, O. Monnereau, and L. F. Cohen, Physical Review B **69**, 214425 (2004).

[154] G. Qu, P. Cheng, Y. Du, Y. Sakuraba, S. Kasai, and K. Hono, Applied Physics Letters **111**, 222402 (2017).

[155] G. Bona, F. Meier, M. Taborelli, E. Bucher, and P. Schmidt, Solid State Communications **56**, 391 (1985).

[156] C. Morari, W. H. Appelt, A. Östlin, A. Prinz-Zwick, U. Schwingenschlögl, U. Eckern, and L. Chioncel, Physical Review B **96**, 205137 (2017).

[157] C. N. Borca, T. Komesu, H. Jeong, P. A. Dowben, D. Ristoiu, C. Hordequin, J. Pierre, and J. P. Nozières, Applied Physics Letters **77**, 88 (2000).

[158] S. Podgornykh, S. Streltsov, V. Kazantsev, and E. Shreder, Journal of Magnetism and Magnetic Materials **311**, 530 (2007).

[159] Y. Wu, , B. Wei, Z. Zhou, C. Zhao, Y. Xiong, S. Tou, S. Yang, B. Zhou, and Y. Shao, Intermetallics **53**, 26 (2014).

[160] M. Pugaczowa-Michalska, Solid State Communications **140**, 251 (2006).

[161] M. Otto, R. A. M. van Woerden, P. J. van der Valk, J. Wijngaard, C. F. van Bruggen, and C. Haas, Journal of Physics: Condensed Matter **1**, 2351 (1989).

[162] J. Rusz, L. Bergqvist, J. Kudrnovský, and I. Turek, Physical Review B **73**, 214412 (2006).

[163] J. Rusz, J. Kudrnovský, and I. Turek, Journal of Magnetism and Magnetic Materials **310**, 1654 (2007), proceedings of the 17th International Conference on Magnetism.

[164] S. Lowitzer, D. Ködderitzsch, and H. Ebert, Physical Review Lett. **105**, 266604 (2010).

[165] K. Takahashi, H. Ishizuka, T. Murata, Q. Wang, Y. Tokura, N. Nagaosa, and M. Kawasaki, Science Advances **4** (2018), 10.1126/sciadv.aar7880.

[166] J. Friedel, The London, Edinburgh, and Dublin Philosophical Magazine and Journal of Science **43**, 153 (1952).

[167] P. Wadley, V. Hills, M. Shahedkhah, K. Edmonds, R. Campion, V. Novák, B. Ouladdiaf, D. Khalyavin, S. Langridge, V. Saidl, P. Němec, A. Rushforth, B. Gallagher, F. Dhesi, S.S. Maccherozzi, J. Železný, and T. Jungwirth, Scientific Reports **5**, 17079 (2015).

[168] X. Zhang, S. Sun, and H. Lei, Physical Review B **96**, 235105 (2017).

[169] M. Veis, J. Minár, G. Steciuk, L. Palatinus, C. Rinaldi, M. Cantoni, D. Kriegner, K. K. Tikuišis, J. Hamrle, M. Zahradník, R. Antoš, J. Železný, L. Šmejkal, X. Marti, P. Wadley, R. P. Campion, C. Frontera, K. Uhlířová, T. Duchoň, P. Kužel, V. Novák, T. Jungwirth, and K. Výborný, Physical Review B **97**, 125109 (2018).

[170] F. Máca, J. Kudrnovský, V. Drchal, K. Carva, P. Baláž, and I. Turek, Physical Review B **96**, 094406 (2017).

[171] P. Němec, M. Fiebig, T. Kampfrath, and A. Kimel, Nature Physics **14**, 229–241 (2018).

[172] A. Regnat, A. Bauer, A. Senyshyn, M. Meven, K. Hradil, P. Jorba, K. Nemkovski, B. Pedersen, R. Georgii, S. Gottlieb-Schönmeyer, and C. Pfleiderer, Physical Review Materials **2**, 054413 (2018).

List of Figures

List of Tables

List of abbreviations

AAM	The alloy analogy model
AFM state	The antiferromagnetic state
AHC	The anomalous Hall conductivity
AHE	The anomalous Hall effect
AMR	The anisotropic magnetoresistance
ASA	The atomic sphere approximation
BZ	The Brillouin zone
CPA	The coherent potential approximation
DLM model	The disordered local moment model
DOS	The density of states
FM state	The ferromagnetic state
FRTA	The finite relaxation time approximation
FSM method	The fixed-spin moment method
GGA	The generalized gradient approximation
HPC	The high performance computing
KKR method	The Korringa-Kohn-Rostoker method
LDA	The local-density approximation
LSDA	The local spin-density approximation
NM state	The nonmagnetic state
PM state	The paramagnetic state
SDR	The spin-disorder resistivity
TB-LMTO method	The tight-binding linear muffin-tin orbital method
uDLM model	The uncompensated DLM model
VCA	The virtual crystal approximation
XC	The exchange–correlation

List of publications

Electrical transport of transition metals and their alloys with atomic displacements

Published: David Wagenknecht, Ilja Turek, and Karel Carva. Ab Initio Calculations of Temperature Dependent Resistivity for Transition Metals, in WDS'15 Proceedings of Contributed Papers – Physics (eds. J. Šafránková and J. Pavlů), Prague, Matfyzpress, pp. 42–47 (2015)

Published: David Wagenknecht, Karel Carva, and Ilja Turek. Fully relativistic temperature dependent electronic transport properties of magnetic alloys from the first principles. IEEE Transactions on Magnetics, vol. 53, issue 11, no. 1700205, p. 1–5 (2017)

Published: David Wagenknecht, Karel Carva, and Ilja Turek. Spin-dependent electronic transport at finite temperatures from the first principles. Proceedings of SPIE, Spintronics X, vol. 10357, p. 103572W (2017)

Electrical transport of iron and alloys at conditions of the Earth's core

Published: Václav Drchal, Josef Kudrnovský, David Wagenknecht, Ilja Turek, and Sergii Khmelevskyi. Transport properties of iron at the Earth's core conditions: the effect of spin disorder. Physical Review B, vol. 96, p. 024432 (2017)

Published: Václav Drchal, Josef Kudrnovský, David Wagenknecht, and Ilja Turek. Alloy disorder and fluctuating magnetic moments in the Earth's core. Journal of Magnetism and Magnetic Materials, vol. 475, p. 767–771 (2019)

Spin-disorder resistivity of magnetic alloys

Published: Václav Drchal, Josef Kudrnovský, David Wagenknecht, and Ilja Turek. Spin-disorder resistivity of random fcc-NiFe alloys. Physical Review B, vol. 98, p. 134442 (2018)

Published: Josef Kudrnovský, Václav Drchal, Ilja Turek, David Wagenknecht, and Sergii Khmelevskyi. The spin-disorder resistivity: the disordered local moment approach. Solid State Phenomena, vol. 289, p. 185–191 (2019)

Structural anisotropy influenced by various scattering mechanism

In preparation (April 2019): David Wagenknecht and Ilja Turek. Anisotropy of resistivity in hexagonal late transition metals and their alloys.

Study of multi-sublattice systems at finite temperatures

Published: David Wagenknecht, Josef Kudrnovský, Libor Šmejkal, Karel Carva, and Ilja Turek. Electrical transport with temperature-induced spin disorder in NiMnSb. Journal of Magnetism and Magnetic Materials, vol. 474, p. 517–521 (2019)

Submitted: David Wagenknecht, Libor Šmejkal, Zdeněk Kašpar, Jairo Sinova, Tomáš Jungwirth, Josef Kudrnovský, Karel Carva, and Ilja Turek. Temperature-dependent resistivity and anomalous Hall effect in NiMnSb from the first-principles. Submitted to Physical Review B (March 2019).

In preparation (April 2019): Jiří Volný, David Wagenknecht, Ilja Turek, Jakub Železný, Karel Výborný, Klára Uhlířová. Transport properties of bulk teragonal CuMnAs.

Theory and experiments focused on optical anisotropy in GaMnAs

Published: David Wagenknecht, Eva Schmoranzerová, František Trojánek, Petr Němec, and Tomáš Ostatnický. Transverse Kerr effect in magnetic (Ga, Mn)As-based semiconductors and its applicability in waveguide isolators. Journal of Applied Physics, vol. 122, p. 023104 (2017)